Equilibrium properties of crystals in the Hard–sphere and the Asakura–Oosawa model

Dissertation

der Mathematisch-Naturwissenschaftlichen Fakultät

der Eberhard Karls Universität Tübingen

zur Erlangung des Grades eines

Doktors der Naturwissenschaften

(Dr. rer. nat.)

vorgelegt von

Mostafa Mortazavifar

aus Teheran/Iran

Tübingen

2016

Gedruckt mit Genehmigung der Mathematisch–Naturwissenschaftlichen Fakultät der Eberhard Karls Universität Tübingen.

Tag der mündlichen Qualifikation:	02.11.2016
Dekan:	Prof. Dr. Wolfgang Rosenstiel
1. Berichterstatter:	Prof. Dr. Martin Oettel
2. Berichterstatter:	Prof. Dr. Roland Roth

to Golzar,

and her passionate soul.

PREFACE

I started working on my PhD thesis in group of Prof. Dr. Martin Oettel in September 2012. At that time, he still did have a juniour research group at *Institute of Physics: Condensed Matter Theory Group* in *Johannes Gutenberg-Universität Mainz*. After two months of temporary stay in Mainz, I moved with the group to Tübingen where Prof. Dr. Martin Oettel established *Computational Soft Matter and Nanoscience group* in *Institut für Angewandte Physik* of *Eberhard Karls Universität Tübingen*.

During the first weeks in Tübingen, Martin suggested working on vacancies which we were considering as a small warm–up project at that time. Ultimately, it turned out to be a quite fascinating subject and we extend it to metals with high hopes of addressing the unanswered problems in material science community. Afterwards, I began working on Density Functional Theory and the Asakura–Oosawa model for colloid–polymer mixtures. Meanwhile, I had the chance to investigate with Dr. Hendrik Hansen–Goos the properties of a new class of density functionals for the hard–sphere system.

The actual writing of the thesis is done from January until July 2016 with some excuses for break in between. I want to thank Dr. Johannes Bleibel, Dr. Hendrik Hansen–Goos, and Dr. Hans Joachim Schöpe for their time in proofreading my thesis and the insightful discussions that we had in between. I also thank my dear colleagues Malte Lütje, Miriam Klopotek, and Stefano da Vela for their support and help in proofreading.

I thank my supervisor, Prof. Dr. Martin Oettel, for his great support, enthusiastic cooperation, and collaborative discussions throughout my PhD studies. I appreciate his thoughtful helps and suggestions for writing this thesis. I also acknowledge my second supervisor, Prof. Dr. Roland Roth, who helped me to achieve a better understanding of Density Functional Theory, through the course he held with Prof. Dr. Oettel on this topic.

Finally, I want to thank my wife, Golzar Alavi, for her patience and encouragements, especially during the past six months in which I was fully engaged in writing this thesis. Without her, I would not be standing where I am now.

PUBLICATIONS

The reported research studies in this thesis have been conducted between November 2012 and December 2015 mainly at *Institut für Angewandte Physik, Eberhard Karls University of Tübingen*. Most of the results of this research have already been published in academic journals, and the corresponding publications are listed in the following.

Thermal vacancies in close–packing solids

M. Mortazavifar and M. Oettel, EPL (Europhysics Letters) **105**, 56005 (2014).

Abstract:We derive an approximate expression for the equilibrium concentration of thermal monovacancies in solids which allows for a transparent interpretation of the vacancy volume and the energetic/entropic part in the corresponding Gibbs energy of vacancy formation ΔG_{v}. For the close–packing crystals of the hard sphere and Lennard–Jones model systems very good agreement with simulation data is found. Application to metals through the embedded–atom method (EAM) reveals a strong sensitivity of the variation of ΔG_{v} with temperature to details of the EAM potential. Our result allows for an approximate, but direct measurement of crystal free energies and vacancy concentration in colloidal model systems using laser tweezers.

Statement of the author: Working on this topic was suggested at the beginning of my PhD studies. The method was already applied to the hard–sphere system by Martin Oettel. Motivated by the successful results for hard–core interaction, we applied the method to systems with soft potentials. I have preformed the calculations for LJ and EAM potentials in this paper.

Fundamental measure theory for the inhomogeneous hard–sphere system based on Santos' consistent free energy

H. Hansen-Goos, M. Mortazavifar, M. Oettel, and R. Roth, Phys. Rev. E **91**, 052121 (2015).

Abstract:Based on Santos' general solution for the scaled-particle differential equation, we construct a free–energy functional for the hard–sphere system. The functional is obtained by a suitable generalization and extension of the set of scaled–particle variables using the weighted densities from Rosenfeld's fundamental measure theory for the hard–sphere mixture. While our general result applies

to the hard–sphere mixture, we specify remaining degrees of freedom by requiring the functional to comply with known properties of the pure hard–sphere system. Both for mixtures and pure systems, the functional can be systematically extended following the lines of our derivation. We test the resulting functionals regarding their behavior upon dimensional reduction of the fluid as well as their ability to accurately describe the hard–sphere crystal and the liquid–solid transition.

Statement of the author: The functional has been built and tested for the fluid phase by Hendrik Hansen–Goos. I performed a full minimization of the functional in order to obtain the liquid–solid coexistence densities and their corresponding free energies, chemical potential, and pressure, as well as the equilibrium vacancy concentration of the solid phase.

A fundamental measure density functional for fluid and crystal phases of the Asakura–Oosawa model

M. Mortazavifar and M. Oettel, Journal of Physics: Condensed Matter **28**, 244018 (2016).

Abstract:We investigate a density functional for the Asakura–Oosawa model of colloid–polymer mixtures, describing both fluid and crystal phases. It is derived by linearizing the two–component fundamental–measure hard sphere tensor functional in the second (polymer) component. We discuss the formulation of an effective density functional for colloids only. For small polymer–colloid size ratios the effective, polymer–induced potential between colloids is short–range attractive and of two–body form but we show that the effective density functional is not equivalent to standard mean–field approaches where attractions are taken into account by terms second order in the colloid density. We calculate numerically free energies and phase diagrams in good agreement with available simulations, furthermore we discuss the colloid and polymer distributions in the crystal and determine equilibrium vacancy concentrations. Numerical results reveal a fairly strong sensitivity to the specific type of underlying fundamental measure hard sphere functional which could aid further development of fundamental measure theory.

Statement of the author: In this extensive work, the equilibrium properties of the fcc crystalline solid of a colloid–polymer mixture is investigated. The linearization trick which is used here to construct the FMT functional, is a well known method in literature for an FMT treatment of the AO model. Martin Oettel has written most of the theoretical part which contains the comparison of the method with the mean–field approximation,

and the derivation of an expression for the equilibrium vacancy concentration for the AO model. I have calculated the required analytical expressions for constrained and full minimization of the linearized WBII(tensor) functional, and performed all the DFT computations.

ABSTRACT

The theoretical studies reported in this thesis concern the equilibrium properties of a crystalline solid in a classical system. For this purpose, Density Functional Theory (DFT) is introduced and its variational principle is explained. For the particular case of a hard–sphere mixture, density functionals of Fundamental Measure Theory form are introduced. Among the more sophisticated versions of the FMT functionals which account for freezing, the tensorial version of the White Bear Mark II (WBII) functional is employed and previously reported accurate results for an fcc crystalline structure are recovered, i.e. the free energy, liquid–solid phase coexistence densities, and the vacancy concentration for a one–component system. Furthermore, by an appropriate extension of a general solution of the scaled–particle differential equation to inhomogeneous systems, a new class of free–energy functional for the hard–sphere system is constructed. The functional is also capable of describing the liquid–solid phase transition. The resulting functional is less complex from a numerical point of view since it does not require tensorial weight functions. The obtained solid and fluid phase coexistence densities of the vectorial functional, as well as their corresponding free energies, the coexistence chemical potential, and the coexistence pressure, are in fairly good agreement with Monte–Carlo (MC) simulation results.

In order to investigate in the following a colloid–polymer mixture in the context of the Asakura–Oosawa (AO) model, the WBII(tensor) functional is linearized with respect to the polymer density. The obtained crystal free energy curves are qualitatively similar to those of a simple fluid with attractive interactions between the particles. Furthermore, a comparison of the method with a standard mean–field approximation shows that the FMT functional takes care of the attractive part of the effective potential between colloidal particles in a fundamentally different way. The mean–field approximation underestimates the attractive part of the potential and thus yields inaccurate phase coexistence densities. On the other side, the obtained liquid–solid phase coexistence densities from constrained minimization of the linearized WBII(tensor) functional are in good agreement with available simulation data for large polymer–colloid size ratios $q \gtrsim 0.6$. While in this limit up to the triple point, the phase coexistence densities remain almost the same as pure hard–sphere system, the broadening of the liquid–solid coexistence region is more pronounced for smaller q's. For sufficiently small polymer–colloid size ratio, i.e. $q \leq 0.31$, the fluid–fluid phase transition becomes metastable. Here, the fluid branch of the fluid–solid coexistence density is determined by a sublimation line whose corresponding colloid density varies from a rather high density at the hard–sphere limit, to very small values at higher polymer reservoir packing fractions. Moreover, using the linearized functional we are able to obtain the equilibrium polymer density distribution in an fcc crystal of the colloidal particles. We have shown

that for smaller q's the majority of polymers fill the interstitial sites. This is not true for larger polymers, $q \gtrsim 0.6$, which tend to fill the vacant lattice sites. By performing a full minimization of the functional, we have observed an anisotropy in the colloidal density profile equivalent to those of a pure hard–sphere system. For small q, these anisotropies are slightly enhanced. We have also observed an increase in the equilibrium polymer density at the lattice site after full minimization.

The thermal vacancies are investigated for the crystalline solid in equilibrium. Based on the work by Stillinger et al., an expansion of the crystal partition function is derived in terms of number of freely moving particles in the background of particles frozen at their lattice sites. Using this expansion, we have derived an expression for the equilibrium vacancy concentration $n_{\mathrm{vac,eq}}$. This expression relates the Gibbs free energy of vacancy formation, $\Delta G_{\mathrm{v}} = -k_{\mathrm{B}} T \ln n_{\mathrm{vac,eq}}$ with k_{B} the Boltzmann constant and T the temperature, to a term corresponding to the crystal equation of state and a "vacancy integral" which contains the vacancy entropy and the missing interaction energy of the removed particle. For hard–spheres as a purely repulsive system, there is a good agreement with obtained results from FMT and MC simulation. For studying the AO model, we have rearranged the proposed series of the crystal partition function. The obtained $n_{\mathrm{vac,eq}}$ in the AO model, shows a fairly good qualitative agreement with FMT results for $q \gtrsim 0.6$. We have also applied the method to the Lennard–Jones (LJ) system. A proper comparison with available simulation results shows good agreement for the obtained values of the Gibbs free energy of the vacancy concentration. Moreover, the obtained equation of state using the first order approximation of the partition function, agrees with the parametrized LJ equation of state proposed by van der Hoef. We have investigated nickel as an exemplary case for a metal with fcc crystalline structure. For this purpose we have used the Embedded–Atom–Model (EAM) which gives a classical description of a many–body potential between atoms. Based on the sensitivity of the obtained result to the parametrization of the EAM potentials, we conclude that the Gibbs free energy of vacancy concentration at finite temperatures should be considered in such parametrizations from the beginning.

Finally, the numerical methods and required analytical expressions for a proper implementation of the FMT functionals are outlined in appendices. Here, for the pure hard–sphere system as well as for the AO model, I have determined explicit analytical forms for the excess chemical potential of the FMT functionals in inhomogeneous systems which are essential for the full minimization of the corresponding functional.

ZUSAMMENFASSUNG

Die theoretischen Untersuchungen in dieser Arbeit beschäftigen sich mit Gleichgewichtseigenschaften eines Kristalls in einem klassischen System. Dafür wird Dichtefunktionaltheorie (DFT) eingeführt und das zugehörige Variationsprinzip erläutert. Für den Spezialfall einer Mischung harter Kugeln werden Dichtefunktionale aus der Fundamentalmaßtheorie (FMT) vorgestellt. Für die weiteren Betrachtungen wird zum einen die Tensorversion des White Bear II(WBII)–Funktionals ausgewählt, welche eine der erweiterten FMT–Formen ist, die den Gefrierübergang beschreiben. Akkurate, aus der Literatur bekannte Resultate für den fcc–Kristall im einkomponentigen System (freie Energie, Koexistenzdichten und die Leerstellenkonzentration) konnten reproduziert werden. Zum anderen wird die Konstruktion einer neuen Klasse von FMT–Funktionalen vorgestellt, die durch eine geeignete Erweiterung der Lösung für die *scaled–particle*–Differentialgleichung gewonnen wird. Funktionale dieses Typs beschreiben auch den Flüssig–Fest–Übergang, und sie sind für die Numerik weniger komplex, da sie keine Tensor–Gewichtsfunktion beinhalten. Die berechneten Koexistenzdichten der flüssigen und festen Phase, die zugehörigen freien Energien, sowie Druck und chemisches Potential bei Koexistenz zeigen eine gute Übereinstimmung mit Monte–Carlo(MC)–Simulationsdaten.

Um im weiteren Kolloid–Polymermischungen mittels des Asakura–Oosawa(AO)–Modells zu behandeln, wird das WBII(Tensor)–Funktional bezüglich der Polymerdichte linearisiert. Die daraus erhaltenen freien Energien für den Kristall zeigen ein qualitativ ähnliches Verhalten wie diejenigen eines einfachen Fluids mit attraktiven Wechselwirkungen zwischen den Teilchen. Der Vergleich mit einer üblichen Mittleren–Feld–Näherung zeigt, dass das FMT–Funktional den attraktiven Teil des effektiven Potentials zwischen den Kolloiden grundlegend anders behandelt. Die Mittlere–Feld–Näherung unterschätzt den Effekt des attraktiven Potentialanteils und ergibt somit ungenaue Koexistenzdichten. Die berechneten Koexistenzdichten aus einer eingeschränkten Minimierung des linearisierten FMT–Funktionals zeigen dagegen eine gute Übereinstimmung mit Simulationsdaten für große Werte $q \gtrsim 0.6$ des Größenverhältnisses zwischen Polymeren und Kolloiden. In diesem Bereich, bis zum Tripelpunkt, bleiben die Koexistenzdichten nahe an denen des reinen Hartkugelsystems, wohingegen eine Verbreiterung des Flüssig–Fest–Koexistenzbereiches für kleinere q einsetzt. Für genügend kleine Größenverhätnisse $q \leq 0.31$ wird der Flüssig–Flüssig–Übergang metastabil. In diesem Bereich nun wird der fluide Zweig der Flüssig–Fest–Koexistenzdichtenkurve durch eine Sublimationslinie bestimmt, die von einer verhältnismäßig hohen Dichte (im Grenzfall reiner harter Kugeln) zu sehr kleinen Dichten bei höheren Polymer–Reservoirpackungsdichten verläuft. Weiterhin konnte mittels des linearisierten Funktionals die Gleichgewichtsdichteverteilung der Polymere im fcc–Kristall der

Kolloide bestimmt werden. Für kleinere q befindet sich die Mehrzahl der Polymere auf Zwischengitterplätzen. Im Gegensatz dazu befinden sich größere Polymere ($q \gtrsim 0.6$) in den Leerstellen des Gitters. Eine volle Minimierung des Funktionals ergab Anisotropien des Dichteprofils der Kolloide im Kristall, die in etwa gleich denen in einem reinen Hartkugelkristall sind. Für kleine q sind die Anisotropien etwas ausgeprägter. Eine Erhöhung der Gleichgewichtsdichte der Polymere an den Gitterplätzen nach voller Minimierung wurde beobachtet.

Thermische Leerstellen wurden für den Kristall im Gleichgewicht untersucht. Aufbauend auf den Arbeiten von Stillinger et al. wurde eine Entwicklung der Zustandssumme des Kristalls bezüglich der Anzahl frei beweglicher Teilchen in einem Hintergrund von an Gitterstellen fixierten Teilchen hergeleitet. Mittels dieser Enntwicklung wurde eine Gleichung für die Leerstellenkonzentration $n_{\mathrm{vac,eq}}$ im Gleichgewicht gewonnen. Dise Gleichung setzt die Gibbs'sche freie Energie der Leerstellenbildung, $\Delta G_{\mathrm{v}} = -k_{\mathrm{B}}T \ln n_{\mathrm{vac,eq}}$ (k_{B} ist die Boltzmann–Konstante und T die Temperatur), in Beziehung zur Zustandsgleichung des Kristalls und zu einem "Leerstellenintegral", welches die Leerstellenentropie und die fehlende Wechselwirkungsenergie des entfernten Teilchens enthält. Für harte Kugeln als rein repulsives System zeigt sich eine hervorragende Übereinstimmung mit den entsprechenden FMT– und MC–Resultaten. Für die Anwendung auf das AO–Modell wurde die Zustandssummenentwicklung umgeschrieben. Die hieraus berechnete Leerstellenkonzentration im Gleichgewicht zeigt eine gute qualitative Übereinstimmung mit FMT–Resultaten für $q \gtrsim 0.6$. Die Methode wurde auch auf das Lennard–Jones(LJ)–System angewandt. Auch hier zeigt sich bei einem entsprechenden Vergleich mit Simulationsdaten eine gute Übereinstimmung für die Gibbs'sche freie Energie der Leerstellenbildung. Weiterhin konnte eine Zustandsgleichung für das LJ–System aus dem führenden Term der Entwicklung berechnet werden, die gut mit der Parametrisierung von van der Hoef übereinstimmt. Weiterhin wurde Nickel als ein Beispiel für ein fcc–Metall mit dieser Methode untersucht. Für die Berechnungen wurde die Methode der eingebetteten Atome (*Embedded–Atom Model*, EAM) benutzt, welche eine klassische Vielteilchenwechselwirkung zwischen den Atomen ansetzt. Aufgrund der beobachteten Empfindlichkeit der Resultate bezüglich der Parametrisierungen der EAM–Potentiale wird die Schlussfolgerung gezogen, dass die Gibbs'sche freie Energie der Leerstellenbildung bei endlichen Temperaturen für solche Parametrisierungen von Anfang an einbezogen werden sollte.

Abschließend werden die numerischen Methoden und die benötigten analytischen Ausdrücke für eine effiziente Implementierung der FMT–Funktionale im Anhang dargestellt. Für das reine Hartkugelsystem wie auch das AO–Modell werden explizite Ausdrücke für den Exzessanteil des chemischen Potentials im inhomogenen System angegeben. Diese sind zentral für die volle Minimierung des entsprechenden Funktionals.

CONTENTS

CHAPTER 1

INTRODUCTION

A crystalline solid is a state of matter in which the individual particles of the system are arranged in a periodically ordered structure. Different types of solids can be classified with respect to the bonding forces between their components: the van der Waals interaction in a molecular or Argon solid, the ionic bonding of two atomic substances (for instance Sodium and Chloride in cooking salt), or the valence electrons holding atoms in an ordered structure, e.g. carbon atoms in diamond. In a metal, the free conduction electrons form a background "glue" in which the positive atomic ions are held together. In all these cases, under proper physical circumstances the crystalline structure has the minimum free energy and is therefore stable [1]. This symmetric form of matter shows splendid physical properties which renders its investigation of great importance.

Crystallization is one of the most common processes in which the disordered components of a material perform a transition and line up in an ordered state. This may happen around a nucleus of the same material which is formed in the disordered state by a scarce probability (homogeneous nucleation). In a more common situation, due to its lower energy barrier, a heterogeneity in the system which can be the walls of the container or a dust particle, plays the role of the critical nucleus (heterogeneous nucleation). In a metallic system the length scale of the nucleus is of order of a few nano–meters and its investigation needs sophisticated experimental methods, e.g. neutron scattering. On the other hand, the interaction between the atoms is determined by the choice of the metal and is of many–body nature.

The length scale of the nucleation seed in a colloidal system is of order micro–meters. As a result, liquid–crystal interfaces can be experimentally *observed* with single particle resolution by using confocal microscopy for instance [2]. On the other hand the effect of a substrate on periodicity of the crystalline state can be neglected due to the length scale of the particles. Finally, the most important advantage of colloidal systems is that the interactions between colloidal particles is pairwise and tunable by modifying the

properties of the solvent or those of the colloids itself [3]. For instance, adding non–adsorbing polymers to a suspension of sterically stabilized colloidal particles induces an effective attraction between the particles [4]. This effective attraction is a function of polymer–colloid size ratio and is proportional to the polymer density [5]. Furthermore, the pairwise interaction between the particles makes it possible to study the system by methods of classical statistical mechanics, e.g. Monte–Carlo simulation or Density Functional Theory (DFT).

In a colloidal suspension, the short–range repulsive part of the potential between colloid particles is the main contribution to particle correlations, thus it determines the properties and structure of the liquid. The smoothly varying attractive forces which act in the ranges beyond repulsive interactions have little to do with the structure of the system [6]. The attractive interactions between the particles induce a liquid–gas phase transition and provide a ground state crystalline structure at densities lower than close–packing. Therefore, hard spheres whose repulsive harsh interaction does not allow overlap of the particles, are of great importance in theoretical studies since they can be used as a reference system, while the attractive interactions are treated as a perturbation [7]. Experimentally, it is possible to tune the van der Waals interaction and combine it with steric stabilization using short brushes, in order to obtain an approximately pure hard–core potential between particles [3]. Since there is no attraction between the hard–sphere (HS) particles, the liquid–solid phase transition is induced completely by entropy.

In order to investigate crystallization, knowledge about bulk properties of the solid and the liquid phases as well as their respective interfaces is mandatory. Density Functional Theory is one of the most important theoretical tools which gives a macroscopic description of the system of interest in equilibrium. The method was originally developed to study the ground state energy of a cloud of electrons in a metallic system, and is hence of quantum physics origins. Later, the method was modified to be applied to classical systems [7, 8]. The challenge in classical DFT is to approximate an excess over ideal gas functional, which describes the interactions of the particles as precisely as possible. In 1989, Rosenfeld introduced Fundamental Measure Theory (FMT) as a density functional treatment for a mixture of hard–spheres [9]. During next 20 years, FMT has been further developed to describe the transition to a solid state and its more sophisticated versions are capable to deliver the free energy and structure of a crystalline state in a good agreement with simulation results [10–12].

Defects are another important aspect of a crystalline solid in equilibrium whose impact on its other physical quantities, e.g. on the diffusion coefficient, has attracted the attention of scientists. Point defects are localised around a lattice site. Thermally induced vacancies are one of the different types of point defects and their presence is an equilibrium property of a solid. A vacant lattice site induces the dominant mechanism in diffusion (migration) of atoms. Here, an atom oscillating in vicinity of its lattice

site jumps to the vacant site after overcoming an activation energy which it need for passing through its neighboring atoms [13]. The equilibrium vacancy concentration, i.e. the probability of finding a vacant site in a stable crystalline solid, is expressed as the Boltzmann factor of the Gibbs energy for formation of a vacancy. In the material science community, the formation energy is further expressed as a sum of the formation enthalpy and the change in configuration entropy. However, a clear description of the mechanisms, which result in the formation of a vacancy in a crystalline solid is not available. In the context of cell–cluster theories, starting from a formally exact relation for the partition function of a crystal [14, 15], two dominant contributions to the vacancy formation energy have been identified, which are a term related to the equation of state and an entropic term [16].

In this thesis, after a brief introduction to thermodynamics and classical statistical physics in Chapter 2, Density Functional Theory is introduced and its variational principle is explained. The main aspect of Chapter 3 is to see, how in a theoretical framework the classically pairwise interactions are treated; specifically the more important hard–core interaction is discussed in detail. Some approximate methods for constructing a free energy functional functional for a system with interacting particles are discussed in the last section of this chapter. In Chapter 4, Fundamental Measure Theory is introduced as a successful density functional treatment for hard–sphere systems. The shortage of the original FMT functional [9] in describing freezing is discussed, and the path towardi free energy functionals which are capable of delivering correct information about an fcc solid is presented. For a unified treatment of a fluid and an fcc structured solid in a colloid–polymer mixture, an FMT functional is derived in Chapter 5. Here, we show, that the linearized functional, which is a known method in the literature for obtaining a functional description of the Asakura–Oosawa model, treats the attractive part of the potential in a fundamentally different way than the classical treatments, e.g. mean–field approximations [17]. Finally, in Chapter 6 we calculate a relation for the equilibrium vacancy concentration based on a formally exact partition function for solids. For classical systems, the expression is applied to a hard–sphere system as well as to a Lennard–Jones (LJ) system. The Embedded–Atom Model (EAM), which is an attempt to describe a metallic system with classical potentials, is used to investigate the vacancy formation energy for Nickel. Based on the comparison of results for three different parametrizations of EAM, we conclude that the Gibbs free energy of vacancy concentration in further parametrizations of EAM should be considered from the beginning.

Chapter 2

Theory

Curiosity has always been a key motivation for mankind to achieve a better understanding of different phenomena occurring in nature. By finding similar patterns under seemingly different circumstances, one may be able to predict what is nature's next step or even create a controlled process on their own. For this purpose, measuring relevant parameters is the first step towards finding a relation between them and eventually extending our knowledge about our surroundings. Physics in this sense, is the science of measuring physical quantities and casting them into theoretical models in an attempt to explain how "things" happen.

Thermodynamics is a branch of physics which gives a "*a phenomenological description of properties of macroscopic systems in thermal equilibrium*" [18]. Thermodynamics tries to find the relation between the energy exchange of a system with its surrounding and some macroscopic physical properties of the system in equilibrium, e.g. temperature, pressure, or changes in the volume or amount of the substance. Such a macroscopic description of mutual transformation of heat and physical work, does not clarify, how exactly the microscopic interactions between the components lead to such a macroscopic action.

Statistical physics fills in the gap between the microscopic description and macroscopic properties of a system with a large number of components, e.g. atoms, molecules, particles, or even individuals in a society, by taking advantage of the statistical tools and probability theory. It describes how the interactions of the components of the system lead to their collective behaviour which is ultimately expressed by a macroscopic quantity of the whole system. For this purpose, an important step is to obtain the partition function, a weighted sum over all possible states of a system. With the partition function at hand, the ensemble average of a quantity gives the most probable outcome of its measurement.

One of the most important theories which has its roots in statistical physics is Density

Functional Theory (DFT). In the framework of DFT, one can obtain a free energy functional depending on the local density of the components of the system. The method was originally formulated and used as a powerful functional treatment for describing the ground state of an inhomogeneous interacting electron gas by Hohenberg and Kohn [19]. Mermin extended the theory to finite temperatures by constructing a grand potential functional for an interacting electron liquid [20]. A corresponding DFT for the equilibrium state of a classical system entails a unique free energy functional of the density profile which allows to calculate the ground state free energy of the system and consequently allows to calculate its equilibrium thermodynamic properties using a variational principle [7, 8].

In this chapter, after a brief introduction to thermodynamics in Section 2.1, the main concepts of the statistical mechanics for classical systems are recapitulated and some specific ensembles are introduced in Section 2.2. In Section 2.3, after a brief excursion to history, the existence of a free energy functional of the density and its uniqueness is proven. While discussions regarding the interactions between the partilces is left for Chapter 3, an ideal gas with non–interacting particles is used as a test case for the presented theories in this chapter.

2.1   Thermodynamics

Thermodynamics is a phenomenological description of a macroscopic system in thermal equilibrium using a number of thermodynamic coordinate or state functions [18]. The state functions are either extensive or intensive. The extensive state variables scale with the size of the system and have a conjugate intensive counterpart. The product of the changes in an extensive state variable and its conjugate intensive counterpart, for instance the volume V and the pressure p of the system respectively, determines the amount of exchanged energy, e.g. in the form of a mechanical work $\mathrm{d}W = -p\mathrm{d}V$.

Since the state variables are not independent, the thermodynamic properties of the system can be fully specified by an appropriate set of them. The relation between the state variables is specified by the laws of thermodynamics which are based on empirical observations. The zeroth law states, that if two systems are separately in equilibrium with a third system, then they are also in equilibrium with one another. According to the first law of thermodynamics the change in the internal energy of an isolated system $\mathrm{d}U$ is equal to the amount of work it does $\mathrm{d}W$, and its heat intake from the surrounding $\mathrm{d}Q$.

$$\mathrm{d}U \;\; = \;\; \mathrm{d}W + \mathrm{d}Q \; . \tag{2.1}$$

The second law which eventually leads to the definition of the entropy as the conjugate

state variable of the temperature[1], has two equivalent forms [18]:

1. *It is impossible to have a thermodynamic process whose sole result is the complete conversion of heat into work* (Kelvin).

2. *It is impossible to have a thermodynamic process whose sole result is the transfer of heat from a colder to a hotter body* (Clausius).

Due to the second law, the difference in the entropy of two states of the system can be calculated by measuring the change in the heat exchange in infinitesimal small steps between the two steps. Experiments at low temperature indicates that this difference vanishes as T goes to zero which leads to the third law of the thermodynamics. According to the formulation of third law by Nernst, *The entropy of all systems at zero absolute temperature is a universal constant that can be taken to be zero* [18].

For an adiabatically isolated system, the second law dictates the path to equilibrium in which the entropy of the system is maximal. It is possible to define other types of thermodynamic potentials for a non–isolated system, where the equilibrium state is marked by extremizing the defined potentials. These potentials, their conserved state variables, their application and differentials with respect to their state variables are summarized in table 2.1.

The relation between the conserved state variables of a thermodynamic system is expressed via the equation of state. In 1662, Robert Boyle carefully measured the volume of trapped air in a tube whose other end was filled with mercury, hence its pressure was known. He concluded that the product of these state variables is a constant $pV = \mathrm{constant}$. About hundred years later, Jacques Charles found a linear relation between the temperature and the volume of the gas. Finally, in 1834 the famous ideal gas law was found by combining the Boyle's law and Charles' law. The ideal gas law relates the volume, the pressure, and the temperature of an ideal gas in equilibrium and it reads

$$pV = N k_{\mathrm{B}} T \, , \tag{2.2}$$

where k_{B} is the Boltzmann constant. For a non–ideal gas however, this relation should be modified in order to express the pressure of a gas as a function of its density and temperature. This will be discussed in Section 3.2.1.

---

[1] See the dedicated section to entropy in Ref. [18] on page 13.

Table 2.1: Different types of thermodynamic potentials, their conserved state variables and differential. The application column indicates the thermodynamic system for which at its equilibrium the thermodynamic potential is minimized.

Potential	differential	application
Internal Energy $U(N, V, S)$	$\mathrm{d}U = T\mathrm{d}S - p\mathrm{d}V + \mu\mathrm{d}N$	adiabatically isolated
Enthalpy $H(N, p, S)$	$\mathrm{d}H = \mathrm{d}U + \mathrm{d}\,(pV)$ $= T\mathrm{d}S + V\mathrm{d}p + \mu\mathrm{d}N$	no heat exchange $\mathrm{d}Q = 0$
Helmholtz free energy $F(N, V, T)$	$\mathrm{d}F = \mathrm{d}U - \mathrm{d}\,(TS)$ $= -S\mathrm{d}T - p\mathrm{d}V + \mu\mathrm{d}N$	isothermal transformation no mechanical work $\mathrm{d}W = 0$
Gibbs free energy $G(N, p, T)$	$\mathrm{d}G = \mathrm{d}U - \mathrm{d}\,(TS) + \mathrm{d}\,(pV)$ $= -S\mathrm{d}T + V\mathrm{d}p + \mu\mathrm{d}N$	isothermal transformation $\mathrm{d}W \neq 0$, constant force
Grand energy $\Omega(\mu, V, T)$	$\mathrm{d}\Omega = \mathrm{d}U - \mathrm{d}\,(TS) + \mathrm{d}\,(\mu N)$ $= -S\mathrm{d}T - p\mathrm{d}V + N\mathrm{d}\mu$	chemical potential is fixed rather than particle number

2.2   Statistical Physics and Classical ensembles

The equation of state describes a system in equilibrium by providing an expression, which relates a set of state variables to each other, e.g. pressure p, volume V, particle number N, and temperature T of an ideal gas in Eq. (2.2). The other thermodynamic variables of the system can be obtained using the relations provided in the context of classical thermodynamics (see table 2.1). However, the route for deriving an equation of state, provided the interaction between individual particles is known, is not clear for most systems. Statistical physics deals with the interactions between a huge number of individual particles of a macroscopic body ($N \sim 10^{23}$) in order to obtain its thermal properties. Since the position $\mathbf{r}$ and the momenta $\mathbf{p}$ of particles are each specified by three variables, the phase space of the system has $6N$ degrees of freedom. The Hamiltonian $\mathcal{H}$ of the system is written as a sum of the total kinetic energy of the particles $\mathcal{T}\,(\{\mathbf{p}_i\})$, the potential energy due to the interaction of the system with an external potential $\mathcal{V}\,(\{\mathbf{r}_i\})$, and the total potential energy $\mathcal{U}\,(\{\mathbf{r}_i\})$ of the classically interacting

particles with a pair potential $u(r)$ which is expressed as a function of their distance.

$$
\begin{aligned}
\mathcal{H}\left(\{\mathbf{r}_i\}, \{\mathbf{p}_i\}\right) &= \mathcal{T}\left(\{\mathbf{p}_i\}\right) + \mathcal{V}\left(\{\mathbf{r}_i\}\right) + \mathcal{U}\left(\{\mathbf{r}_i\}\right) \\
&= \sum_{i=1}^{N}\left(\frac{p_i^2}{2m_i} + V_{\text{ext}}(\mathbf{r}_i)\right) + \frac{1}{2}\sum_{i,j=1}^{N} u(|\mathbf{r}_i - \mathbf{r}_j|)\,,
\end{aligned}
\tag{2.3}
$$

where m_i is the mass of the particles, and the external potential acts on each particle depending on its position $\mathbf{r}_i$. Having the information about the Hamiltonian of a classical system, it is possible to determine the time evolution of the position and the momenta of each individual particle [21]. This is equivalent to writing down Newton equation of motion for each particle and solving; a quite complicated task. Rather than this, statistical mechanics deals with an ensemble of equally probable micro–states which correspond to a given macro–state. Here each micro–state ψ is a "point" in phase space $(\{\mathbf{p}_i\}, \{\mathbf{r}_i\})$ determined by the momenta and the position of each particle, while a macro–state is specified by the macroscopic thermodynamic variables of the system. There are different types of classical ensembles in statistical physics which differ only in their conserved state variables. However, in the thermodynamic limit, with $N \to \infty$ while N/V is kept constant, all of these ensembles are equivalent.

2.2.1 Microcanonical ensemble

Consider a mechanically and adiabatically isolated system with a given internal energy E_0. Each of the micro–state in the phase space ψ which belong to this macro–state, lies in the manifold which is described by $\mathcal{H}(\psi) = E_0$. Boltzmann's assumption of equally probable micro–states, the unbiased probability estimate in constrained phase space to a constant energy, is given by the following postulate:

$$
f_{\text{m}}\left(\psi; \mathcal{H}(\psi) = E_0\right) = \frac{1}{\mathcal{A}(N, V, E_0)}\,.
\tag{2.4}
$$

Here, the normalization factor $\mathcal{A}(N, V, E_0)$ is the area of the surface of constant energy E_0 in phase space. The entropy of this uniform probability distribution is given by,

$$
S(N, V, U) = -k_{\text{B}} \ln f_{\text{m}}(\psi) = k_{\text{B}} \ln \mathcal{A}(N, V, E_0)\,.
\tag{2.5}
$$

Consider the mixture of two micro–states ψ_1 and ψ_2, with equilibrium internal energies E_1 and E_2 and entropies denoted by S_1 and S_2. In the equilibrium state of the new micro–state $\psi = \psi_1 \otimes \psi_2$, the entropy should be maximized. As a consequence the partial derivative of the entropies S_i with respect to internal energy E_i which defines a "new" state variable, should becomes equal in the new equilibrated state. This newly

defined state variable is in fact equivalent to the empirical temperature and is given by[2],

$$\frac{\partial S}{\partial E} = \frac{1}{T} \ .$$

(2.6)

2.2.2 Canonical Ensemble

In a canonical ensemble, rather than fixing the internal energy U and obtaining the temperature T, one starts with a macro–state in which the temperature is fixed by coupling the system to a heat bath and derives the energy of the system. The probability of finding a micro–state ψ is given by the Boltzmann factor of its Hamiltonian.

$$f_{\rm c}\left(\psi\right) \;=\; \frac{\exp\left(-\beta\mathcal{H}(\psi)\right)}{\sum'_{\{\psi\}}\exp\left(-\beta\mathcal{H}(\psi)\right)} \qquad \text{with } {\sum_{\{\psi\}}}' = \frac{1}{N!}\sum_{\{\psi\}},$$

(2.7)

where the denominator is the canonical partition function $Z = \sum'_{\{\psi\}}\exp\left(-\beta\mathcal{H}(\psi)\right)$, and the sum is over all possible micro–states $\{\psi\}$. Using the probability function from Eq. (2.7), the ensemble average of the energy of the system $\langle\mathcal{H}\rangle$ is calculated as follows:

$$
\begin{aligned}
\langle\mathcal{H}\rangle \;&=\; {\sum_{\{\psi\}}}' f_{\rm c}\mathcal{H}(\psi) = {\sum_{\{\psi\}}}'\mathcal{H}(\psi)\frac{\exp\left(-\beta\mathcal{H}(\psi)\right)}{Z} \\
&=\; -\frac{1}{Z}\frac{\partial}{\partial\beta}{\sum_{\{\psi\}}}'\exp\left(-\beta\mathcal{H}(\psi)\right) = -\frac{\partial\ln Z}{\partial\beta}
\end{aligned}
$$

(2.8)

On the other hand, using the thermodynamic relations (table 2.1) the internal energy of the system E is related to the Helmholtz free energy F as,

$$E \;=\; F + TS = F - T\left.\frac{\partial F}{\partial T}\right|_{N,V} = -T^2\frac{\partial}{\partial T}\left(\frac{F}{T}\right) = \frac{\partial(\beta F)}{\partial\beta} \ .$$

(2.9)

By comparing the right hand side of Eqs. (2.8) and (2.9) we arrive to the important relation between Helmholtz free energy and partition function of a canonical ensemble.

$$\beta F(N,V,T) \;=\; -\ln Z(N,V,T) \ .$$

(2.10)

Once the Helmholtz free energy is obtained, the other state variables of the system are calculated as its differential with respect to their conjugated counterparts (see table 2.1).

---

[2] See Ref. [18] page 101 for a detailed calculation and discussion

As an example, the Hamiltonian of an ideal gas in the absence of any external potential is given by the total kinetic energy of the particles. Therefore, the partition function of an ideal gas with N identical particles and volume V is given by,

$$Z(N,V,T) = \frac{1}{h^{3N}N!} \int d\mathbf{r}^N \int d\mathbf{p}^N \exp\left(-\beta \sum_{i=1}^{N} \frac{p_i^2}{2m}\right) = \frac{V^N}{h^{3N}N!}\left(\int d\mathbf{p}\, \exp\left(-\beta \frac{p^2}{2m}\right)\right)^N$$

$$= \frac{V^N}{N!\lambda^{3N}} \quad \text{with } \lambda = \frac{h}{\sqrt{2\pi m k_\mathrm{B} T}}\ , \tag{2.11}$$

Here, λ is the de Broglie thermal wavelength which for numerical considerations is usually set to 1, and h is the Planck constant which is used to mkae Z dimensionless. Using Eq. (2.11), the Helmholtz free energy of the system $\beta F = -\ln Z$ reads

$$\begin{aligned} \beta F(N,V,T) &= -\ln\left(\frac{V^N}{N!\lambda^{3N}}\right) \\ &= N\left(\ln\left(\frac{N\lambda^3}{V}\right) - 1\right)\ , \end{aligned} \tag{2.12}$$

where we have used the Stirling's approximation for the factorial of large numbers[3]. Consequently, the chemical potential and the pressure of an ideal gas are obtained as follows:

$$\begin{aligned} \beta\mu &= \frac{\partial \beta F}{\partial N} = \ln\left(\frac{N}{V}\lambda^3\right)\ , \\ \beta p &= -\frac{\partial \beta F}{\partial V} = \frac{N}{V}\ . \end{aligned} \tag{2.13}$$

Note that the latter is the same as the empirical expression for the ideal gas equation of state from Eq. (2.2).

2.2.3 Grand–canonical ensemble

The thermodynamic macro–state whose chemical potential is fixed rather than its particle number and does not exchange energy with its surrounding in the form of mechanical work, is described by the grand–canonical ensemble. The corresponding micro–states $\{\psi\}$ have an indefinite number of particles but are coupled to a reservoir of particles which maintains the chemical potential of the system at a constant

---

[3] $\lim_{N\to\infty} \ln N! \approx N \ln N - N$

value. The probability distribution for a micro–state ψ with Hamiltonian $\mathcal{H}(\psi)$ is given as follows.

$$f_{\text{gc}}(\psi) = \frac{\exp\left(-\beta\mathcal{H}(\psi) + \beta\mu N(\psi)\right)}{\Xi} \, , \tag{2.14}$$

where the normalization factor Ξ is the grand partition sum whose relation to the canonical partition function Z is exhibited by grouping the micro–states ψ_N with a specific particle number N.

$$
\begin{aligned}
\Xi(\mu, V, T) &= \sideset{}{'}\sum_{\{\psi\}} \exp\left(-\beta\mathcal{H}(\psi) + \beta\mu N(\psi)\right) \\
&= \sum_{N=0}^{\infty} \exp\left(\beta\mu N\right) \sideset{}{'}\sum_{\{\psi_N\}} \exp\left(-\beta\mathcal{H}(\psi_N)\right) \\
&= \sum_{N=0}^{\infty} \exp\left(\beta\mu N\right) Z(N, V, T) \, .
\end{aligned}
\tag{2.15}
$$

In a classical system, the sum over all possible micro–states in the first line of Eq. (2.15) is equivalent to the classical trace Tr_{cl}, defined as follows:

$$\text{Tr}_{\text{cl}} \equiv \sum_{N=0}^{\infty} \frac{1}{h^{3N} N!} \int \mathrm{d}\mathbf{r}^N \int \mathrm{d}\mathbf{p}^N \, . \tag{2.16}$$

It is trivial to show that the classical trace of the grand–canonical probability distribution function is one, $\text{Tr}_{\text{cl}} f_{\text{gc}} = 1$. Moreover, the ensemble average of an observable $\hat{O}$, which for an ergodic system is equivalent to its time average, is given by,

$$\langle \hat{O} \rangle = \text{Tr}_{\text{cl}} \, f_{\text{gc}} \, \hat{O} \, . \tag{2.17}$$

In a system with N particles, an important observable is the particle distribution $\hat{\rho}(\mathbf{r})$ which basically counts the number of particles at a given position $\mathbf{r}$. Therefore, integrating $\hat{\rho}$ over the whole space gives the number of particles N. The ensemble average of the particle distribution is the single–particle density $\rho^{(1)}(\mathbf{r})$.

$$\hat{\rho}(\mathbf{r}) = \sum_{i=1}^{N} \delta(\mathbf{r} - \mathbf{r}_i) \tag{2.18}$$

$$\rho^{(1)}(\mathbf{r}) = \langle \hat{\rho}(\mathbf{r}) \rangle = \text{Tr}_{\text{cl}} \, f_{\text{gc}} \, \hat{\rho}(\mathbf{r}) \tag{2.19}$$

Moreover, the ensemble average of the number of particles $\langle N \rangle$ is calculated as follows.

$$
\begin{aligned}
\langle N \rangle &= \mathrm{Tr}_{\mathrm{cl}} \, f_{\mathrm{gc}} \, N = \sum_{N=0}^{\infty} \left(\frac{\exp\left(\beta\mu N\right) Z(N, V, T)}{\Xi(\mu, V, T)} \, N \right) \\
&= \frac{1}{\Xi(\mu, V, T)} \frac{\partial}{\partial \beta\mu} \left(\sum_{N=0}^{\infty} \exp\left(\beta\mu N\right) Z(N, V, T) \right) \\
&= \frac{1}{\Xi(\mu, V, T)} \frac{\partial \, \Xi(\mu, V, T)}{\partial \beta\mu} = \frac{\partial \ln \, \Xi(\mu, V, T)}{\partial \beta\mu} \; .
\end{aligned}
\tag{2.20}
$$

Similarly, one can calculate the fluctuation of the particle number $\langle N^2 \rangle - \langle N \rangle^2$, see that it is proportional to N and conclude, that the distribution function of particle number is sharply peaked at $N = N_0 = \langle N \rangle$. Therefore, in this limit the sum in Eq. (2.15) can be approximated by its largest term.

$$
\begin{aligned}
\Xi(\mu, V, T) &= \exp\left(\beta\mu N_0\right) Z(N_0, V, T) = \exp\left(\beta\mu N_0\right) \exp\left(-\beta F(N_0, V, T)\right) \\
&= \exp\left(-\beta \Omega(\mu, V, T)\right) \; ,
\end{aligned}
\tag{2.21}
$$

where $\Omega(\mu, V, T)$ is the grand potential (see table 2.1). Once the partition sum is calcualted for a particular system, one can obtain its grand potential using Eq. (2.21). As an example, the grand partition sum and the grand potential for an ideal gas is calculated as follows.

$$
\begin{aligned}
\Xi(\mu, V, T) &= \sum_{N=0}^{\infty} \exp\left(\beta\mu N\right) Z(N, V, T) = \sum_{N=0}^{\infty} \frac{1}{N!} \left(\frac{e^{\beta\mu}}{\lambda^3} V \right)^N \\
&= e^{z \, V} \; , \qquad \text{with } z = \frac{e^{\beta\mu}}{\lambda^3}
\end{aligned}
\tag{2.22}
$$

$$
\beta\Omega(\mu, V, T) = -\ln \, \Xi(\mu, V, T) = -z \, V \; ,
\tag{2.23}
$$

where we introduced the fugacity of the system $z = e^{\beta\mu}/\lambda^3$. Having the grand potential, one can use its differential in table 2.1 to obtain the pressure and the particle number of an ideal gas.

$$
\beta p = -\frac{\partial \beta\Omega}{\partial V} = z \; ,
\tag{2.24}
$$

$$
N = -\frac{\partial \Omega}{\partial \mu} = z \, V \; .
\tag{2.25}
$$

Therefore, the pressure of an ideal gas is equal to its fugacity. The resulting ideal gas equation of state which is obtained by replacing the fugacity z in Eq. (2.25) by p, is the same as the empirical expression (Eq. (2.2)).

2.2.4   The Ornstein-Zernike relation

Similar to the single–particle density $\rho^{(1)}(\mathbf{r})$ (Eq. (2.19)) one can define an n–particle density $\rho^{(n)}(\mathbf{r}^n)$ which simultaneously keeps track of the changes in the density of n different particles at $\mathbf{r}^n = (\mathbf{r}_1, \ldots, \mathbf{r}_n)$ and is useful for obtaining information about a correlation between these particles, if there is any. One can calculate this quantity by calculating the ensemble average of the n–particle density distribution $\hat{\rho}_n(\mathbf{r}^n)$ which is equivalent to integrating out the spatial degrees of freedom of $N - n$ remaining particles from a distribution function, e.g. the grand canonical distribution function f_{gc}.

$$
\hat{\rho}_n(\mathbf{r}^n) = \sum_{i_1=1}^{N}\sum_{i_1<i_2}^{N}\cdots\sum_{i_1<i_2<\cdots<i_n=1}^{N}\delta(\mathbf{r}_1 - \mathbf{r}_{i_1})\delta(\mathbf{r}_2 - \mathbf{r}_{i_2})\cdots\delta(\mathbf{r}_n - \mathbf{r}_{i_n}) , \qquad (2.26)
$$

$$
\rho^{(n)}(\mathbf{r}^n) = \langle\hat{\rho}_n(\mathbf{r}^n)\rangle = \mathrm{Tr}_{\mathrm{cl}} f_{\mathrm{gc}}\,\hat{\rho}_n(\mathbf{r}^n)
$$

$$
= \sum_{N=n}^{\infty}\frac{1}{h^{3N}(N-n)!}\int \mathrm{d}\mathbf{r}^{N-n}\int \mathrm{d}\mathbf{p}^N f_{\mathrm{gc}}(\mathbf{r}^N, \mathbf{p}^N) . \qquad (2.27)
$$

For instance, the n–particle density distribution of a homogeneous ideal gas with N identical particles in the absence of any external potential, hence $\mathcal{U} = \mathcal{V} = 0$ and $\mathcal{H} = \mathcal{K}$, is obtained as follows.

$$
\rho_{\mathrm{id}}^{(n)}(\mathbf{r}^n) = \frac{1}{\Xi}\sum_{N=n}^{\infty}\frac{1}{h^{3N}(N-n)!}\int \mathrm{d}\mathbf{r}^{N-n}\int \mathrm{d}\mathbf{p}^N \exp\left(-\beta\frac{p^2}{2m} + \beta\mu N\right)
$$

$$
= \frac{1}{\Xi}\sum_{N=n}^{\infty}\frac{e^{\beta\mu N}V^{N-n}}{\lambda^N(N-n)!} = \frac{z^n}{\Xi}\sum_{N=0}^{\infty}\frac{(zV)^N}{N!} = \rho^n , \qquad (2.28)
$$

where in the last step we have used the identity $\rho = z$ for an ideal gas (see Eq. (2.25)). A more informative observable is the n–particle distribution function which is defined as

$$
g^{(n)}(\mathbf{r}^n) =: \frac{\rho^{(n)}(\mathbf{r}^n)}{\prod_{i=1}^{n}\rho^{(1)}(\mathbf{r}_i)} . \qquad (2.29)
$$

Note that for a homogeneous system the denominator is simply ρ^n and the n–particle distribution function is a normalized n–particle density. The distribution function for an ideal gas always obeys $g^{(n)} = 1$ and therefore, deviation from $g^{(n)} = 1$ delivers information about the structure of the system. For an isotropic system, e.g. a fluid, the pair distribution function $g^{(2)}(\mathbf{r}_i, \mathbf{r}_j)$ is only a function of the distance $r = |\mathbf{r}_i - \mathbf{r}_j|$. When r is much larger than the range of the interaction between the particles, the distribution

function tends to its ideal gas limit and $g(r \to \infty) \approx 1$. Since an ideal gas has no correlation by definition, one can define a total correlation function as $h = g^{(2)} - 1$ which is $\neq 0$ due to the interaction of the particles in the system. Finally, the direct pair correlation function $c^{(2)}(\mathbf{r}_i, \mathbf{r}_j)$ is defined via the Ornstein–Zernike equation [22].

$$h(\mathbf{r}_i, \mathbf{r}_j) = c^{(2)}(\mathbf{r}_i, \mathbf{r}_j) + \int d\mathbf{r}_k \, c^{(2)}(\mathbf{r}_i, \mathbf{r}_k)\rho^{(1)}(\mathbf{r}_k)h(\mathbf{r}_k, \mathbf{r}_j) \ . \tag{2.30}$$

The interpretation of this "recursive" relation may be understood by writing it as a series in h and reading it term by term: The total correlation function between $\mathbf{r}_i$ and $\mathbf{r}_j$, $h(\mathbf{r}_i, \mathbf{r}_j)$, is obtained by the sum of the direct correlation function between these two points, $c^{(2)}(\mathbf{r}_i, \mathbf{r}_j)$, and an indirect correlation function via all possible third points in space, $\mathbf{r}_k$. This indirect correlation function depends on the direct correlation function between $\mathbf{r}_i$ and the third point $\mathbf{r}_k$, the density at this point $\rho^{(1)}(\mathbf{r}_k)$, and finally the total correlation function between the third and second point $h(\mathbf{r}_k, \mathbf{r}_j)$. For a uniform and isotropic system the correlation functions are expressed as a function of the distance between two points $r = |\mathbf{r}_i - \mathbf{r}_j|$. Therefore, the Ornstein–Zernike relation turns into,

$$h(r) = c(r) + \rho \int d\mathbf{r}' \, c(|\mathbf{r} - \mathbf{r}'|)h(r') \ . \tag{2.31}$$

where we have omitted the superscripts (2) for convenience. Note that the integral term is the convolution between total and direct pair correlation functions. By taking the Fourier transform of both sides we can write the following relation between the Fourier transform of total correlation function $\tilde{h}(k)$ and direct correlation function $\tilde{c}(k)$.

$$\tilde{h}(k) = \frac{\tilde{c}(k)}{1 - \rho\tilde{c}(k)} = \frac{S(k) - 1}{\rho} \ , \tag{2.32}$$

where we introduced the structure factor $S(k)$. The structure factor is an important observable in experiments since it is proportional to the scattering intensity for point particles [6]. Furthermore, $\beta S(k \to 0)/\rho$ gives the isothermal compressibility $\chi_T = (\partial\rho/\partial p)_T/\rho$ of the fluid. As a result, one can obtain χ_T if the direct correlation function is known.

$$\chi_T = \frac{1}{\rho k_{\mathrm{B}}T \left(1 - \rho\hat{c}(k = 0)\right)} \ . \tag{2.33}$$

2.3 Density Functional Theory

In 1964 Hohenberg and Kohn used a variational principle to obtain the equilibrium density distribution of an inhomogeneous electron gas in its ground state [19]. They

have shown that the intrinsic part of the ground state energy is a unique functional of the electron density, hence it is independent of the external potential. The method, known as Density Functional Theory, was extended to finite temperatures by Mermin for a treatment of an electron liquid [20]. Later in the 1970's, DFT has been adopted for classical systems in order to obtain the thermodynamic properties of a classical fluid and the vapor–liquid interface [7, 8]. Since this energy functional is claimed to be a unique functional of the local density profile, the free energy of the system, and consequently, its thermodynamic properties, are obtained by having the knowledge of the density distribution. In the following section, the existence of this unique energy functional is proven.

2.3.1   Existence of a unique energy functional

Consider a classical system with N particles and intrinsic chemical potential denoted by μ, whose Hamiltonian is expressed as $\mathcal{H}$ from Eq. (2.3). The grand potential functional of the probability distribution f[4],

$$\Omega\left[f\right] \;=: \; \mathrm{Tr}_{\mathrm{cl}}\, f\left(\mathcal{H} - \mu N + k_{\mathrm{B}}T\ln f\right), \tag{2.34}$$

is at its minimum for the equilibrium probability distribution $f = f_{\mathrm{gc}}$ from Eq. (2.14). The minimum value is the grand potential $\beta\Omega = -\ln\Xi$ where Ξ is the partition sum of the grand–canonical ensemble (see Eqs. (2.15) and (2.21)). The proof is given in the following.

1. $\Omega[f_{\mathrm{gc}}] = \Omega$

$$
\begin{aligned}
\Omega[f_{\mathrm{gc}}] &= \mathrm{Tr}_{\mathrm{cl}}\, f_{\mathrm{gc}}\left(\mathcal{H} - \mu N + k_{\mathrm{B}}T\ln f_{\mathrm{gc}}\right) \\
&= \mathrm{Tr}_{\mathrm{cl}}\, f_{\mathrm{gc}}\left(\mathcal{H} - \mu N + k_{\mathrm{B}}T\left(-\beta\mathcal{H} + \beta\mu N\right) - k_{\mathrm{B}}T\ln\Xi\right) \\
&= -k_{\mathrm{B}}T\ln\Xi \qquad \text{since } \mathrm{Tr}_{\mathrm{cl}}\, f_{\mathrm{gc}} = 1 \\
&= \Omega\,.
\end{aligned}
\tag{2.35}
$$

---

[4] This section follows the steps in the DFT lecture given by M. Oettel and R. Roth in summer semester 2013 in University of Tübingen.

2. $\Omega[f \neq f_{\text{gc}}] > \Omega$

$$
\begin{aligned}
\ln f_{\text{gc}} &= -\beta \mathcal{H} + \beta \mu N - \ln \Xi \quad \Rightarrow \mathcal{H} - \mu N = -k_{\text{B}} T \ln f_{\text{gc}} + \Omega \ , \quad (2.36) \\
\Omega[f \neq f_{\text{gc}}] &= \text{Tr}_{\text{cl}} \, f \, (\mathcal{H} - \mu N + k_{\text{B}} T \ln f) \\
&= \text{Tr}_{\text{cl}} \, f \, (-k_{\text{B}} T \ln f_{\text{gc}} + \Omega + k_{\text{B}} T \ln f) \\
&= \Omega + k_{\text{B}} T \, \text{Tr}_{\text{cl}} \, f \ln \frac{f}{f_{\text{gc}}} \\
&= \Omega + k_{\text{B}} T \, \text{Tr}_{\text{cl}} \, f_{\text{gc}} \, (x \ln x + 1 - x) \qquad \text{with } x = \frac{f}{f_{\text{gc}}} \\
&= \Omega + k_{\text{B}} T \, \langle g(x) \rangle \qquad \text{with } g(x) = x \ln x + 1 - x \\
&> \Omega \qquad \text{since } g(x) > 1 \text{ for } x \neq 1 \qquad\qquad\qquad (2.37)
\end{aligned}
$$

Now we want to prove that the proposed functional in Eq. (2.34) is a unique functional of the equilibrium density ρ_{eq}. For this purpose, first note that the probability distribution f_{gc} depends on the external potential V_{ext} via the Hamiltonian of the system $\mathcal{H}$. Furthermore, the one–particle equilibrium density $\rho_{\text{eq}} = \rho^{(1)}$ is by definition a functional of f_{gc} (see Eq. (2.19)). Therefore, for a given external potential V_{ext} one can obtain the equilibrium density. The uniqueness is proven, if one can determine the external potential, and as a result the probability distribution, only by the knowledge of the equilibrium density.

Proof by contradiction:

Consider two different external potentials V_{ext} and $V'_{\text{ext}} \neq V_{\text{ext}}$ which give rise to two different Hamiltonians $\mathcal{H} = \mathcal{T} + \mathcal{V} + \mathcal{U}$ and $\mathcal{H}' = \mathcal{T} + \mathcal{V}' + \mathcal{U} \neq \mathcal{H}$, and consequently two equilibrium probability distributions f and $f' \neq f$. The grand potential functional of the probability distribution f' can be written as follows:

$$
\begin{aligned}
\Omega\,[f'] &= \text{Tr}_{\text{cl}} \, f' \, (\mathcal{H}' - \mu N + k_{\text{B}} T \ln f') \\
&< \text{Tr}_{\text{cl}} \, f \, (\mathcal{H}' - \mu N + k_{\text{B}} T \ln f) \ , \qquad\qquad\qquad (2.38)
\end{aligned}
$$

where we have replaced f' with f. Since $\mathcal{H}' = \mathcal{H} - \mathcal{V}' + \mathcal{V}$, we can write the second line in Eq. (2.38) as,

$$
\begin{aligned}
\text{Tr}_{\text{cl}} \, f \, (\mathcal{H}' - \mu N + k_{\text{B}} T \ln f) &= \text{Tr}_{\text{cl}} \, f \, (\mathcal{H} - \mu N + k_{\text{B}} T \ln f) \\
&\quad + \text{Tr}_{\text{cl}} \, f \, (\mathcal{V} - \mathcal{V}') \\
&= \Omega[f] + \text{Tr}_{\text{cl}} \, f \, (\mathcal{V} - \mathcal{V}') \ . \qquad (2.39)
\end{aligned}
$$

Furthermore, using the definition of density distribution from Eq. (2.18), one can rewrite the classical trace of $f\mathcal{V}$ as follows.

$$\begin{aligned}
\mathrm{Tr}_{\mathrm{cl}} \, f\mathcal{V} &= \mathrm{Tr}_{\mathrm{cl}} \, f\left(\sum_{i=1}^{N} V_{\mathrm{ext}}(\mathbf{r}_i)\right) = \mathrm{Tr}_{\mathrm{cl}} \, f\left(\sum_{i=1}^{N} \int \mathrm{d}\mathbf{r} V_{\mathrm{ext}}(\mathbf{r})\delta(\mathbf{r} - \mathbf{r}_i)\right) \\
&= \int \mathrm{d}\mathbf{r} V_{\mathrm{ext}}(\mathbf{r})\mathrm{Tr}_{\mathrm{cl}} \, f \, \hat{\rho} = \int \mathrm{d}\mathbf{r} V_{\mathrm{ext}}(\mathbf{r})\rho(\mathbf{r}) \,,
\end{aligned} \tag{2.40}$$

Now assume that both of the distribution functions f and f' give rise to the same equilibrium density ρ. Note that by making this assumption, it is impossible to determine a unique distribution function by knowing the equilibrium density. Under this assumption, the classical trace of $f\mathcal{V}'$ has the same form as Eq. (2.40) with V_{ext} replaced by V'_{ext}. As a result, by combining Eqs. (2.38)-(2.40) we can write,

$$\Omega\left[f'\right] \quad < \quad \Omega[f] + \int \mathrm{d}\mathbf{r}\rho(\mathbf{r})\left(V_{\mathrm{ext}}(\mathbf{r}) - V'_{\mathrm{ext}}(\mathbf{r})\right) \,. \tag{2.41}$$

However, the choice of f' as an starting point in Eq. (2.38) is completely arbitrary and one can start from writing the grand potential functional of f and obtain a similar expression.

$$\Omega\left[f\right] \quad < \quad \Omega[f'] - \int \mathrm{d}\mathbf{r}\rho(\mathbf{r})\left(V_{\mathrm{ext}}(\mathbf{r}) - V'_{\mathrm{ext}}(\mathbf{r})\right) \,. \tag{2.42}$$

The contradiction between Eqs. (2.41) and (2.42) is due to the wrong assumption that these two probability densities result in the same equilibrium density. Therefore, the probability density is a unique functional of the equilibrium density.

Since the probability density is a unique functional of the equilibrium density we have $\Omega[f] = \Omega[\rho]$. The equilibrium density minimizes the grand potential functional and the minimum value is the grand potential of the system:

$$\left.\begin{array}{rcl}
\Omega[\rho_{\mathrm{eq}}] &=& \Omega \\
\Omega[\rho \neq \rho_{\mathrm{eq}}] &>& \Omega
\end{array}\right\} \quad \Leftrightarrow \quad \left.\frac{\delta\Omega}{\delta\rho}\right|_{\rho=\rho_{\mathrm{eq}}} = 0 \,. \tag{2.43}$$

Furthermore, one can rewrite the grand potential functional as a Legendre transformation of the free energy functional.

$$\begin{aligned}
\Omega[\rho] &= \mathrm{Tr}_{\mathrm{cl}} \, f\left(\mathcal{H} - \mu N + k_{\mathrm{B}}T\ln f\right) \\
&= \mathrm{Tr}_{\mathrm{cl}} \, f\left(\mathcal{T} + \mathcal{U} + k_{\mathrm{B}}T\ln f\right) + \mathrm{Tr}_{\mathrm{cl}} \, f\left(\mathcal{V} - \mu N\right) \\
&= \mathcal{F}[\rho] + \int \mathrm{d}\mathbf{r}\rho(\mathbf{r})\left(V_{\mathrm{ext}}(\mathbf{r}) - \mu\right),
\end{aligned} \tag{2.44}$$

where $\mathcal{F}[\rho]$ is the intrinsic Helmholtz free energy functional of the system. Once the form of this functional is determined, one can apply it to a system of interest and obtain its Helmholtz free energy.

The assumption, that a one–body density distribution ρ is generated by some external potential, the so–called V_{ext}–representability of ρ, is known to be not necessarily guaranteed for an arbitrary density distribution in quantum DFT [19,23,24]. Based on a constrained search of the density profile, Levy has introduced an alternative approach, in which a weaker condition,known as N–representability, is imposed in order to directly obtain the density distribution from an N–body antisymmetric wave function [23]. Consequently, the existence of a generating external potential is not needed [23, 25]. The corresponding classical representation of Levy's free energy functional reads [26]

$$\mathcal{F}_{\text{Levi}}[\rho] \;=\; \min_{f \to \rho} \left[\text{Tr}_{\text{cl}} f \left(\mathcal{T} + \mathcal{U} + k_{\text{B}} T \ln f \right) \right], \tag{2.45}$$

in which, for a given one–body density profile ρ, among the corresponding normalized density distributions f (see Eq. (2.19)), we are looking for the one which minimizes the term in brackets. Note that here the functions f are general normalized distribution functions and are not necessarily of Boltzmann–type containing the interaction between particles. Hence, ρ is constrained to be f–representable but not necessarily V_{ext}–representable. By constraining the search in Eq. (2.45) to the class of V_{ext}–representable densities, the obtained free energy functional is equivalent to $\mathcal{F}$ from Eq. (2.44). For a given external potential, it can be proven that the variational principle from Eq. (2.43) holds for the corresponding grand potential functional Ω_{Levi} while the variational principle turns into a two–stage minimization [26].

$$\Omega_{\text{Levi}}[\rho] \;=\; \mathcal{F}_{\text{Levi}}[\rho] + \int d\mathbf{r} \rho(\mathbf{r}) \left(V_{\text{ext}}(\mathbf{r}) - \mu \right), \tag{2.46}$$

$$\Omega \;=\; \min_{\rho} \min_{f \to \rho} \left[\text{Tr}_{\text{cl}} f \left(\mathcal{H} - \mu N + k_{\text{B}} T \ln f \right) \right] = \min_{\rho} \Omega_{\text{Levi}}[\rho_{\text{eq}}]. \tag{2.47}$$

In practice, such a minimization is as complicated as solving the many–body problem itself. However, for a constrained or fixed number of particles where the grand and the canonical ensembles are not equivalent in general [27–30], Levy's method may result in construction of approximate free energy functionals in the canonical ensemble.

2.3.2 Helmholtz free energy functional for an ideal gas

Consider an ideal gas with N identical particles in the presence of an external potential V_{ext}. Since the particles do not interact, the Hamiltonian of the system is given by

$\mathcal{H} = \mathcal{T} + \mathcal{V}$. The grand partition sum, and consequently the grand potential, of this system is calculated as follows:

$$
\begin{aligned}
\Xi^{\text{id}} &= \text{Tr}_{\text{cl}} \ \exp\left(-\beta\mathcal{H} + \beta\mu N\right) \\
&= \sum_{N=0}^{\infty} \frac{1}{h^{3N}N!} \int d\mathbf{r}^N \int d\mathbf{p}^N \exp\left(-\beta\sum_{i=1}^{N}\left(\frac{p_i^2}{2m_i} + V_{\text{ext}}(\mathbf{r}_i)\right) + \beta\mu N\right) \\
&= \sum_{N=0}^{\infty} \frac{e^{\beta\mu N}}{h^{3N}N!} \left(\int d\mathbf{r} \exp\left(-\beta V_{\text{ext}}(\mathbf{r})\right)\right)^N \left(\int d\mathbf{p} \exp\left(\frac{-\beta p^2}{2m}\right)\right)^N \\
&= \sum_{N=0}^{\infty} \frac{1}{N!} \left(\frac{e^{\beta\mu}}{\lambda^3} Q\right)^N = e^{zQ} , \quad \text{with } Q = \int d\mathbf{r} \exp\left(-\beta V_{\text{ext}}(\mathbf{r})\right) \qquad (2.48) \\
\beta\Omega^{\text{id}} &= -\ln\Xi^{\text{id}} = -zQ . \qquad\qquad\qquad\qquad\qquad\qquad\qquad\qquad\qquad\qquad\qquad (2.49)
\end{aligned}
$$

Here λ is de Broglie thermal wave length as introduced in Eq. (2.11), and $z = e^{\beta\mu}/\lambda^3$ is the fugacity of the ideal gas. In order to express the ideal gas grand potential $\beta\Omega^{\text{id}}$ as a functional of density, one should obtain the ensemble average of the particle distribution $\hat{\rho}(\mathbf{r})$.

$$
\begin{aligned}
\rho(\mathbf{r}) &= \langle\hat{\rho}(\mathbf{r})\rangle = \text{Tr}_{\text{cl}} \ f_{\text{gc}} \ \hat{\rho}(\mathbf{r}) = \text{Tr}_{\text{cl}} \ \frac{\exp\left(-\beta\mathcal{H} + \beta\mu N\right)}{\Xi^{\text{id}}} \sum_{i=1}^{N} \delta\left(\mathbf{r} - \mathbf{r}_i\right) \\
&= \frac{1}{\Xi^{\text{id}}} \sum_{N=1}^{\infty} \frac{e^{\beta\mu N}}{N!\lambda^{3N}} \int d\mathbf{r}_1 \cdots \int d\mathbf{r}_N \exp\left(-\beta\sum_{j=1}^{N} V_{\text{ext}}(\mathbf{r}_j)\right) \sum_{i=1}^{N} \delta\left(\mathbf{r} - \mathbf{r}_i\right) \\
&= \frac{1}{\Xi^{\text{id}}} \sum_{N=1}^{\infty} \frac{z^N}{N!} \sum_{i=1}^{N} \left[\exp\left(-\beta V_{\text{ext}}(\mathbf{r})\right) \left(\int d\mathbf{r}_{j\neq i} \exp\left(-\beta V_{\text{ext}}(\mathbf{r}_j)\right)\right)^{N-1}\right] \\
&= \frac{1}{\Xi^{\text{id}}} \sum_{N=1}^{\infty} \frac{z^N}{N!} N \exp\left(-\beta V_{\text{ext}}(\mathbf{r})\right) Q^{N-1} \\
&= z \ \exp\left(-\beta V_{\text{ext}}(\mathbf{r})\right) \frac{1}{\Xi^{\text{id}}} \sum_{N=0}^{\infty} \frac{(zQ)^N}{N!} = z \ \exp\left(-\beta V_{\text{ext}}(\mathbf{r})\right) , \qquad (2.50)
\end{aligned}
$$

where in the last step we have used Eq. (2.48). The resulting expression for the equilibrium density profile of an ideal gas in Eq. (2.50) is in the form of the barometric law. Combining Eqs. (2.49) and (2.50) we obtain the ideal gas grand potential functional of the density.

$$
\beta\Omega^{\text{id}}[\rho(\mathbf{r})] = -\int d\mathbf{r}\rho(\mathbf{r}) . \qquad\qquad\qquad\qquad\qquad\qquad\qquad (2.51)
$$

Note that for a bulk density $\rho(\mathbf{r}) = N/V$ we obtain $\beta\Omega = -N$, the same results as one can obtain by combining Eqs. (2.23) and (2.25). Furthermore, one can use Eq. (2.50) to replace $V_{\text{ext}}(\mathbf{r}) - \mu$ in equation Eq. (2.44) by $-k_{\text{B}}T \ln\left(\lambda^3 \rho(\mathbf{r})\right)$ and obtain the Helmholtz free energy functional for an ideal gas.

$$\beta\mathcal{F}^{\text{id}}[\rho(\mathbf{r})] = \int d\mathbf{r}\rho(\mathbf{r})\left(\ln\left(\lambda^3\rho(\mathbf{r})\right) - 1\right) . \tag{2.52}$$

Conveniently, the Helmholtz free energy functional of a system with interacting particles is decomposed into its ideal gas part from Eq. (2.52) and the excess (over) ideal gas part $\beta\mathcal{F}^{\text{ex}}$ due to the interaction of the particles in the system. The important task in taking advantage of DFT for studying classical system, is to obtain an excess Helmholtz free energy functional which is taking care of the corresponding potential governing the system. The derivation of such functionals will be discussed in more details in Section 3.3.

2.3.3 Excess part of the free energy functional and direct correlation functions

The excess part of the Helmholtz free energy is a generating functional for a hierarchy of direct correlation functions $c^{(n)}(\mathbf{r}^n)$. The first functional derivative of $\beta\mathcal{F}^{\text{ex}}$ with respect to single–particle density $\rho(\mathbf{r})$ gives the single-particle direct correlation function $c^{(1)}(\mathbf{r})$. The pair correlation function $c^{(2)}(\mathbf{r}, \mathbf{r}')$ is obtained by taking the functional derivative of $c^{(1)}(\mathbf{r})$ with respect to $\rho(\mathbf{r}')$. The higher order functions are defined similarly.

$$c^{(1)}(\mathbf{r}) = -\frac{\delta\beta\mathcal{F}^{\text{ex}}[\rho]}{\delta\rho(\mathbf{r})} , \tag{2.53}$$

$$c^{(2)}(\mathbf{r}, \mathbf{r}') = \frac{\delta c^{(1)}(\mathbf{r})}{\delta\rho(\mathbf{r}')} = -\frac{\delta^2\beta\mathcal{F}^{\text{ex}}[\rho]}{\delta\rho(\mathbf{r})\delta\rho(\mathbf{r}')} \tag{2.54}$$

$$\vdots$$

$$c^{(n+1)}(\mathbf{r}^{n+1}) = \frac{\delta c^{(n)}(\mathbf{r}^n)}{\delta\rho(\mathbf{r}_{n+1})} = -\frac{\delta^{n+1}\beta\mathcal{F}^{\text{ex}}[\rho]}{\delta\rho(\mathbf{r})_1\delta\rho(\mathbf{r}_2)\cdots\delta\rho(\mathbf{r}_{n+1})} . \tag{2.55}$$

By minimizing the grand potential functional and using the expression for the Helmholtz free energy functional of an ideal gas (see Eqs. (2.44) and (2.52)), the equilibrium density profile of a system in the presence of an external potential V_{ext} is written as follows:

$$\lambda^3\rho_{\text{eq}}(\mathbf{r}) = \exp\left[-\beta V_{\text{ext}}(\mathbf{r}) + \beta\mu + c^{(1)}(\mathbf{r})\right] , \tag{2.56}$$

where $c^{(1)}$ is the single–particle direct correlation function defined in Eq. (2.53). By comparing this result with the barometric law for the equilibrium density profile of an ideal gas from Eq. (2.50), one can conclude that the one–particle direct correlation function contains all the information regarding the interactions between the particles. Furthermore, $c^{(1)}$ can be interpreted as the excess part of the intrinsic chemical potential[5]. In the absence of any external potential $V_{\text{ext}} = 0$, one can write,

$$-c^{(1)}(\mathbf{r}) \;=\; \beta\mu - \ln\left(\lambda^3 \rho_{\text{eq}}(\mathbf{r})\right) = \beta\mu^{\text{ex}} \;, \tag{2.57}$$

This relation is later used for obtaining the equilibrium density profile ρ_{eq} of a hard–sphere system (see Appendix A.4).

---

[5] See the discussion in Section 3.5 of Ref. [6].

CHAPTER 3

CLASSICAL PAIRWISE INTERACTIONS

A theoretical ideal gas whose particles do not interact with each other is an important educational model. However, a system with non–interacting particles is not usually the case in nature. In a metallic system for instance, there is an electromagnetic interaction between the positively charged nuclei and the electrons with negative charge. This many–body potential between the nuclei and electronic gas leads to a cohesive energy which makes it possible to have a stable crystalline state at low enough temperatures [31].

In a colloidal system, the length scales are much larger and the components are super–molecules with typical size of 10 nm to 10 μm consisting of many atoms. Here, the electromagnetic interaction between the atoms leads to an effective interaction between colloidal particles. This effective interaction is often expressed as a function of relative distance between the particles and is assumed to be pairwise. Therefore, the total potential of a single particle is computed as a sum of its interactions with all other particles in the system. The thermodynamic properties of the system are mainly dictated by the short–range repulsive part of this effective potential [6].

It was common to assume a system with a stable crystalline state necessarily needs an attractive potential between its particles. However, in 1957 Wood et al. and Adler et al. performed computer simulations and showed a phase transition from a disordered liquid phase to an ordered state for particles with a purely repulsive interaction [32, 33]. This simple form of potential known as hard–spheres, has served as a reference system for theoretical studies of liquid and solid states of a colloidal system ever since. The difference of the hard–sphere potential with the "real" interaction between the colloidal particles can be taken into account as a perturbation [6,7].

In the context of classical DFT, the free energy functional is decomposed into an ideal and an excess (over ideal) part. While the ideal gas part of the free energy functional is known (see Section 2.3.2), the excess part is not known exactly in most cases. There

are some methods which give approximate excess free energy functionals, for instance the Low Density Approximation, Taylor expansion in density, or the phase field crystal model, to name a few. In 1989, Rosenfeld introduced Fundamental Measure Theory (FMT) for hard–core interactions which during the next 20 years evolved into an accurate description of hard–sphere systems [9, 10, 12, 34].

In this chapter different types of colloidal interactions are shortly discussed in Section 3.1. The hard–sphere system and some theoretical methods for investigating a hard–core interaction are presented in Section 3.2. Finally, in Section 3.3 some approximate methods for constructing the excess energy functional for a hard–sphere system are introduced. A more detailed discussion on the FMT functionals for hard–spheres is presented in Chapter 4.

3.1 Interactions between colloidal particles

Colloidal particles are super–molecules dispersed in a medium that is often a liquid. The term super–molecule refers to the typical size order of the colloidal particles, roughly between 10 nm and 10μm which is much larger than those of the solvent molecules. Due to their small mass and size, the molecules in medium are often integrated out with their trace cast into the effective potential between the colloidal particles.

In a colloidal suspension, there is a van der Waals attraction between the colloidal particles. This short–ranged attraction arises due to the cooperative oscillations in the electronic clouds of the atoms constructing colloidal particles. The van der Waals attraction between colloidal particles must be opposed by a repulsion in order to prevent irreversible flocculation. This stabilization can be done for instance by using charged colloidal particles as in DLVO. The DLVO model which is named after Derjaguin, Landau, Verwey, and Overbeek, is historically one of the first models which describes the interactions between colloidal particles [35, 36]. Here, the compensating repulsive interaction is the electrical double layer repulsion which depends on the concentration of the salt in the suspension (see Fig. 3.1). Another way for stabilizing the suspension, is inducing a repulsion by coating the colloidal particles with long polymer chains [3].

The effective potential between colloidal particles is tunable by modifying the properties of the solvent or those of the colloidal particles, e.g. changing the concentration of the salt in the solvent, adding polymers to the suspension, or modifying the surface of the colloidal molecules [3]. The physical properties of a colloidal dispersion and hence the phase diagram of the system are dictated by the effective potential. In an atomic system whose interactions are described by potentials with attractive and repulsive parts similar to the Lennard–Jones potential, the law of corresponding states indicates
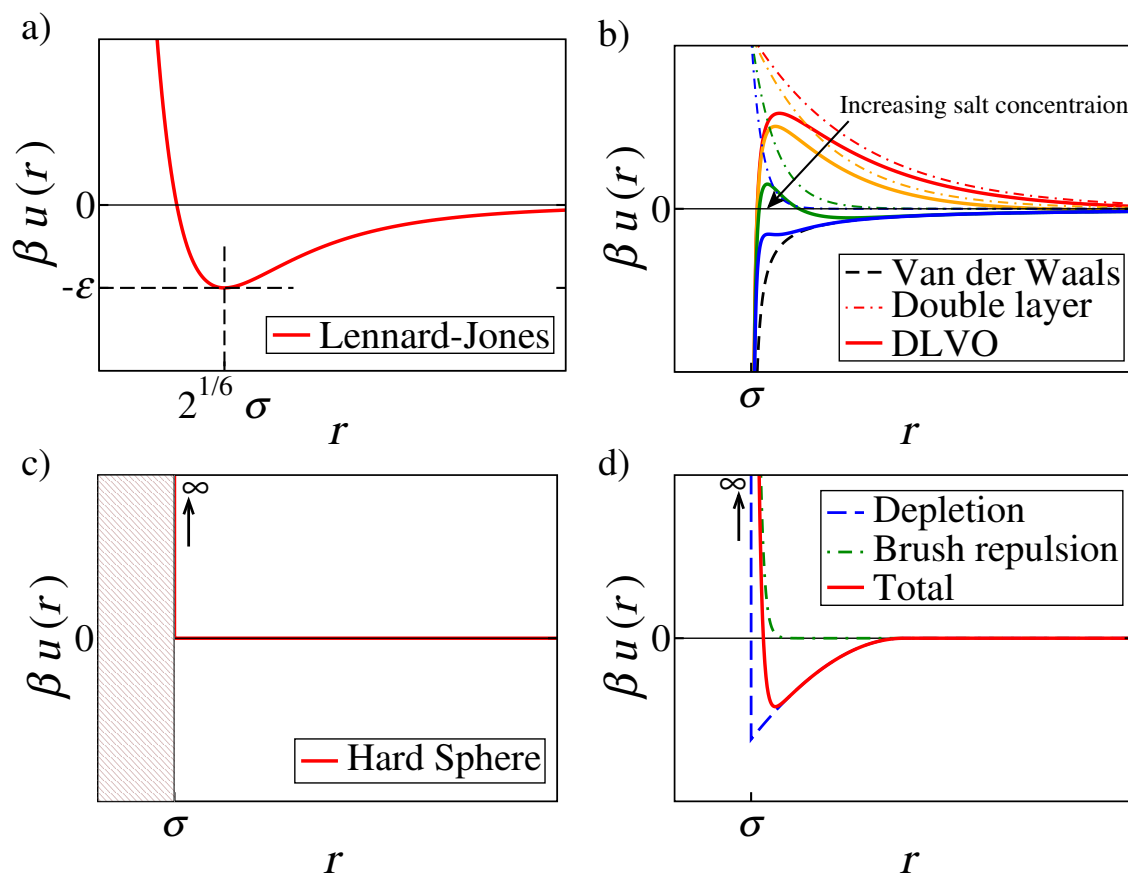
Figure 3.1: Schematic illustration of selected types of pair interactions. a) The Lennard–Jones potential is an important pairwise interaction which describes the components interaction in some atomic system, e.g. noble gases like Argon. b) In DLVO the short–range attraction is opposed by a repulsive interaction due to the electric force between ions with like charge attracted to the surface of the colloidal particles. c) Attaching short polymer chains to the surface of the colloidal particles results in a net repulsive potential which in a proper combination with van der Waals attraction leads to a realization of the theoretical hard–sphere model. d) Adding non–adsorbing polymer chains results in a net attractive interaction between the colloidal particles known as depletion interaction. The attractive potential depends on the density of polymers in the suspension as well as the polymer–colloid size ratio.

that the phase diagram is scaled by the thermodynamic properties of the critical point, thus the phase diagram topology of such fluids is approximately the same [6]. Similarly the knowledge about the potential of the mean force between spherical colloidal particles allows to estimate the phase diagram topology of a colloidal suspension [37]. These expected similarities with an atomic system, makes colloidal suspensions even

more interesting to study.

The depletion interaction is another important potential which comes about by adding non–adsorbing polymer chains to a colloidal suspension [4,5]. As a consequence of the repulsive colloid–polymer interaction there exists an effective depletion layer around a colloidal particle in which the configurational entropy of the polymer chains is decreased. In order to maximize their entropy, the polymers exert an osmotic pressure onto the colloidal particles to increase the overlap of the depletion layers. This results in an effective short–range attraction between the colloidal particles which depends on the colloid–polymer size ratio and the density of the polymers (see Chapter 5).

The properties and structure of a colloidal suspension are mainly determined by the short–range repulsive interaction between the particles [6]. The van der Waals interaction between the colloidal particles is tunable by matching the refractive index of the solvent to the one of the colloidal particles. By a combination of the such minimized attraction and repulsive thin brushes, the colloidal particles behave almost as hard–spheres [3]. The hard–sphere model is important in theory since it can be used as a reference system with the additional attractions acting as a perturbation [7].

3.2   Hard Spheres

In a hard–sphere system the particle are not allowed to overlap with each other, hence the pairwise potential between two spheres with radius R_i and R_j reads

$$
u_{\mathrm{HS}}(r_{ij}) = \begin{cases} \infty & r_{ij} = |\mathbf{r}_i - \mathbf{r}_j| < R_i + R_j \ , \\ 0 & \text{otherwise} \end{cases} \quad ,
\tag{3.1}
$$

with $\mathbf{r}_i$ and $\mathbf{r}_j$ denoting the position of the particles in space. Since the interaction potential is either 0 or ∞ temperature does not play a role in the behavior of a hard–sphere system. In fact, the internal energy of the system is zero, $U = 0$, and its free energy is $F = -TS$. As a result, the thermodynamic properties of the system are solely affected by entropy. The equilibrium configuration is obtained by maximizing the entropy of the system. At low densities, the disordered arrangement in the liquid corresponds to maximum entropy. However, by increasing the density, the number of possible disordered arrangements reduces and the system undergoes a transition into an ordered state in order to maximize its entropy. Hence, the phase transition of a hard–sphere fluid into an fcc crystalline structure, is completely entropy driven. This kind of fluid–solid phase transition was first observed in simulations for mono–disperse repulsive colloidal particles in 1950's [38,39].

For realization of a hard–sphere system silica or Polymethyl methacrylate (PMMA) particles are often used. PMMA is a synthetic resin produced from the polymeriza-

tion of methyl methacrylate. The van der Waals attraction between the particles is minimized by matching the refractive index of the solvent with the one of the colloidal particles. In order to compensate any residual attraction, the particles are sterically stabilized by coating with polymers [40, 41]. Polydispersity, the deviation of the particle size from their average value, is an important parameter in determination of the phase diagram of the hard–sphere system [41]. While it is possible to prepare a sample with a narrow of particle size distribution [42], subtle differences in particle size distributions are induced in a controlled process in order to investigate the effect of polydispersity on physical properties of the system, e.g. the crystallization kinetics [43, 44].

Simulation studies on hard–sphere systems date back to the 1950's, when Wood et al. [32], and Alder et al. [33], showed the entropic phase transition in such a system. An important difficulty in simulating the hard core interaction, is the discontinuity of the potential (Eq. (3.1)). From another point of view, this is an advantage of the system since each particle only is affected by and has influence on its nearest neighbour particles. The fast advancements in computer technologies in the last decade has lead to less expensive computing tools and availability of the super–computers to a larger crowd. This has made it possible to use more sophisticated simulating methods and larger system sizes to prevent finite size effects and obtain more reliable results. Such reliable results backs up the theoretical studies for investigating the systems for which the experimental realization is either impossible or too costly.

3.2.1 Virial expansion and the Carnahan–Starling equation of state

Due to the interaction of the particles in the system, the equation of state is different from that of an ideal gas where $u(r) = 0$ (Eq. (2.2)). Defining the Mayer–f bond (function) as a function of the interaction between particles,

$$f(r) = \exp(-\beta u(r)) - 1 , \tag{3.2}$$

for a system with N particles in a physical volume V, the deviation of the equation of state from an ideal gas can be expressed as a virial expansion in the density $\rho = N/V$ as follows [6],

$$\frac{\beta p}{\rho} = 1 + \sum_{n=2}^{\infty} B_n(T)\rho^{n-1} , \quad \text{with } \beta = \frac{1}{k_{\mathrm{B}}T}. \tag{3.3}$$

Here, the virial coefficients B_n are expressed as a function of temperature T. The first coefficient is $B_1 = 1$ and the higher order ones rise due to the n–body interactions in a

non–ideal gas and are defined in terms of Mayer–f function f (Eq. (3.2)).

$$B_2(T) = -\frac{1}{2V}\iint \mathrm{d}\mathbf{r}_i \mathrm{d}\mathbf{r}_j f(r_{ij}) = -\frac{1}{2}\int \mathrm{d}\mathbf{r} f(r) , \quad \text{with } r_{ij} = |\mathbf{r}_i - \mathbf{r}_j| \qquad (3.4)$$

$$B_3(T) = -\frac{1}{3V}\iiint \mathrm{d}\mathbf{r}_i \mathrm{d}\mathbf{r}_j \mathrm{d}\mathbf{r}_k f(r_{ij})f(r_{jk})f(r_{ik}) , \qquad (3.5)$$

$$\vdots$$

$$B_n(T) = -\frac{1}{nV}\int \mathrm{d}\mathbf{r}^n \prod_{\{ij\}} f(r_{ij}) , \qquad (3.6)$$

where the product in $B_n(T)$ is over all possible pairs of i and j. Note that $B_3(T)$ already contains information about simultaneous interactions between three particles. In the low density limit, it is reasonable to assume that such interactions do not exist, hence $B_{n\geq 3} = 0$. Therefore, in this limit it is sufficient to consider the second virial coefficient.

For a hard–sphere system, the Mayer-f functions are given as follows.

$$f(r) = \exp(-\beta u(r)) - 1 = \begin{cases} -1 & r < \sigma \\ 0 & \text{otherwise} \end{cases} \qquad (3.7)$$

where σ is the hard–sphere diameter. In this case, the virial coefficients $B_n(T)$ are independent of temperature, hence constant values [6, 45]. The first three virial coefficient, i.e. B_2, B_3, and B_4, have been found analytically [6]. Some of the higher order terms, B_5 to B_{12}, have been evaluated numerically [45–49].

As a result, the hard–sphere equation of state is given by [6],

$$\begin{aligned} \frac{\beta p}{\rho} &= 1 + \sum_{n=2}^{\infty} B_n(T)\eta^{n-1} \\ &= 1 + 4\eta + 10\eta^2 + 18.365\eta^3 + 28.225\eta^4 \\ &\quad + 39.74\eta^5 + 53.5\eta^6 + 70.8\eta^7 + \mathcal{O}\left(\eta^8\right) , \end{aligned} \qquad (3.8)$$

where the hard–sphere packing fraction is denoted by $\eta = \frac{\pi}{6}\sigma^3\rho$. Carnahan and Starling approximated the virial coefficients by $n^2 + n - 2$, i.e. 4, 10, 18, 28, 40, 54, and 70 for B_2 to B_8 which slightly deviate from their calculated values presented in Eq. (3.8). Using this approximation, the resulting sum is a geometric series which has a closed form [50].

$$\begin{aligned} \frac{\beta p_{\text{CS}}}{\rho} &= 1 + \sum_{n=2}^{\infty} (n^2 + n - 2)\eta^{n-1} = 1 + \sum_{n=1}^{\infty} (n^2 + 3n)\eta^n \\ &= \frac{1 + \eta + \eta^2 - \eta^3}{(1 - \eta)^3} \end{aligned} \qquad (3.9)$$
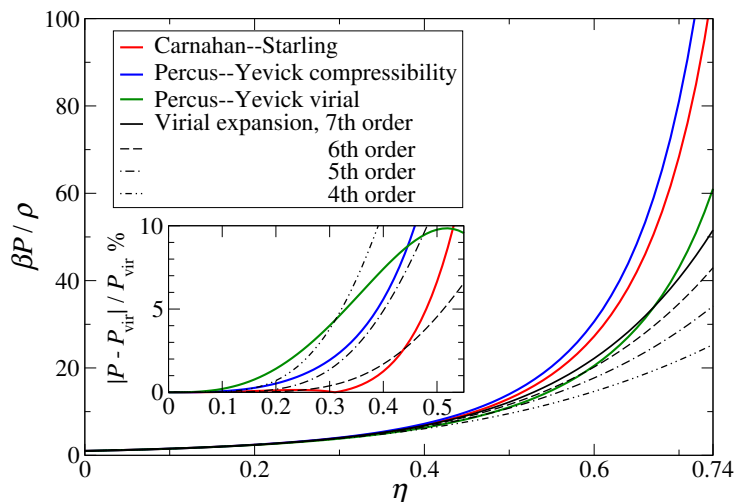
Figure 3.2: Equation of state of a hard–sphere fluid obtained by different theoretical methods: Carnahan–Starling from Eq. (3.9), Percus–Yevick compressibility from Eq. (3.18), Percus–Yevick virial from Eq. (3.20), and virial expansion truncated after specified orderin legends. The inset shows the relative deviation with respect to the 7th order virial expansion $|p - p_{\mathrm{vir}}^{7\mathrm{th}}|/p_{\mathrm{vir}}^{7\mathrm{th}}$ up to the vicinity of fluid–solid phase transition $\eta \approx 0.5$.

The Carnahan–Starling equation of state is a good fit to computer simulations in the range of fluid densities and its largest deviation occurs at higher packing fractions and is of the order of 1% (see Fig. 3.2). In particular one can obtain the excess free energy density f_{ex} of a hard–sphere system from the Carnahan–Starling equation of state.

$$
\begin{aligned}
\beta f^{\mathrm{ex}} &= \frac{\beta F - \beta F^{\mathrm{id}}}{V} = \rho \int_0^\eta \frac{\mathrm{d}\eta'}{\eta'} \left(\frac{\beta p(\eta')}{\rho'} - 1 \right) \\
&= \rho \, \frac{\eta(4 - 3\eta)}{(1 - \eta)^2} \, .
\end{aligned}
\tag{3.10}
$$

3.2.2 The Percus–Yevick approximation

The Ornstein–Zernike relation (Eq. (2.30)) gives a recursive relation between the total pair correlation function $h(\mathbf{r}_i, \mathbf{r}_j)$ and the direct pair correlation function $c^{(2)}(\mathbf{r}_i, \mathbf{r}_j)$. However, this relation is open and it is necessary to have information about $c^{(2)}$ in order to solve it. In order to obtain a closure, consider an isotropic homogeneous system with a single particle pinned at $\mathbf{r} = 0$. The remaining $N - 1$ particles feel the force field of the pinned particle as an external potential $V_{\mathrm{ext}}(\mathbf{r}) = u(r)$ with $r = |\mathbf{r}|$. The single–particle density $\rho^{(1)}(\mathbf{r})$ is equivalent to $\rho^{(2)}(0, \mathbf{r})/\rho$ where $\rho^{(2)}(0, \mathbf{r})$ is the two–particle

density in the absence of the external potential. Using the definition of the distribution function from Eq. (2.29), one can relate $g(\mathbf{r})$ to the single–particle density as [51, 52],

$$\rho^{(1)}(\mathbf{r}) = \rho g(\mathbf{r}) . \tag{3.11}$$

Furthermore, one can consider the external potential as a perturbation to the homogeneous system and expand $\exp\left(c^{(1)}(r)\right)$ in terms of deviations in the single–particle density $\Delta\rho^{(1)}$. The expansion to the first order in $\Delta\rho^{(1)}$ reads [6]

$$\exp\left(c^{(1)}(r)\right) \approx \exp\left(c_{\text{ref}}^{(1)}(r)\right)\left(1 + \int d\mathbf{r}'\Delta\rho^{(1)}(\mathbf{r}')c_{\text{ref}}^{(2)}(\mathbf{r},\mathbf{r}')\right) ,$$

$$\text{with } \Delta\rho^{(1)}(\mathbf{r}) = \rho^{(1)}(\mathbf{r}) - \rho_{\text{ref}}^{(1)}(\mathbf{r}) = \rho g(\mathbf{r}) - \rho = \rho h(\mathbf{r}) , \tag{3.12}$$

where $c_{\text{ref}}^{(1)}$ is the single–particle correlation function for the reference system (see Eqs. (2.56) and (2.57)). Using the expressions for the single–particle density from Eq. (2.56), one can obtain the Percus–Yevick approximation ("closure relation").

$$g(r) = \exp\left(-\beta u(r)\right)\left(1 + \rho\int d\mathbf{r}'\, c(|\mathbf{r}-\mathbf{r}'|)h(r')\right)$$

$$= \exp\left(-\beta u(r)\right)\left(1 + h(r) - c(r)\right) , \tag{3.13}$$

$$\Rightarrow c(r) = g(r)\left(\exp\left(\beta u(r)\right) - 1\right) \tag{3.14}$$

where we have used the Ornstein–Zernike relation for an isotropic homogeneous system (Eq. (2.31)) in the second line and the definition of total correlation function $h = g - 1$ in the last one. The Percus–Yevick approximation is important in the theory of simple fluids since it has an analytical solution for the hard–sphere fluid. Defining $\tau(r) =: g(r)\exp(\beta u(r))$, the Percus–Yevick approximation for a hard–sphere fluid is written as follows:

$$c(r) = \tau(r)\left(\exp(-\beta u(r)) - 1\right) = \begin{cases} -\tau(r) & r < \sigma \\ 0 & \text{otherwise} \end{cases} \tag{3.15}$$

On the other hand, the distribution function for $r > \sigma$ is equal to $\tau(r)$ and for $r < \sigma$ it is zero since we have hard–spheres. As a result, using the Ornstein–Zernike relation one can write the following integral equation for $\tau(r)$ [53].

$$\tau(r) = 1 + \rho\int_{r<\sigma} d\mathbf{r}'\tau(r') - \rho\int_{\substack{r'<\sigma \\ |\mathbf{r}-\mathbf{r}'|>\sigma}} d\mathbf{r}'\tau(r')\tau(|\mathbf{r}-\mathbf{r}'|) . \tag{3.16}$$

The equation is solved by taking the one-side Laplace transformation of the integral equation and assuming the direct pair correlation function $c(r)$ as a cubic polynomial in

r/σ. Finally, the direct pair correlation function of a hard–sphere fluid for $x = r/\sigma > 1$ is given as follows.

$$c(x) \;=\; -\alpha + \frac{3}{2}\eta\beta x - \frac{1}{2}\eta\alpha x^3 \,, \quad \text{with } \alpha = \frac{(1+2\eta)^2}{(1-\eta)^4} \,,\; \beta = \frac{(2+\eta)^2}{(1-\eta)^4} \,. \tag{3.17}$$

The Percus–Yevick compressibility equation of state is obtained by calculating the compressibility of the hard–sphere fluid using Eq. (2.33) with $c(r)$ from Eq. (3.17) and integrating with respect to η.

$$\frac{\beta p_{\mathrm{PY}}^{\mathrm{com}}}{\rho} \;=\; \frac{1+\eta+\eta^2}{(1-\eta)^3} \,. \tag{3.18}$$

Alternatively, one can start from the virial theorem which expresses the equation of state as a time average of the interactions between particles, and relate it to the distribution function. The equation of state in this case is related to $\tau(r)$ as [6][1],

$$\frac{\beta p}{\rho} \;=\; 1 + \frac{2\pi}{3}\rho \lim_{r\to\sigma^+} r^3\tau(r) \,. \tag{3.19}$$

By replacing the obtained expression for $\tau(r) = -c(r < \sigma)$ (Eq. (3.17)) in Eq. (3.19), the Percus–Yevick virial equation of state is obtained.

$$\frac{\beta p_{\mathrm{PY}}^{\mathrm{vir}}}{\rho} \;=\; \frac{1+2\eta+3\eta^2}{(1-\eta)^2} \,. \tag{3.20}$$

The difference between two versions of the Percus–Yevick equation of state increases with density (see Fig. 3.2). In comparison with the more exact Carnahan–Starling equation of state $\beta p_{\mathrm{CS}}/\rho$, the compressibility equation of state overestimates the pressure at higher densities at which the transition to a crystal is expected. This will lead to wrong predictions of the coexistence densities[2].

3.2.3 Scaled–particle theory

The equation of state of a hard–sphere system can be derived in an extrapolation scheme known as Scaled Particle Theory (SPT). Here the required work for inserting

---

[1] See Section 2.5 of Ref. [6] for a detailed derivation.

[2] See for instance the difference between coexistence densities predicted by two versions of FMT functionals in Section 4.5 which is due to their different underlying equation of state.
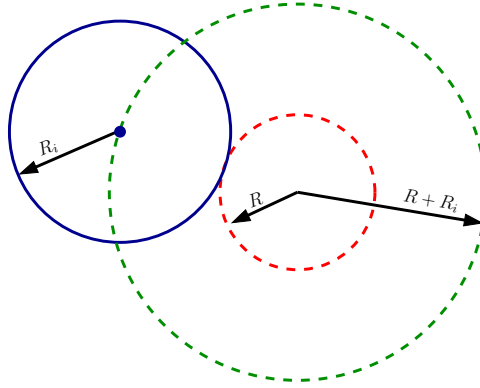
Figure 3.3: A schematic illustration of a modified cavity in the scaled–particle theory. Depicted is a single hard–sphere (solid blue) with radius R_i in vicinity of an assumed cavity of size R (dashed red). The center of the hard–sphere is not allowed to enter the modified cavity with radius $R + R_i$ (dashed green).

a hard–sphere particle with radius R into a mixture of hard–sphere particles with radius R_i is calculated in two extreme limits, i.e. $R \to 0$ and $R \to \infty$. This reversible work is equivalent to the excess chemical potential of the system due to the insertion of the new particle. The corresponding excess chemical potential for mid–range sizes is obtained by an extrapolation [6,54,55].

Consider a mixture of ν species of hard–spheres in a physical volume V. Each species have N_i particles with radius R_i, hence the number density of each species is $\rho_i = N_i/V$. In order to insert a new particle $R \ll R_i$, one should find a cavity of the same size R in the system. Due to the spontaneous fluctuation of the particles, there is a finite probability f_{cav} of finding such cavity which is given as follows:

$$f_{\text{cav}}(R) = \exp(-\beta\mu^{\text{ex}}(R)) . \tag{3.21}$$

Here, the probability is expressed as a function of excess chemical potential μ^{ex}. This probability is equivalent to the probability of finding modified cavities with radius $R + R_i$ in which the *center* of the corresponding hard–sphere with radius R_i is not allowed (see Fig. 3.3). Obviously, if there is a hard–sphere in a modified cavity we are not able to insert the new hard–sphere in it. Therefore one can express f_{cav} as the complementary probability f_{occ} that all such modified cavities are occupied.

$$f_{\text{cav}} = 1 - f_{\text{occ}} . \tag{3.22}$$

Now, consider modified cavities whose radius are smaller than or equal to their corresponding hard sphere species, i.e. $R + R_i \leq R_i$. This implies an extension of R to unphysical negative values. In this limit, a modified cavity can be occupied at most

with one particle. Therefore, f_{occ} is expressed as a sum over probabilities $f_{i,\text{occ}}$ of finding a hard–sphere with radius R_i in its corresponding modified cavity.

$$f_{\text{occ}}(R) = \sum_{i=1}^{\nu} f_{i,\text{occ}}(R) = \sum_{i=1}^{\nu} \frac{4}{3}\pi (R + R_i)^3 \rho_i \qquad \text{for } R \leq 0 \,. \tag{3.23}$$

Combining Eq. (3.21) with Eq. (3.23) we can write,

$$\beta\mu^{\text{ex}}(R) = -\ln\left(1 - \sum_{i=1}^{\nu} \frac{4}{3}\pi (R_i + R)^3 \rho_i\right) \qquad \text{for } R \leq 0 \,. \tag{3.24}$$

In the other extreme limit, the required reversible work for creating a large cavity of size $R \gg R_i$ is given by,

$$\mu^{\text{ex}}(R) = \frac{4}{3}\pi R^3 \, p \quad \text{for } R \gg R_i \,. \tag{3.25}$$

Here, p is the total pressure of the hard–sphere mixture. Motivated by the form of the function in Eq. (3.25), we will use the following ansatz for the excess chemical potential.

$$\mu^{\text{ex}}(R) = \frac{4}{3}\pi R^3 \, p + 4\pi R^2 \, \gamma + 4\pi R \, \kappa + 1 \, \bar\kappa \quad \text{for } R \geq 0 \,. \tag{3.26}$$

Here, the reversible required work for creating a sphere cavity with radius $R \geq 0$ is expressed as a function of its fundamental measures (see Eq. (4.5)). The continuity of μ^{ex} and its derivatives at $R = 0$ which is imposed by equating them in two limits, i.e. $\mu^{\text{ex}}(0^-)$ from Eq. (3.24) and $\mu^{\text{ex}}(0^+)$ from Eq. (3.26), implies that,

$$\begin{aligned}
\beta\bar\kappa &= -\ln(1 - \xi_3) \,, \\
4\pi\beta\kappa &= \frac{\xi_2}{1 - \xi_3} \,, \\
4\pi\beta\gamma &= \frac{4\pi\xi_1}{1 - \xi_3} + \frac{\xi_2^2}{2(1 - \xi_3)^2} \,.
\end{aligned} \tag{3.27}$$

where ξ_i's are scaled–particle variables defined as

$$\begin{aligned}
\xi_3 &= \sum_{i=1}^{\nu} \frac{4}{3}\pi R_i^3 \rho_i \,, \\
\xi_2 &= \sum_{i=1}^{\nu} 4\pi R_i^2 \rho_i \,, \\
\xi_1 &= \sum_{i=1}^{\nu} R_i \rho_i \,.
\end{aligned} \tag{3.28}$$

Using these coefficients in Eq. (3.26), the excess chemical potential of inserting a hard–sphere particle with radius $R = R_i$ is obtained as follows.

$$\beta\mu_i^{\text{ex}} = -\ln(1 - \xi_3) + \frac{4\pi R_i^2 \xi_1 + R_i \xi_2}{1 - \xi_3} + \frac{R_i^2 \xi_2^2}{2(1 - \xi_3)^2} + \frac{4}{3}\pi R_i^3 \beta p \,. \tag{3.29}$$

By using the thermodynamic relation,

$$\frac{\partial \beta p}{\partial \rho_j} = \sum_{i=1}^{\nu} \rho_i \frac{\partial \beta \mu_i}{\partial \rho_j} = \sum_{i=1}^{\nu} \rho_i \left(\frac{\partial \beta \mu_i^{\text{id}}}{\partial \rho_j} + \frac{\partial \beta \mu_i^{\text{ex}}}{\partial \rho_j} \right) = 1 + \sum_{i=1}^{\nu} \rho_i \frac{\partial \beta \mu_i^{\text{ex}}}{\partial \rho_j} \,, \tag{3.30}$$

the equation of state for a mixture of hard–spheres is obtained as follows.

$$\beta p = \frac{\xi_0}{(1 - \xi_3)} + \frac{\xi_1 \xi_2}{(1 - \xi_3)^2} + \frac{\xi_2^3}{12\pi (1 - \xi_3)^3} \,, \tag{3.31}$$

where ξ_0 is the total number density of the mixture,

$$\xi_0 = \sum_{i=1}^{\nu} \rho_i \,. \tag{3.32}$$

Note that for a single–component system $\nu = 1$ the equation of state reduces to the Percus–Yevick compressibility equation (Eq. (3.18)). Furthermore, the corresponding excess free energy density for the hard–sphere mixture is obtained as ,

$$\beta f^{\text{ex}} = -\xi_0 \ln (1 - \xi_3) + \frac{\xi_1 \xi_2}{1 - \xi_3} + \frac{\xi_2^3}{24\pi (1 - \xi_3)^2}. \tag{3.33}$$

3.3   Excess Helmholtz free energy functional

As mentioned in Section 2.3, in the framework of the classical DFT, it is proven that there exist a grand potential functional $\Omega[\rho]$ which is minimized by the equilibrium density profile $\rho_{\text{eq}}(\mathbf{r})$. The minimum value is the grand potential of the system Ω from Eq. (2.21). Furthermore, the Helmholtz free energy functional which is defined as the Legendre transformation of the grand potential functional, is conveniently decomposed into an ideal gas part $\beta\mathcal{F}^{\text{id}}$ and an excess (over ideal) part $\beta\mathcal{F}^{\text{ex}}$. This is

summarized as follows.

$$
\begin{aligned}
\Omega[\rho] &= \mathcal{F}^{\mathrm{id}}[\rho(\mathbf{r})] + \mathcal{F}^{\mathrm{ex}}[\rho(\mathbf{r})] + \int \mathrm{d}\mathbf{r}\rho(\mathbf{r}) \left(V_{\mathrm{ext}}(\mathbf{r}) - \mu\right), \\
\left.\frac{\delta\Omega[\rho]}{\delta\rho(\mathbf{r})}\right|_{\rho=\rho_{\mathrm{eq}}} &= 0, \quad \Omega[\rho_{\mathrm{eq}}] = \Omega, \\
\beta\mathcal{F}^{\mathrm{id}}[\rho(\mathbf{r})] &= \int \mathrm{d}\mathbf{r}\rho(\mathbf{r}) \left(\ln\left(\lambda^3\rho(\mathbf{r})\right) - 1\right).
\end{aligned}
\tag{3.34}
$$

The main task in implementing the density functional theory for classical systems with interacting particles is determining an excess free energy functional which describes the interactions between the particles appropriately. However, the only functional which has an exact analytical soultuion is for 1D hard–rods [56–58]. For other systems there are approximate energy functionals which in some cases are applicable only to special type of potentials [7, 59].

3.3.1 Low density limit and local density approximation

The excess part of the free energy functional can be expressed in terms of the Mayer–f function (Eq. (3.2)) as follows.

$$
\begin{aligned}
\beta\mathcal{F}^{\mathrm{ex}}[\rho] &= -\frac{1}{2} \iint \mathrm{d}\mathbf{r}_i \mathrm{d}\mathbf{r}_j \rho(\mathbf{r}_i)\rho(\mathbf{r}_j) f(r_{ij}) \\
&\quad -\frac{1}{6} \iiint \mathrm{d}\mathbf{r}_i \mathrm{d}\mathbf{r}_j \mathbf{r}_k \rho(\mathbf{r}_i)\rho(\mathbf{r}_j)\rho(\mathbf{r}_k) f(r_{ij}) f(r_{jk}) f(r_{ik}) + \mathcal{O}(\rho^3),
\end{aligned}
\tag{3.35}
$$

where $r_{ij} = |\mathbf{r}_i - \mathbf{r}_j|$. In the low density limit $\rho \to 0$, the exact form of the excess free energy functional is found by truncating Eq. (3.35) after the first term. Consequently, the direct pair correlation function is obtained using its definition from Eq. (2.54). For the low density limit, the direct pair correlation function reads

$$
\begin{aligned}
c^{(2)}(\mathbf{r}_i, \mathbf{r}_j) &= f(|\mathbf{r}_i - \mathbf{r}_j|) + \mathcal{O}(\rho^2) \\
&= -\beta u(|\mathbf{r}_i - \mathbf{r}_j|) + \mathcal{O}(u^2, \rho^2).
\end{aligned}
\tag{3.36}
$$

where for the latter, we have assumed $\beta u(r) \ll 1$. The provided expression is known as Random Phase Approximation (RPA) and predicts the correct asymptotic behaviour of the direct correlation function, i.e. at long–ranges it should behave as the interacting potential between particles [7, 60]. The approximation is good for a system with smoothly varying density.

Motivated by the expression for the excess free energy density from the Carnahan–Starling equation of state (Eq. (3.10)), one can introduce the following excess free energy functional for a hard–sphere system.

$$\beta\mathcal{F}_{\text{LDA}}^{\text{ex}}[\rho] \;=\; \int \mathrm{d}\mathbf{r}\rho(\mathbf{r})\frac{\eta(\mathbf{r})(4 - 3\eta(\mathbf{r}))}{(1 - \eta(\mathbf{r}))^2} \; . \tag{3.37}$$

This so–called local density approximation is valid for a smoothly varying density distribution over the range of several particle size. Therefore, this approximation can not be used for a hard–sphere system due to rapid changes in the density. The LDA functionals are mainly used for treating a system with attractions. Here, the potential is decomposed into a hard–core interaction and an attractive part which is often treated with a mean–field free energy [7, 60].

An improvement beyond local density approximation is achieved by introducing additional terms which are dependent on local gradient of the density $\nabla\rho(\mathbf{r})$. This non–local description is able to account for inhomogeneities of small amplitude [6]. The gradient expansion fails when it is applied to a system with hard–core interaction due to a sharp finite–range interference of the density profile of two hard bodies [7].

3.3.2   Ramakrishnan–Yussouff functional

Consider a reference system whose pairwise particle interaction is given by $u_{\text{ref}}(r)$ and the excess free energy density $\beta\mathcal{F}_{\text{ref}}$ is known. For studying a system of interest with a different particle interaction $u(r)$, one can consider the difference as a perturbation to the system $w(r)$ which is switched on gradually: $u = u_{\text{ref}} + \lambda w$, and eventually gives the potential of the system of interest when $\lambda = 1$. The excess free energy functional of this system is given in a formally exact relation as a correction to $\beta\mathcal{F}_{\text{ref}}$. Consequently, the deviation of the direct correlation function from the reference system is approximated in a mean–field form. As a result of this approximation known as Random–Phase Approximation (RPA), the direct pair correlation function which behaves asymptotically as the interaction potential, is exact for long distances [6, 7].

In a rather similar way, one may relate the single–particle density of a reference state of the system of interest to its final state via a linear integration path [6].

$$\rho^{(1)}(\mathbf{r}; \lambda) = \rho_{\text{ref}}^{(1)}(\mathbf{r}) + \lambda\Delta\rho^{(1)}(\mathbf{r}) \; . \tag{3.38}$$

The direct correlation functions are given hierarchically as functional derivatives of the

excess free energy functional (Eq. (2.55)). Integrating them using Eq. (3.38) results in,

$$
\begin{aligned}
\beta \mathcal{F}^{\text{ex}}[\rho^{(1)}] &= \beta \mathcal{F}^{\text{ex}}[\rho^{(1)}_{\text{ref}}] - \int_0^1 \mathrm{d}\lambda \int \mathrm{d}\mathbf{r} \frac{\partial \rho^{(1)}(\mathbf{r})}{\partial \lambda} c^{(1)}(\mathbf{r}; \lambda) , \\
&= \beta \mathcal{F}^{\text{ex}}[\rho^{(1)}_{\text{ref}}] - \int_0^1 \mathrm{d}\lambda \int \mathrm{d}\mathbf{r} \Delta\rho^{(1)}(\mathbf{r}) c^{(1)}(\mathbf{r}; \lambda) , \quad (3.39)
\end{aligned}
$$

$$
c^{(1)}(\mathbf{r}; \lambda) = c^{(1)}_{\text{ref}}(\mathbf{r}) + \int_0^\lambda \mathrm{d}\lambda' \int \mathrm{d}\mathbf{r}' \Delta\rho^{(1)}(\mathbf{r}') c^{(2)}(\mathbf{r}, \mathbf{r}'; \lambda') . \quad (3.40)
$$

$$
\vdots
$$

$$
c^{(n-1)}(\mathbf{r}; \lambda) = c^{(n-1)}_{\text{ref}}(\mathbf{r}) + \int_0^\lambda \mathrm{d}\lambda' \int \mathrm{d}\mathbf{r}' \Delta\rho^{(1)}(\mathbf{r}') c^{(n)}(\mathbf{r}, \mathbf{r}'; \lambda') . \quad (3.41)
$$

Note that the excess free energy functionals on the two sides of Eq. (3.39) are the same unique energy functional of the single–particle density. Moreover, the correlation functions in the integrals belong to the final state of the system. Using $c^{(1)}$ from Eq. (3.40) in Eq. (3.39) we can write,

$$
\begin{aligned}
\beta \mathcal{F}^{\text{ex}}[\rho^{(1)}] &= \beta \mathcal{F}^{\text{ex}}[\rho^{(1)}_{\text{ref}}] - \int_0^1 \mathrm{d}\lambda \int \mathrm{d}\mathbf{r} \Delta\rho^{(1)}(\mathbf{r}) c^{(1)}_{\text{ref}}(\mathbf{r}) , \\
&\quad - \int_0^1 \mathrm{d}\lambda \int_0^\lambda \mathrm{d}\lambda' \iint \mathrm{d}\mathbf{r}\mathrm{d}\mathbf{r}' \Delta\rho^{(1)}(\mathbf{r}) \Delta\rho^{(1)}(\mathbf{r}') c^{(2)}(\mathbf{r}, \mathbf{r}'; \lambda') , \quad (3.42)
\end{aligned}
$$

Since $c^{(1)}_{\text{ref}}$ in the second term does not depend on λ, we can evaluate the integral $\int_0^1 \mathrm{d}\lambda = 1$. By replacing $c^{(2)}$ in the integral of the third term in Eq. (3.42) with the expression in Eq. (3.41) with $n = 2$, an integral in the term containing $c^{(2)}_{\text{ref}}$ is obtained which can be evaluated as $\int_0^1 \mathrm{d}\lambda \int_0^\lambda \mathrm{d}\lambda' = \frac{1}{2}$. Following the same steps, one can write down a formally exact Taylor expansion of the excess free energy functional as follows [6, 61].

$$
\begin{aligned}
\beta \mathcal{F}^{\text{ex}}[\rho^{(1)}] &= \beta \mathcal{F}^{\text{ex}}[\rho^{(1)}_{\text{ref}}] - \int \mathrm{d}\mathbf{r} \Delta\rho^{(1)}(\mathbf{r}) c^{(1)}_{\text{ref}}(\mathbf{r}) \\
&\quad - \frac{1}{2} \iint \mathrm{d}\mathbf{r}\mathrm{d}\mathbf{r}' \Delta\rho^{(1)}(\mathbf{r}) \Delta\rho^{(1)}(\mathbf{r}') c^{(2)}_{\text{ref}}(\mathbf{r}, \mathbf{r}') \\
&\quad - \frac{1}{6} \iiint \mathrm{d}\mathbf{r}\mathrm{d}\mathbf{r}'\mathrm{d}\mathbf{r}'' \Delta\rho^{(1)}(\mathbf{r}) \Delta\rho^{(1)}(\mathbf{r}') \Delta\rho^{(1)}(\mathbf{r}'') c^{(3)}_{\text{ref}}(\mathbf{r}, \mathbf{r}', \mathbf{r}'') - \cdots . (3.43)
\end{aligned}
$$

By truncating the series after the second term, the only required inputs for constructing the functional are the excess free energy functional evaluated at a reference density, and the direct pair correlation function which may be obtained from the solution of integral equation theory or RPA [7]. A homogeneous fluid is often taken as the reference state,

hence $\rho_{\text{ref}}(\mathbf{r}) = \rho$ and the excess free energy is provided by an equation of state, and the single–particle correlation $c_{\text{ref}}^{(1)} = -\mu^{\text{ex}}$ from Eq. (2.57).

Ramakrishnan and Yussouff constructed their functional by using the Percus–Yevick approximation (Eq. (3.17)) as the undetermined direct pair correlation function [62]. Furthermore, they used the Carnahan–Starling equation of state for description of their hard–sphere fluid which provides expressions for the excess free energy density (Eq. (3.10)) and consequently the direct pair correlation function for the reference system. The functional is capable of describing the hard–sphere fluid–solid coexistence. Although the obtained transition densities are different from exact MC simulation results, the method is quite useful since it allows fast numerical calculations as a test case. For instance in Ref. [61], the method has been used in a combination with Fundamental Measure Functionals (see Chapter 4). Here, the excess free energy and the direct pair correlation function of the reference system are obtained from the provided fundamental measure functional. Their results for phase coexistence densities are surprisingly in good agreement with those of simulation results. However, the Taylor expanded FMT functionals which are truncated after second order in density fail to deliver correct order of magnitude for the equilibrium vacancy concentration in the solid[3].

3.3.3   Phase Field Crystal model

In the context of phase field models, after proper coarse graining of the system a scalar order parameter ψ is defined for determination of the fluid and the crystalline state. The order parameter evolves continuously from its value at the bulk fluid phase $\psi = 0$ to the bulk crystalline state $\psi = 1$. The order parameter is usually coupled to a density field with conserved dynamic equations. In contrast, the dynamic evolution of the order parameter is not conserved in general. However, at equilibrium the phase boundary which separates the bulk states, is stationary, i.e. none of the phases are growing. The free energy functional of the system is approximated in the form of a Ginzburg-Landau functional of the order parameter [61, 63].

Using the same framework, Elder et al. developed a method called the Phase Field Crystal (PFC) model in order to investigate elastic properties of a solid and study the crystallization on atomic scale [64, 65]. The order parameter in PFC Ψ is a density field and has a periodic ground state. The ground state of Ψ is obtained by minimizing the free energy functional of the order parameter [66]. However, it turns out that PFC

---

[3] The reported coexistence densities of fluid $\rho_{\text{fl}}\sigma^3$ and fcc $\rho_{\text{cr}}\sigma^3$ crystal in Ref. [61] are respectively 0.944 and 1.049 for RF(tensor) functional (see Section 4.2) and 1.021 and 1.123 for WBII(tensor) functional (see Section 4.3). The vacancy concentration of an fcc solid is reported 0.1 for RF(tensor) and 0.09 for WBII(tensor). See table 4.1 and table 4.2 for a comparison of the results with FMT functionals.

is in fact an approximative Density Functional Theory [67–69]. The PFC free energy functional which describes the static and dynamic properties of a conserved field Ψ is given in its simplest symmetric form as follows [64],

$$\mathcal{F}[\Psi] = \int d\mathbf{r} \left\{ \frac{1}{2}\Psi(\mathbf{r}) \left[-\epsilon + \left(q_0^2 + \nabla^2 \right)^2 \right] \Psi(\mathbf{r}) + \frac{1}{4}\Psi^4(\mathbf{r}) \right\} , \qquad (3.44)$$

where q_0 and ϵ are constants and ∇ represent the gradient of the order parameter field. Consider the order parameter defined as the normalized deviation of the density from the density of homogeneous fluid state ρ_{ref}[4].

$$\Psi(\mathbf{r}) = \frac{\rho(\mathbf{r}) - \rho_{\text{ref}}}{\rho_{\text{ref}}} . \qquad (3.45)$$

Note that the order parameter is equivalent to the normalized single–particle density deviation $\Delta\rho^{(1)}/\rho_{\text{ref}}$ from Eq. (3.38) if $\lambda = 1$. The ideal gas free energy functional (Eq. (2.52)) may be expressed as a functional of order parameter as follows.

$$\begin{aligned}
\beta\mathcal{F}^{\text{id}}[\Psi] &= \int d\mathbf{r}\rho(\mathbf{r}) \left(\ln\left(\lambda^3\rho(\mathbf{r}) \right) - 1 \right) \\
&= \beta\mathcal{F}^{\text{id}}[\rho_{\text{ref}}] + \beta\mu^{\text{id}}\rho_{\text{ref}} \int d\mathbf{r} \ \Psi(\mathbf{r}) \\
&\quad + \rho_{\text{ref}} \int d\mathbf{r} \ \left\{ \frac{1}{2}\Psi^2(\mathbf{r}) - \frac{1}{6}\Psi^3(\mathbf{r}) + \frac{1}{12}\Psi^4(\mathbf{r}) + \mathcal{O}(\Psi^5) \right\} , \qquad (3.46)
\end{aligned}$$

where $\beta\mu^{\text{id}} = \ln\left(\lambda^3\rho_{\text{ref}} \right)$ is the ideal gas chemical potential. Note that the integral over the linear term in Ψ results in a constant value. Assuming a spherical symmetry, hence $c^{(2)}(\mathbf{r}, \mathbf{r}') = c^{(2)}(|\mathbf{r}-\mathbf{r}'|)$, and using the definition of Ψ from Eq. (3.45) one can rewrite the Ramakrishnan–Yussouff approximation of the excess free energy functional (Eq. (3.43) truncated after $\mathcal{O}(\rho^2)$) as follows.

$$\begin{aligned}
\beta\mathcal{F}^{\text{ex}}[\Psi] &= \beta\mathcal{F}^{\text{ex}}[\rho_{\text{ref}}] + \beta\mu^{\text{ex}}\rho_{\text{ref}} \int d\mathbf{r}\Psi(\mathbf{r}) \\
&\quad - \frac{\rho_{\text{ref}}^2}{2} \iint d\mathbf{r}d\mathbf{r}'\Psi(\mathbf{r})c_{\text{ref}}^{(2)}(|\mathbf{r} - \mathbf{r}'|)\Psi(\mathbf{r}') . \qquad (3.47)
\end{aligned}$$

where $\beta\mu^{\text{ex}} = -c_{\text{ref}}^{(1)}$ is the excess chemical potential of the reference system. One can consider the integral over $\mathbf{r}'$ as the convolution of $c^{(2)}$ and $\Psi(\mathbf{r}')$, i.e. the product of their Fourier transformations in the Fourier space. Since the direct pair correlation function

---

[4] This derivation is presented by Robert Spatschek in the Phase Field summer school [70]

has rotational symmetry, its Fourier transform is only a function of $k = |\mathbf{k}|$ and only even terms appear in the Taylor expansion of $\tilde{c}^{(2)}(k)$,

$$\tilde{c}^{(2)}(k) = \tilde{c}_0 + \tilde{c}_2 k^2 + \tilde{c}_4 k^4 + \mathcal{O}(k^6) \,. \tag{3.48}$$

Taking the backward Fourier transform, each term containing k^n in Fourier space gives ∇^n in real space and Eq. (3.47) turns into

$$\begin{aligned}
\beta \mathcal{F}^{\text{ex}}[\Psi] &= \beta \mathcal{F}^{\text{ex}}[\rho_{\text{ref}}] + \beta \mu^{\text{ex}} \rho_{\text{ref}} \int d\mathbf{r} \Psi(\mathbf{r}) \\
&\quad - \frac{\rho_{\text{ref}}}{2} \int d\mathbf{r} \Psi(\mathbf{r}) \left[c_0 - c_2 \nabla^2 + c_4 \nabla^4 \right] \Psi(\mathbf{r}) \,, \quad \text{with } c_i = \frac{\tilde{c}_i}{\rho_{\text{ref}}}
\end{aligned} \tag{3.49}$$

Finally, the total free energy functional is obtained by combining Eqs. (3.46) and (3.49).

$$\begin{aligned}
\beta \mathcal{F}[\Psi] &= \rho_{\text{ref}} \int d\mathbf{r} \left\{ \frac{1}{2}(1 - c_0) \Psi^2(\mathbf{r}) + \frac{1}{2} c_2 \Psi(\mathbf{r}) \nabla^2 \Psi(\mathbf{r}) \right. \\
&\quad \left. - \frac{1}{2} c_4 \Psi(\mathbf{r}) \nabla^4 \Psi(\mathbf{r}) - \frac{1}{6} \Psi^3(\mathbf{r}) + \frac{1}{12} \Psi^4(\mathbf{r}) \right\} \\
&\quad + \beta \mathcal{F}[\rho_{\text{ref}}] + \beta \mu \rho_{\text{ref}} \int d\mathbf{r} \Psi(\mathbf{r}) \,.
\end{aligned} \tag{3.50}$$

The functional in Eq. (3.50) is a local functional of the order parameter Ψ, and therefore is also local in density, in contrast with the Taylor expansion functional (Eq. (3.43)) which is non–local in density. The last two terms in Eq. (3.50) are constant, thus irrelevant in the determination of the physical properties, e.g. the phase diagram [61, 66]. Rescaling the order parameter $\Psi' = \alpha(1 - 2\Psi)$ with $\alpha = 1/\sqrt{-12c_4}$ results in the same form of PFC functional from Eq. (3.44) scaled with a factor. The scaling value of the functional and the relation between the constants ϵ and q and the coefficients A_i are given as follows.

$$\begin{aligned}
\mathcal{F}_{\text{PFC}} &= \frac{\beta \mathcal{F}}{3 \rho_{\text{ref}} c_4^2} \,, \\
q_0 &= \sqrt{-\frac{c_2}{4 c_4}} \,, \\
\epsilon &= \frac{c_2^2 - c_4 (3 + 4 c_0)}{4 c_4^2} \,.
\end{aligned} \tag{3.51}$$

As it is mentioned earlier, PFC is mainly used to study the crystallization and investigating the properties of the liquid–solid interfaces. Generally, the peaks of the order

parameter which represents the crystalline state are almost sinusoidal in PFC while in DFT they have Gaussian form [67]. On the other hand, using the full form of the functional (Eq. (3.50)) Oettel et al. have shown that a proper matching between the Taylor expanded DFT and PFC is achieved by identification of the PFC order parameter $\Psi(\mathbf{r})$ with a rescaled and shifted "smeared density" $\rho(\mathbf{r}) * w(\mathbf{r})$ [61]. However, the functional results in peculiar negative values for vacancy concentration at coexistence densities of hard–sphere system. Furthermore, a direct calculation of A_i's from a Taylor–expanded FMT functional gives a PFC functional which does not account for fluid–solid phase transition [61].

In the following chapter, we will discuss the Fundamental Measure Theory (FMT) which is introduced by Rosenfeld in 1989 and provides an excess free energy functional for a hard–sphere mixture. Starting from the low density limit and using a deconvolution of the Mayer–f functions at this limit, Rosenfeld showed that the excess free energy density is a function of a set a weighted (smeared out) densities [9].

CHAPTER 4

BULK CRYSTALS OF HARD SPHERES IN FUNDAMENTAL MEASURE THEORY

In 1989, Rosenfeld introduced Fundamental Measure Theory (FMT) which expresses the excess free energy density of a hard sphere mixture as a function of a set of weighted (smeared–out) densities [9]. Inspired by the bulk behavior of the hard sphere mixture described by the Percus–Yevick (PY) integral equation [57,71], Rosenfeld built his excess free energy functional based on scaled–particle theory [54].

FMT is quite successful in describing a hard–sphere mixture in bulk fluid, by for instance delivering the pair direct correlation function approximately correct. However, the proposed functional by Rosenfeld diverges when it is applied to a particle which is caged by its neighbors; a situation which should be addressed for a correct description of fluid–crystal phase transition. In a wider point of view, a functional which is constructed for a 3D system with density profile $\rho^{3D}(x, y, z)$ should be able to handle cases in which the system is confined to a lower dimension. For instance, by imposing an appropriate external potential which restricts the density profile in the $z = 0$ plane, i.e. $\rho^{3D}(x, y, z) = \delta(z)\rho^{2D}(x, y)$, the functional must deliver the free energy of a 2D system. The ultimate dimensional crossover is confining a particle in a "0D cavity" with density profile $\rho^{3D}(x, y) = \delta(x)\delta(y)\delta(z)$, reminiscent of a caged particle by its neighbors. The Rosenfeld functional is not able to treat the density crossover; a defect which ultimately leads to its divergence when it is applied to a highly packed system. In an early attempt to overcome this problem the functional was modified by a geometrically based empirical approach [34,72]. In a more systematic approach, one can start from a 0D cavity for which the free energy is exactly known, and construct a functional for higher dimensions. This low dimensional considerations ultimately lead to introduction of the tensorial version of the FMT functionals [10,73]. The tensorial version of the functional is capable of describing crystals [11,74]. However, as the underlying thermodynamics of the FMT is based on the PY equation of state, the resulting coex-

istence densities are shifted compared to simulation results [75–77]. Using the more exact Carnahan–Starling (CS) equation of state [50,78] instead of the PY compressibility equation, Roth et al. and Yu et al. in two separate studies overcame this problem by introducing the equation of state as an input in the derivation of the functional [11,79]. The obtained coexistence densities from this functional are consistent with simulation results [11,74,80].

Extending scaled–particle theory for the bulk, Santos has presented a general solution for the scaled–particle differential equation [81]. This is possible by considering the limit in which in a ν–component system of homogeneous hard sphere fluid one of the components consists of point particles. This approach has been extended to inhomogeneous systems and the formulation of a corresponding functional which is shown to be capable of predicting crystallization as well as a correct order of magnitude for the equilibrium thermal vacancies in crystalline state [82].

In the following sections of this chapter, we will discuss the low density expansion of the excess free energy as a function of the Mayer-f bonds. Rosenfeld's deconvolution of Mayer-f bonds in terms of weighted densities is the starting point of the derivation of his fundamental measure functional. In Section 4.2 the concept of 0D cavities and the Tarazona treatment of the functional is discussed. While the underlying equation of state of these functionals is Percus–Yevick, the White Bear versions introduced in Section 4.3 take advantage of the Carnahan–Starling equation of state. Santo's general solution for the scaled–particle differential equation and the self–consistent functional based on this solution is presented in Section 4.4. Finally, in Section 4.5 the implementation of the FMT and numerical results concerning the liquid–solid phase transition and their thermodynamic properties, equilibrium thermal vacancies and anisotropies in density profiles of crystals are discussed.

4.1 Fundamental Measure Theory

In this section, we will follow Ref. [9] to derive Rosenfeld's expression for the excess free energy. As discussed in Section 3.3.1, one can write down an expansion of the excess free energy functional in terms of Mayer–f functions $f_{ij}(r)$ (see Eqs. (3.2) and (3.35)). For a ν–component system, this expansion reads

$$
\begin{aligned}
\beta \mathcal{F}^{\mathrm{ex}}\left[\{\rho_i\}\right] = \ & -\frac{1}{2} \sum_{i,j} \iint \mathrm{d}\mathbf{r}_1 \mathrm{d}\mathbf{r}_2 \, \rho_i(\mathbf{r}_1)\rho_j(\mathbf{r}_2)f_{ij}(r_{12}) \\
& -\frac{1}{6} \sum_{i,j,k} \iiint \mathrm{d}\mathbf{r}_1 \mathrm{d}\mathbf{r}_2 \mathrm{d}\mathbf{r}_3 \, \rho_i(\mathbf{r}_1)\rho_j(\mathbf{r}_2)\rho_k(\mathbf{r}_3)f_{ij}(r_{12})f_{ik}(r_{13})f_{jk}(r_{23}) \\
& + \cdots,
\end{aligned}
\tag{4.1}
$$

where the sums run over different species and $r_{ij} = |\mathbf{r}_i - \mathbf{r}_j|$. In a hard sphere system in which the interaction between particle i and j with radii R_i and R_j is defined by Eq. (3.1), the Mayer–f function is either -1 for $r_{ij} < R_i + R_j$, or 0 when there is no interaction between them. Hence the geometrical interpretation of the Mayer-f function for a hard–sphere potential is the excluded volume around each particle. Using a set of weight functions $\{w_i\}$, Rosenfeld proposed a deconvolution of the Mayer–f function for hard-spheres as follows,

$$-f_{ij}(r) = w_i^3 * w_j^0 + w_i^0 * w_j^3 + w_i^1 * w_j^2 + w_i^2 * w_j^1 - \mathbf{w}_i^2 * \mathbf{w}_j^1 - \mathbf{w}_i^1 * \mathbf{w}_j^2. \tag{4.2}$$

Here, $*$ is the 3–dimensional convolution defined as

$$\left[w_i^\alpha * w_j^\beta \right](\mathbf{r}_i - \mathbf{r}_j) = \int d\mathbf{r}' w_i^\alpha (\mathbf{r}_i - \mathbf{r}') w_j^\beta (\mathbf{r}_j - \mathbf{r}'), \tag{4.3}$$

and the weight functions w_i^α are given by:

$$w_i^3(\mathbf{r}) = \theta (R_i - |\mathbf{r}|) \ ,$$

$$w_i^2(\mathbf{r}) = \delta (R_i - |\mathbf{r}|) \ , \qquad w_i^1(\mathbf{r}) = \frac{w_i^2(\mathbf{r})}{4\pi R_i} \ , \qquad w_i^0(\mathbf{r}) = \frac{w_i^2(\mathbf{r})}{4\pi R_i^2} \ ,$$

$$\mathbf{w}_i^2(\mathbf{r}) = \delta (R_i - |\mathbf{r}|) \, \mathbf{e}_r \ , \quad \mathbf{w}_i^1(\mathbf{r}) = \frac{\mathbf{w}_i^2(\mathbf{r})}{4\pi R_i} \ , \tag{4.4}$$

where $\theta(r)$ is the Heaviside step function, $\delta(r)$ is the Dirac delta function, and $\mathbf{e}_r = \mathbf{r}/|\mathbf{r}|$ is the unit vector in direction of $\mathbf{r}$. Integrating over the scalar weight functions gives the fundamental measures of a sphere,

$$\int d\mathbf{r} \ w_i^3(\mathbf{r}) = \frac{4}{3}\pi R_i^3 \qquad \text{Volume}$$

$$\int d\mathbf{r} \ w_i^2(\mathbf{r}) = 4\pi R_i^2 \qquad \text{Surface}$$

$$\int d\mathbf{r} \ w_i^1(\mathbf{r}) = \quad R_i \qquad \text{Mean radius of curvature}$$

$$\int d\mathbf{r} \ w_i^0(\mathbf{r}) = \quad 1 \qquad \text{Euler characteristic}, \tag{4.5}$$

hence the name of the theory. The deconvolution of the Mayer–f function proposed by Rosenfeld (Eq. (4.2)) is not unique. For instance Kierlik and Rosinberg proposed a deconvolution which avoids vectorial weight functions [83]. However, it can be shown that the different expressions for the deconvolution are equivalent [84]. Rosenfeld has used the vectorial weight functions $\mathbf{w}^\alpha$ in order to express the jump discontinuity of the Mayer–f function at $r = \sigma$ in the form of convolutions in Eq. (4.2) [9].

The weighted (smeared–out) densities $\{n_\alpha(\mathbf{r})\}$ are obtained by calculating the convolution of the weight functions and the density profile.

$$n_\alpha(\mathbf{r}) = \sum_i [\rho_i * w_i^\alpha](\mathbf{r}) = \sum_i \int d\mathbf{r}' \rho_i(\mathbf{r}') w_i^\alpha(\mathbf{r} - \mathbf{r}'). \tag{4.6}$$

In the bulk homogeneous state, the vectorial weight functions vanish and the scalar ones reduce to the scaled–particle variables (Eqs. (3.28) and (3.32)), $n_\alpha(\mathbf{r}) \to \xi_\alpha$. Using Eq. (4.2) and the definitions of the weighted densities from Eq. (4.6), one can rewrite the low density approximation of $\beta \mathcal{F}^{\text{ex}}$ from Eq. (4.1) as follows,

$$\beta \mathcal{F}^{\text{ex}}[\{\rho_i\}] = \int d\mathbf{r} \ \{n_0(\mathbf{r})n_3(\mathbf{r}) + n_1(\mathbf{r})n_2(\mathbf{r}) - \mathbf{n}_1(\mathbf{r}) \cdot \mathbf{n}_2(\mathbf{r})\}. \tag{4.7}$$

In this approximation only the first term in the expansion of $\beta \mathcal{F}^{\text{ex}}$ by Mayer–f functions (Eq. (4.1)) is considered and the three-, four–, and more–body overlaps of the hard spheres contained in the higher order terms are neglected. Since the relation in its present form is only valid in dilute systems, one should extrapolate the result to higher densities in order to take advantage of FMT in more confined systems. For this purpose, and inspired by the form of the low density limit, Rosenfeld proposed a reasonable ansatz for the excess free energy,

$$\beta \mathcal{F}^{\text{ex}}[\{\rho_i\}] = \int d\mathbf{r} \ \Phi(\{n_\alpha(\mathbf{r})\}). \tag{4.8}$$

Note that the right hand side of the equation should be dimensionless as its left hand side. Therefore, the dimension of the free energy volume density Φ is $\mathbf{L}^{-3}$ where $\mathbf{L}$ denotes the length dimension. Considering the dimensions of the weighted densities, $[n_0] = \mathbf{L}^{-3}$, $[n_1] = [\mathbf{n}_1] = \mathbf{L}^{-2}$, $[n_1] = [\mathbf{n}_1] = \mathbf{L}^{-1}$, and $[n_3] = 1$, Rosenfeld assumed that the correct dimension for Φ is delivered by a sum of different terms each constructed by a product of undetermined functions of n_3 and a suitable set of other weighted densities. By using this dimensional analysis, the excess free energy density is given as follows.

$$\begin{aligned} \Phi(\{n_\alpha\}) &= f_1(n_3)n_0 + f_2(n_3)n_1 n_2 + f_3(n_3)\mathbf{n}_1 \cdot \mathbf{n}_2 \\ &\quad + f_4(n_3)n_2^3 + f_5(n_3)n_2 \mathbf{n}_2 \cdot \mathbf{n}_2. \end{aligned} \tag{4.9}$$

Using this excess free energy density, the Fourier transform of the direct correlation function $c_{ij}^{(2)}$ reads

$$c_{ij}^{(2)}(k) = -\sum_{\alpha_1, \alpha_2} \frac{\partial^2 \Phi}{\partial n_{\alpha_1} \partial n_{\alpha_2}} w_i^{\alpha_1}(k) w_j^{\alpha_2}(k), \tag{4.10}$$

where the scalar product is used between the vectorial quantities. The undesired $1/r$ singularity of the obtained direct correlation function, which is a consequence of the convolution of two delta shells, implies that the undetermined functions of n_3 are related to each other as follows.

$$
\begin{aligned}
f_3(n_3) &= -f_2(n_3)\,, \\
f_5(n_3) &= -3f_4(n_3)\,.
\end{aligned}
\tag{4.11}
$$

Therefore, each term containing vectorial weight functions is bundled with a scalar one and the excess free energy density is expressed as,

$$
\begin{aligned}
\Phi &= \Phi_1 + \Phi_2 + \Phi_3 \\
&\quad \Phi_1 = f_1(n_3)n_0 \\
&\quad \Phi_2 = f_2(n_3)\left(n_1 n_2 - \mathbf{n}_1 \cdot \mathbf{n}_2\right) \\
&\quad \Phi_3 = f_4(n_3)\left(n_2^3 - 3n_2 \mathbf{n}_2 \cdot \mathbf{n}_2\right)\,.
\end{aligned}
\tag{4.12}
$$

As the vectorial terms vanish in a homogeneous system, it is reasonable to do the further calculation for obtaining f_i's for a bulk system in which the thermodynamic relations are valid. Here, the weight functions are reduced to the scaled–particle variables and one can take advantage of the ideas from scaled–particle theory (see Section 3.2.3). The required reversible work for inserting a particle with radius R_i, i.e. pV_i, is equivalent to the excess chemical potential μ_i^{ex} of the system. Since the excess free energy density is related to the density via the weighted densities, for the excess chemical potential of species we have,

$$
\beta\mu_i^{\text{ex}} = \frac{\partial \Phi}{\partial \rho_i} = \sum_\alpha \frac{\partial n_\alpha}{\partial \rho_i}\frac{\partial \Phi}{\partial n_\alpha}\,.
\tag{4.13}
$$

Note that in a homogeneous system the derivatives of weighted densities with respect to density is equivalent to the fundamental measures (Eq. (4.5)). In the limit of $R_i \to \infty$, using Eq. (4.13) the pressure of the system reads

$$
\beta p = \lim_{R_i \to \infty} \frac{\beta\mu_i^{\text{ex}}}{V_i} = \frac{\partial \Phi}{\partial n_3}\,.
\tag{4.14}
$$

On the other hand, the grand free energy density w is written as follows:

$$
\beta w = \beta f - \sum_{i=1}^{\nu} \beta\mu_i \rho_i = \Phi - \sum_{i=1}^{\nu} \rho_i\left(1 + \beta\mu_i^{\text{ex}}\right)\,.
\tag{4.15}
$$

Finally, since in the bulk we have $w = -p$, combining Eqs. (4.14) and (4.15) we derive the scaled particle differential equation.

$$\frac{\partial \Phi}{\partial n_3} = n_0 - \Phi + \sum_\alpha \frac{\partial \Phi}{\partial n_\alpha}\, n_\alpha. \tag{4.16}$$

The expressions given in Eq. (4.12) for Φ are used to obtain differential equations for f_1, f_2, and f_4 by comparing the factors of n_0, $n_1 n_2$, and n_2^3. The integral constant are determined by requiring that the single particle direct correlation function $c_i^{(1)} = -\frac{\delta \beta \mathcal{F}^{\text{ex}}}{\delta \rho_i}$ and the third virial coefficient are recovered in the low density limit. As a result, the f_i's are obtained as [9],

$$\begin{aligned}
f_1(n_3) &= -\ln(1 - n_3)\,, \\
f_2(n_3) &= \frac{1}{1 - n_3}\,, \\
f_4(n_3) &= \frac{1}{24\pi(1 - n_3)^2}\,.
\end{aligned} \tag{4.17}$$

Finally, by using these expressions for f_i's in Eq. (4.12), the Rosenfeld excess free energy density is obtained as follows.

$$\begin{aligned}
\Phi^{\text{RF}} &= \Phi_1^{\text{RF}} + \Phi_2^{\text{RF}} + \Phi_3^{\text{RF}}\,, \\
\Phi_1^{\text{RF}} &= -n_0 \ln(1 - n_3) \\
\Phi_2^{\text{RF}} &= \frac{n_1 n_2 - \mathbf{n}_1 \cdot \mathbf{n}_2}{1 - n_3} \\
\Phi_3^{\text{RF}} &= \frac{n_2^3 - 3n_2 \mathbf{n}_2 \cdot \mathbf{n}_2}{24\pi(1 - n_3)^2}\,.
\end{aligned} \tag{4.18}$$

The Rosenfeld functional is successful in generating the Percus-Yevick compressibility equation of state for a hard sphere mixtures [53,71,85] and the direct correlation function $c_{ij}^{(2)}(r)$ in a fluid [9]. However, it is unable to describe the hard sphere crystals. The crystalline state is a highly inhomogeneous system in which each particle is confined by its neighbors to stay in a small cavity. A functional which is built for a 3D system is able to successfully describe such confinement if it is reducible to lower dimensions by appropriate external potentials. This idea, known as dimensional crossover with 0D cavities as its ultimate limit, is discussed in the following section.

4.2   0D–Cavities and the Tarazona functional

Assuming an external potential such that the system is held between two close walls in the x–y plane, the local density profile of species i is given by $\rho(\mathbf{r}) = \rho_{2D}(x, y)\delta(z)$. In

this way a homogeneous density profile in 2D denoted by $\rho_{2D}(x, y)$, may be treated as a highly confined 3D system. Although the resulting excess free energy density obtained by applying Rosenfeld functional to this density profile differs in its functional form from that of scaled–particle theory, the numerical results are still in good agreement [86, 87]. By further confinement of the system along the x–axis, the local density profile turns into $\rho(\mathbf{r}) = \rho_{1D}(x)\delta(y)\delta(z)$. While the first two terms in Rosenfeld functional (Eq. (4.18)) yield the exact result for the excess free energy density of a 1D hard rod system (see Eq. (4.27)), the overlapping delta shells of n_2 (see Eqs. (4.4) and (4.6)) results in divergence of its third term.

The ultimate dimensional crossover is to a 0D situation, a cavity which can not hold more than one particle and therefore its average occupation number is $N \leq 1$. Independent of its geometrical form, the grand partition sum for a 0D cavity in a grand canonical ensemble is written as follows:

$$\Xi = \sum_{N=0}^{\infty} \exp(\beta\mu N)\frac{Z_N}{N!} = 1 + Z_1 \exp(\beta\mu) \,, \tag{4.19}$$

where μ is the chemical potential, N is the number of particles, and $Z_{N=1}$ is the only non–zero canonical partition function of a 0D cavity since $N \leq 1$. The average occupation number is obtained by,

$$N = \frac{\partial \ln \Xi}{\partial \beta\mu} = \frac{Z_1 \exp(\beta\mu)}{1 + Z_1 \exp(\beta\mu)} \,. \tag{4.20}$$
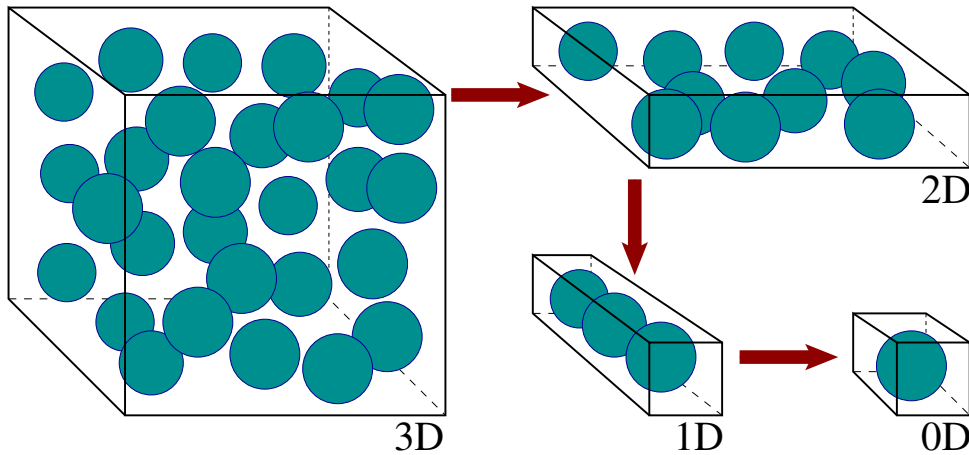
Figure 4.1: Dimensional crossover: confining the system to lower dimensions by applying appropriate external potentials. An FMT functional which has this property yields the excess free energy of lower dimensions when applied to their corresponding density profile; e.g. for 2D $\mathcal{F}_{3D}^{ex}[\rho(x, y)\delta(z)] = \mathcal{F}_{2D}^{ex}[\rho(x, y)]$

This enables us to write down the undetermined single–particle partition function Z_1 as $N \exp(-\beta\mu)/(1 - N)$. Therefore, the pressure of the system can be expressed as a function of N.

$$\beta P = \ln \Xi = -\ln(1 - N)$$

(4.21)

Using Eqs. (4.20) and (4.21), the free energy of a 0D cavity is written as follows:

$$\begin{aligned} \beta F_{0D} &= -\beta P + \beta\mu N \\ &= \ln(1 - N) + N \ln \left(\frac{N}{Z_1(1 - N)} \right). \end{aligned}$$

(4.22)

For an ideal gas, the particles may occupy the cavity without any restriction on their number. The canonical partition function for such system with N particles is $Z_N = Z_1^N$ and the grand partition sum from Eq. (4.19) turns into $\Xi = \exp\left(Z_1 e^{\beta\mu}\right)$. Consequently, the occupation number, the pressure, and the free energy of an ideal gas in a 0D cavity are given as follows.

$$N = \frac{\partial \ln \Xi}{\partial \beta\mu} = Z_1 e^{\beta\mu} ,$$

(4.23)

$$\beta P = \ln \Xi = Z_1 e^{\beta\mu} = N ,$$

(4.24)

$$\Rightarrow \beta F_{0D}^{id} = -N + N \ln \left(\frac{N}{Z_1} \right).$$

(4.25)

By subtracting this ideal gas part from the full form of the free energy of a 0D cavity, βF_{0D} from Eq. (4.22), the excess free energy of a 0D cavity Φ_{0D} is obtained. Considering $N \leq 1$, one can substitute the average occupation number of the system with its packing fraction η and write down Φ_{0D} as [34],

$$\Phi_{0D}(\eta) = \eta + (1 - \eta) \ln(1 - \eta).$$

(4.26)

One of the most important aspects of the 0D cavity is that the crystalline state can be interpreted as a highly confined inhomogeneous system in which each particle is caged by its own neighbors. Therefore, an appropriate functional for describing this system must necessarily recover the exactly known free energy density for a 0D cavity Φ_{0D} (Eq. (4.26)) when it is applied to the 0D density profile $\rho_{0D}(x, y, z) = \delta(x)\delta(y)\delta(z)$.

By replacing the numerator of Φ_3^{RF} (Eq. (4.12)) with $3n_2^3\xi\left(1 - \xi\right)^2$ where $\xi(\mathbf{r}) = |\mathbf{n}_2(\mathbf{r})/n_2(\mathbf{r})|$ the divergence of the Rosenfeld functional in 1D is removed [34]. As a result of this empirical modification, the functional yields the correct excess free

energy density in 1D by its first two terms $\Phi_1^{\mathrm{RF}} + \Phi_2^{\mathrm{RF}}$. Moreover, the exact form of excess free energy density in 0D (Eq. (4.26)) is recovered when the functional is applied to $\rho_{0\mathrm{D}}$. However, the bulk properties of the system in 3D are not retrieved by this empirical functional since in the bulk $\xi \to 0$ and Φ_3 vanishes. By anti–symmetrizing Φ_3 with respect to ξ, which is achieved by replacing its numerator by $n_2^3 \left(1 - \xi\right)^q$ with $q \geq 2$, the results for a 3D system are improved with the cost of the exactness in the 0D limit [34,72].

In a more systematic approach Tarazona et al. have proposed to build up the functional based on the exactly known excess free energy of the 0D cavities [73]. This ensures the exactness of the obtained 0D free energy from the functional as well as the dimensional crossover property. The starting point is the exactly known excess free energy functional for 1D hard rods [57].

$$\beta \mathcal{F}_{1\mathrm{D}}^{\mathrm{ex}} \left[\rho(x)\right] \;\; = \;\; - \int_{-\infty}^{\infty} \mathrm{d}x \; n_0(x) \ln \left(1 - n_1(x)\right) \;, \tag{4.27}$$

where n_0 and n_1 are the weighted densities obtained by the convolution of the density profile and the weight functions w_0 and w_1 which in 1D are defined as follows:

$$\begin{aligned} w_1(x) &= \theta(x - R) \,, \\ w_0(x) &= \frac{1}{2} \left(\delta(x - R) + \delta(x + R)\right) \,. \end{aligned} \tag{4.28}$$

Here, R is half of the length of a hard rod. Note that in 1D, n_1 serves as a length($\equiv$ volume) weighted density, hence the packing fraction in a homogeneous state, and n_0 marks the two ends of a hard rod, thus its "surface". Applying the functional to a single 0D cavity (Fig. 4.2.a) with density profile $\rho(x) = \delta(x)$, results in the excess free energy of a 0D cavity (Eq. (4.26)). As an ansatz, the excess free energy density in D dimensions has the same dependence on the volume weighted density n_D and the weighted surface density n_0 as in Eq. (4.27),

$$\begin{aligned} \beta \mathcal{F}_1^{\mathrm{ex}} \left[\rho(\mathbf{r})\right] &= - \int \mathrm{d}\mathbf{r} \; n_0(\mathbf{r}) \ln \left(1 - n_D(\mathbf{r})\right) \,, \\ &= - \int \mathrm{d}\mathbf{r} \; n_0(\mathbf{r}) \psi_1 \left(n_D(\mathbf{r})\right) \,, \quad \text{with } \psi_1(\eta) =: \frac{\partial \Phi_{0\mathrm{D}}(\eta)}{\partial \eta} \,. \end{aligned} \tag{4.29}$$

which indeed results in the exact 0D excess free energy when it is applied to a single 0D cavity. However, additional spurious terms are obtained when the functional is applied to a more complicated 0D cavity, the simplest of which is a double 0D cavity as shown in Fig. 4.1.b. In order to compensate for these deficiencies, additional terms should be added to $\beta \mathcal{F}_1^{\mathrm{ex}}$. The more sophisticated 0D cavities correspond to the
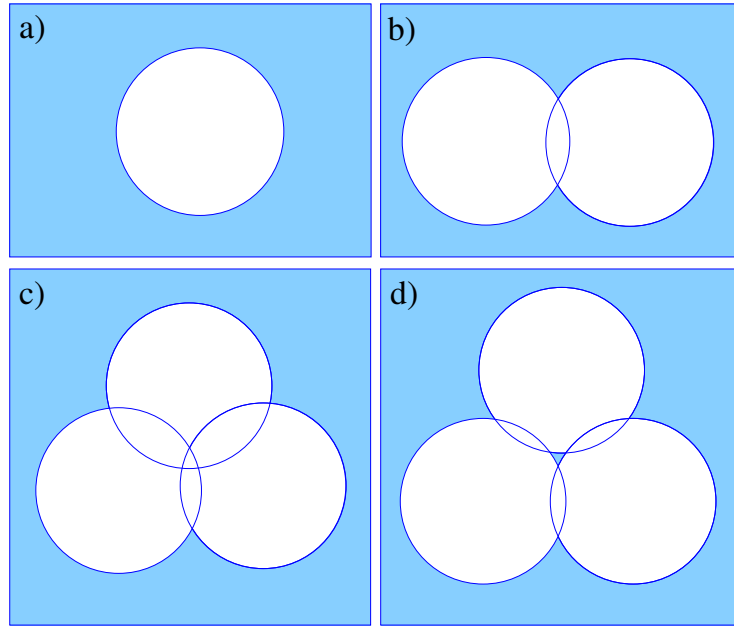
Figure 4.2: Four different geometrical situations for 0D cavities which only hold one hard–sphere particle. While it can be shown the first two forms correspond to Φ_1 and Φ_2, FMT functionals are not capable of exactly yielding a third term for three overlapping cavities and Φ_3 is given as an approximation. The triple cavity with only pair overlaps in d) is an example of "lost–cases" which cannot be described by an FMT functional.

supplementary information which is required for describing the possible geometrical intersections of $D > 1$ dimensional spheres. For hard rods, these intersections are points which can be handled by a single delta function. Therefore, it is quite rational that a single 0D cavity yields sufficient insight for describing this limit. For a 3D system, in addition to the surface of the spheres, there should be information regarding the lines corresponding to the intersection of these surfaces and the points where these lines cross.

The density profile for the double 0D cavity (Fig. 4.2. b) can be expressed as $\rho(\mathbf{r}) = \eta_1\rho(\mathbf{r}_1) + \eta_2\rho(\mathbf{r}_2)$, where the average occupation number $\eta = \eta_1 + \eta_2$ is between 0 and 1, and the distance between the centers of the cavities is smaller than the diameter of the hard–spheres $|\mathbf{r}_1 - \mathbf{r}_2| \leq 2R$. This situation should be reducible to the single 0D cavity when the cavities are far apart from each other. Therefore, the additional term corresponding to the double cavity vanishes for $|\mathbf{r}_1 - \mathbf{r}_2| > 2R$. The excess free energy functional for a double cavity is expressed conveniently as the product of the second derivative of Φ^{0D} and a function of n_1, n_2, and the vectorial weighted densities $\mathbf{n}_1$ and

$\mathbf{n}_2$.

$$\beta\mathcal{F}_2^{\text{ex}}[\rho(\mathbf{r})] = \int d\mathbf{r}\ (n_1 n_2 - \mathbf{n}_1 \cdot \mathbf{n}_2)\,\psi_2\left(n_D(\mathbf{r})\right)$$

$$\text{with } \psi_2(\eta) =: \frac{\partial^2 \Phi^{0D}(\eta)}{\partial\eta^2} = \frac{1}{1-\eta}\ . \tag{4.30}$$

The corresponding excess free energy functional to the single and double 0D cavities (Fig. 4.2.a and Fig. 4.1.b), i.e. $\beta\mathcal{F}^{\text{ex}} = \beta\mathcal{F}_1^{\text{ex}} + \beta\mathcal{F}_2^{\text{ex}}$, is identical to the first two terms of the Rosenfeld functional (Eq. (4.18)). One may expect the constructed functional to handle the triple cavities with only pair overlaps between the cavities (Fig. 4.2.d). However, these so called "lost–cases" do not give an exact 0D free energy and an FMT functional is not capable of describing them [73].

In order to describe the triple cavity with three–body overlap (Fig. 4.2.c) it is possible to assign a delta function to each of them and write down the density profile as a sum of these delta functions. The excess free energy of the constructed functional up to this step, results in undesired additional terms when applied to this density profile which implies the necessity to add a third term to the functional $\beta\mathcal{F}_3^{\text{ex}}$. The third term obtained by this method vanishes when it is applied to a double or a single cavity, hence for hard rods, and therefore recovers the exact form of the excess free energy density in 1D and for a 0D cavity. However, it results in peculiar bulk properties in 3D, for instance marked deviations in the direct correlation function from the Percus-Yevick results [10]. Moreover, the obtained Φ_3 may not be expressed in the form of single convolutions of the density profile which makes its application troublesome. In order to overcome these problems, Tarazona has introduced a new tensorial weight function for constructing Φ_3 in a way that it reproduces the pair correlation function of a triangle formed cavity (Fig. 4.2.c) as well as its full PY form for the bulk fluid [10,74,88]. The tensorial weight function reads

$$\mathbf{w}_i^{\text{T}}(\mathbf{r}) = \delta(R_i - |\mathbf{r}|)\mathbf{e}_r \otimes \mathbf{e}_r\ , \tag{4.31}$$

where $\otimes$ denotes the dyadic product.

In the tensorial version of Rosenfeld functional the first two terms are identical to the original Rosenfeld functional (Eq. (4.18)), while the last term is calculated as a function of scalar (n_3 and n_2), vectorial ($\mathbf{n}_2$), and tensorial ($\mathbf{n}_\text{T}$) weight functions and is given by [74,88],

$$\Phi_3^{\text{RFT}} = \frac{3\left(-n_2\,\mathbf{n}_2 \cdot \mathbf{n}_2 + \mathbf{n}_2 \cdot \mathbf{n}_\text{T} \cdot \mathbf{n}_2 + n_2 \text{Tr}[(\mathbf{n}_\text{T})^2] - \text{Tr}[(\mathbf{n}_\text{T})^3]\right)}{16\pi(1-n_3)^2}. \tag{4.32}$$

The tensorial version of Rosenfeld's fundamental measure functional does not diverge in a highly confined system and is a good candidate for describing the crystalline state

of a hard–sphere system. However, as it is shown in Section 4.5, due to the fact that the derivation of the functional is based on scaled particle theory and its underlying equation of state is the Percus–Yevick equation of state, the obtained phase coexistence densities are shifted to lower densities in comparison with MC simulation results. In the next section, the White Bear functional is introduced which is based on the Carnahan–Starling equation of state and therefore yields more precise results for free energies of crystalline state and phase coexistence densities.

4.3   White Bear versions of FMT

While in its original form, FMT produces the Percus–Yevick compressibility equation of state for fluid as an *output*, Roth et al. [11] and Yu et al. [79] have used the Mansouri–Carnahan–Starling–Leland (MCSL) equation of state [78], as an *input* to the thermodynamic equation (Eqs. (4.14) and (4.16)).

$$\beta p = \frac{\partial \Phi}{\partial n_3} = n_0 - \Phi + \sum_{\alpha=0}^{3} n_\alpha \frac{\partial \Phi}{\partial n_\alpha} \tag{4.33}$$

The MCSL equation of state is a generalization of the exact one–component Carnahan–Starling (CS) equation of state [50] to the ν–component hard–sphere fluid. Using this equation of state as an input to the thermodynamic equation is valid since it is also based on the same scaled–particle variables as the PY compressibility equation of state. In the bulk, weighted densities turn into scaled–particle variables and the MCSL equation of state is rewritten as

$$\beta p_{\mathrm{MCSL}} = \frac{n_0}{1-n_3} + \frac{n_1 n_2}{(1-n_3)^2} + \frac{n_2^3}{12\pi(1-n_3)^3} - \frac{n_3 n_2^3}{36\pi(1-n_3)^3}. \tag{4.34}$$

Note that the last term is an additional term compared to the PY compressibility equation of state (Eq. (3.18)). Replacing βp_{MCSL} in Eq. (4.33), and comparing the factors of the n_0, $n_1 n_2$, and n_2^3 on both sides, the same f_1 and f_2 as for the RF functional are obtained (Eq. (4.17)), while for f_4 we have,

$$f_4(n_3) = \frac{n_3 + (1-n_3)^2 \ln(1-n_3)}{36\pi n_3^2 (1-n_3)^2}. \tag{4.35}$$

As this solution results in the same low density limit as the one for the RF functional, $\lim_{n_3 \to 0} f_4(n_3) = 1/(24\pi)$, the low density approximation is recovered in this case as

well. The first two terms of the White Bear functional are the same as Rosenfeld fundamental measure functional (Eq. (4.18)), and the third term reads [11]

$$\Phi_3^{\mathrm{WB}} = \left(n_2^3 - 3n_2 \mathbf{n}_2 \cdot \mathbf{n}_2 \right) \frac{n_3 + (1 - n_3)^2 \ln(1 - n_3)}{36\pi n_3^2 (1 - n_3)^2} . \tag{4.36}$$

As this third term, just like its predecessor, diverges in a highly confined system, the functional is not capable of describing the crystalline state. The solution is either replacing the diverging term by empirical expressions for hard sphere mixtures [34,72], or using the tensorial weight functions for one–component hard sphere and replace the numerator of Φ_3^{WB} with the one from Φ_3^{RFT} (Eq. (4.32)).

On the other hand, the equation of state is used as an input for obtaining the functional, and therefore the self-consistency with the thermodynamic equation (Eq. (4.14)) is not necessarily ensured in this case. From the scaled–particle equation (Eq. (4.16)), the derivative of the excess free energy density with respect to n_3 should be identical to the pressure from the equation of state βp_{MCSL} (Eq. (4.33)). However, here we obtain

$$\frac{\partial \Phi_{\mathrm{bulk}}^{WB}}{\partial n_3} = \frac{n_0}{1 - n_3} + \frac{n_1 n_2}{(1 - n_3)^2} - \frac{n_2^3 \left(2 - 5n_3 + n_3^2 \right)}{36\pi n_3^2 \left(1 - n_3 \right)^3} - \frac{n_2^3 \ln \left(1 - n_3 \right)}{18\pi n_3^3}. \tag{4.37}$$

Although this expression is different in its functional form from Eq. (4.34), its numerical deviation remains below 2% with one–component fluid. Note that the numerical result from the PY compressibility route, overestimates the pressure close to freezing up to 7% [11]. As for the phase transition result, this functional improves the transition densities, shifting them to $\rho_{\mathrm{fl}} = 0.934$ and $\rho_{\mathrm{cr}} = 1.023$, but still different from MC simulation results $\rho_{\mathrm{fl}} = 0.940$ and $\rho_{\mathrm{cr}} = 1.040$ [80].

By introducing a new version of the Carnahan–Starling equation of state, which improves the results for the binary and ternary hard sphere mixtures in comparison with computer simulations [89], Hansen–Goos et al. built up the mark II of White–Bear functional [12]. The new equation of state, is constructed in a way to be consistent with the scaled–particle equation (Eq. (4.33)) for the one–component fluid in the first place and reads [89]

$$\beta p_{\mathrm{CSIII}} = \frac{n_0}{1 - n_3} + \frac{n_1 n_2 (1 + \frac{1}{3} n_3^2)}{(1 - n_3)^2} + \frac{n_2^3 \left(1 - \frac{2}{3} n_3^2 + \frac{1}{3} n_3^2 \right)}{12\pi (1 - n_3)^3}. \tag{4.38}$$

Following the same analysis for deriving the White Bear excess free energy density, the White Bear Mark II functional is obtained [12],

$$\Phi^{\mathrm{WBII}} = -n_0 \ln(1 - n_3) + \varphi_1(n_3) \frac{n_1 n_2 - \mathbf{n}_1 \cdot \mathbf{n}_2}{1 - n_3} + \varphi_2(n_3) \frac{n_2^3 - 3n_2 \mathbf{n}_2 \cdot \mathbf{n}_2}{24\pi (1 - n_3)^2}, \tag{4.39}$$

with

$$\varphi_1(n_3) = 1 + \frac{2n_3 - n_3^2 + 2(1-n_3)\ln(1-n_3)}{3n_3} \ ,$$

$$\varphi_2(n_3) = 1 - \frac{2n_3 - 3n_3^2 + 2n_3^3 + 2(1-n_3)^2\ln(1-n_3)}{3n_3^2} . \tag{4.40}$$

By this modification, the self consistency holds to a higher level in the context of morphological thermodynamics. In the framework of morphological thermodynamics, it is assumed that the grand potential of a fluid in a complexly shaped container, or equivalently the grand partition of a fluid surrounding a complexly shaped particle, satisfies the requirements of the Hadwiger theorem and therefore can be expressed as as a linear combination of four fundamental measures of the container, i.e. its volume V, its surface area A, its mean curvature C, and its Gaussian curvature X [90]. The restrictions imposed by Hadwiger theorem implies that the grand potential should be a motion invariant, continuous, and additive functional of the shape of the container. It is reasonable to assume that the solvation free energy of a convex body away from the critical point and the wetting or drying transition meets these requirements and is related to its geometric measures via specific thermodynamic coefficients as [91,92],

$$\Delta\Omega = pV + \sigma A + \kappa C + \bar{\kappa} X \ . \tag{4.41}$$

The thermodynamic coefficients which are independent of the shape of the convex body are pressure p, the planar wall surface tension σ, and two bending rigidities κ and $\bar{\kappa}$. Considering the convex body a sphere with radius R_s which is inserted into a hard–sphere mixture with radius R, the solvation free energy (Eq. (4.41)) should be evaluated at the surface at which the equilibrium density profile of the fluid jumps discontinuously to zero, i.e. the solvent–accessible surface [93,94]. The solvent–accessible surface is parallel to the physical wall of the inserted hard–sphere particle, hence is simply a sphere with radius $R + R_S$. Therefore, the solvation free energy (Eq. (4.41)) is written as follows:

$$\Delta\Omega(R_s) = p \frac{4}{3}\pi(R_s + R)^3 + \sigma \, 4\pi(R_s + R)^2 + \kappa \, 4\pi(R_s + R) + \bar{\kappa} \, 4\pi \ . \tag{4.42}$$

On the other hand, considering a binary bulk mixture of a hard–sphere fluid with radius R and a single sphere with radius R_s, thus $\rho_2 = \rho_s \to 0$, the solvent free energy $\Delta\Omega$ is equivalent to the excess chemical potential $\mu_s^{\rm ex}$ and is obtained as follows [12,93].

$$\beta\Delta\Omega = \beta\mu_s^{\rm ex} = \lim_{\rho_s \to 0} \frac{\partial\Phi}{\partial\rho_s}$$

$$= \frac{\partial\Phi}{\partial n_0} + R_s \frac{\partial\Phi}{\partial n_1} + 4\pi R_s^2 \frac{\partial\Phi}{\partial n_2} + \frac{4}{3}\pi R_s^3 \frac{\partial\Phi}{\partial n_3} . \tag{4.43}$$

By comparing this expression with Eq. (4.42), a set of relations for the pressure, the surface tension and the bending rigidities in the bulk is obtained [12].

$$
\begin{aligned}
\beta p &= \frac{\partial \Phi}{\partial n_3} \,, \\
\beta \sigma &= \frac{\partial \Phi}{\partial n_2} - R \frac{\partial \Phi}{\partial n_3} \,, \\
\beta \kappa &= \frac{1}{4\pi} \frac{\partial \Phi}{\partial n_1} - 2R \frac{\partial \Phi}{\partial n_2} + R^2 \frac{\partial \Phi}{\partial n_3} \,, \\
\beta \bar{\kappa} &= \frac{1}{4\pi} \frac{\partial \Phi}{\partial n_0} - \frac{R}{4\pi} \frac{\partial \Phi}{\partial n_1} + R^2 \frac{\partial \Phi}{\partial n_2} - \frac{1}{3} R^3 \frac{\partial \Phi}{\partial n_3} \,.
\end{aligned}
\tag{4.44}
$$

Note that the first relation is exactly the same expression for the pressure in the scaled–particle theory (Eq. (4.14)). Using the WBII functional, the obtained pressure is exactly the same as βp_{CSIII} from Eq. (4.38). Moreover, the numerical results for the remaining thermodynamic coefficients are in good agreement with their analytical forms [12].

Finally, in order to avoid divergence of the functional in a highly confined system and be able to calculate the free energy of the crystalline state, the numerator of the third term in the excess free energy density is replaced with the tensorial version of Tarazona.

$$
\begin{aligned}
\Phi^{\mathrm{WBIIT}} = &-n_0 \ln(1 - n_3) + \varphi_1(n_3) \frac{n_1 n_2 - \mathbf{n}_1 \cdot \mathbf{n}_2}{1 - n_3} \\
&+ \varphi_2(n_3) \frac{3\left(-n_2\, \mathbf{n}_2 \cdot \mathbf{n}_2 + \mathbf{n}_2 \cdot \mathbf{n}_\mathrm{T} \cdot \mathbf{n}_2 + n_2 \mathrm{Tr}[(\mathbf{n}_\mathrm{T})^2] - \mathrm{Tr}[(\mathbf{n}_\mathrm{T})^3]\right)}{16\pi(1 - n_3)^2} \,,
\end{aligned}
\tag{4.45}
$$

with φ_1 and φ_2 given in Eq. (4.40). The one–component WBII(tensor) functional gives very precise bulk crystal free energies, correct order of magnitude for thermal vacancy concentrations, and precise density profiles and surface tensions for the crystal-fluid interface [12, 61, 80, 95]. In Section 4.5 numerical results for the liquid–crystal phase transition and the thermal vacancy concentration obtained by WBII(tensor) functional are presented.

By modifying the Carnahan–Starling equation of state, the inconsistency of the first version of the WB functional with the scaled–particle differential equation is lifted in the WBII functional for a one-component system. In a different approach, Santos expressed the bulk free energy density of the one–component system by taking advantage of a scaling relation [96], and proposed a general solution to the scaled–particle differential equation [81]. Hansen–Goos et al. developed the solution to an inhomogeneous system and have shown that the obtained functional delivers crystallization without the use of the tensorial weight functions [82]. This will be discussed in the next section.

4.4 A new class of self-consistent functionals

For a ν–component system of a hard sphere fluid in 3–D, the free energy is called truncatable [97–99], if the excess free energy density $\Phi\left(\{\rho_i\}\right)$ is expressed as a function of the partial number densities of species $\{\rho_i\}$ by means of the scaled–particle variables $\{\xi_\alpha\}$ defined in Eqs. (3.32) and (3.28). Considering the limit in which one of the components is made of a point particle, Santos has proved that a truncatable free energy of this system has the scaling property as follows [96].

$$\Phi_{\text{Santos}}\left(\{\xi_\alpha\}\right) = -\xi_0 \ln(1 - \xi_3) + \xi_1\xi_2 H(\xi_3, z). \tag{4.46}$$

Here, $z = \xi_2^2/12\pi\xi_1$ and H is a dimensionless scaling function which remains undetermined for now. Using this form of the excess free energy density for the scaled–particle differential equation (Eq. (4.16) with $n_\alpha = \xi_\alpha$), one obtains the following differential equation and the solution for the undetermined scaling function H.

$$
\begin{aligned}
H(\xi_3, z) &= -(1 - \xi_3)\frac{\partial H(\xi_3, z)}{\partial \xi_3} - z\frac{\partial H(\xi_3, z)}{\partial z} \\
\Rightarrow H(\xi_3, z) &= \frac{1}{1 - \xi_3}\Psi\left(\frac{z}{1 - \xi_3}\right).
\end{aligned}
\tag{4.47}
$$

As a result, the excess free energy density Φ_{Santos} is related to an undetermined function $\Psi(y)$ of a single dimensionless variable $y = z/(1 - \xi_3)$. By choosing $\Psi(y) = 1 + \frac{y}{2}f_0(y)$, Φ_{Santos} takes the following form,

$$\Phi_{\text{Santos}}\left(\{\xi_\alpha\}\right) = -\xi_0 \ln\left(1 - \xi_3\right) + \frac{\xi_1\xi_2}{1 - \xi_3} + \frac{\xi_2^3}{24\pi\left(1 - \xi_3\right)^2}f_0\left(y\right),$$

$$\text{with} \qquad y = \frac{\xi_2^2}{12\pi\xi_1\left(1 - \xi_3\right)} \quad, \tag{4.48}$$

which reduces to the original solution of the scaled–particle theory (Eq. (3.33)) if $f_0(y) = 1$. Moreover, by adjusting f_0 any arbitrary equation of state, e.g. the Carnahan–Starling equation of state, may be recovered in the limit of a pure hard sphere fluid [50].

$$
\begin{aligned}
f_0^{\text{PY}}\left(y\right) &= 1 \\
f_0^{\text{CS}}\left(y\right) &= \frac{2}{3}y + \frac{2}{3} - \frac{2\ln\left(1 + y\right)}{3y^2} = 1 - \frac{2}{9}y + \frac{1}{6}y^2 + \mathcal{O}\left(y^3\right).
\end{aligned}
\tag{4.49}
\tag{4.50}
$$

In order to derive a functional for an inhomogeneous system based on Santos' solution,

Hansen–Goos et al. defined two additional weighted densities [82],

$$
\begin{aligned}
\bar{n}_1 &= n_1 - \frac{\mathbf{n}_1 \cdot \mathbf{n}_2}{n_2}, \\
\bar{n}_2 &= n_2 - \frac{\mathbf{n}_2 \cdot \mathbf{n}_2}{n_2}
\end{aligned}
\tag{4.51}
$$

Considering the sum in the scaled–particle differential equation Eq. (4.16) over $\{n_0, n_1, \bar{n}_1, n_2, \bar{n}_2, n_3\}$, they have derived the most general formal form of the excess free energy density Φ_{gen}.

$$
\begin{aligned}
\Phi_{\mathrm{gen}}\left(\{n_\alpha\}\right) = &- n_0 \ln\left(1 - n_3\right) + \frac{\bar{n}_1 n_2}{1 - n_3} \\
&+ \frac{\bar{n}_2^2 n_2}{24\pi\left(1 - n_3\right)^2} \times F\left[\frac{\bar{n}_2^2}{12\pi\bar{n}_1\left(1 - n_3\right)}, \frac{\bar{n}_1}{n_1}, \frac{\bar{n}_2}{n_2}\right],
\end{aligned}
\tag{4.52}
$$

with F being an undetermined function of three dimensionless arguments. In the low density limit, the first argument vanishes and F is required to remain finite. This requirement ensures that the functional results in the exact free energy density for a 0–D cavity [34]. In the following, we obtain an expression for F as it has been done in Ref. [82].

For specificity, we assume to have a pure one–component hard sphere system in order to build a functional. Using the weight functions from Eq. (4.4) with the defined weighted densities from Eq. (4.51), one can relate the weighted densities as

$$
\begin{aligned}
n_1 &= \frac{n_2}{4\pi R}, \qquad n_0 = \frac{n_2}{4\pi R^2}, \\
\bar{n}_1 &= \frac{\bar{n}_2}{4\pi R},
\end{aligned}
\tag{4.53}
$$

where R denotes the radius of hard spheres. This leaves the F from Eq. (4.52) with two arguments.

$$
y = \frac{R\bar{n}_2}{3\left(1 - n_3\right)}, \qquad x = \frac{\bar{n}_2}{n_2} = \frac{\bar{n}_1}{n_1}
\tag{4.54}
$$

Moreover, one can expand F around its limit for a homogeneous fluid in which $x = 1$.

$$
F_m(y, x) = f_0\left(y\right) - \sum_{k=1}^{m} f_k\left(y\right)\left(1 - x\right)^k.
\tag{4.55}
$$

Choosing y as the argument of the expansion coefficients f_i is arbitrary and any other combination of x and y may be used as well; e.g. y/x. However, in the 0–D limit

at which $y \to 0$, the expansion coefficient functions in Eq. (4.55) are well behaved while choosing y/x as the argument of f_i results in a divergence of F_m in this limit (see Appendix A of Ref. [82]). Combining Eqs. (4.55) and (4.52), Φ_{gen} is rewritten as

$$
\begin{aligned}
\Phi_{\text{m}} = \quad & -\frac{n_2}{4\pi R^2} \ln(1 - n_3) + \frac{\bar{n}_2 n_2}{4\pi R (1 - n_3)} \\
& + \frac{\bar{n}_2^2 n_2}{24\pi (1 - n_3)^2} \times F_m \left[\frac{R\bar{n}_2}{3(1 - n_3)}, \frac{\bar{n}_2}{n_2} \right],
\end{aligned}
\tag{4.56}
$$

In a homogeneous fluid the expansion term in F_m becomes zero, leaving this function with only its first term $f_0(y)$. One can determine $f_0(y)$ by comparing Eq. (4.56) with Santos general solution for scaled–particle differential equation (Eq. (4.48)), and set its value to either f_0^{PY} from Eq. (4.49) for imposing the Percus–Yevick equation of state or f_0^{CS} from Eq. (4.50) for the Carnahan–Starling equation of state.

The direct correlation function of the system which is expressed as the second functional derivative of the excess free energy with respect to the density profile, does not depend on the expansion coefficients except for the first one $f_1(y)$. This can be used to overcome the divergence of direct correlation function of a fluid for $r \to 0$ which is reported for previous versions of functional based on Santos general solution [81, 100]. This implies that,

$$
f_1(y) = f_0(y) + 2y f_0'(y) + \frac{1}{2} y^2 f_0''(y).
\tag{4.57}
$$

Depending on the input equation of state, f_0^{PY} or f_0^{CS} is used to determine the first coefficient in the expansion.

$$
\begin{aligned}
f_1^{\text{PY}}(y) & = 1 & \tag{4.58} \\
f_1^{\text{CS}}(y) & = \frac{1 + \frac{4}{3}y + \frac{2}{3}y^2}{(1 + y)^2} = 1 - \frac{2}{3}y + y^2 + \mathcal{O}\left(y^3\right). & \tag{4.59}
\end{aligned}
$$

The functional in its current form is exact in the 0–D limit and obeys the input equation of state in 3–D. In line with the idea of dimensional crossover, the second coefficient f_2 is determined in a way that the functional expression for a homogeneous fluid in the 1–D limit becomes correct (see Appendix B of [82]). Following this route, we obtain an expression for f_2 which reads

$$
\begin{aligned}
f_2(y) = \quad & \frac{1}{8}\left\{ (35 + 78y + 54y^2) f_0(y) + (13 + 21y + 54y^2) f_0'(y) + y^2(1 + 3y)^2 f_0''(y) \right\} \\
& - \frac{1}{4}\left\{ (7 + 6y) f_1(y) + (1 + 3y) f_1'(y) \right\}.
\end{aligned}
\tag{4.60}
$$

For the PY and CS equations of state, this leads to,

$$
f_2^{\mathrm{PY}}(y) = \frac{3}{8}(7 + 22y + 18y^2) \tag{4.61}
$$

$$
f_2^{\mathrm{CS}}(y) = \frac{15 + 69y + 221y^2 + 438y^3 + 459y^4 + 269y^5 + 54y^6}{12y(1+y)^3} - \frac{5\ln(1+y)}{4y^2}
$$

$$
= \frac{3}{8}\left(7 + 22y + \frac{19}{2}y^2\right) + \mathcal{O}(y^3). \tag{4.62}
$$

However, by choosing these expressions for f_2 the functional does not give a stable crystal. It appears that obeying 0–D limit is a necessary condition for describing the crystallization, but not a sufficient one. There are specific configurations, for instance two cavities kept at a distance of $2R$ while touching at a single point, at which f_2 diverges as it contains terms proportional to y^2. This results in the divergence of the free energy density in a confined system. As an alternative suggestion, Hansen–Goos et al. propose using a constant value λ for f_2 while for f_0 and f_1 the expressions in Eqs. (4.49) and (4.58) are used for the Percus–Yevick equation of state and Eqs. (4.50) and (4.59) for the Carnahan–Starling equation of state. By this choice of parameters, the functional predicts crystallization for a hard sphere system as it is shown in the presented numerical results in Section 4.5.

4.5 Bulk properties of the hard–sphere crystal

In the framework of classical DFT, the crystalline state is treated as an inhomogeneous fluid in the grand ensemble. In order to find the equilibrium properties of a bulk crystalline state, the hard–sphere particles are initiated at the lattice sites of an fcc cubic unit cell with side length a, as Gaussian peaks.

$$
\rho(\mathbf{r}) = \sum_i (1 - n_{\mathrm{vac}})\left(\frac{\alpha_{\mathrm{G}}}{\pi}\right)^{\frac{3}{2}} \exp\left(-\alpha_{\mathrm{G}}|\mathbf{r} - \mathbf{r}_i|^2\right). \tag{4.63}
$$

Here, the sum is over the fcc lattice sites, α_{G} is the Gaussian width, and n_{vac} is the number density of vacant positions in a non–ideal crystal and is defined as

$$
\int_{\mathrm{cell}} \mathrm{d}\mathbf{r}\, \rho(\mathbf{r}) =: 4(1 - n_{\mathrm{vac}}). \tag{4.64}
$$

The free energy density of the desired functional should then be minimized. This can either be done with Constrained minimization or Full minimization.

1. **Constrained minimization**: In constrained minimization, the free energy density is minimized while the density profile is constrained to keep its initial Gaussian form. The Gaussian width α_G and the vacancy concentration n_{vac} are the minimization parameters.

$$F_{eq} = \min_{\{n_{vac}, \alpha_G\}} \mathcal{F}[\rho_i]. \tag{4.65}$$

2. **Full minimization**: Here, for obtaining the equilibrium density profile, after specifying the chemical potentials of the species μ_i, the resulting integral equation from minimizing the grand free energy functional with respect to density profile, $\delta\Omega/\delta\rho_i = 0$, should be solved for each of the species.

$$\ln\left(\sigma^3 \rho_i(\mathbf{r})\right) = -\frac{\delta\beta\mathcal{F}^{ex}[\rho_i]}{\delta\rho_i(\mathbf{r})} + \beta V_i^{ext}(\mathbf{r}) - \beta\mu_i(\mathbf{r}). \tag{4.66}$$

During the minimization procedure, the equilibrium lattice constant a_{eq} and vacancy concentration $n_{vac,eq}$ should adjust themselves accordingly. However, such a procedure is not feasible [80]. Keeping the number density of the hard–spheres constant throughout the minimization, enables us to reach the equilibrium state. After initiating the Gaussian density profile with a specified lattice constant and fixed vacancy concentration, the changes in excess chemical potential acquired by the functional derivative of the excess free energy density functional is computed numerically and the density profile is updated accordingly. This self–consistent procedure which leads to the minimization of the free energy density is repeated until the changes in the density profile are negligible (see Appendix A.4.1). In order to reach the global minimum of F, the vacancy concentration is changed and the minimization is set up from the beginning.

$$F_{eq} = \min_{\{n_{vac}\}} \min_{\{\rho_i(\mathbf{r})\}} \mathcal{F}[\rho_i]. \tag{4.67}$$

4.5.1   Phase transition

Having the free energy density curves for the crystalline state as well as the homogeneous fluid phase, one can obtain the phase transition using the Maxwell construction (see Appendix D). We present here the numerical results for three classes of functionals which indeed give rise to a hard–sphere crystal.

- **RF(tensor)** The tensorial version of Rosenfeld's functional (Eq. (4.18) with Φ_3 from Eq. (4.32)). This functional is based on Percus-Yevick equation of state,

- **WBII(tensor)** The tensorial version of White Bear Mark II (Eq. (4.45)) which is based on the more exact Carnahan-Starling equation of state,

- **VEC(PY & CS)** The FMT version of Santos general solution for the scaled particle equation (Eq. (4.56)) with the expansion terms in F_{m} (Eq. (4.55)) considered up to the second order. By assigning $f_1(y)$ to either Eq. (4.58) or Eq. (4.59) the Percus-Yevick and the Carnahan–Starling equation of states are imposed consequently. f_2 is set to a constant value λ. The excess free energy density will be shown as $\Phi_{2,\lambda}^{\mathrm{PY/CS}}$. The examined cases are $\lambda = 0, 1/2, 1$.

The phase coexistence densities for the fluid and the crystalline state, ρ_{fl} and ρ_{cr}, are represented in table 4.1 along with the pressure βp_{coex} and the chemical potential $\beta \mu_{\mathrm{coex}}$ at coexistence . The RF(tensor) results show a discrepancy in the estimation of the coexistence result due to its underlying equation of state being the Percus–Yevick EoS. However, the WBII(tensor) functional shows good agreement with the simulation results as it is based on the more exact Carnahan–Starling equation of state. The VEC(PY/CS) are numerically less complex as they are not using tensorial weight functions and allow fast numerical calculations. This could justify using them as a test case. For this functional, the $\Phi_{2,\lambda=0}^{\mathrm{PY}}$ and $\Phi_{2,\lambda=\frac{1}{2}}^{\mathrm{CS}}$ are the most promising ones.

4.5.2 Vacancy concentration

As it has been mentioned earlier, the free energy per particle is minimized either with respect to the density profile (full minimization), or simultaneously with respect to the Gaussian width and the vacancy concentration (constrained minimization). In either case, the occupation number of particles which is 4 for an ideal fcc unit cell, is less than this value due to the presence of an average vacant lattice site. Here, we focus on another powerful aspect of FMT functionals which is delivering the correct order of magnitude for the vacancy concentration, $n_{\mathrm{vac}} \sim \mathcal{O}(10^{-4})$. This ability, along with their successful description of a stable solid phase, is of great importance in further applications of a FMT functional, e.g. describing crystal–fluid interfaces using DFT [80].

The vacancy concentration for a hard–sphere crystal obtained from some other theoretical tools, such as Taylor expanded functionals or the Phase Field Crystal model, are not only unphysical ($\sim \mathcal{O}(0.1)$), but also negative in some cases which corresponds to excess interstitials [61]. This is due to the fact that these approximations do not respect the 0D-limit [80].

A more detailed discussion on the theoretical aspects of the vacancy concentration and its physical interpretation is presented in Chapter 6. In this section, we are going to

compare the capability of different type of FMT functionals in delivering n_{vac} for a one–component hard–sphere fluid.

In the case of tensorial functionals, RF(tensor) does not yield a minimum for free energy per particle as a function of varying vacancy concentration in full minimization. The WBII(tensor) however, predicts the order of magnitude correctly. Using $\Phi_{\lambda=1}^{\text{PY/CS}}$ as the excess free energy density, the functional does not deliver a stable crystal with a finite vacancy concentration. However, for $\lambda = 0, 1/2$ the results show better agreement with the simulation results than those of the WBII(tensor) (Fig. 4.3). At the exemplary case of the solid coexistence density, $\rho\sigma^3 = 1.04$, the vacancy concentration obtained from different functionals are presented in table 4.2.

Table 4.1: Coexistence densities (packing fraction) of the fluid $\rho_{\text{fl}}(\eta_{\text{fl}})$ and the crystal $\rho_{\text{cr}}(\eta_{\text{cr}})$ as well as the pressure, the chemical potential, and the free energy per particle at coexistence calculated by full minimization of the free energy density for three different types of functionals: the tensorial White Bear Mark II functional (WBII(tensor)), the tensorial Rosenfeld functional (RF(tensor)), and the FMT version of the Santos general solution for the scaled particle theory. For the latter, the second term in the expansion of F_m (Eq. (4.55)) is set to be a constant value $f_2 = \lambda = 0, 1/2, 1$. The simulation results for the coexistence densities and pressure are obtained by Monte–Carlo simulation [77]. The free energy per particle and chemical potential for $\rho_{\text{fl}}\sigma^3 = 0.940$ are obtained using Carnahan–Starling equation of state [61]. The crystal free energy density is calculated using an improved fit in the form of Speedy equation of state for hard–sphere crystals [80, 101]. The thermal de Broglie wavelength λ is set to σ.

	$\rho_{\text{fl}}\sigma^3(\eta_{\text{fl}})$	$\rho_{\text{cr}}\sigma^3(\eta_{\text{cr}})$	$\beta\mu_{\text{coex}}$	$\beta p_{\text{coex}}\sigma^3$	$(\beta F/N)_{\text{fl}}$	$(\beta F/N)_{\text{cr}}$
WBII(tensor)	0.945(0.495)	1.040(0.544)	16.40	11.89	3.82	4.96
RF(tensor)	0.892(0.467)	0.984(0.515)	15.75	11.28		
VEC(PY), $\lambda = 0$	0.925(0.484)	0.995(0.521)	16.24	11.57	3.45	4.58
, $\lambda = \frac{1}{2}$	0.907(0.475)	0.973(0.509)	15.07	10.50	3.17	4.16
, $\lambda = 1$	0.892(0.467)	0.965(0.505)	14.08	9.61	2.95	3.98
VEC(CS), $\lambda = 0$	0.980(0.513)	1.059(0.555)	18.43	13.84	4.21	5.68
, $\lambda = \frac{1}{2}$	0.960(0.503)	1.025(0.536)	17.29	12.74	3.86	4.98
, $\lambda = 1$	0.936(0.490)	1.003(0.525)	15.89	11.41	3.47	4.52
SIM	0.940(0.492)	1.041(0.545)	16.09	11.58	3.75	4.96
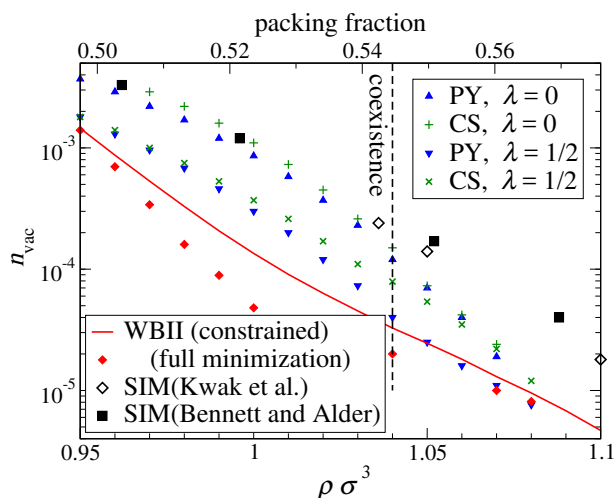
Figure 4.3: The thermal vacancy concentration n_{vac} of a hard–sphere crystal obtained by full minimization of the free energy functional are shown along with the simulation results from Kwak et al. [102] and Bennett and Alder [103]. In the case of the WBII(tensor) the constrained minimization results are also included.

4.5.3 Density distribution

The final density profile obtained by full minimization deviates from the Gaussian approximation. For comparison, the density distribution along the fcc unit cell [100], [110], and [111] directions is shown in Fig. 4.4 for the bulk density $\rho\sigma^3 = 1.04$. Note that in this representation a Gaussian approximation is a straight line. For the WBII(tensor) functional, the anisotropy is more pronounced in [110] and [111] direction and its deviation from the MC simulation result increases away from lattice site $r = 0$. In the case

Table 4.2: The thermal vacancy concentration of the crystalline state obtained by full minimization of different functionals at $\rho\sigma^3 = 1.04$. The simulation result is obtained for $\rho = 1.036$ [102].

|		n_{vac}
WBII(tensor)	constrained	0.33×10^{-4}
	full minimization	0.20×10^{-4}
VEC(PY)	$\lambda = 0$	1.2×10^{-4}
	$\lambda = \frac{1}{2}$	0.5×10^{-4}
VEC(CS)	$\lambda = 0$	1.5×10^{-4}
	$\lambda = \frac{1}{2}$	0.79×10^{-4}
SIM		2.4×10^{-4}

of the VEC(PY/CS) functional, generally there is an overestimation at the lattice site and the overlapping of the relaxed Gaussian peaks, especially in 110 direction, results in a significantly higher value than what is expected from the simulation results (see Fig. 4.4.b-e).

4.6   Summary and Conclusions

In this chapter, we have presented a brief introduction to Fundamental Measure Theory (FMT) as a powerful theoretical tool for studying hard–sphere mixtures in equilibrium. Within the framework of classical density functional theory, the crystalline state is treated as an extreme inhomogeneous state. Therefore, the extension of the theory tools from one which solely describes a bulk homogeneous state (scaled–particle theory) to one which is capable of delivering the equilibrium properties of an inhomogeneous system is necessary. Rosenfeld has done this by introducing a minimal set of weight functions which are used to obtain the weighted (smeared out) densities. The local weighted densities are used for calculating the excess (over ideal) free energy density which is due to the interaction of the particles in the system. The Rosenfeld functional delivers a pair direct correlation function for the hard–sphere fluid which is the same as that from PY theory of the uniform mixtures [9]. This functional has many applications for specific types of confinement, for instance the adsorption at a single planar wall [83], and hard–sphere mixtures adsorbed at walls in model pores [88,104]. However, its excess free energy diverges when it is applied to a particle which is caged by its neighbors [9,72]. We have discussed the problem in the context of dimensional crossover and 0D cavities. The divergence of Rosenfeld's fundamental measure functional is resolved by introducing a tensorial weight function proposed by Tarazona [10,73].

While the underlying equation of state for Rosenfeld's fundamental measure functionals and its derivatives is the Percus–Yevick compressibility equation of state, Roth et al. have used the more exact Carnahan–Starling equation of state as an input to derive the White Bear functional [11]. The tensorial version of the White Bear Mark II is not only consistent with the restrictions imposed by the scaled–particle differential equation, but also has a higher level of consistency in the context of morphological thermodynamics [12]. Santos' general solution for the scaled–particle equation leads to a fundamental measure functional which is less complex from a numerical point of view as it does not require tensorial weight functions [81,82].

The most promising functional for studying the crystalline state and the fluid-solid phase transition is the WBII(tensor) which is consistent with morphological thermodynamics [12]. The bulk crystal free energies for a one–component hard–sphere mixture obtained by the WBII(tensor) functional are in good agreement with simulation
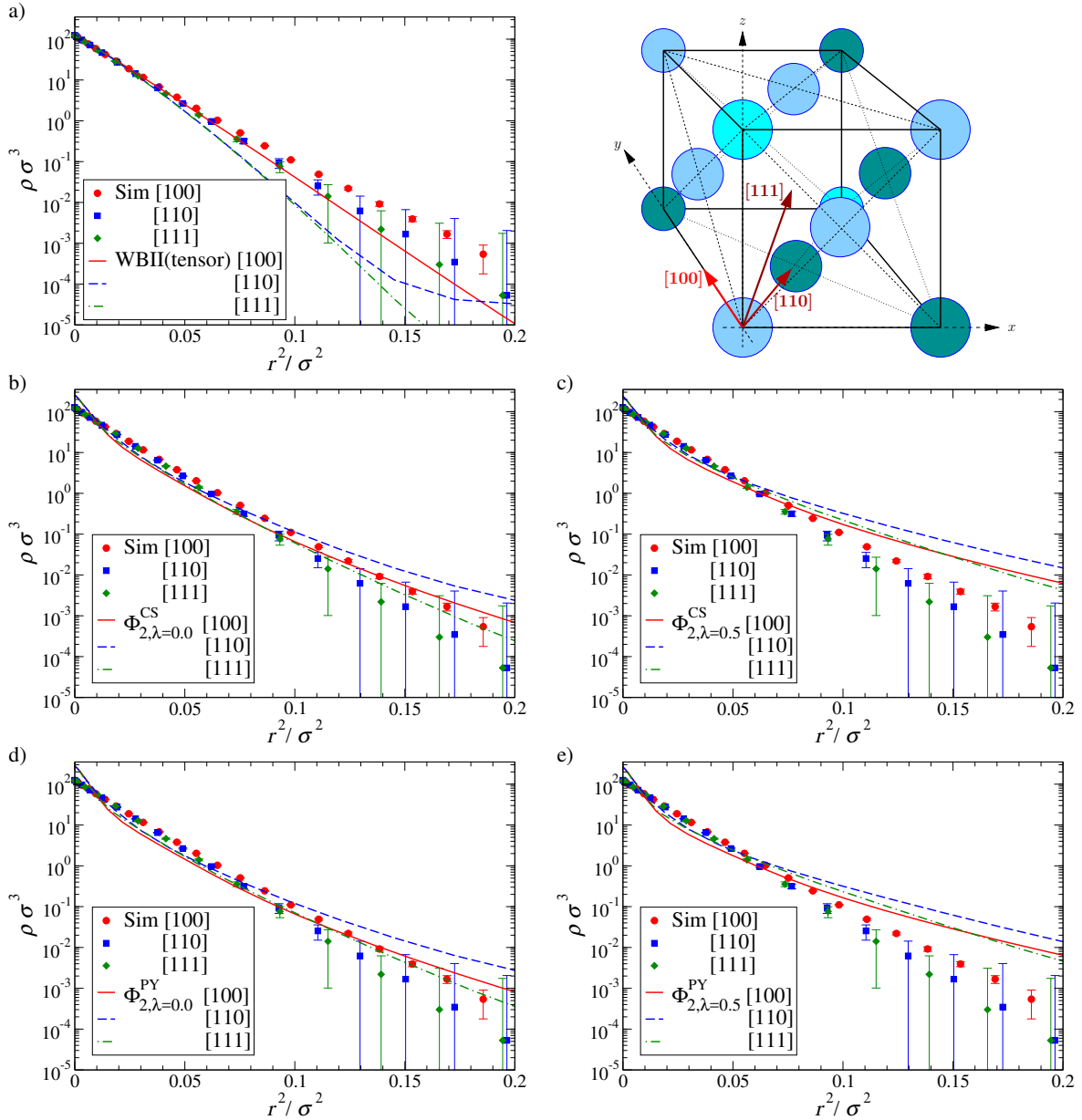
Figure 4.4: The density distribution of the hard–sphere crystal along the fcc lattice directions [100], [110], and [111] obtained by full minimization of different functionals for the solid coexistence density $\rho\sigma^3 = 1.04$. Shown is a log–plot of the density versus the square of the distance from the lattice site. A Gaussian distribution is therefore a straight line in this representation. Full symbols with error bars represent the MC simulation result from [80]. The cartoon in which the particles laying in the same close–packing layer are marked with the same color, indicates the lattice directions in an fcc unit cell.

results [80]. Moreover, this functional delivers a correct order of magnitude for thermal vacancy concentrations [80]. In the case of the crystal–fluid interface, precise density profiles and surface tensions are obtained [61, 95]. We will use the WBII(tensor) functional of 2–component hard–sphere mixtures to derive a density functional for a colloid–polymer mixture in the next chapter.

CHAPTER 5

AN FMT FUNCTIONAL FOR FREEZING IN THE ASAKURA–OOSAWA MODEL

The physical properties of a colloidal suspension, i.e. macromolecules dispersed in a solution, depend firmly on the effective interactions between the colloidal particles. There is an effective attraction between two colloidal particles when they get close enough due to the Van der Waals interaction between their atomic building blocks. This net attractive force between two atoms is the result of the interaction of spontaneous dipoles formed by the oscillations of their clouds of electron. For having a stable solution, the effective attraction between two colloidal particles is normally balanced by a repulsive force to prevent flocculation of the colloidal particles. This can be done by the electrostatic repulsion of the counter–ions of the suspension which are attracted to the charged surface of the particles. Another way is steric stabilization which is done by coating the surface of the colloidal particles by polymeric chains [3,6].

The depletion potential is another important type of effective interactions between colloidal particles. This occurs in mixtures of hard colloidal particles and non–adsorbing polymeric chains. In such a suspension, the polymer configurational degrees of freedom are restricted in the vicinity of the colloidal particles. The tendency to maximize the entropy of polymeric chains results in an effective attraction between colloidal particles whose strength is controlled by the polymer concentration. Therefore, the polymer concentration can be used as a control parameter to induce phase separation into colloid–poor (gas), colloid–rich (liquid), and crystal (solid) phases [3].

A minimalistic theoretical model for such a mixture has been proposed by Asakura and Oosawa [4] and developed further by Vrij [5]. In the framework of the Asakura–Oosawa (AO) model, the colloid–polymer mixture is treated as a non–additive binary hard sphere suspension. The particles of species 1 which represent the colloidal particles interact with each other as hard–spheres of diameter σ_c. The polymers which are assigned to particles of species 2 in the mixture are hard spheres of diameter $\sigma_p = q\sigma_c$

when they interact with colloidal particles. Here, the polymer–colloid size ratio is denoted by q. The polymers are assumed to have no interaction with each other and therefore are an ideal gas in the absence of the colloidal particles. Moreover, a polymer reservoir is assumed to be coupled to the system. This reservoir of polymers keeps the chemical potential of the polymer in the suspension at a constant value and therefore dictates its concentration.

A simple, analytic approximation for the free energy of the AO model is represented by free volume theory [105]. Since it is treating the colloid–polymer mixture in the bulk, the obtained free energy has been mainly used to describe the gas–liquid phase transition densities. The obtained results give qualitative description of the corresponding binodals from experimental data [106, 107]. Moreover, except for the vicinity of the critical point, the binodals obtained by free volume theory are in good agreement with the results from simulations [108, 109]. For the treatment of the crystal phase of the AO model, the accurately known free energy of the pure hard sphere solid is borrowed as a reference system for applying perturbation methods [105, 110].

The AO model is a special case of a binary hard sphere mixture in which the interactions between one of the species (polymers) is missing. Therefore, it is reasonable to assume that fundamental measure theory is capable of describing it within the framework of classical density functional theory. As it is introduced in Chapter 4, FMT is very precise in the description of bulk and inhomogeneous hard sphere mixtures and delivering the crystal–liquid phase transition densities. By linearizing the binary hard sphere functional with respect to the density of polymers a proper functional for describing the AO model is constructed [111]. The obtained polymer–polymer direct correlation function is zero, thus they do not interact with each other as it is desired. The AO functional obtained by linearization of the Rosenfeld functional (Eq. (4.18)) recovers free volume theory for the bulk fluid state. Moreover, it is also able to calculate pair correlations and structure factors, wetting behaviour at walls and associated layering transition. The obtained results for the linearized Rosenfeld functional are in good agreement with simulations [112]. However, as it is discussed in Section 4.2 the Rosenfeld functional does not account for crystallization and therefore, any functional which is derived from it also shares this deficiency.

In this chapter, by linearizing the White Bear II (tensor) functional which is the most promising FMT functional for the hard sphere crystal[1], with respect to the polymer density, we construct a density functional for a unified treatment of fluid and crystalline states of the colloids in the AO model.

Subsequently, the free energies of an fcc crystal of the colloids are computed and the phase coexistence densities are obtained using the common tangent construction. Furthermore, for the crystalline state the colloid and polymer density distributions are

---

[1]see Eq. (4.45) and the numerical results for comparison of different type of functionals in Section 4.5.

presented. For the more interesting case of small polymer–colloid size ratio q it can be shown that the polymers degree of freedom may be integrated out and their effect be represented by an exact pair interaction between colloidal particles [4]. This specific limit makes the AO model a suitable candidate as a generic colloid model to investigate some longstanding problems in the general theory of fluid systems, e.g. interfacial effects in the vapor–liquid phase transition [113]. We have shown that in the limit of small q the conventional mean–field treatments of the AO crystals fails due to an underestimation of the attractive part of the effective free energy of the colloidal particles. Therefore, the presented AO functional is a prototype functional for colloidal systems with short–range attraction and will eventually give a precise description of the crystallization phenomena in such systems.

In the next section, the AO model is introduced as a minimalistic model for studying a mixture of colloids in the presence of non–adsorbing polymers. In Section 5.2, after recapitulating the free volume theory, a comparison of the attractive part of the effective free energy for the bulk fluid with the naive mean–field treatment of the AO model is presented. The linearization of the FMT functional and a justification on its validity for the AO model is presented in Section 5.3. The linearized FMT functional results in an effective one–component colloid functional. Our previously reported results in Ref. [17] obtained by this effective functional are presented in Section 5.4. The free energies of an fcc crystalline state of the colloids are reported in Section 5.4.1 and the FMT results for small polymer–colloid size ratio are compared with a simple free volume model for an ideal crystal, and with the results from a mean–field functional. The phase coexistence densities are obtained by the Maxwell construction and are compared with other available numerical results (see Section 5.4.2). A discussion on the effect of polmyer–colloid size ratio q on the equilibrium polymer density distribution is given in Section 5.4.3. In Section 5.4.4 the full minimization of the effective free energy of the colloids and its effect on the phase coexistence density and on the colloid/polymer density distribution is discussed. The crystal free energies and the phase coexistence densities obtained by linearization of the RF(tensor) functional are compared with those of the WBII(tensor) in Section 5.4.5. Finally, Section 5.5 gives a short summary and outlook.

5.1 Asakura–Oosawa Model

Adding non–adsorbing polymers to a colloid suspension enriches its phase behavior. This is due to the osmotic pressure exerted on colloidal particles by polymers. A minimalistic yet powerful model for describing this system has been presented by Asakura and Oosawa [4] and later on formulated by Vrij [5]. According to the Asakura–Oosawa (AO) model, the colloids are hard spheres with diameter $\sigma_{\rm c}$ and their interaction is de-

scribed by ϕ_{cc} in Eq. (5.1). While the polymer coils with radius of gyration $R_g = \sigma_p/2$ are allowed to interpenetrate each other and therefore behave as an ideal gas, the polymer–colloid interaction, ϕ_{cp}, is again assumed to be of hard sphere type and therefore, their center of mass does not get closer to the center of a colloid than $R_g + \sigma_c/2$. This is summarized as follows,

$$
\begin{aligned}
\phi_{cc}(r) &= \begin{cases} \infty & r < \sigma_c \\ 0 & \text{otherwise,} \end{cases} \\
\phi_{cp}(r) &= \begin{cases} \infty & r < \frac{1}{2}(\sigma_c + \sigma_p) \\ 0 & \text{otherwise,} \end{cases} \\
\phi_{pp}(r) &= 0 \, .
\end{aligned}
\tag{5.1}
$$

Here, r is the distance between centers of the particles. Due to ϕ_{cp} there is a depletion layer around a colloidal particle, i.e. an excluded volume in which a polymer can not enter. If the excluded volume of two colloid particle overlap, as is shown in Fig. 5.1, the available volume for the polymers increases, hence their entropy.

From a different point of view, the absence of polymers in the overlapping excluded volumes and their presence around all other surfaces of the two colloidal particles, result in an osmotic pressure exerting a net short–range attraction between colloids. The resulting effective two–body potential between colloids $\phi_{AO}(r)$ due to the depletion interaction is proportional to the overlapping excluded volumes. Integrating out the polymers degree of freedom in a more formal way (see Eq. (5.6) and the discussion thereafter) leads to the same effective potential:

$$
\beta\phi_{AO}(r) = \begin{cases} \infty & (r < \sigma_c) \\ -\frac{\pi}{6}\sigma_p^3 \rho_{p,r} \left(1 + \frac{1}{q}\right)^3 \left(1 - \frac{3r}{2\sigma_c(1+q)} + \frac{r^3}{2\sigma_c^3(1+q)^3}\right) & (\sigma_c \le r \le \sigma_c + \sigma_p) \\ 0 & (\text{otherwise}) \end{cases}
\tag{5.2}
$$

where $\rho_{p,r}$ is the density of the polymer reservoir coupled to the system (see Eq. (5.4)). The AO potential from Eq. (5.2) is exact as long as there are only two–body overlaps of excluded volumes.

For examining the onset of three-body overlaps, one may put three particles on the edges of an equilateral triangle with the side length of σ_c. The three exclusion spheres should meet at most in one point at the center of the triangle (see Fig. 5.3b). The height of this triangle is $h = l + m$ with $l = \frac{1}{2}(\sigma_c + \sigma_p)$ and $m = \frac{1}{4}(\sigma_c + \sigma_p)$. On the other hand, since the side length of this equilateral triangle is σ_c, its height is equal to $h = \frac{\sqrt{3}}{2}\sigma_c$. Therefore,

$$
q = \frac{\sigma_p}{\sigma_c} = \frac{2}{\sqrt{3}} - 1 \approx 0.1547,
\tag{5.3}
$$
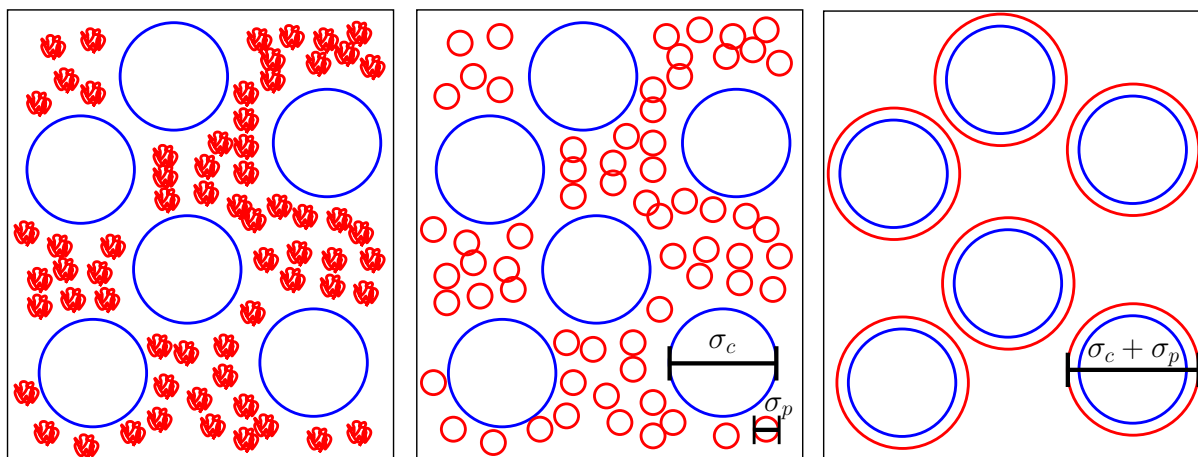
Figure 5.1: Adding non–adsorbing polymer chains to a colloidal suspension induces a depletion layer around colloidal particles where the configurational entropy of the polymeric chains is reduced. Depicted is the simplifications made in the AO model in order to express the presence of polymers in the form of an effective attraction between colloidal particles. The non–adsorbing polymeric chains in the suspension (left) are approximated by spheres with diameter σ_p which are allowed to overlap (middle). As a result, in the absence of the colloidal particles, we have an ideal gas of the polymers. The colloid–colloid and the colloid–polymer interactions are of hard–sphere type. The diameter of the colloidal particles is σ_c. Hence the diameter of the polymers exclusion sphere, the sphere into which the center of a polymer is not allowed, is $\sigma_c + \sigma_p$. Overlapping of the exclusion spheres increases the total available volume for polymers and therefore induces a depletion attraction among the colloidal particles. For small polymer–colloid size ratios, $q = \sigma_p/\sigma_p \leq 0.1547$ (see text), the polymers degree of freedom may be integrated out in order to write down an exact effective interaction between colloids (right).

where q is the polymer to colloid size ratio. As long as $q \leq 0.1547$, there is only 2–body overlapping of excluded volumes and the effective interaction between colloids is given exactly by ϕ_{AO} (Eq. (5.2)).

For small polymer–colloid size ratios, one may integrate out the polymers degree of freedom and write down an effective Hamiltonian only for the colloidal particles [114–117]. In this sense, the polymers contribute to the total Hamiltonian of the system as fictitious attractive agents for the colloids. For this purpose, rather than using a canonical ensemble and assuming a constant particle number for each of the species, it is more convenient to use a semi–grand ensemble in which the polymer chemical potential μ_p is kept constant. In this picture, a polymer reservoir is assumed to be coupled to the system, maintaining the polymer chemical potential at $\mu_p = \mu_{p,r}$.
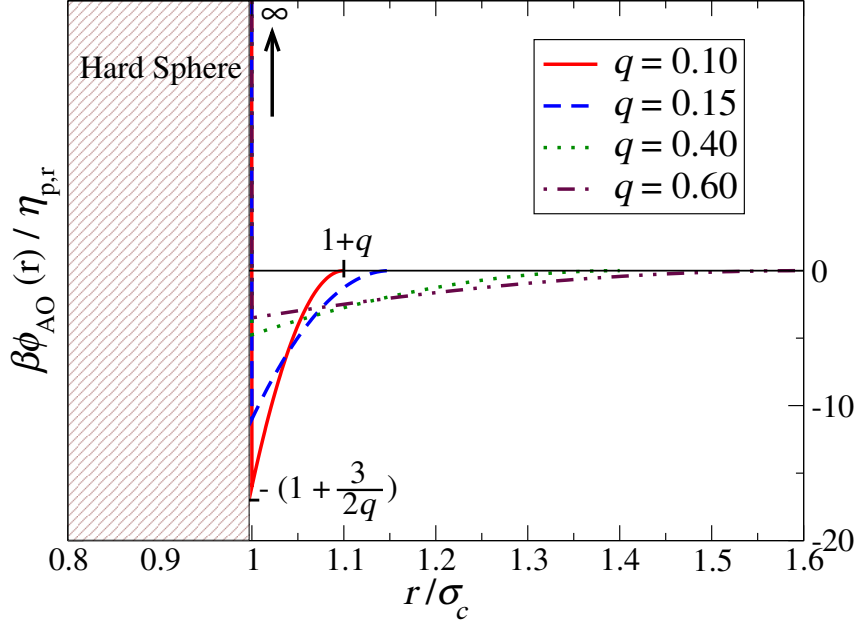
Figure 5.2: The effective colloid–colloid potential in the AO model ϕ_{AO} (Eq. (5.2)) which is obtained by integrating out the polymers degree of freedom. The effective potential is normalized to the polymer reservoir packing fraction $\eta_{p,r}$ and plotted for four different polymer–colloid size ratios q. The cut–off range of the potential $1 + q$ and its minimum value $- \left(1 + \frac{3}{2q}\right)$ is marked on the curve for $q = 0.1$.

For practical reasons, it useful to define a reservoir polymer density $\rho_{p,r}$ which for an ideal gas is proportional to its fugacity $z_p = e^{\beta\mu_p}$, and a reservoir polymer packing fraction $\eta_{p,r}$ as a function of $\mu_{p,r}$.

$$\rho_{p,r} = \frac{\exp(\beta\mu_p)}{\lambda_p^3} = \frac{z_p}{\lambda_p^3}. \tag{5.4}$$

$$\eta_{p,r} = \frac{\pi}{6}\sigma_p^3\rho_{p,r}. \tag{5.5}$$

Here, λ_p is the thermal de Broglie wavelength of the polymers. In the results section it will be shown that the polymer reservoir packing fraction $\eta_{p,r}$ is playing the role of an inverse temperature in a simple fluid, e.g. Lennard–Jones, in which the pair interaction between particles contains an attractive tail.

The Helmholtz free energy $F'(N_c, z_p, V)$ of a system with physical volume V and con-

(a) $q = 0.1$ **(b)** $q = 0.1547$ **(c)** $q = 0.4$
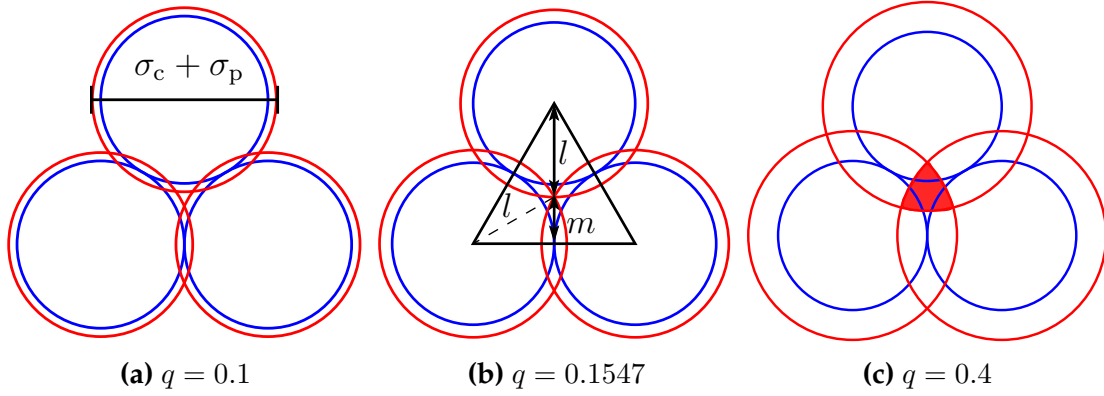
Figure 5.3: A 2D representation of overlapping of the exclusion spheres of three colloidal particles, with different values of polymer–colloid size ratio q. In (b) the colloids are sitting at the corners of an equilateral triangle with side length σ_c, while the exclusion spheres meet at one point in the center of this triangle. The height of this triangle $h = \frac{\sqrt{3}}{2}\sigma_c$ is equal to $l + m$ with $l = \frac{1}{2}(\sigma_c + \sigma_p)$ and $m = \frac{1}{4}(\sigma_c + \sigma_p)$, hence $q \approx 0.1547$. The two–body AO potential (Eq. (5.2)) is exact as long as there is only overlap of excluded volumes between two colloids which is true for $q \leq 0.1547$.

stant number of colloidal particles N_c is written as

$$\exp\left[-\beta F'\right] = \sum_{N_p=0}^{\infty} \frac{z_p^{N_p}}{\lambda_p^{3N_p} N_p!} \int d\mathbf{r}_p^{N_p} \frac{1}{\lambda_c^{3N_c} N_c!} \int d\mathbf{r}_c^{N_c} \exp\left[-\beta\left(H_{cc} + H_{cp}\right)\right]. \quad (5.6)$$

Here, $\beta = 1/k_B T$, λ_c is the thermal de Broglie wavelength of colloids, N_p denotes number of the polymers, and $\mathbf{r}_c$ ($\mathbf{r}_p$) indicate the colloid (polymer) coordinates. The contribution of the interacting particles to the total Hamiltonian of the system is written as a sum of the Hamiltonian due to the colloid–colloid interaction H_{cc} and that due to the colloid–polymer interaction H_{cp} which are defined as

$$H_{cc} = \sum_{i<j}^{N_c} \phi_{cc}(|\mathbf{r}_{c,i} - \mathbf{r}_{c,j}|)$$

$$H_{cp} = \sum_{i=1}^{N_c} \sum_{j=1}^{N_p} \phi_{cp}\left(|\mathbf{r}_{c,i} - \mathbf{r}_{p,j}|\right). \quad (5.7)$$

Here, we have used $\phi_{cc}(r)$ and $\phi_{cp}(r)$ as defined in Eq. (5.1). The corresponding term for the polymer–polymer interaction H_{pp} is zero as they are treated as an ideal gas and $\phi_{pp}(r) = 0$. In a fixed configuration of N_c colloids acting as an external potential for the

polymers, the grand potential of the polymers Ω_p may be extracted from Eq. (5.6) as,

$$\exp\left[-\beta\Omega_p\right] = \sum_{N_p=0}^{\infty} \frac{z_p^{N_p}}{\lambda_p^{N_p} N_p!} \int \mathrm{d}\mathbf{r}_p^{N_p} \exp\left[-\beta \sum_{i=1}^{N_c} \sum_{j=1}^{N_p} \phi_{cp}\left(|\mathbf{r}_{c,i} - \mathbf{r}_{p,j}|\right)\right]. \tag{5.8}$$

This enables us to rewrite Eq. (5.6) as the Helmholtz free energy of a one–component hard sphere suspension with an effective Hamiltonian given by $H_{\mathrm{eff}} = H_{cc} + \Omega_p$,

$$\exp\left[-\beta F'\right] = \frac{1}{\lambda_c N_c!} \int \mathrm{d}\mathbf{r}_c^{N_c} \exp\left(-\beta H_{\mathrm{eff}}\right). \tag{5.9}$$

Furthermore, since the polymers are non–interacting, the exponential in Eq. (5.8) factorizes into N_p identical terms and the grand potential of the polymers may be written as

$$
\begin{aligned}
-\beta\Omega_p &= \ln\left\{\sum_{N_p=0}^{\infty} \frac{z_p^{N_p}}{\lambda_p^{3N_p} N_p!} \left(\int \mathrm{d}\mathbf{r}_p \exp\left[-\beta \sum_{i=1}^{N_c} \phi_{cp}\left(|\mathbf{r}_{c,i} - \mathbf{r}_p|\right)\right]\right)^{N_p}\right\} \\
&= \frac{z_p}{\lambda_p^3} \int \mathrm{d}\mathbf{r}_p \exp\left[-\beta \sum_{i=1}^{N_c} \phi_{cp}\left(|\mathbf{r}_{c,i} - \mathbf{r}_p|\right)\right] \\
&= \rho_{p,r} \int \mathrm{d}\mathbf{r}_p \prod_{i=1}^{N_c} \exp\left[-\beta \phi_{cp}\left(|\mathbf{r}_{c,i} - \mathbf{r}_p|\right)\right], \tag{5.10}
\end{aligned}
$$

where in the last step we have used the definition of $\rho_{p,r}$ from Eq. (5.4). We can expand the integrand of Eq. (5.10) in terms of the colloid–polymer Mayer–f functions,

$$f_i = \exp\left[-\beta\phi_{cp}(|\mathbf{r}_{c,i} - \mathbf{r}_p|)\right] - 1. \tag{5.11}$$

Note that as the colloid–polymer interaction is of hard sphere type, the Mayer–f function is 0 as long as the particles do not see each other, and is -1 when they overlap. The expansion of the polymers' grand potential in terms of Mayer–f functions is given as follows,

$$
\begin{aligned}
-\beta\Omega_p &= \rho_{p,r} \int \mathrm{d}\mathbf{r}_p \prod_{i=1}^{N_c} (1 + f_i) \\
&= \rho_{p,r} \int \mathrm{d}\mathbf{r}_p + \rho_{p,r} \sum_{i=1}^{N_c} \int \mathrm{d}\mathbf{r}_p f_i + \rho_{p,r} \sum_{i=1}^{N_c-1} \sum_{j>i}^{N_c} \int \mathrm{d}\mathbf{r}_p f_i f_j + \cdots \tag{5.12}
\end{aligned}
$$

The integral in the first term is the volume of the system, which gives the grand free energy of the polymer ideal gas in the absence of the colloids. In the second term, the integral is the total excluded volume of N_c non–interacting colloidal hard spheres in the system. The polymers are free to move in this "swiss cheese" made by colloids. The integrand of the third term, is the product of two Mayer–f functions and is non–zero only for polymers which interact simultaneously with both of the corresponding colloid particles. This is equivalent to the overlap of excluded volumes of colloids i and j (see Fig. 5.1). Hence, $\rho_{p,r}$ times this excluded volume is the attractive part of the effective AO potential $\phi_{AO}^{att}(r)$ between colloids i and j [2]. Therefore,

$$
\begin{aligned}
\beta\Omega_p &= \beta\Omega_{p,0} + \beta\Omega_{p,1} + \beta\Omega_{p,2} + \cdots , \\
\text{with} \quad \beta\Omega_{p,0} &= -\rho_{p,r}V \\
\beta\Omega_{p,1} &= \rho_{p,r}N_c\frac{4\pi}{3}(R_c + R_p)^3 = \rho_{p,r}\eta_c(1+q)^3V \\
\beta\Omega_{p,2} &= \sum_{i=1}^{N_c-1}\sum_{j>i}^{N_c}\beta\phi_{AO}^{att}(|\mathbf{r}_{c,i} - \mathbf{r}_{c,j}|).
\end{aligned}
\tag{5.13}
$$

Moreover, the first two terms in the expansion of $\beta\Omega_p$ do not affect determination of thermodynamic properties of colloids, e.g. phase coexistence densities, as these terms are either constant or linear in the colloid density. Therefore, in order to obtain an effective free energy volume density βf_{eff} for colloids these terms may be subtracted with no harm.

$$
\beta f_{eff} = \beta f' - \rho_{p,r}\left(-1 + \eta_c(1+q)^3\right).
\tag{5.14}
$$

Here, f' is the volume density of the Helmholtz free energy given by Eq. (5.9).

In the next section free volume theory is introduced as a successful model for studying AO model in bulk fluid and its relation to the effective Hamiltonian which is derived here is discussed.

5.2 Free Volume Theory

One of the well-known theoretical tools for studying the AO-Model is free volume theory which has been introduced by Lekkerkerker et al. [105]. In the framework of this theory, the Helmholtz free energy density of the system whose physical volume is V is decomposed into two independent terms; the hard sphere free energy density of colloids f_c, and the ideal gas free energy density of the polymers f_p^{id}. The latter is

---

[2] $\phi_{AO}^{att}(r) = \phi_{AO}(r)$ from Eq. (5.2) with $\sigma_c \leq r \leq \sigma_c + \sigma_p$.

calculated while N_p polymer chains are assumed to move freely in the sub–volume of the system which is not occupied by the colloids. This colloid–free volume is expressed as the product of the free volume fraction α and the total volume of the system V. The expressions for the free energy densities in the context of free volume theory is given as follows.

$$
\begin{aligned}
f_{\mathrm{FV}}(\rho_\mathrm{c}, \rho_\mathrm{p}) &= f_\mathrm{c}(\rho_\mathrm{c}) + f_\mathrm{p}^{\mathrm{id}}(N_\mathrm{p}, \alpha V) \\
f_\mathrm{p}^{\mathrm{id}}(N_p, \alpha V) &= \rho_\mathrm{p}\left[\ln\left(\frac{\rho_\mathrm{p}\lambda_\mathrm{p}^3}{\alpha}\right) - 1\right]
\end{aligned}
\tag{5.15}
$$

where $\rho_\mathrm{c} = N_c/V$ is the colloid number density and $\rho_\mathrm{p} = N_p/V$ is the polymer number density.

One can use the ideas of the scaled–particle theory (Section 3.2.3) to obtain the free volume fraction α of the system by considering two extreme limits for the polymer size, $R_\mathrm{p} \ll R_\mathrm{c}$ and $R_\mathrm{p} \to \infty$. The corresponding mid–range values of R_p are extrapolated from these two limits [6, 54, 55]. For the small polymer size $R_\mathrm{p} \ll R_\mathrm{c}$, the probability of finding a cavity with radius R_p due to the spontaneous fluctuation of the colloids within the system can be expressed as the exponential of minus the excess chemical potential, i.e. the required reversible work for creating such a cavity. Note that, in the limit of $\rho_\mathrm{p} \to 0$ this probability is equivalent to the free volume fraction of the system.

$$
\lim_{\rho_\mathrm{p}\to 0} \alpha(\rho_\mathrm{c}) = p_{\mathrm{cav}}(R_\mathrm{p}) = \exp(-\beta\mu^{\mathrm{ex}}) .
\tag{5.16}
$$

This is the same as the probability of existence of a cavity of size $R_\mathrm{p} + R_\mathrm{c}$ in which the *centers* of the colloids are not allowed. Now, we can extend Eq. (5.16) to negative polymer sizes $-R_\mathrm{c} \le R_\mathrm{p} \le 0$ by considering cavities with radius $0 \le R_\mathrm{c} + R_\mathrm{p} \le R_\mathrm{c}$. The probability of finding a colloid in this cavity p_{occ}, and therefore not being able to put a polymer in it $1 - p_{\mathrm{cav}}$, is equal to its volume times the colloid density. Therefore, using Eq. (5.16) one can write,

$$
\beta\mu^{\mathrm{ex}}(R_\mathrm{p}) = -\ln(\alpha) = -\ln\left(1 - \frac{4}{3}\pi(R_\mathrm{c} + R_\mathrm{p})^3 \rho_\mathrm{c}\right) \quad \text{for } R_\mathrm{p} \le 0 .
\tag{5.17}
$$

On the other hand, the required reversible work for creating a large cavity of size $R_\mathrm{p} \gg R_\mathrm{c}$ is equal to the size of the cavity times the pressure of the colloids.

$$
\beta\mu^{\mathrm{ex}}(R_\mathrm{p}) = \frac{4}{3}\pi R_\mathrm{p}^3 P \quad \text{for } R_\mathrm{p} \gg R_\mathrm{c} .
\tag{5.18}
$$

The essential ansatz in relating these two limits is that for $R_\mathrm{p} \ge 0$ the excess chemical potential is related to the size of the cavity R_p via its fundamental measures (see

Eq. (4.5)).

$$\mu^{\mathrm{ex}}(R_{\mathrm{p}}) \;=\; \frac{4}{3}\pi R_{\mathrm{p}}^3\, P + 4\pi R_{\mathrm{p}}^2\, \gamma + 4\pi R_{\mathrm{p}}\, \kappa + 1\, \bar{\kappa} \quad \text{for } R_{\mathrm{p}} \geq 0 \,. \tag{5.19}$$

The undetermined coefficients, γ, κ, and $\bar{\kappa}$, are obtained by requiring the continuity of μ^{ex} and its derivatives at $R_{\mathrm{p}} = 0$ for $R_{\mathrm{p}} \leq 0$ (Eq. (5.17)) and $R_{\mathrm{p}} \geq 0$ (Eq. (5.19)). Denoting the packing fraction of colloids by η_{c}, these requirements are met as follows.

$$\beta\bar{\kappa} \;=\; -\ln(1 - \eta_{\mathrm{c}}) \,. \tag{5.20}$$

$$4\pi\beta\kappa \;=\; \frac{1}{R_{\mathrm{c}}}\frac{3\eta_{\mathrm{c}}}{1 - \eta_{\mathrm{c}}} \,. \tag{5.21}$$

$$4\pi\beta\gamma \;=\; \frac{1}{R_{\mathrm{c}}^2}\left(\frac{3\eta_{\mathrm{c}}}{1 - \eta_{\mathrm{c}}} + \frac{9\eta_{\mathrm{c}}^2}{2(1 - \eta_{\mathrm{c}})^2}\right) \,. \tag{5.22}$$

Furthermore, since $\rho_{\mathrm{p}} \to 0$ the colloids may be assumed to be the only component of the system. Therefore, the pressure βP can be replaced by the expression for the scaled–particle equation of state for a single–component hard sphere system, i.e. the Percus–Yevick compressibility equation of state Eq. (3.18).

$$\frac{\beta P}{\rho_{\mathrm{c}}} \;=\; \frac{1 + \eta_{\mathrm{c}} + \eta_{\mathrm{c}}^2}{(1 - \eta_{\mathrm{c}})^3} \,. \tag{5.23}$$

The obtained thermodynamic coefficients, i.e. $\beta\bar{\kappa}$, $\beta\kappa$, $\beta\gamma$, and βP from Eq. (5.20) to Eq. (5.23) are used to calculate the excess chemical potential μ^{ex} for $R_{\mathrm{p}} \geq 0$ (Eq. (5.19)). As a result, the free volume fraction of the system which is given by Eq. (5.17) for $\rho_{\mathrm{p}} \to 0$ reads

$$\alpha(\rho_{\mathrm{c}}) = (1 - \eta_{\mathrm{c}})\exp\left(-A\gamma - B\gamma^2 - C\gamma^3\right) \,, \qquad \text{with} \quad \gamma = \frac{\eta_{\mathrm{c}}}{1 - \eta_{\mathrm{c}}} \,,$$
$$A = 3q + 3q^2 + q^3 \,,$$
$$B = \frac{9}{2}q^2 + 3q^3 \,,$$
$$C = 3q^3 \,. \tag{5.24}$$

The obtained free volume fraction is used to calculate the ideal gas free energy density of the polymers $f_{\mathrm{p}}^{\mathrm{id}}$ and consequently the free energy density of the colloid–polymer mixture f_{FV} from Eq. (5.15). But as mentioned earlier, it is more convenient to use a semi–grand ensemble for such a mixture. In this ensemble a semi–grand free energy density is defined as

$$f_{\mathrm{FV}}'(\rho_{\mathrm{c}}, \mu_{\mathrm{p}}) = f_{\mathrm{FV}}(\rho_{\mathrm{c}}, \rho_{\mathrm{p}}) - \mu_{\mathrm{p}}\rho_{\mathrm{p}}. \tag{5.25}$$

The polymer equilibrium density minimizes the semi–grand free energy density. Using Eqs. (5.15) and (5.25) we can write,

$$
\begin{aligned}
\frac{\partial f'_{\mathrm{FV}}}{\partial \rho_{\mathrm{p}}} &= \frac{\partial f_{\mathrm{p}}^{\mathrm{id}}}{\partial \rho_{\mathrm{p}}} - \mu_{\mathrm{p}} \overset{!}{=} 0 \\
\Rightarrow \rho_{\mathrm{p}} &= \alpha(\rho_{\mathrm{c}})\rho_{\mathrm{p,r}}
\end{aligned}
\tag{5.26}
$$

where $\rho_{\mathrm{p,r}}$ is the reservoir polymer density (Eq. (5.4)). Finally, we can rewrite the semi–grand free energy density by combining Eqs. (5.15), (5.25), and (5.26).

$$
\beta f'_{\mathrm{FV}}(\rho_{\mathrm{c}}, \mu_{\mathrm{p}}) = \beta f_{\mathrm{c}}(\rho_{\mathrm{c}}) - \alpha(\rho_{\mathrm{c}})\rho_{\mathrm{p,r}},
\tag{5.27}
$$

Once the chemical potential of the polymer reservoir is specified, $\beta f'_{\mathrm{FV}}$ is solely a function of the colloid density ρ_{c}. This is a convenient relation for determination of the phase coexistence densities of the colloidal particles. For obtaining the coexistence densities, the pressure of the system in two phases should be equated as well as the chemical potential of colloids and polymers. As the chemical potential of the polymers is already fixed at its reservoir value, the problem is reduced to determination of the coexistence densities for a one–component system. Comparing the free energy density proposed by free volume theory in Eq. (5.15) with Eq. (5.14), $\beta f'_{\mathrm{FV}}$ misses a constant and a term linear in packing fraction of colloidal particles corresponding to $\Omega_{\mathrm{p,0}}$ and $\Omega_{\mathrm{p,1}}$ (see Eq. (5.13)). Adding these missing terms does not affect the phase coexistence determination. Therefore, the effective free energy density for colloids is defined as

$$
\begin{aligned}
\beta f_{\mathrm{eff}}(\rho_{\mathrm{c}}, \mu_{\mathrm{p}}) &= \beta f_{\mathrm{c}}(\rho_{\mathrm{c}}) + \rho_{\mathrm{p,r}}\left(-1 + \eta_{\mathrm{c}}(1+q)^3\right) - \rho_{\mathrm{p,r}}\alpha(\rho_{\mathrm{c}}) \\
&= \beta f_{\mathrm{c}}(\rho_{\mathrm{c}}) + \beta f_{\mathrm{eff,att}}(\rho_{\mathrm{c}}, \mu_{\mathrm{p}}) \;.
\end{aligned}
\tag{5.28}
$$

Motivated by this decomposition of the effective free energy density of colloids into a pure hard sphere part and an attractive term, we will use a *naive mean–field approach* in which the attractive term is related to the effective two–body potential ϕ_{AO} (*Eq.* (5.2)) via a virial expansion.

$$
f_{\mathrm{eff,att}}(\rho_{\mathrm{c}}, \mu_{\mathrm{p}}) \approx \frac{1}{2}b_2^{\mathrm{att}}\rho_{\mathrm{c}}^2 + \cdots ,
\tag{5.29}
$$

$$
b_2^{\mathrm{att}} = \int \mathrm{d}\mathbf{r}\; \phi_{\mathrm{AO}}(r)\theta(r - \sigma_{\mathrm{c}}) \;.
\tag{5.30}
$$

The virial coefficient b_2^{att} is calculated by a volume integral over the attractive part of ϕ_{AO} using the Heaviside step function $\theta(x)$. This method works reasonably well for simple fluids like the Lennard–Jones fluid whose attractive range is not as short as in ϕ_{AO}. However, in the case of the AO model, the naive mean–field approach does not
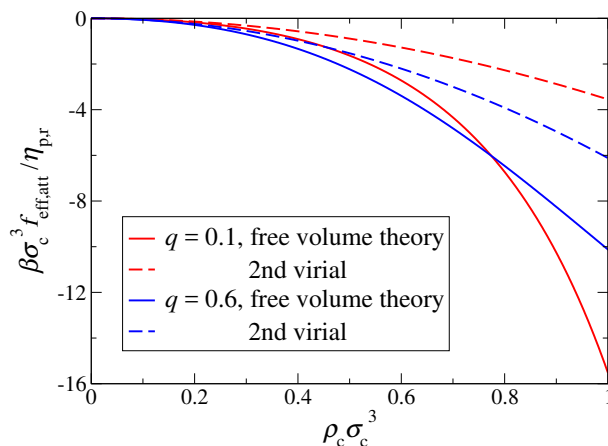
Figure 5.4: Effective free energy density of attraction between colloids "per polymer" for two different size ratios $q = 0.1$ (red) and 0.6 (blue). Full lines correspond to free volume theory, dashed lines to the virial expansion to second order (naive mean field approximation). For higher densities, the naive mean field approximation underestimates the attractive part of the effective free energy density.

work very well. This is shown in Fig. 5.4 in which $f_{\text{eff,att}}$ from free volume theory is compared with the naive mean–field approach for size ratios $q = 0.1$ and $q = 0.6$. In both cases the difference increases with the colloid density. However, the difference is worse for $q = 0.1$ which corresponds to a shorter ranged effective attraction between the colloidal particles.

In free volume theory, the effective colloid free energy density (Eq. (5.28)) is linear in $\rho_{\text{p,r}}$. Therefore, any viral coefficient related to $\rho_{\text{p,r}}^n$ with $n \geq 2$ is zero. This is not true for the full AO model as it is shown in the evaluation of the first few virial coefficients and their relation to the effective attraction [118]. Nevertheless, $f_{\text{eff,att}}$ from free volume theory is a very good approximation also for higher $\rho_{\text{p,r}}$ as a comparison with simulations shows [109][3].

The effective attraction leads to vapor–liquid phase separation as has been calculated first in Ref. [105] and discussed in a number of subsequent papers. Fluid–crystal phase separation has been discussed by using Eq. (5.24) for the fluid and crystal phases and using a hard–sphere equation of state for the crystal [105] or perturbation theory [110, 117].

---

[3]There, a comparison for $q = 1.0$ is shown in their Fig. 4. Their attractive free energy density f_{att} is defined without subtraction, i.e. the relation to our $f_{\text{eff,att}}$ is given by $\beta f_{\text{eff,att}} = 6/\pi[\beta f_{\text{att}} + (\eta_{\text{p,r}}/q^3)(1 - \eta_{\text{c}}(1 + q)^3)]$

5.3   Fundamental Measure Theory for the AO–model

In order to take advantage of FMT for investigating the AO–model, consider a non–additive binary hard sphere mixture while assigning the species 1 to the colloids and species 2 to the polymers. In the physical volume V, the system contains $N_1 = N_c$ colloids and $N_2 = N_p$ polymers and its grand potential functional reads

$$\Omega_{AO}[\rho_c, \rho_p] = \mathcal{F}_{AO}^{id}[\rho_c, \rho_p] + \mathcal{F}_{AO}^{ex}[\rho_c, \rho_p] - \sum_{i=1}^{2} \int d\mathbf{r} \, \rho_i(\mathbf{r}) \left(\mu_i - V_i^{ext}(\mathbf{r}) \right) , \qquad (5.31)$$

where μ_i and V_i^{ext} are respectively the chemical potential and the external potential for species i. The ideal gas Helmholtz free energy of this 2–component system $\mathcal{F}_{AO}^{id}$ is written as the sum of the ideal gas contribution of each species.

$$\begin{aligned}
\mathcal{F}_{AO}^{id}[\rho_c, \rho_p] &= \mathcal{F}_c^{id}[\rho_c] + \mathcal{F}_p^{id}[\rho_p] \\
\mathcal{F}_\alpha^{id}[\rho_\alpha] &= \int d\mathbf{r} \, \rho_\alpha(\mathbf{r}) \left(\ln \left(\lambda_\alpha^3 \rho_\alpha(\mathbf{r}) \right) - 1 \right) .
\end{aligned} \qquad (5.32)$$

Here, λ_α is the thermal de Broglie wavelength of species α. The excess free energy functional $\mathcal{F}_{AO}^{ex}$ is written as the volume integral of the excess free energy density which is a function of the local weighted densities. The latter is given by the sum of the local weighted density of each species as we have a non–additive system.

$$\mathcal{F}_{AO}^{ex}[\rho_c, \rho_p] = \int d\mathbf{r} \, \Phi_{AO}\left(\{n_\alpha\}\right), \qquad \text{with} \quad \begin{aligned} n_\alpha &= n_{\alpha,c} + n_{\alpha,p}, \\ n_{\alpha,i} &= \rho_i * w_i^\alpha. \end{aligned} \qquad (5.33)$$

Here, $*$ denotes the 3D convolution. The weight functions for each species w_i^α are given by Eq. (4.4) and/or Eq. (4.31) depending on the functional in use. The proper excess free energy density for a colloid–polymer mixture described by the AO model is obtained by an appropriate linearization of the hard sphere mixture functional Φ_{HS} in terms of the polymer density ρ_p [111].

$$\Phi_{AO}\left(\{n_{\alpha,c}\}, \{n_{\alpha,p}\}\right) = \Phi_{HS}\left(\{n_{\alpha,c}\}\right) + \sum_\alpha n_{\alpha,p} \frac{\partial \Phi_{HS}\left(\{n_{\alpha,c}\}\right)}{\partial n_{\alpha,c}} \qquad (5.34)$$

The proposed density functional delivers the desired properties of the colloid–polymer mixture. By removing the polymers from the system ($n_{\alpha,p} = 0$), the excess free energy density of the HS is recovered. Moreover, the functional is linear in ρ_p and the polymer–polymer direct pair correlation function is zero,

$$c_{pp}^{(2)}(|\mathbf{r}_i - \mathbf{r}_j|) = -\frac{\delta^2 \mathcal{F}_{AO}^{ex}}{\delta \rho_p(\mathbf{r}_i) \delta \rho_p(\mathbf{r}_j)} = 0 \qquad (5.35)$$

This is indeed expected as the polymers are assumed to behave as an ideal gas in the AO model.

For building up the functional in a more systematic approach, one can adopt the ideas of the dimensional cross over explained in Section 4.2. In this case the 0D free energy is given by [111],

$$\Phi_{0D}^{AO} = \eta_c + \ln(1 - \eta_c)(1 - \eta_c - \eta_p) \,, \tag{5.36}$$

where η_c and η_p respectively denote the packing fraction of the colloidal particles and of the polymers. Since the functional in higher dimensions is constructed by a series of derivatives with respect to ρ_i and multiplications by ρ_i, the resulting 3D functional remains linear in the polymer density ρ_p. For instance the first two terms of the functional which are given for a one–component hard sphere syatem in Eqs. (4.29) and (4.30), are modified in the following way to be applied to a binary mixture [111].

$$\Phi_1^{AO} = -\sum_{i=c,p} \int d\mathbf{r}\, n_{0,i}(\mathbf{r})\psi_i\left(n_{3,c}(\mathbf{r}), n_{3,p}(\mathbf{r})\right) \,,$$

$$\Phi_2^{AO} = -\sum_{i=c,p} \int d\mathbf{r}\, \left(n_{1,i}n_{2,j} - \mathbf{n}_{1,i}\cdot\mathbf{n}_{2,j}\right)\psi_{ij}\left(n_{3,c}(\mathbf{r}), n_{3,p}(\mathbf{r})\right) \,,$$

$$\text{with } \psi_i(\eta_c, \eta_p) =: \frac{\partial\Phi_{0D}^{AO}}{\partial\eta_i} \,, \quad \psi_{ij}(\eta_c, \eta_p) =: \frac{\partial^2\Phi_{0D}^{AO}}{\partial\eta_i\partial\eta_j} \tag{5.37}$$

Note that the terms in the sum with polymer weighted density are multiplied by a derivative of 0D excess free energy density (Eq. (E.12)) with respect to polymer packing fraction. Since Φ_{0D}^{AO} is linear in η_p, this product remains linear in polymer density. Moreover, this linear property of the excess free energy density may be rationalized in the context of the scaled–particle theory (Section 3.2.3) as follows. Here, the scaled–particle differential equation corresponding to the required reversible work for introducing a polymer coil into a suspension of the colloids is given by,

$$\lim_{\rho_p\to 0}\frac{\beta\mu_p^{ex}}{V_p} = \frac{\partial\Phi_{AO}}{\partial\xi_3} \qquad \text{with} \quad \xi_3 = \sum_{i=1}^{2}\rho_i V_i = \eta_c + \eta_p \tag{5.38}$$

This relation must also hold for higher values of ρ_p since in the AO model the system is assumed to be coupled to a polymer reservoir which maintains the polymer chemical potential at a fixed $\mu_{p,r}$. This is achieved if Φ_{AO} contains only constant and linear terms in ρ_p as it is proposed in Eq. (5.34).

In a semi–grand ensemble with a given μ_p and in the absence of external potential, the appropriate quantity for minimization is,

$$\mathcal{F}'_{AO}[\rho_c, \rho_p] = \mathcal{F}^{id}[\rho_c, \rho_p] + \mathcal{F}^{ex}_{AO}[\rho_c, \rho_p] - \mu_p\int d\mathbf{r}\,\rho_p(\mathbf{r})\,. \tag{5.39}$$

Note that minimization of $\mathcal{F}'_{\text{AO}}$ and the grand potential functional from Eq. (5.31) with respect to ρ_{p} are equivalent. The equilibrium polymer density $\rho_{\text{p,eq}}$ is obtained by such minimization.

$$\frac{\delta \mathcal{F}'_{\text{AO}}\left[\rho_{\text{c}}, \rho_{\text{p}}\right]}{\delta \rho_{\text{p}}(\mathbf{r})}\Bigg|_{\rho_{\text{p}}(\mathbf{r})=\rho_{\text{p,eq}}(\mathbf{r})} \overset{!}{=} 0$$

$$\Rightarrow \rho_{\text{p,eq}}(\mathbf{r}) = \rho_{\text{p,r}} \exp\left[-\int d\mathbf{r}' \sum_{\alpha} \frac{\partial \Phi_{\text{HS}}}{\partial n_{\alpha,\text{c}}}(\mathbf{r})\, w_{\text{p}}^{\alpha}(\mathbf{r}'-\mathbf{r})\right]$$

$$= \rho_{\text{p,r}} \exp\left[c_{\text{p}}^{(1)}\left(\rho_{\text{c}}(\mathbf{r})\right)\right]. \tag{5.40}$$

Here $c_{\text{p}}^{(1)}$ is a polymeric direct correlation function which is only function of the colloid density. Therefore, after fixing the polymer reservoir chemical potential $\mu_{\text{p,r}}$, the equilibrium polymer density is explicitly known for a given colloid density $\rho_{\text{c}}(\mathbf{r})$. By comparing Eq. (5.40) for the bulk fluid with Eq. (5.26), we can define an FMT free volume fraction.

$$\alpha_{\text{FMT}} = \exp(c_{\text{p}}^{(1)}) \tag{5.41}$$

The free volume fraction in the bulk, calculated by this relation, is exactly the one from free volume theory (Eq. (5.24)) if the Rosenfeld excess free energy density (Eq. (4.18)) is used as the underlying hard sphere functional for linearization (Φ_{HS} in Eq. (5.34)). This is indeed expected as both theories are based on the scaled particle theory formalism.

The effective free energy functional for colloids $\mathcal{F}_{\text{eff}}$ is obtained by subtracting the non-trivial constant and linear term in the colloid density $\beta\Omega_0 + \beta\Omega_1$ (Eq. (5.13)) from $\mathcal{F}'_{\text{AO}}$. The latter is evaluated with $\rho_{\text{p,eq}}$ from Eq. (5.40). This effective free energy is decomposed into a hard sphere and an effective attractive term and reads [17]

$$\beta\mathcal{F}_{\text{eff}}\left[\rho_{\text{c}}(\mathbf{r}); \mu_{\text{p,r}}, q\right] = \beta\mathcal{F}_{\text{HS}}\left[\rho_{\text{c}}(\mathbf{r})\right] + \beta\mathcal{F}_{\text{eff,att}}\left[\rho_{\text{c}}(\mathbf{r}); \mu_{\text{p,r}}, q\right], \tag{5.42}$$

$$\beta\mathcal{F}_{\text{HS}}\left[\rho_{\text{c}}(\mathbf{r})\right] = \int d\mathbf{r}\, \rho_{\text{c}}(\mathbf{r})\left(\ln\left[\rho_{\text{c}}(\mathbf{r})\lambda_{\text{c}}^3\right]-1\right) + \int d\mathbf{r}\, \Phi_{\text{HS}}\left(n_{\text{c}}^{\alpha}(\mathbf{r})\right),$$

$$\beta\mathcal{F}_{\text{eff,att}}\left[\rho_{\text{c}}(\mathbf{r}); \mu_{\text{p,r}}, q\right] = \rho_{\text{p,r}}\int d\mathbf{r}\left(-e^{c_{\text{p}}^{(1)}(\mathbf{r})} + \left(1-\eta_{\text{c}}\left(1+q\right)^3\right)\right). \tag{5.43}$$

Moreover, considering the discussion on the naive mean field approximation for the bulk fluid (see Section 5.2 page 80), we can assume that $\mathcal{F}_{\text{eff,att}}$ is related to the attractive part of the AO pair potential $\phi_{\text{AO}}^{\text{att}}$ (Eq. (5.2) with $r > \sigma_{\text{c}}$) via a virial expansion for the non–homogeneous state.

$$\beta\mathcal{F}_{\text{eff,att}}\left[\rho_{\text{c}}(\mathbf{r}); \mu_{\text{p,r}}, q\right] \approx \frac{1}{2}\int d\mathbf{r}\int d\mathbf{r}'\, \rho_{\text{c}}(\mathbf{r})\rho_{\text{c}}(\mathbf{r}')\beta\phi_{\text{AO}}^{\text{att}}(|\mathbf{r}-\mathbf{r}'|; \mu_{\text{p,r}}, q), \tag{5.44}$$

This relation is used as the *naive mean–field approximation* for the FMT functional. The mean–field approximation is often applied to the Lennard–Jones system which decomposes the free energy functional into a pure hard–sphere part and a perturbation in the form of a weighted density approximation of the attractive part. The method is quite successful at describing the liquid–solid phase equilibria and the corresponding interfacial tensions [119].

5.4 Bulk Crystals in the AO–Model

For obtaining the equilibrium free energy for the homogeneous crystalline state in the AO–model, we have assumed an fcc crystalline structure for the solid state of the colloids with a denoting the side length of the cubic unit cell as in the case of pure hard spheres (see Section 4.5). The number of colloid particles in an ideal fcc unit cell is 4, but here we will assume a non-vanishing vacancy concentration n_{vac}, which results in $4(1 - n_{\mathrm{vac}})/a^3$ being the number density of colloid particles. The colloid density profile is initialized by Gaussian peaks at the fcc lattice sites.

$$\rho_{\mathrm{c}}\left(\mathbf{r}\right) = \sum_i \left(1 - n_{\mathrm{vac}}\right) \left(\frac{\alpha_{\mathrm{G}}}{\pi}\right)^{\frac{3}{2}} \exp\left(-\alpha_{\mathrm{G}}|\mathbf{r} - \mathbf{r}_i|^2\right). \tag{5.45}$$

After choosing the reference excess free energy density of the hard spheres Φ_{HS}, the polymer density profile is obtained by Eq. (5.40) and the effective free energy of the colloids is then calculated from Eq. (5.43). In constrained minimization, the effective free energy, or equivalently F', is minimized with respect to α_{G} and n_{vac}.

$$F'_{\mathrm{eq}}\left(\eta_{\mathrm{p,r}}, q\right) = \min_{\{n_{\mathrm{vac}}, \alpha_{\mathrm{G}}\}} \mathcal{F}'\left[\rho_{\mathrm{c}}, \rho_{\mathrm{p,eq}}[\rho_{\mathrm{c}}]\right]. \tag{5.46}$$

For the full minimization, the colloid density profile is initiated as Gaussian peaks with α_{G} obtained from the constrained minimization and a reasonably small n_{vac}, e.g. $\sim 2 \times 10^{-4}$. After computing $\rho_{\mathrm{p,eq}}$ from Eq. (5.40), the colloid density profile is updated according to,

$$\log \lambda_{\mathrm{c}}^3 \rho_{\mathrm{c}} = -\frac{\delta \mathcal{F}^{\mathrm{ex}}\left[\rho_{\mathrm{c}}; \rho_{\mathrm{p}}[\rho_{\mathrm{c}}]\right]}{\delta \rho_{\mathrm{c}}} - \mu_{\mathrm{c}}. \tag{5.47}$$

This self–consistent process, known as Picard iteration[4], leads to the simultaneous minimization of the effective free energy density F' with respect to ρ_{p} and ρ_{c}. In order to

---

[4]See Appendix A.4.1 for more information.

obtain the global minimum of F', the minimization procedure is re–initiated with an updated n_{vac}.

$$F'_{\mathrm{eq}}\left(\eta_{\mathrm{p,r}}, q\right) = \min_{\{n_{\mathrm{vac}}\}} \min_{\{\rho_{\mathrm{c}}(\mathbf{r})\}} \mathcal{F}'\left[\rho_{\mathrm{c}}, \rho_{\mathrm{p,eq}}[\rho_{\mathrm{c}}]\right]. \tag{5.48}$$

The obtained values for the equilibrium vacancy concentration using the constrained minimization (Eq. (5.46)) of the linearized FMT functionals are of order $\lesssim 10^{-4}$. On the other hand, the difference between the obtained effective free energy from constrained and full minimization is small (see Fig. 5.15). Therefore, as in Ref. [17] the focus of the results section is on constrained minimization. In Section 5.4.1, using the linearized WBII(tensor) functional the effective free energy for colloids is obtained by constrained minimization. The main purpose of Section 5.4.3 is to address two questions about the polymer density: Where do polymers sit in the fcc unit cell? And what is the effect of the polymer–colloid size ratio? Using the effective free energy of colloidal particles, their phase diagram is computed and discussed in Section 5.4.2. Section 5.4.4 is dedicated to full minimization results of the effective free energy, its difference with the constrained minimization, and the effect of this difference on the equilibrium properties, e.g. the phase behavior. Finally, in Section 5.4.5 the obtained results from the linearized RF(tensor) functional are compared with those from the linearized WBII(tensor) functional.

5.4.1   Effective free energy of the colloid crystals

For a certain range of colloid–polymer size ratios q, polymer reservoir packing fractions $\eta_{\mathrm{p,r}}$, and colloid bulk number densities ρ_{c}, we have calculated the effective free energy density for the crystalline state by constrained minimization with respect to α_{G} and n_{vac}, and for the homogeneous fluid state. The calculation is done using the linearized version of two type of functionals, RF(tensor) functional whose underlying equation of state for fluid is Percus–Yevick (Section 4.2) and WBII(tensor) functional with the more accurate Carnahan–Starling equation of state (Section 4.3). Due to different underlying equation of states, there is a difference between the effective free energy densities obtained by these functionals. This difference becomes more significant as q decreases. For a more detailed discussion see Section 5.4.5.

We have shown the free energy curves $\beta f_{\mathrm{eff}}(\rho_{\mathrm{c}})\sigma_{\mathrm{c}}^3$ for fixed values of $\eta_{\mathrm{p,r}}$ (isotherms) obtained by constrained minimization of the linearized WBII(tensor) functional in Fig. 5.5 for three different size ratios, i.e. $q = 0.6, 0.4, 0.1$. The free energy curves are qualitatively reminiscent to those of a simple fluid, Lennard-Jones for instance [120]. Here, by decreasing the polymer–colloid size ratio q the attractive part of the pair interaction becomes stronger. The polymer reservoir packing fraction $\eta_{\mathrm{p,r}}$ acts as an inverse tem-
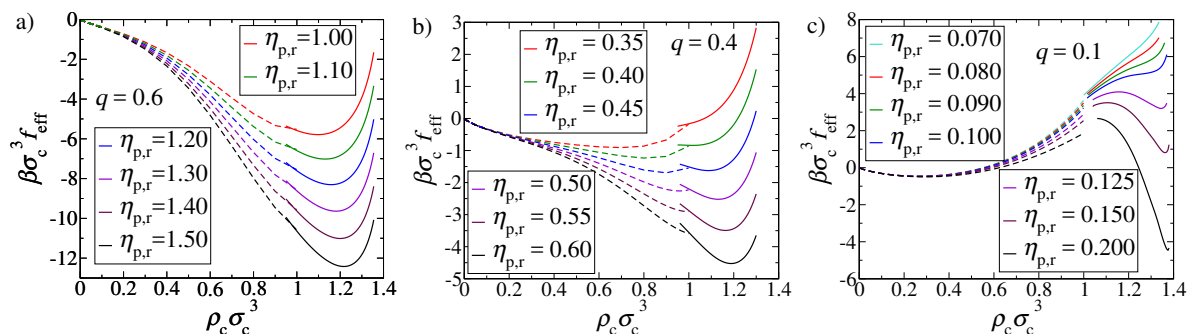
Figure 5.5: Comparison of the effective free energy density $\beta\sigma_c^3 f_{\text{eff}}(\rho_c)$ for different values of the reservoir polymer packing fraction $\eta_{\text{p,r}}$ ("isotherms") and for three different values of the polymer–colloid size ratios (a) $q = 0.6$, (b) $q = 0.4$, and (c) $q = 0.1$. The results for the homogeneous fluid branch (dashed curves) are obtained using the linearized WBII(tensor) functional. The effective free energy for crystal branch (solid curves) is computed by constrained minimization of the same functional with respect to α_G and n_{vac}. The thermal de Broglie wavelength λ_c is set to σ_c.

perature and by its increment (decreasing temperature) the effective attraction due to polymers increases which results in more negative values for the crystal free energies.

For a better understanding of the effect of polymers on the attractive part of the effective free energy, we use the expression of free volume theory, Eq. (5.28), as a crude approximation for the crystal. Here, we will calculate the excluded volume for an ideal fcc crystal in which the colloids are fixed at their lattice sites. The free volume fraction is calculated in different geometrical situations which arises due to increasing bulk number density of the colloids and consequently decreasing fcc lattice constant $a = (4/\rho_c)^{1/3}$. For a given q, the colloid densities may be divided in four ranges representing four different types of excluded volume overlaps:

(i) $\rho_c\sigma_c^3 \leq \sqrt{2}/(1+q)^3$: The distance between the nearest neighbors in the fcc unit cell $r_{\text{nn}} = \frac{a\sqrt{2}}{\sqrt{2}}$ is larger than diameter of the exclusion spheres. Therefore, the exclusion spheres do not have any overlap and the free volume fraction is simply given by $\alpha = 1 - \eta_c(1+q)^3$. Consequently, the attractive part of the effective free energy $f_{\text{eff,att}}$ is zero.

(ii) $\rho_c\sigma_c^3 \in [\sqrt{2}/(1+q)^3, 2/(1+q)^3]$: The exclusion spheres of the colloidal particles sitting at the nearest neighbors lattice sites in the fcc unit cell have an overlap which can be expressed as a function of their distance. Hence, the free volume fraction is

$$\alpha = 1 - \eta_c(1+q)^3\left[1 - 6\left(1 - \frac{3}{2}r' + \frac{1}{2}r'^3\right)\right] \qquad \text{with } r' = \frac{a}{\sqrt{2}(1+q)\sigma_c} \quad (5.49)$$

Using Eq. (5.28) the attractive part of the effective free energy density is given by,

$$\beta f_{\text{eff,att}} \sigma_c^3 = -6\rho_c \eta_{\text{p,r}} \left(1 + \frac{1}{q} \right)^3 \left(1 - \frac{3r'}{2} + \frac{r'^3}{2} \right) , \tag{5.50}$$

where r' is the same as introduced in Eq. (5.49).

(iii) $\rho_c \sigma_c^3 \in [2/(1+q)^3, 4/(1+q)^3]$: Four–body overlaps of the exclusion spheres occur between each colloid sitting at a corner of fcc unit cell with the ones at the center of its adjacent faces. In this case, we have determined numerical values for the free volume fraction and consequently the attractive part of the effective free energy density is computed.

(iv) $\rho_c \sigma_c^3 \geq 4/(1+q)^3$: Considering typical crystalline solid densities of the colloidal particles, i.e. $0.95 \lesssim \rho_c \sigma_c^3 \leq \sqrt{2}$, this highly dense state can only occur for large polymer–colloid size ratios $q \gtrsim 0.5$ (see Fig. 5.6). In this case, the available free volume for polymers, and consequently the free volume fraction, are zero. However, according to its definition from Eq. (5.28), the attractive part of the effective free energy density is not zero and reads

$$\beta f_{\text{eff,att}} \sigma_c^3 = \rho_{\text{p,r}} (1 - \eta_c (1+q)^3) . \tag{5.51}$$

For large values of polymer–colloid size ratio $q \gtrsim 0.6$, and for typical crystal densities, $\rho_c \sigma_c^3 \geq 1.0$, we are always in regime (iv), as it is shown in Fig. 5.6. Therefore, $\alpha = 0$ and the polymers do not affect the effective free energy density. This is also seen in the obtained values of α_G which are close to those of a pure hard sphere system. There is a linear decrease in the effective free energy density proportional to $\eta_{\text{p,r}}$ (see Fig. 5.5) which is due to its definition in which the trivial constant and the linear term in the colloid bulk density are subtracted (Eq. (5.43)).

By decreasing the size ratio to $q = 0.4$ (Fig. 5.5. b), we are in regime (iii) and $\alpha \ll 1$. Therefore, a linear increase in the effective free energy as a function of $\eta_{\text{p,r}}$ is observed and the situation is similar to larger q's. As it is shown in Fig. 5.7. a, except for small deviation at low colloid densities, the Gaussian width obtained by constrained minimization is close to the pure hard sphere system.

By further decreasing the size ratio to $q = 0.1$, the regimes (i) and (ii) are reached. In this case the free volume fraction and as a result the contribution of polymers to the attractive part of the effective free energy is large enough to have a major effect on the total effective free energy density. This explains the qualitative behavior of the effective free energy by increasing $\eta_{\text{p,r}}$ in Fig. 5.5. On the other hand, the deviation of the Gaussian width from its pure hard sphere value is more pronounced as $\eta_{\text{p,r}}$ increases (Fig. 5.7. b).
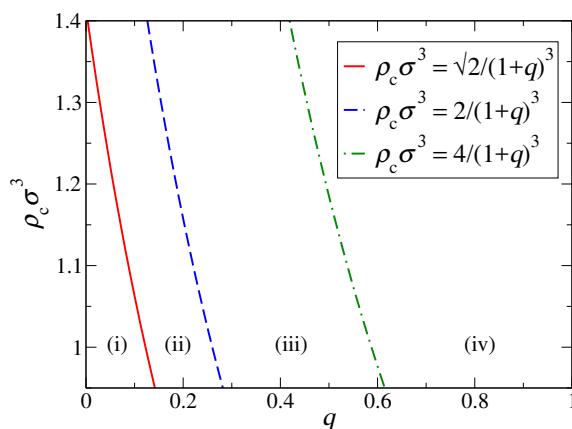
Figure 5.6: Typical crystal densities for colloid $\rho_c \sigma_c^3$ versus size ratio q, marking the different geometrical situations of overlapping exclusion spheres in an ideal fcc crystal. For region (i) in which the colloid density is $\rho_c \sigma_c^3 \leq \sqrt{2}/(1+q)^3$, there is no overlap. For region (ii) colloid density is bigger than $\sqrt{2}/(1+q)^3$ and smaller than $2/(1+q)^3$ and 2–body overlap of nearest neighbors occurs. In region (iii), $\rho_c \in [2/(1+q)^3, 4/(1+q)^3]$ and four–body overlaps of exclusion spheres occur between each colloid sitting at a corner of fcc lattice unit cell with the ones at the center of their adjacent faces. Finally, in region (iv) the overlapping of exclusion spheres results in zero volume fraction. The free volume fraction of an ideal crystal with colloids fixed at their lattice sites is used for obtaining an approximation for attractive part of effective free energy.

For the last case, since $q \leq 0.1546$ and the effective AO pair potential (Eq. (5.2)) exactly describes the interaction between colloids, we can take advantage of the naive mean–field functional as introduced in Eq. (5.44). Here, the free energy functional can be decomposed into an FMT part which solely describes the hard–core interaction and a naive mean–field part which is responsible for the attractive part of the potential. This technique is quite successful in describing Lennard–Jones crystal for obtaining liquid-crystal interface tension and phase transitions [119]. However, here there is a substantial underestimation of the attractive part of effective free energy using the naive mean–field functional due to the short range of the attraction in $\phi_{AO}(r)$.

For $q = 0.1$ we compare the attractive part of effective free energy density per polymer, $\beta f_{\text{eff,att}} \sigma_c^3 / \eta_{\text{p,r}}$, for the naive mean–field crystal, free volume theory for the ideal crystal, and the linearized WBII(tensor) functional in Fig. 5.8. Although the qualitative behavior of the free energy density predicted by free volume theory is the same as the FMT functional, quantitatively it has a constant shift for all values of ρ_c. For the naive mean–field functional, the curves for different values of $\eta_{\text{p,r}}$ collapse onto a single one and $\beta f_{\text{eff,att}} \sigma_c^3 / \eta_{\text{p,r}}$ does not depend on the polymer reservoir packing fraction. This is not true for the FMT functional in which by increasing $\eta_{\text{p,r}}$ the attractive
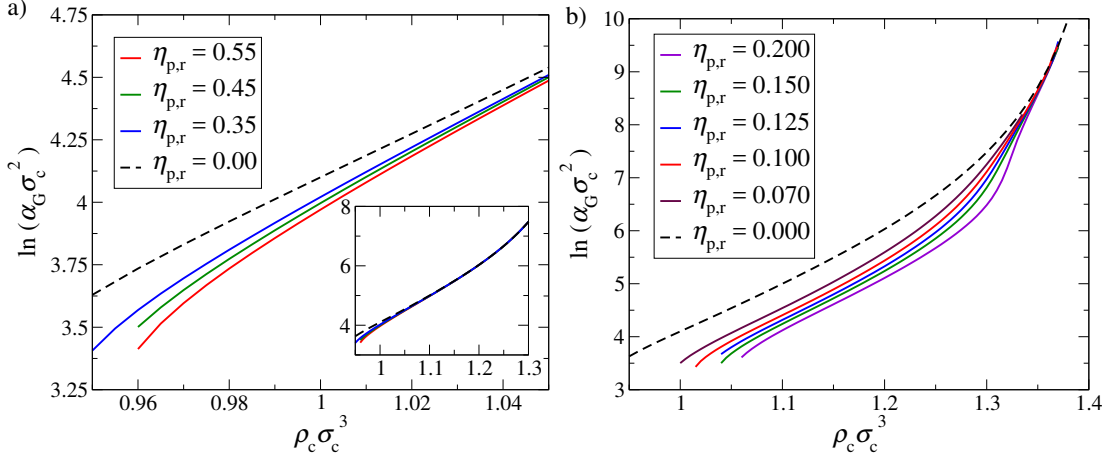
Figure 5.7: Comparison of the Gaussian width of the pure hard–sphere system $\eta_{p,r} = 0$ (black dashed curve) with that of the colloid density profile obtained by constrained minimization of the WBII(tensor) functional for a) $q = 0.4$ and b) $q = 0.1$. As a general rule, by increasing the polymer reservoir packing fraction the curves deviate from their hard sphere case specifically at lower densities. The inset for $q = 0.4$ is the same plot shown for colloid densities up to $\rho_c \sigma_c^3 = 1.30$.

part of effective free energy becomes slightly stronger. On the other hand, the naive mean–field functional gives only about 20% of the attractive free energy predicted by the linearized WBII(tensor) functional. This is consistent with our findings from the comparison of the naive mean–field approximation and free volume theory for bulk fluid in higher densities as shown in Fig. 5.4.

5.4.2 Phase Behavior

For each q, the crystal–fluid coexistence densities $\rho_{c,cr}$ and $\rho_{c,fl}$ are calculated using the common tangent construction for the effective free energy density of the bulk fluid and the crystalline fcc solid at a given $\eta_{p,r}$ (see Appendix D). The crystalline free energy density is obtained by constrained minimization of the linearized WBII(tensor) and RF(tensor) functionals, with respect to α_G and n_{vac}. The results are presented in Figs. 5.9–5.12 and 5.18. In all cases, by removing the polymers from the system, i.e. $\eta_{p,r} \to 0$, the corresponding known results for pure hard–sphere system is recovered for the linearized functionals (see table 4.1). In Section 5.4.5 a quantitative comparison of the phase diagrams obtained by the RF(tensor) and the WBII(tensor) functionals is demonstrated (see Fig. 5.18). Here, we are presenting the results for the WBII(tensor) functional in three categories of colloid–polymer size ratios.
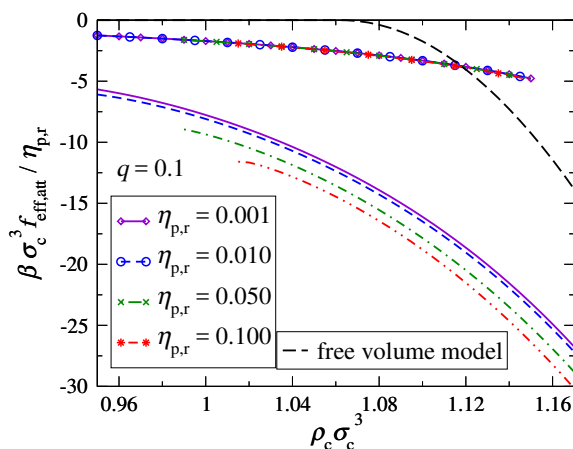
Figure 5.8: Comparison for the attractive part of the effective free energy density "per polymer" $\beta\sigma_c^3 f_{\text{eff,att}}(\rho_c)/\eta_{\text{p,r}}$ for polymer–colloid size ratio $q = 0.1$ between the linearized WBII(tensor) functional, the free volume theory for ideal fcc crystal (Eq. (5.49)), and the naive mean–field functional for different values of the reservoir polymer packing fraction $\eta_{\text{p,r}}$.
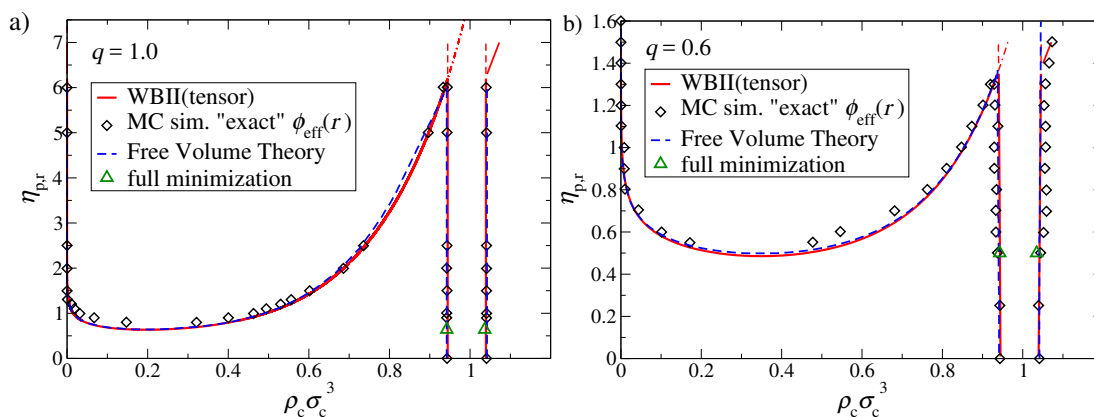
Figure 5.9: Phase diagram of AO model for a) $q = 1.0$ and b) $q = 0.6$. Solid red curves represents the binodals for the linearized WBII(tensor) functional, dashed red curves indicate metastable branches, and blue dashed lines are results from free volume theory (fluid) and parametrized HS crystal equation of states [110]. The results from simulations of the full AO model (using an "exact" effective pair potential) are marked with black diamonds [109]. Green triangles show liquid–crystal coexistence densities for full minimization (see Section 5.4.4).

5.4.2.1   Large q's

For large values of polymer–colloid size ratio, and for a state with highly dense colloidal particles the available free volume for polymers is almost zero. As a consequence, in a vicinity of the fluid and the crystal coexistence densities, the contribution of the polymers to the effective free energy is negligible. Therefore, the obtained phase coexistence densities is mainly dictated by the contribution of the colloidal hard–spheres to the effective free energy and remains the same as the hard–sphere system $\eta_{p,r} \to 0$. This holds even for larger polymer reservoir packing fractions up to the triple point $\eta_{p,r}^{tr}$. As shown in Fig. 5.9, our obtained binodals as well as triple points for $q = 1.0$ and $q = 0.6$ are in very good agreement with simulations [109, 110]. The MC simulations in Ref. [109] are done using an "exact" AO potential while the presented results from Ref. [110] are obtained using free volume–theory for the fluid and a parametrized equation of state for the hard–sphere crystal [121]. This good agreement for these polymer–colloid size ratios are of course expected due to the accuracy of free volume theory which is based on the scaled–particle theory (see Section 5.2), and the precise results of the WBII(tensor) functional for pure hard–sphere systems.

For $q = 0.6$, the obtained numerical values for the stable liquid–crystal phase coexistence densities for different values of $\eta_{p,r}$, and their corresponding coexistence chemical potential $\beta\mu_{coex}$ and pressure $\beta\sigma_c^3 p_{coex}$ are presented in table 5.1. Note the liquid–crystal coexistence pressure which decreases from its hard–sphere value ($\beta\sigma_c^3 p_{coex} \approx 11.89$) at $\eta_{p,r} \to 0$, to zero at triple point $\eta_{p,r} = \eta_{p,r}^{tr} \simeq 1.35$. For higher values of the polymer reservoir packing fraction $\eta_{p,r} > \eta_{p,r}^{tr}$, the liquid–crystal phase transition becomes metastable ($\beta\sigma_c^3 p_{coex} < 0$) with respect to the vapor–crystal phase coexistence ($\beta\sigma_c^3 p_{coex} \approx 0$) as presented in table 5.2.

5.4.2.2   Intermediate q's

For $q = 0.4$, increasing $\eta_{p,r}$ has a more significant effect on the difference between the liquid and the solid coexistence densities $\Delta\rho_c\sigma_c^3 = \rho_{c,cr}\sigma_c^3 - \rho_{c,fl}\sigma_c^3$. In this case, the width of the coexistence region is almost doubled from $\Delta\rho_c\sigma_c^3 = 0.0964$ at $\eta_{p,r} = 0.01$, to $\Delta\rho_c\sigma_c^3 = 0.2125$ at the triple point $\eta_{p,r} = \eta_{p,r}^{tr} \approx 0.54$. As shown in Fig. 5.10, the obtained binodals agree well with the results computed by using free volume theory for the fluid and the equation of state for the hard–sphere crystal proposed by Hall [110, 121]. This agreement was expected by considering the discussions which we have made in the framework of free volume theory for an ideal crystal in Section 5.4.1 (see page 87). There, we concluded that for this size ratio the total polymer density is still small, and hence the contribution of the polymers to the effective free energy density is negligible.

One can approximate the effective interaction between the colloidal particles by the effective pair potential of the AO model ϕ_{AO} (Eq. (5.2)). Note that ϕ_{AO} is obtained

Table 5.1: Stable crystal and fluid coexistence densities of the AO model for $q = 0.6$ obtained by constrained minimization of linearized WBII(tensor) functional with respect to α_G and n_{vac}. The last column is the difference between crystal and fluid densities $\Delta\rho_c\sigma_c^3 = \rho_{c,cr}\sigma_c^3 - \rho_{c,fl}\sigma_c^3$, which grows with increasing $\eta_{p,r}$.

$\eta_{p,r}$	$\rho_{c,cr}\sigma_c^3(\eta_{c,cr})$	$\rho_{c,fl}\sigma_c^3(\eta_{c,fl})$	$\beta\mu_{coex}$	$\beta\sigma_c^3 p_{coex}$	$\Delta\rho_c\sigma_c^3$
0.01	1.040(0.545)	0.945(0.495)	16.22	11.81	0.095
0.10	1.040(0.545)	0.944(0.494)	14.53	11.03	0.096
0.20	1.040(0.545)	0.944(0.494)	12.65	10.16	0.096
0.30	1.041(0.545)	0.944(0.494)	10.77	9.30	0.097
0.40	1.041(0.545)	0.943(0.494)	8.89	8.43	0.098
0.50	1.042(0.546)	0.943(0.494)	7.02	7.57	0.099
0.60	1.042(0.546)	0.943(0.494)	5.14	6.70	0.099
0.70	1.043(0.546)	0.943(0.494)	3.26	5.84	0.100
0.80	1.043(0.546)	0.942(0.493)	1.38	4.97	0.101
0.90	1.043(0.546)	0.942(0.493)	-0.50	4.11	0.101
1.00	1.044(0.547)	0.942(0.493)	-2.37	3.24	0.102
1.10	1.044(0.547)	0.941(0.493)	-4.25	2.38	0.103
1.20	1.045(0.547)	0.941(0.493)	-6.13	1.52	0.104
1.25	1.045(0.547)	0.941(0.493)	-7.07	1.08	0.104
1.30	1.045(0.547)	0.941(0.493)	-8.01	0.65	0.104
1.35	1.045(0.547)	0.940(0.492)	-8.95	0.22	0.105

by considering only two–body overlaps of the exclusion spheres. Simulations using ϕ_{AO} for $q = 0.4$, results in peculiar metastable vapor–liquid binodal [110]. Therefore, we conclude that in this case the effect of simultaneous interaction of three or more colloidal particles is too important to be neglected and these terms should also be considered in the effective colloid potential as in higher q's. In Fig. 5.10, we have compared our results with the obtained binodal from simulation using ϕ_{AO}, as well as the phase coexistence densities obtained by using fluid and crystal perturbation theory [110,122].

By further decreasing polymer–colloid size ratio, the stable vapor–liquid binodal will be restricted to a smaller range in the colloid density. Ultimately, the vapor–liquid binodal becomes completely metastable for $q \leq q_{trans}$. Here, the fluid branch of the fluid–solid coexistence density is determined by a sublimation line whose corresponding colloid density varies from a rather high density at hard–sphere limit, i.e. $\eta_{p,r} \rightarrow 0$ to very small values at higher polymer reservoir packing fractions. For the linearized WBII(tensor) functional this cross–over occurs at $q_{trans} \approx 0.31$ as shown in Fig. 5.11. At this polymer–colloid size ratio, the liquid branch skews rapidly toward lower colloid densities and hits the critical point $\eta_{p,r}^{cr}$ of the vapor–liquid binodal (Fig. 5.11. b). For
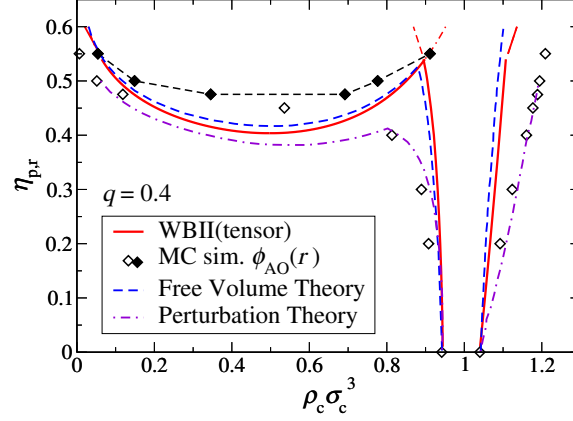
Figure 5.10: Phase diagram of AO model for $q = 0.4$. Solid red curves represents the binodals for the linearized WBII(tensor) functional, dashed red curves indicate metastable branches, and blue dashed lines are results from free volume theory (fluid) and parametrized HS crystal equation of states [110]. The results from simulations of the approximated AO model (using only the two–body potential ϕ_{AO}) are given by the black diamonds, the connecting dashed line indicates metastability. Dot–dashed lines are results from fluid and crystal perturbation theory using ϕ_{AO} [110, 122].
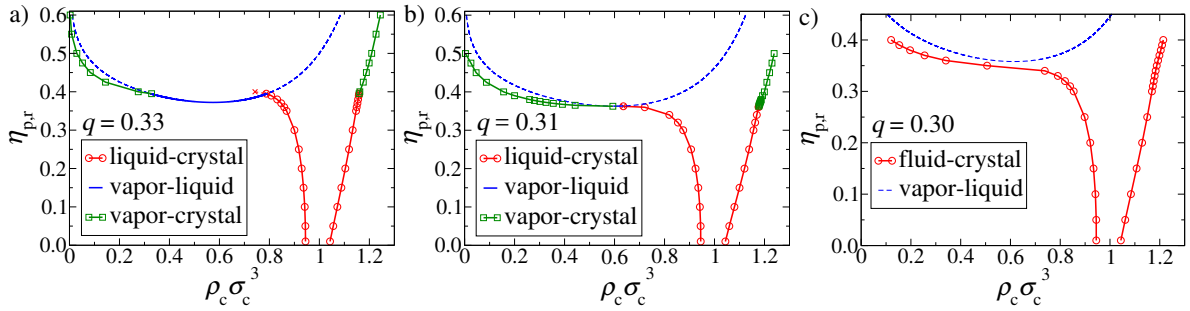
Figure 5.11: Phase diagram of AO model for a) $q = 0.33$, b) $q = 0.31$, and c) $q = 0.30$ using the linearized WBII(tensor) functional, showing the crossover to complete metastability of the vapor–liquid binodal. Open red circles represent the stable liquid–crystal binodal (for $q = 0.30$ fluid–crystal), green squares represent stable vapor–crystal binodal, and the blue curve is the vapor–liquid binodal. In all cases, metastability is indicated by dashed curves.

Table 5.2: Stable vapor–crystal phase transition of AO model for $q = 0.6$ along with metastable liquid-crystal phase transition obtained by constrained minimization of linearized WBII(tensor) functional with respect to α_G and n_{vac}. Note the negative coexistence pressure of the metastable liquid-crystal phase transition.

	stable vapor-crystal			
$\eta_{p,r}$	$\rho_{c,cr}\sigma_c^3(\eta_{c,cr})$	$\rho_{c,fl}\sigma_c^3(\eta_{c,fl})$	$\beta\mu_{coex}$	$\beta\sigma_c^3 p_{coex}$
1.40	1.051(0.550)	6.3e-05(3.3e-05)	- 9.68	6.3e-05
1.45	1.061(0.556)	3.7e-05(1.9e-05)	-10.21	3.7e-05
1.50	1.071(0.561)	2.2e-05(1.2e-05)	-10.74	2.2e-05
	metastable liquid-crystal			
$\eta_{p,r}$	$\rho_{c,cr}\sigma_c^3(\eta_{c,cr})$	$\rho_{c,fl}\sigma_c^3(\eta_{c,fl})$	$\beta\mu_{coex}$	$\beta\sigma_c^3 p_{coex}$
1.40	1.045(0.547)	0.940(0.492)	- 9.89	-0.22
1.45	1.046(0.548)	0.940(0.492)	-10.83	-0.66
1.50	1.046(0.548)	0.939(0.492)	-11.77	-1.09

higher values of $\eta_{p,r} > \eta_{p,r}^{cr}$, the liquid branch is metastable with respect to a corresponding phase transition to a lower (vapor) density. Decreasing the polymer–colloid size ratio by a slight value, e.g. to $q = 0.30$, results in a completely metastable vapor–liquid binodal (Fig. 5.11. c).

Using ϕ_{AO} as the effective interaction between colloidal particles in simulations and assuming a linear dependence of $\eta_{p,r}^{cr}$ and $\eta_{p,r}^{tr}$ on polymer–colloid size ratio, an approximate value for cross–over size ratio is obtained as $q_{trans} = 0.45$ [110]. The same value for q_{trans} is also reported by another simulation study with a lattice version of the AO model in which the polymers are restricted to a cubic lattice [123]. The obtained cross–over value from the linearized WBII(tensor) is closer to that of the perturbation theory using ϕ_{AO}, and also that of free volume theory, i.e. 0.31 and 0.32 respectively [105, 110, 122]. In Ref. [124], the renormalization theory is used in order to obtain analytical forms for the first, second, and third derivatives of the grand potential with respect to the colloid density. These derivatives are then used for computing the colloid chemical potential, the pressure, and the vapor–liquid critical points. Consequently, in the colloid limit where thickness of the depletion layer is assumed to be independent of the polymer density, the cross–over value to a metastable vapor–liquid binodal is reported as $q_{trans} = 1/3$ [124].

There are limited number of experimental studies reporting the value of q_{trans}. In Ref. [106], colloidal polystyrene suspensions are used which are electrostatically stabilized by sulfate groups. For preparing the samples, hydroxyethyl cellulose which are used as polymeric chains are made non–adsorbing by adding non–ionic surfac-

tant to the suspension. Three different samples of polystyrene suspension are used whose particles diameter are $\sigma_c = 0.12$, 0.16, and 0.19 micrometers with about 10% polydispersity. The effective polymer coil diameter is approximated as $\sigma_p = 400\mathring{A}$, i.e. the polymer–colloid size ratio of the samples are $q = 0.33$, 0.25, and 0.21. Only in the latter case a coexistence of colloid–poor (vapor) and colloid–rich (liquid) regions could not observed [106]. In Ref. [107], two different samples of Polymethyl–methacrylate (PMMA) with about 5% polydispersity are used as colloidal particles. The particles are sterically stabilized by coating with thin chemically grafted layers of poly-12-hydroxystearic acid and suspended in cis–decalin. Polystyrene in cis–decalin is used as non–adsorbing polymers. The samples are prepared by mixing PMMA suspension with different polystyrene stock solutions. The experiments are done for three different polymer–colloid size ratios $q = 0.08$, 0.25, and 0.57. Here, for $q \geq 0.25$ a stable three–phase coexistence of the colloidal vapor, liquid, and crystal is observed [107].

5.4.2.3   Small q's

The main importance of this regime is that the effective pair potential of the AO model, ϕ_{AO} from Eq. (5.2) with $q \lesssim 0.1547$, is exact. As a result the suspension can be used as a prototype for a simple fluid with short–range attractions. Here, we have investigated the phase diagram for $q = 0.1$ as an exemplary case. As shown in Fig. 5.12. a the broadening of the phase coexistence region is more significant. Here, a small increasing in the polymer reservoir packing fraction is enough for a rapid skew of the liquid branch toward smaller colloid densities. A comparison with the obtained phase diagram from simulations with the effective pair potential using $N_c = 108$ colloidal particles shows a fairly good agreement [110]. Although an investigation on the finite size effects in simulations and its influence on the obtained binodal is not performed, we will compare these results with ours in the following.

On the crystal branch, the obtained solid coexistence density from simulation shifts slowly toward higher colloid densities from its hard–sphere value at $\eta_{p,r} \to 0$ up to $\eta_{p,r} \approx 0.07$ where it shows a rapid shift to highly packed densities $\rho_{c,cr} \approx 1.3$ and stays there for higher $\eta_{p,r}$'s. This transition is more moderate in the obtained solid coexistence density from linearized WBII(tensor) functional. Moreover, for $\eta_{p,r} \gtrsim 0.06$ a meta–stable isostructural solid–solid phase transition is observed in simulations. We could not confirm such a phase transition. In Fig. 5.12. b, we have plotted the effective free energy βf_{eff} for selected values of $\eta_{p,r}$. Although the topology of the curves at higher colloid densities suggest a phase transition, the constrained minimization does not yield a metastable solid for $\rho_c \sigma_c^3 < 1.02$. Nevertheless, the spinodal points, the colloid densities at which $\partial^2 \beta f_{eff} / \partial \rho_c^2 = 0$, are computed and marked with red triangles in Figs. 5.12. a and 5.12. b. Using the obtained spinodal curve, we can make a rough estimate of the critical point of the solid–solid phase transition. In comparison
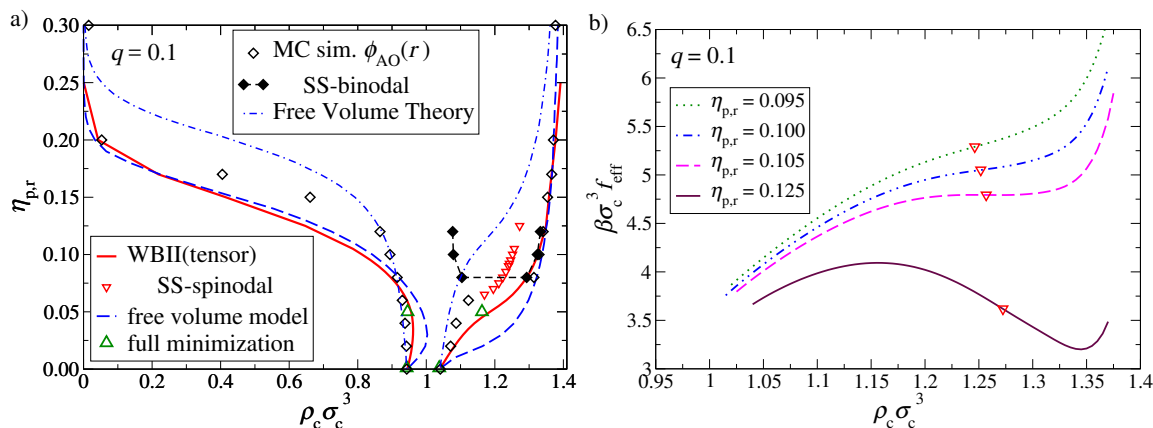
Figure 5.12: a) Phase diagram of the AO model for $q = 0.1$. Red solid curves are the binodals from the linearized WBII(tensor) functional. The solid–solid spinodal for the high density branch is shown by red triangles. Diamonds show simulation results [109, 110]. The solid–solid spinodal curve is shown for higher branch of the density with red triangles. Free volume theory binodals [110] (dash–dotted lines) employ Eq. (5.27) for the free energy with α always taken from the bulk fluid expression (Eq. (5.24)) and f_c parametrized by accurate equation of states for the HS fluid and crystal phase. Long–dashed curves show the result from the free volume model for an ideal crystal (see Section 5.4.1). Green triangles show liquid–crystal coexistence densities for full minimization (see Section 5.4.4).

b) Effective free energy density of the crystalline state of AO model for $q = 0.1$ obtained by constrained minimization of linearized WBII(tensor) functional with respect to $\{\alpha_G, n_{vac}\}$. The circles at each $\eta_{p,r}$ represent the colloid density at which $\partial^2 \beta f_{eff}/\partial \rho_c^2 = 0$ (spinodal points). Only a branch of spinodal points at higher densities has been found. For smaller ρ_c, a constrained minimization of the effective free energy functional is not possible.

with simulation, our critical point occurs approximately at the same polymer reservoir packing fraction, but at smaller colloid density.

The deviation of FMT results and simulations from Ref. [110] is more pronounced on the fluid branch. The obtained curve from simulations has a negative slope at $\eta_{p,r} \to 0$ similar to those of the higher polymer–colloid size ratios. In contrast, we have obtained a positive slope for the fluid branch at this limit. This unusual behavior is also observed in a more recent and larger–scale simulation of the AO model with more than 500 colloidal particles for $q = 0.15$ [77]. As shown in table 5.3, the obtained coexistence densities from simulation of HS limit, i.e. $\eta_{p,r} = 0$, and $\eta_{p,r} = 0.1$, suggest a slight positive slope for the fluid branch. In Ref. [110], a second order perturbation theory is also investigated. The hard–sphere system is used as a reference system whose free

Table 5.3: Comparison of the obtained values for coexistence densities of the AO model for $q = 0.15$. The FMT results are obtained from constrained minimization of linearized WBII(tensor) functional with respect to α_G and n_vac. The simulation results are from Ref. [77].

$\eta_\mathrm{p,r}$	FMT:			SIM:		
	$\rho_\mathrm{c,cr}\sigma_\mathrm{c}^3(\eta_\mathrm{c,cr})$	$\rho_\mathrm{c,fl}\sigma_\mathrm{c}^3(\eta_\mathrm{c,fl})$	$\beta\sigma_\mathrm{c}^3 p_\mathrm{coex}$	$\rho_\mathrm{c,cr}\sigma_\mathrm{c}^3(\eta_\mathrm{c,cr})$	$\rho_\mathrm{c,fl}\sigma_\mathrm{c}^3(\eta_\mathrm{c,fl})$	$\beta\sigma_\mathrm{c}^3 p_\mathrm{coex}$
0.000				1.041(0.545)	0.940(0.492)	11.576
0.001	1.041(0.545)	0.945(0.495)	11.88			
0.025	1.074(0.562)	0.953(0.499)	11.37			
0.050	1.117(0.585)	0.955(0.500)	10.43			
0.075	1.173(0.614)	0.945(0.495)	9.03			
0.100	1.223(0.641)	0.920(0.482)	7.25	1.222(0.640)	0.943(0.494)	8.00

energy is provided by the Carnahan–Starling and the Hall expressions. The attractive part of ϕ_AO is then treated as a perturbation and the total free energy is calculated. The obtained binodal by this method also shows a positive slope for the fluid branch at $\eta_\mathrm{p,r} \to 0$ [110].

In Fig. 5.12. a, we have also shown the obtained binodals for free volume theory and the *free volume model*. For obtaining the results for free volume theory, the effective free energy density is computed using Eq. (5.27) [110]. The free volume fraction α from Eq. (5.24) is used for both the fluid and the solid phases. The corresponding hard–sphere free energy density f_c are calculated by the Carnahan–Starling (fluid) and the Hall (solid) expressions. For the *free volume model*, the free volume fraction of the solid phase is calculated for an ideal fcc unit cell (see page 87) and for the fluid α from Eq. (5.24) is used. The hard–sphere free energy density is calculated using the WBII(tensor) functional, i.e. the Carnahan–Starling expression for the fluid and constrained minimization of the functional with respect to α_G and n_vac for the solid.

5.4.3   The polymer density profile

The colloid density in in crystalline state is approximated by Gaussian peaks which are ordered in an fcc cubic unit cell. But where do the polymers sit in this crystalline state? As an exemplary case, we show here the results for the polymer density profile from constrained minimization with respect to the Gaussian width while keeping fixed the vacancy concentration at a reasonably low value, $n_\mathrm{vac} = 2 \cdot 10^{-4}$. The calculations are done for $\rho_\mathrm{c}\sigma_\mathrm{c}^3 = 1.04$ which is the pure hard–sphere coexistence density.

Since we have a finite value for the vacancy concentration n_vac, it is possible for poly-

mers to fill in the lattice sites. However, this is not the case for small polymer–colloid size ratios, e.g. $q = 0.1$, for which there is enough space in an ideal lattice. Here, the polymers tend to fill the interstitials in the fcc unit cell (see Fig. 5.13. a). By increasing the polymer–colloid size ratio, and consequently decreasing the available free volume at the interstitials, it is reasonably expected that the majority of polymers fill the vacant positions at lattice sites.

In order to quantify this transition, one can define $\gamma(q)$ as the ratio of polymer number density at lattice sites $\mathbf{r}_{\text{latt}}$, to that at the interstitials $\mathbf{r}_{\text{inter}}$.

$$\gamma(q) =: \frac{\rho_{\text{p}}\left(\mathbf{r}_{\text{latt}}\right)}{\rho_{\text{p}}\left(\mathbf{r}_{\text{inter}}\right)} \; . \tag{5.52}$$

Note that the obtained polymer density shares the same symmetries as the colloid density profile in an fcc unit cell (see Appendix A.1), Therefore, we have used the polymer number density at $\mathbf{r}_{\text{latt}} = (0,0,0)$ and $\mathbf{r}_{\text{inter}} = (\frac{a}{2},0,0)$ for obtaining γ. A cross–over from the interstitial–filling–polymers being the majority to that of the lattice–filling–polymers, occur at q_0 where $\gamma(q_0) = 1$. In Fig. 5.14 we have shown $\gamma(q)$ as a function of polymer–colloid size ratio for our selected set of parameters, i.e. $\eta_{\text{p,r}} = 0.05$ and $\rho_{\text{c}} = 1.04$. In this case, we have obtained $q_0 \approx 0.65$. In Fig. 5.13. b, we have shown the polymer density profile for $q = 0.65$ on one of the faces of the fcc unit cell. Here, one can see that the density of the lattice–filling– and the interstitial–filling–polymers have almost the same values.

For larger values of q, the free available volume at interstitials vanishes. In Fig. 5.13. c we have shown the density profile for $q = 1.0$ where the majority of polymers are on scarce vacant lattice sites.

As a general rule, the polymer density at the lattice site $\rho_{\text{p}}(\mathbf{r}_{\text{latt}})$ is increased after full minimization in comparison with its initially constrained minimized case. Performing a full minimization of the linearized WBII(tensor) functional is discussed in Section 5.4.4 and the results for the polymer density profiles are presented in Fig. 5.16 for $q = 0.1$.

5.4.4 Full minimization

We have investigated the effect of full minimization on the equilibrium properties of the fcc solid phase for three exemplary parameter pairs $\{q, \eta_{\text{p,r}}\} = \{1.0, 0.64\}, \{0.6, 0.5\}$ and $\{0.1, 0.05\}$. For this purpose, after fixing the vacancy concentration, an iterative solution is initiated with a Gaussian profile for colloidal particles. At each step, using the current density profile of colloids $\rho_{\text{c}}^{(i)}$, the equilibrium polymer density profile $\rho_{\text{p,eq}}^{(i)}$ is calculated. Consequently, the excess chemical potential of the colloids and a new
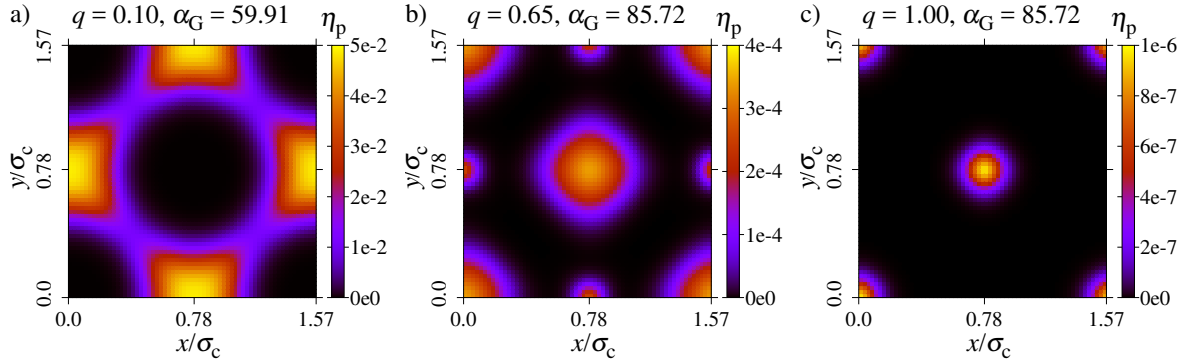
Figure 5.13: The local polymer packing fraction $\eta_p(\mathbf{r}) = (\pi\sigma_p^3/6)\rho_p(\mathbf{r})$ on one of the faces of the fcc cubic unit cell ($z = 0$) for $\eta_{p,r} = 0.05$, $\rho_c\sigma_c^3 = 1.04$, and three different values of polymer–colloid size ratios: (a) $q = 0.1$, (b) $q = 0.65$, and (c) $q = 1.0$. The results are obtained by constrained minimization of the linearized WBII(tensor) functional with respect to α_G while the vacancy concentration is fixed $n_{vac} = 2 \cdot 10^{-4}$.
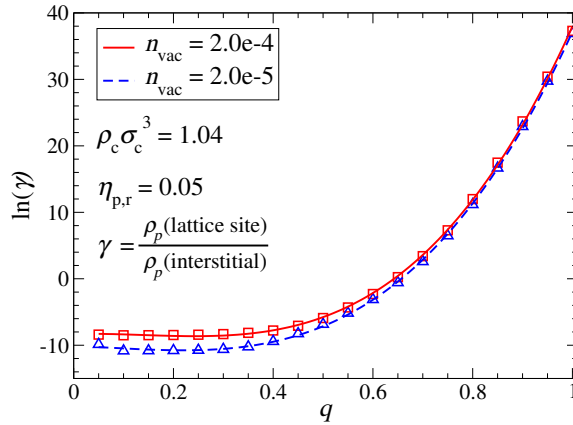
Figure 5.14: Logarithm of the ratio of polymer number density at lattice site $\rho_p(\mathbf{r}_{latt})$ to that of an interstitial $\rho_p(\mathbf{r}_{inter})$ is plotted as a function of polymer–colloid size ratio q for $\rho_c\sigma_c^3 = 1.04$, $\eta_{p,r} = 0.05$. The results are obtained by constrained minimization of the linearized WBII(tensor) functional with respect to α_G while the vacancy concentration is fixed at $n_{vac} = 2 \cdot 10^{-4}$ (red squares) and $n_{vac} = 2 \cdot 10^{-5}$ (blue circles). The lines are fitted polynomials of third order.
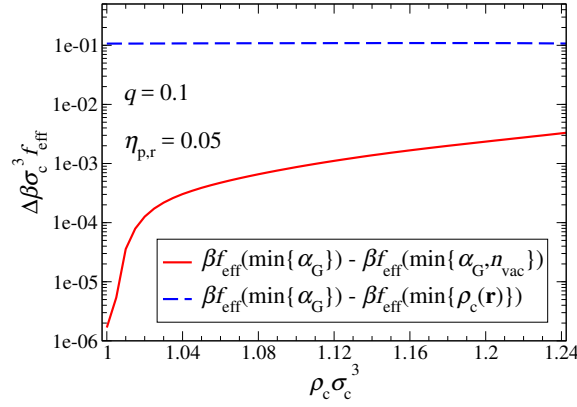
Figure 5.15: Difference of the effective free energy density of the AO model obtained by different minimization schemes. The red solid line represents the difference in obtained βf_{eff} by the constrained minimization with respect to $\{\alpha_G\}$ ($n_{\text{vac}} = 2 \cdot 10^{-4}$ fixed) and the constrained minimization with respect to $\{\alpha_G, n_{\text{vac}}\}$. Blue dashed line is difference between constrained minimization with respect to $\{\alpha_G\}$ ($n_{\text{vac}} = 2 \cdot 10^{-4}$ fixed) and full minimization ($n_{\text{vac}} = 2 \cdot 10^{-4}$ fixed). It is seen that the free energy is not very sensitive to minimization with respect to n_{vac} whereas the full minimization with respect to $\rho_c(\mathbf{r})$ introduces noticeable decreases.

Table 5.4: Comparison of phase coexistence densities $\rho_{\text{c,cr}}$ and $\rho_{\text{c,fl}}$ for selected parameter pairs $\{q, \eta_{\text{p,r}}\}$ obtained by constrained minimization with respect to α_G and n_{vac}, and full minimization with fixed $n_{\text{vac}} = 2 \cdot 10^{-4}$ of linearized WBII(tensor) functional.

q	$\eta_{\text{p,r}}$	constrained		full minimization	
		$\rho_{\text{c,cr}}\sigma_c^3(\eta_{\text{c,cr}})$	$\rho_{\text{c,fl}}\sigma_c^3(\eta_{\text{c,fl}})$	$\rho_{\text{c,cr}}\sigma_c^3(\eta_{\text{c,cr}})$	$\rho_{\text{c,fl}}\sigma_c^3(\eta_{\text{c,fl}})$
1.0	0.64	1.039(0.544)	0.944(0.494)	1.036(0.542)	0.942(0.493)
0.6	0.50	1.042(0.546)	0.943(0.494)	1.035(0.542)	0.943(0.494)
0.1	0.05	1.186(0.621)	0.956(0.501)	1.162(0.608)	0.945(0.495)

density profile ρ_c^{new} is computed. The updated colloid density profile $\rho_c^{(i+1)}$ is obtained by a mixture of $\rho_c^{(i)}$ and ρ_c^{new}. In order to obtain a global minimum for the free energy density, the procedure should be re–initiated by an updated n_{vac} (see Appendix A.4 for more details).

We will denote the effective free energy obtained by their corresponding minimization methods as follows,

$$
\begin{aligned}
\beta f_{\text{eff},0} &\quad : \quad \text{constrained minimization with respect to } \alpha_G \text{ with fixed } n_{\text{vac}} = 2 \cdot 10^{-4}, \\
\beta f_{\text{eff},1} &\quad : \quad \text{constrained minimization with respect to } \alpha_G \text{ and } n_{\text{vac}}, \\
\beta f_{\text{eff},2} &\quad : \quad \text{full minimization with fixed } n_{\text{vac}} = 2 \cdot 10^{-4},
\end{aligned}
\tag{5.53}
$$

Furthermore, in order to quantify the efficiency of minimization methods, we define the following effective free energy differences,

$$
\Delta \beta f_{\text{eff},i} \quad = \quad \beta f_{\text{eff},0} - \beta f_{\text{eff},i} , \qquad \text{with } i = 1, 2 ,
\tag{5.54}
$$

with $\beta f_{\text{eff},i}$ defined in Eq. (5.53). As it is shown in Fig. 5.15 for $q = 0.1$ and $\eta_{\text{p,r}} = 0.05$, we observe that difference made by minimization with respect to n_{vac} is negligible in comparison to performing a full minimization. We conclude that n_{vac} does not have a noticeable effect on the obtained free energy density, and hence the corresponding phase coexistence densities. Therefore, we have done full minimization only for $n_{\text{vac}} = 2 \cdot 10^{-4}$.

Generally, $\Delta f_{\text{eff},2}$ is more significant for the AO model in comparison with pure hard–sphere system where it is of the order of $10^{-3} k_{\text{B}} T$ per particle [80]. By decreasing the polymer–colloid size ratio, this difference increases and reaches $0.1 k_{\text{B}} T$ for $q = 0.1$ (see Fig. 5.15). The effect of full minimization on the phase coexistence densities is indicated in Figs. 5.9 and 5.12 by the green triangles. The numerical values of the binodals are compared in table 5.4. Only for $q = 0.1$ a noticeable shift is observed.

In the constrained approximation, colloid density profiles are isotropic around lattice sites, except for tiny effects of overlapping Gaussians from neighboring sites. According to full minimization, small anisotropies occur. For $q = 1.0$ and 0.6, polymers have no effect on the colloid profiles, and these anisotropies are more or less equivalent to those in pure HS crystals [80]. For $q = 0.1$, we see that the anisotropies are slightly enhanced compared to the pure hard–sphere system (Figs. 5.16. a and 5.16. b) but these anisotropy differences are surprisingly small. Nevertheless, the free energy difference of approximately $0.1 \, k_{\text{B}} T$ per particle due to anisotropy is lager by a factor of 100 compared to pure HS, so the attractive part of the free energy functional is much more sensitive to those anisotropies. The corresponding polymer profiles are shown in Figs. 5.16. c and 5.16. d. Since for small q polymers go to the interstitials, we have put the origin of the coordinate system at interstitials. The polymer profiles are
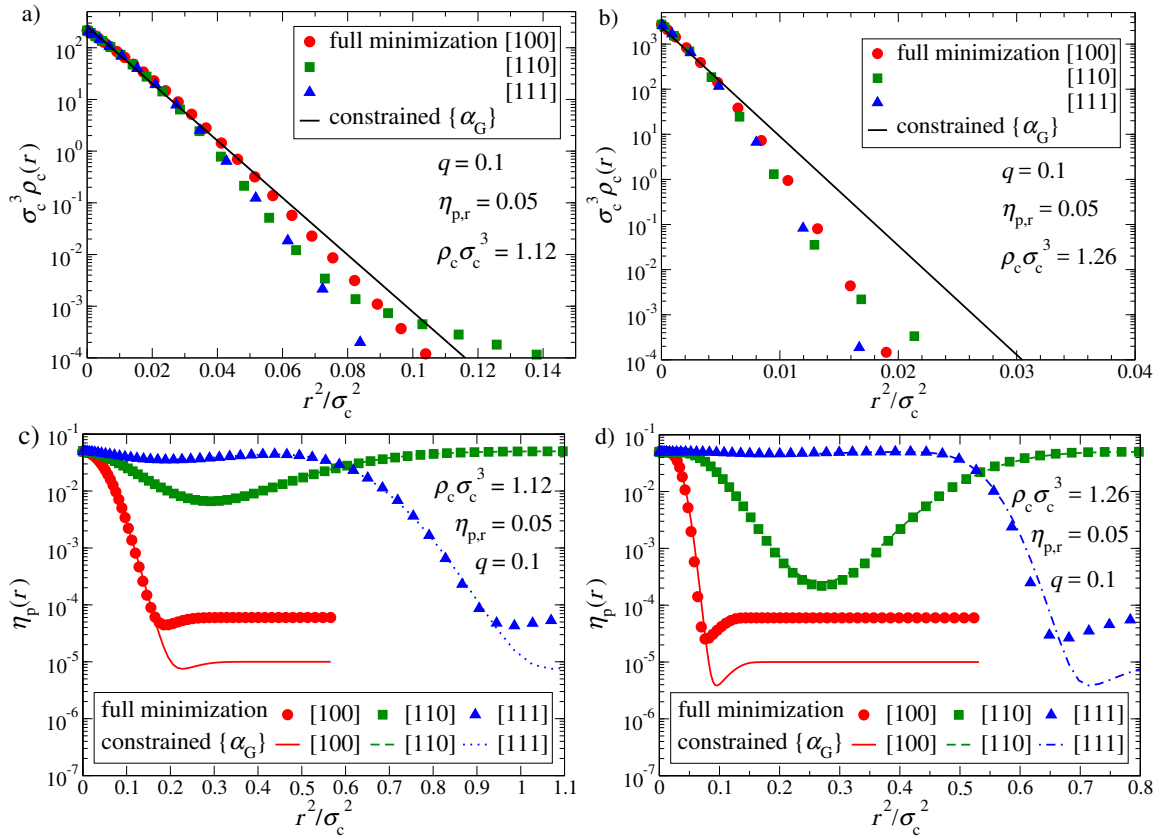
Figure 5.16: Lattice site density distributions along the lattice directions [100], [110] and [111] for $q = 0.1$ and $\eta_{\mathrm{p,r}} = 0.05$: comparison between constrained minimization w.r.t α_G and full minimization ($n_{\mathrm{vac}} = 2 \cdot 10^{-4}$ fixed). Panels a) and b) show the colloid density, full lines correspond to constrained minimization. Panels c) and d) show the polymer density deviation from its maximum value at interstitial, full lines correspond to the constrained minimization. The colloid density is $\rho_{\mathrm{c}}\sigma_{\mathrm{c}}^3 = 1.12$ (below coexistence) for a) and c), and $\rho_{\mathrm{c}}\sigma_{\mathrm{c}}^3 = 1.26$ (above coexistence) for b) and d).

anisotropic around lattice sites also in the constrained approximation. The main effect of full minimization is seen in the polymer occupancy near the lattice sites, i.e. in colloid vacancies. For the fully minimized crystal, much more polymers are sitting at the lattice sites compared to the crystal within constrained minimization.

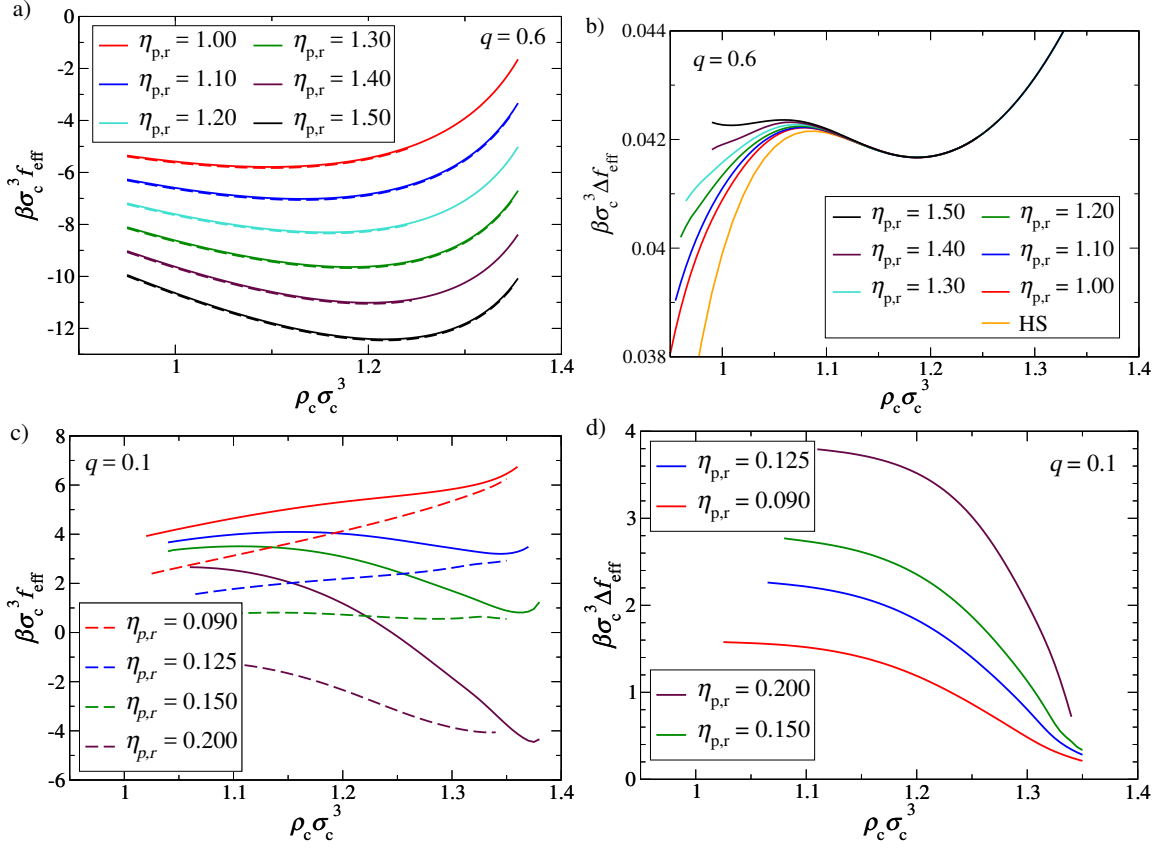### 5.4.5   Comparison of RF(tensor) and WBII(tensor)

It is possible to linearize another type of FMT functional, e.g. RF(tensor), to obtain the free energies and the phase coexistence densities of the AO model. In this section, the results for constrained minimization of linearized RF(tensor) functional is compared with those of the linearized WBII(tensor).

5.4.6   Crystal free energies

The main difference between the two type of functionals is their underlying equation of states which is Percus–Yevick for RF(tensor) versus Carnahan–Starling for WBII(tensor) (see Section 4.1 and Section 4.3). This difference results in a difference in the free energy density $\beta\sigma_c^3 f$ of the pure hard sphere crystal which remains below 1% at its phase coexistence density $\rho_c\sigma_c \approx 1.04$. For the linearized version of these functionals which are supposed to describe the AO model, the difference in the effective free energy density $\beta\sigma_c^3 f_{\mathrm{eff}}$ is a nontrivial function of the polymer–colloid size ratio q, and the polymer reservoir packing fraction $\eta_{p,r}$, as well as the colloid bulk density ρ_c. In case of the latter, as a general rule by increasing the colloid density this difference converges to its counterpart of the hard sphere system. This is rationalized by the fact that in this limit the colloidal hard spheres are nearly close–packed, leaving little space for the polymers. As a result, in this regime the effective free energy is mainly dominated by the contribution from the colloidal particles.

For larger size ratios $q \gtrsim 0.6$, the difference in the effective free energy density $\beta\sigma_c^3 \Delta f_{\mathrm{eff}}$ increases with $\eta_{p,r}$ for a given ρ_c. The difference stays within 5% of the total effective free energy density up to the triple point $\eta_{p,r} \simeq \eta_{p,r}^{\mathrm{tr}}$. Note that in this case the effective free energy density is similar to the corresponding hard sphere free energy density since $\rho_p \approx 0$ (see Fig. 5.17).

As the polymer–colloid size ratio decreases, the polymer density in the crystal increases and affects the value of the effective free energy density. For small polymer–colloid size ratios, e.g. $q = 0.1$, the significant increment of polymer density results in a substantial difference in the effective free energy density. Furthermore, in this limit the difference between the effective free energy density obtained by these linearized functionals becomes more pronounced and is not a marginal effect anymore. This is shown in Fig. 5.17 where $\beta\sigma_c^3 f_{\mathrm{eff}}$ for the linearized WBII(tensor) and RF(tensor) functionals along with their differences is shown for typical solid densities of colloid $\rho_c\sigma_c^3 \gtrsim 1$.

Figure 5.17: Comparison of the effective free energy density $\beta\sigma_c^3 f_{\rm eff}(\rho_c)$ of the crystalline state of the AO model obtained by constrained minimization of the linearized WBII(tensor) functional and the RF(tensor) functional. a) For higher polymer–colloid size ratios, $q \gtrsim 0.6$, the difference in the obtained $\beta\sigma_c^3 f_{\rm eff}(\rho_c)$ stays within 5% of the total effective free energy for different values of polymer reservoir packing fraction. b) The difference in effective free energy is plotted as a function of colloid bulk density. All the curves for different $\eta_{\rm p,r}$ lie on the same curve after $\rho_c\sigma_c^3 \gtrsim 1.1$ which is the difference between the free energy densities for HS ($\eta_{\rm p,r} = 0$). c) For $q = 0.1$ the substantial difference in the polymer equilibrium density results in a noticeable difference between the obtained results from the two functionals. The obtained results from constrained minimization of WBII(tensor) functional and RF(tensor) functional are respectively presented by solid and long–dashed curves. d) By increasing the colloid density there is little space for polymers, thus the free energy density is mainly dominated by colloidal hard spheres and the curves converge to the difference in the free energy density in case of pure hard spheres. The thermal de Broglie wavelength λ_c is set to σ_c.
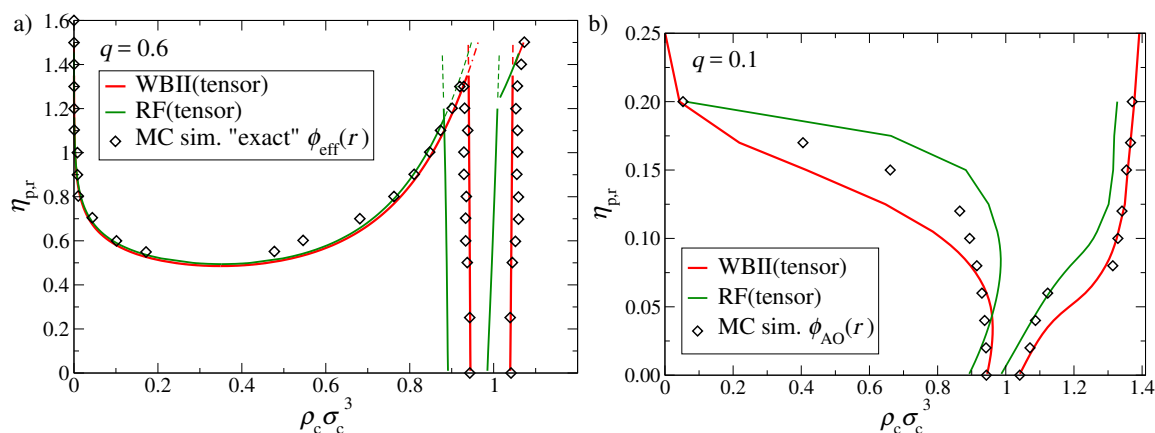
Figure 5.18: Comparison for phase diagram of the AO model for a) $q = 0.6$ and b) $q = 0.1$ obtained by the linearized WBII(tensor) and RF(tensor) functionals. The stable binodals obtained by constrained minimization of effective free energy of the linearized functionals are represented by red (WBII(tensor)) and green (RF(tensor)) solid curves. For $q = 0.6$ the dashed curves correspond to the meta–stable phase coexistence densities. The back diamonds are MC simulations results from Refs. [109, 110].

5.4.7 Phase diagram

The linearized functionals turn into their corresponding pure hard sphere functionals in the limit of $\eta_{\mathrm{p,r}} \to 0$. As it is expected, in this limit the known phase coexistence densities obtained by constrained minimization of the crystal free energy density are recovered [80]: $\rho_{\mathrm{c,cr}}\sigma_{\mathrm{c}}^3 = 1.040$ and $\rho_{\mathrm{c,fl}}\sigma_{\mathrm{c}}^3 = 0.945$ for WBII(tensor) and $\rho_{\mathrm{c,cr}}\sigma_{\mathrm{c}}^3 = 0.984$ and $\rho_{\mathrm{c,fl}}\sigma_{\mathrm{c}}^3 = 0.892$ for RF(tensor).

For large polymer–colloid size ratios, e.g. $q = 0.6$, this difference in the phase coexistence densities is also present at higher $\eta_{\mathrm{p,r}}$. The absolute value of the difference slightly decreases by increasing the polymer reservoir packing fraction to $\eta_{\mathrm{p,r}}^{\mathrm{tr}}$ (see Fig. 5.18.b).

For $q = 0.1$, where the fluid–fluid binodal is meta–stable with respect to fluid–solid phase transition, the broadening of the fluid–crystal coexistence region is noticeably different for the two types of investigated linearized functionals (see Fig. 5.18.a). Here, the solid branch of the binodals keeps almost the same difference as the pure hard sphere limit for higher $\eta_{\mathrm{p,r}}$. On the fluid branch however, the positive slope of the binodal is present up to $\eta_{\mathrm{p,r}} \approx 0.1$ for the linearized RF(tensor) functional. By slightly increasing the polymer reservoir packing fraction, the curve turns toward lower colloid densities very rapidly. For the linearized WBII(tensor) functional, the turn–over occurs at $\eta_{\mathrm{p,r}} \approx 0.04$ and the broadening toward lower colloid densities happens in a broader range of $\eta_{\mathrm{p,r}}$.

5.5   Summary and Conclusions

Using classical density functional theory, we are able to describe the fluid and crystal phases of the AO model in a unified way. A fundamental measure type functional for the free energy of the model is derived by linearization of a pure hard sphere functional with respect to the polymer density. The effective free energy of the colloids in an fcc crystalline state is obtained by constrained minimization of the linearized functional. The free energy curves are qualitatively similar to those of a system with attractive interaction between particles. In the limit of small q in which the effective potential of the AO model describes precisely the short–range attraction between colloids, we have compared the attractive part of the effective free energy of the colloids with those of the simplified free volume for ideal crystal and a naive mean–field approximation in which the attractions are of second order in the colloid density. While the free volume theory captures the qualitative behaviour of $\beta f_{\text{eff,att}}$ with increasing colloid density, the naive mean–field curves account for only 20% of it and fails to give a good description of the AO model. We conclude that a successful description of colloidal systems with short–range attractions should start with a "translation" of the attractive interaction into fictitious polymeric attractive agents which are treated as a second species in the construction of the functional from the beginning rather than the conventional mean–field treatments which are successful for longer–ranged potentials, e.g. the Lennard–Jones potential.

The phase diagrams which are obtained by the common tangent construction of effective free energy curves are in good agreement with available simulation data. By decreasing the polymer–colloid size ratio the fluid–fluid binodal becomes unstable with respect to the fluid–solid phase transition. We have shown that the transition into metastability of the fluid–fluid binodal occurs at $q \approx 0.31$. The rather interesting polymer distribution in the crystalline state of the colloids is discussed and it is shown that for smaller size ratios the interstitial spaces in cubic unit cell is more favourably occupied by the polymers. This scenario is changed for higher size ratios where the polymers tend to fill the vacant lattice sites for $q \gtrsim 0.6$.

The most important aspect of the AO model is the small q regime in which there is an exact mapping of the colloid–polymer mixture onto a single–component colloid suspension with short–range attractive interactions. In this case, the linearized functional takes care of the pairwise attractions in a fundamentally different way than the conventional methods in which the total free energy is extrapolated from a reference bulk liquid state. As a result of this extrapolation, the obtained direct correlation functions from this free energy inherit a spurious isotropic part from the liquid state. The linearized functional however, genuinely results in anisotropic direct correlation functions which are essential for a correct description of the crystalline state as is reported also for Taylor–expanded density functionals [125]. Furthermore, these anisotropic

direct correlation functions can be useful for investigation of a generalized theory of elasticity which is potentially applicable to the colloidal system [126].

The small q regime of the AO model as a prototype of short–range attractive systems is a good candidate for investigation of interfacial and nucleation phenomenal by simulations [113], for instance the estimation of nucleation barriers via finite–size Monte–Carlo methods [127, 128]. The proposed linearized functional in this study can also be applied to flat and curved fluid–solid interfaces for instance in order to compute rather precise free energies and obtain detailed information on the density distributions.

CHAPTER 6

# THERMAL VACANCIES IN CLOSE−PACKING SOLIDS

An ideal crystal with perfectly ordered particles at their lattice sites and complete translational symmetries, is the simplest situation for a substance to be investigated theoretically. However, this is not often the case in reality: Crystals contain defects. In spite of their scarceness, these deviations from an ideal crystal affect physical properties of the material considerably. Point defects which are localised around a lattice site are the simplest deviation from an ideal crystal. Substitutional impurities, interstitials, and vacancies are a few examples for point defects (see Fig. 6.1).

Vacancies are lattice sites at which there is no particle. They occur at finite temperatures when particles move more frequently and change their position randomly. By virtue of this thermal motion, vacant sites are left behind resulting in an inevitable finite equilibrium concentration of vacancies $n_{\mathrm{vac,eq}}$ in lattice. Thus $n_{\mathrm{vac,eq}}$ is a very basic property of a crystalline material which has a significant effect on other physical properties, e.g. diffusion coefficient and compressibility. Although its magnitude and temperature dependency in different materials have been studied for nearly a century [129, 130], conclusive experimental results as well as a unified description for $n_{\mathrm{vac,eq}}$ is missing.

Since point defect in general enhance the entropy of a crystal, they are thermodynamically stable in an equilibrium state. The equilibrium vacancy concentration is expressed as,

$$n_{\mathrm{vac,eq}} \;=\; \exp\left(-\beta \Delta G_{\mathrm{v}}\right)\,, \tag{6.1}$$

which serves to *define* equilibrium Gibbs energy of vacancy formation [129]. Here, $\beta = (k_{\mathrm{B}}T)^{-1}$ with k_{B} the Boltzmann constant and T denoting the temperature. In the material science community, ΔG_{v} is decomposed into the enthalpic ΔH_{v} and entropic parts $T\Delta S_{\mathrm{v}}$. The enthalpic part is the sum of the formation energy E_{v} at finite tem-
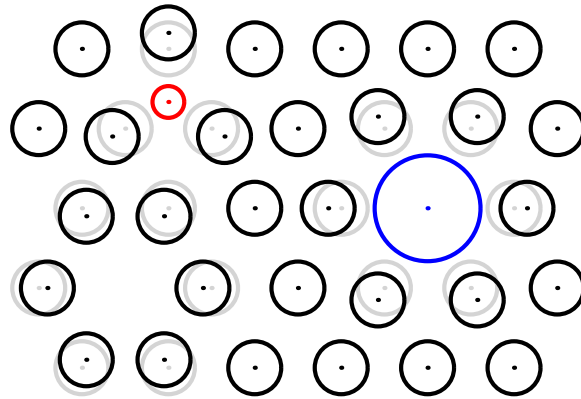
Figure 6.1: Point defects in a 2D ideal crystalline lattice. The lattice is assumed to be in equilibrium and the exaggerated effect of point defects on their neighboring particles (black circles) is sketched by a displacement from their ideal lattice site (dark gray). The particles around a vacant position rest at a different place other than equilibrium site in an ideal lattice without a vacancy. The adjacent particles to an interstitial (red) or a substitutional (blue) particle are shifted outward in relation to the impurity.

peratures and the required work for creating a vacant site with volume V_v in a system with pressure p; i.e. pV_v. Since the main contribution of E_v is from its zero temperature value, the calculation of ΔH_v is computationally less costly than the entropic part. The formation entropy $T\Delta S_v$ results from changes in the lattice vibration frequencies due to presence of vacancies. The frequency of a lattice vibration mode is expected to decrease since the lattice becomes softer with vacant sites [129]. The mutual interactions of these vibrations (anharmonic excitations) is another quantity which should be addressed at finite temperatures for a metallic system [131]. One can use quantum DFT (qDFT) to obtain these quantities. However, even using approximate exchange and correlation functionals E_{xc} with the cost of uncertainties in the obtained results, does not help to decrease the usual computational cost of qDFT and the use of supercomputers is required for such calculations [131, 132].

Assuming the particles interactions is expressed as a classical potential, one can take advantage of the tools from classical statistical physics. Here, the problem of vacancies and other point defects can be addressed by writing down an appropriate partition function Q for the crystalline state. Having the partition function at hand, a closed expression for the desired physical quantity can be derived by minimizing the Helmholtz free energy of the system $\beta F = -\ln Q$. In case the resulting expression is not analytically solvable, computational numerics is used which is much less costly than those needed for qDFT for instance. On the other hand, the form of obtained expression might result in a better understanding of the physics of vacancies.

In this chapter, we will follow the steps taken in Ref. [16] for deriving an expression for the concentration of the thermal vacancies in equilibrium $n_{\text{vac,eq}}$. In the first section, an expansion of the crystal partition function is presented in terms of number n of particles which are free to move. The series is based on the work by Stillinger et al. developed by the ideas from the cell cluster theory [14]. According to the cell cluster theory, in a nearly closed–packed system each particle is free to move in the vicinity of its designated lattice site. The restriction of particles to their Wigner–Seitz (WS) cell, chops the volume space of the integration domain in the partition function into sub–volumes with boundaries set on the borders of the WS cell (see Fig. 6.2). For $T = 0$, all particles are frozen at their lattice site and $n = 0$. By truncating the partition function series after the second term $n = 1$, we obtain a simple relation for ΔG_{v} (Eq. (6.25)). This relation reveals the dependency of ΔG_{v} on the equation of state and some three-dimensional configuration integrals.

In case of HS as a purely repulsive system, the agreement with quantitative results obtained mainly by Monte Carlo simulations is very good [102, 103, 133]. By tweaking the series, the method is applied to the AO model for investigating the vacancy concentration in a colloid–polymer mixture. The qualitative behaviour as a function of polymer reservoir packing fraction is what we were expecting from the FMT results for larger polymer–colloid size ratios. As a third example for a simple model potential, we apply the theory to the Lennard–Jones system. The equation of state for LJ obtained by the first order approximation of the partition function series matches well the parametrized van der Hoef equation of state [120]. The vacancy concentration is calculated for a range of temperatures and densities and is compared to the limited number of simulation results [134].

Motivated by these results, we have examined Nickel as an exemplary case for metal with face–centered cubic crystal structure. For this purpose, the embedded–atom potentials (EAM) are used. These potentials in their original form, are decomposed into a pair potential which is purely repulsive and a more complex attractive part. The repulsive part is due to the interaction of the nuclei and the attractive part is given in the form of an embedding function of the local electron density [135]. The results obtained by the EAM potentials with the same physical interpretations, show the same temperature behaviour of the vacancy concentration as the LJ solid. For another form of EAM whose potentials are fitted in a more elaborate way and do not have a clear physical interpretation, the behavior is somewhat different.

In the following section, the appropriate partition function for describing a closed–packed solid with vacancies is presented. Using the Stillinger series obtained by this partition function in Section 6.2, our central result on the thermal vacancies is presented in Section 6.3. We report our numerical results in Section 6.4 for the classical systems, i.e. HS, the AO model, and LJ, and for exemplary case of Nickel via EAM.

6.1 The crystal partition function

Consider the partition function of a face–centered cubic (fcc) reference lattice for the crystalline state of a one–component substance. In a canonical ensemble with fixed number of particles N, physical volume of the system V, and temperature T, by integrating out the trivial kinetic part of the partition function, its configurational part reads

$$Q(N, V, T) \ = \ \frac{1}{N! \lambda^{3N}} \int_{\mathbb{R}^3} \mathrm{d}\mathbf{r}_1 \cdots \int_{\mathbb{R}^3} \mathrm{d}\mathbf{r}_N \ \exp\left(-\beta \Phi(\mathbf{r}_1, \dots, \mathbf{r}_N)\right) . \tag{6.2}$$

The internal energy of the system Φ depends on the individual atom positions $\mathbf{r}_1, \dots, \mathbf{r}_N$, and it is assumed to be decomposable into a sum over 1–particle potential energies ϕ_i.

$$\Phi\left(\mathbf{r}_1, \dots, \mathbf{r}_N\right) \ = \ \sum_{i=1}^{N} \phi_i(\mathbf{r}_1, \dots, \mathbf{r}_N) . \tag{6.3}$$

The 1–particle energies ϕ_i are resulting from the interaction between particles which is assumed to be a classical potential of possibly many–body nature. For a substance with a pairwise potential $u(r_{ij}) = u(|\mathbf{r}_i - \mathbf{r}_j|)$, these 1-particle energies become,

$$\phi_i^{2\mathrm{p}}(\mathbf{r}_1, \dots, \mathbf{r}_N) = \frac{1}{2} \sum_{\substack{j=1 \\ j \neq i}}^{N} u(r_{ij}) . \tag{6.4}$$

We have also investigated a many–body form for the 1–particle energies in the context of the Embedded-Atom Model (EAM) which is designed for classical treatment of a metallic system. For a detailed description see Appendix F. Here, the total 1–particle energy ϕ_i^{EAM} is decomposed into a pair part and an embedding potential part,

$$\phi_i^{\mathrm{EAM}}(\mathbf{r}_1, \dots, \mathbf{r}_N) = \phi_i^{2\mathrm{p}}(\mathbf{r}_1, \dots, \mathbf{r}_N) + \phi_i^{N\mathrm{p}}(\mathbf{r}_1, \dots, \mathbf{r}_N), \tag{6.5}$$

where $\phi_i^{2\mathrm{p}}$ is calculated from Eq. (6.4) using a pair potential between the nuclei and the N–body embedding potential $\phi_i^{N\mathrm{p}}$ is given by,

$$\phi_i^{N\mathrm{p}}(\mathbf{r}_1, \dots, \mathbf{r}_N) = F\left(\rho_i^{\mathrm{a}}(\mathbf{r}_1, \dots, \mathbf{r}_N)\right) . \tag{6.6}$$

In this relation, F is the embedding function and ρ_i^{a} is the total electron density at the position of particle i, originating from all the other particles. This electron density is a superposition of single particle electron densities $\rho_{ij}^{\mathrm{a}}(r)$ which is given for a distance

$r = |\mathbf{r}_i - \mathbf{r}_j|$ of particle j. As a result, the total electron density ρ_i^{a} is calculated as follows,

$$\rho_i^{\mathrm{a}}(\mathbf{r}_1, \ldots, \mathbf{r}_N) = \sum_{\substack{j=1 \\ j \neq i}}^{N} \rho_{ij}^{\mathrm{a}}(|\mathbf{r}_i - \mathbf{r}_j|) \ . \tag{6.7}$$

The embedding function $F(\rho_i^{\mathrm{a}})$ determines the potential energy of "embedding" the particle i in the system as a function of the local host electron density. This function along with the pair potential of the nuclei $\phi_{ij}(r)$ and the single particle electron density $\rho_{ij}^{\mathrm{a}}(r)$ must be determined by material–specific fits [136]. In the original formalism of the EAM, these functions have a physical interpretation. The single electron density is modeled on Hartree–Fock solutions for the outermost orbitals of the investigated atom. The pair interaction of the nuclei is assumed to be the Coulomb interaction of a screened charge of the nuclei $Z^2(r)e^2/(4\pi\epsilon_0 r)$. The undetermined functions, the screening function $Z(r)$ and the embedding function $F(\rho_i^{\mathrm{a}})$, are obtained by fitting parameters to measured physical properties of the material [137,138]. In another form of parametrization, the physical interpretation is left aside and all the functions are obtained by fitting to the experimental and *ab initio* simulation results [139]. For detailed information on different parametrization of the EAM see Appendix F.

For further developments, one can use the ideas of the cell cluster theory [14]. Suppose the fcc reference lattice has $M \geq N$ lattice sites at positions $\mathbf{s}_j$ with $j = 1 \cdots M$ which span the physical volume of the system V. In the following, we want to decompose the full configuration space $\Omega = \mathbb{R}^{3N}$ into smaller volumes where particle coordinates $\mathbf{r}_j$ are integrated over suitable unit cells. For this purpose, we denote by $p(i)$ a mapping of a particle indexed by $i = 1 \cdots N$ to the lattice site $p(i) \in \{1, \ldots, M\}$ such that $p(i) \neq p(j)$ for $i \neq j$. Consider R_p as the sum of the square of the particle displacement from their assigned lattice site.

$$R_p = \sum_{i=1}^{N}(\mathbf{r}_i - \mathbf{s}_{p(i)})^2 \ . \tag{6.8}$$

For any set of particle coordinates $\mathbf{R} = \{\mathbf{r}_1, ..., \mathbf{r}_N\}$ we may minimize R_p with respect to the possible mappings p and call the minimal p an association of $\mathbf{R}$ with p. The configuration space of all $\mathbf{R}$ associated with a particular p forms Ω_p and thus $\Omega = \sum_p \Omega_p$. Obviously, there are $N!$ mappings of p onto the same set of lattice sites, differing only in the order of lattice sites. Each of these mappings give the same contribution to Q. Let l number only the mappings onto distinct lattice sites, $p \equiv p_l$. Then the configuration integral in Eq. (6.2) is decomposed into a sum over these distinct mappings since the combinatorial factor $1/N!$ takes care of the sum over p's which map on to the same

set of lattice sites,

$$Q(N, V, T) \;\; = \;\; \frac{1}{\lambda^{3N}} \sum_l \int_{\omega_1^l} \mathrm{d}\mathbf{r}_1 \cdots \int_{\omega_N^l} \mathrm{d}\mathbf{r}_N \; \exp\left(-\beta \Phi(\mathbf{r}_1, \ldots, \mathbf{r}_N)\right) \; . \tag{6.9}$$

Note that the integration domain of each particle j is now restricted to its associated unit cell ω_j^l, and the full configuration space is given by $\Omega_{p_l} = \omega_1^l \otimes \cdots \otimes \omega_N^l$. For $M = N$ the union of the integration domains sweeps the whole space, i.e. $\mathbb{R}^3 = \omega_1^l \oplus \cdots \oplus \omega_N^l$.

6.2   The Stillinger series

The partition function Q (Eq. (6.9)) can be written as a formally exact product series involving *reduced* configuration integrals Z_i^l, Z_{ij}^l, ... These *reduced* configuration integrals describe the correlated motion of one , two , ... free particles which are labelled as i , ij , ... while the remaining $N-1$, $N-2$, ... particles are fixed at their associated lattice sites $\mathbf{s}_k$. We define these *reduced* configuration integrals as,

$$Z_i^l := \int_{\omega_i^l} \mathrm{d}\mathbf{r}_i \exp\left(-\beta\phi_i(\mathbf{r}_i; \{\mathbf{r}_j\})\right) \text{ with } \mathbf{r}_j = \mathbf{s}_j \; (j \neq i) \; ,$$

$$Z_{ij}^l := \int_{\omega_i^l} \mathrm{d}\mathbf{r}_i \int_{\omega_j^l} \mathrm{d}\mathbf{r}_j \exp\left(-\beta\left[\phi_i(\mathbf{r}_i, \mathbf{r}_j; \{\mathbf{r}_k\}) + \phi_j(\mathbf{r}_i, \mathbf{r}_j; \{\mathbf{r}_k\})\right]\right) \text{ with } \mathbf{r}_k = \mathbf{s}_k \; (k \neq \{i, j\}) \; ,$$

$$\vdots \quad . \tag{6.10}$$

The integration domains fulfill $\omega_i^l, \omega_j^l, \cdots \subset \Omega_{p_l}$, and they depend on the indices of the free particles i, j and also on the mapping p_l determining at which lattice sites the other particles are fixed. Note that Z_{ij} for two non–interacting particles i and j reduces to the product of the corresponding configuration integrals of the individual particles $Z_i^l Z_j^l$. The higher order terms can also be decomposed into the product of configuration integrals of non–interacting subsets of particles. For instance, for three moving particles from which only two of them, e.g. i and j, interact with each other, the configuration integral can be written as $Z_{ijk}^l = Z_{ij}^l Z_k^l$. The full partition function Q is equivalent to the Nth order configuration integral $Z_{1\ldots N}^l$ in which all of the particles are free to move.

$$Q = \frac{1}{\lambda^{3N}} \sum_l Z_{1\ldots N}^l \; . \tag{6.11}$$

Now we are able to write down an expansion for the partition function in terms of number of free moving particles in the system.

$$Q(N, V, T) = \frac{1}{\lambda^{3N}} \sum_l \left\{ \prod_i^N Y_i^l \prod_{i<j}^N Y_{ij}^l \prod_{i<j<k}^N Y_{ijk}^l \cdots \right\} \tag{6.12}$$

The Y's are defined in terms of the Z's in a way that for nth term the contribution of lower order terms are cancelled out and the remainder delivers the corresponding value for configuration partition function of n free moving particles. The lowest order term Y_i^l corresponds to a single moving particle and therefore is equivalent to Z_i^l. The higher order terms are defined in a recursive relation as follows.

$$\begin{aligned}
Y_i^l &:= Z_i^l, \\
Y_{ij}^l &:= \frac{Z_{ij}^l}{Y_i^l Y_j^l} = \frac{Z_{ij}^l}{Z_i^l Z_j^l}, \\
Y_{ijk}^l &:= \frac{Z_{ijk}^l}{Y_{ij}^l Y_{jk}^l Y_{ik}^l Y_i^l Y_j^l Y_k^l} = \frac{Z_{ijk}^l}{\frac{Z_{ij}^l Z_{jk}^l Z_{ik}^l}{Z_i^l Z_j^l Z_k^l}}, \\
&\vdots \\
Y_{i_1 \ldots i_n}^l &:= \frac{Z_{i_1 \ldots i_n}^l}{\prod_{\{j\}} Y_{j_1 \ldots j_m}^l}.
\end{aligned} \tag{6.13}$$

The product in the denominator of the nth order term sweeps over all proper subsets of $\{i_1 \ldots i_n\}$ with $n-1$ elements. The inclusion of the last term $Y_{1 \ldots N}^l$ in the series of Eq. (6.12) leads to a cancellation of all lower–order Y's by the denominator of $Y_{1 \ldots N}^l$ and the identity for partition function (Eq. (6.11)) holds. Thus, the series is formally exact.

Consider a single freely moving particle among the otherwise frozen particles at their lattice sites or equivalently more non–interacting moving particles. The series in Eq. (6.12) is truncated after the first term and the partition function reads

$$Q \approx Q_1 = \frac{1}{\lambda^{3N}} \sum_l \prod_i^N Z_i^l. \tag{6.14}$$

For an ideal crystal with no vacant lattice site there is only one distinct mapping p_l and all single-particle configuration integrals are equal, $Z_i^l \equiv Z_s$. Therefore, the Helmholtz free energy of the system in this approximation turns into,

$$\frac{\beta F_1}{N} = -\ln \frac{Z_s}{\lambda^3}. \tag{6.15}$$

In the low temperature limit $T \to 0$, any displacement of the single free moving particle from its equilibrium lattice site, i.e. minimal single–particle potential ϕ_i, substantially decreases the integrand in the configuration integral $\exp(-\beta\phi_i(\mathbf{r}_i; \{\mathbf{r}_j\}))$. Therefore, in the low temperature limit one can approximate Z_s with its integrand. Subsequently, the first order approximation of the Helmholtz free energy density F_1/N is equal to ϕ_i which is equivalent to the cohesive energy per particle u_{coh}. Assuming $\lambda = 1$, the free energy density reads

$$\lim_{T\to 0} \frac{F_1}{N} = \phi_i =: u_{\mathrm{coh}} . \tag{6.16}$$

This confirms that in this limit the leading–order truncation is exact.

In the next section, we will introduce vacant sites to the ideal crystal lattice in order to obtain the Helmholtz free energy and calculate the equilibrium thermal vacancy density.


6.3   Equilibrium thermal vacancies

Suppose we have a finite number of vacant sites N_{v} with a small number density in our fcc lattice,

$$n_{\mathrm{vac}} = \frac{N_{\mathrm{v}}}{M} = 1 - \frac{N}{M} \ll 1 . \tag{6.17}$$

This implies that statistically the vacancies do not interact with each other and each particle at its lattice site feels the presence of at most one of them due to the finite range of the interaction potential. Therefore, there are two types of Z_i's in the leading term of the Stillinger series Q_1 (Eq. (6.14)). We will represent the contribution of the particles which do not have any interaction with vacancies by Z_{s}, while $Z_{\mathrm{sv},i}$ denotes the contribution of those who feel a vacant position at their ith neighboring layer, $i \in \{1..n_{\mathrm{m}}\}$. Here, n_{m} represents the cut–off range of the potential in units of layers around a lattice site.

In an fcc close–packed lattice, there are certain number of particles in each layer around a particle (for a 2D representation see Fig. 6.2). This number is denoted by g_i here. Therefore, in our lattice we have $g_i N_{\mathrm{v}}$ particles in the ith neighboring layer of a vacant site which consequently feel this vacant site at their ith layer. The neighboring lattice sites of the remaining $N - N_{\mathrm{v}} \sum_{i=1}^{n_{\mathrm{m}}} g_i$ particles are completely filled. Moreover, the distinct mappings p_l in the sum over l from Eq. (6.14) is now interpreted as different configurations of N identical particles in M lattice sites. This results in a combinatorial
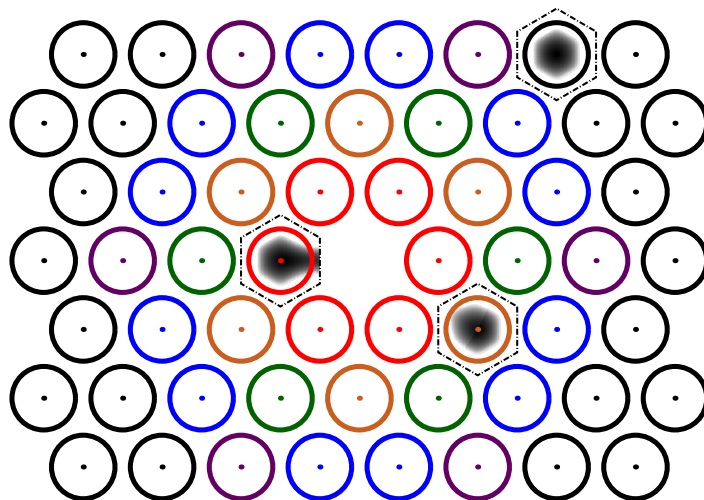
Figure 6.2: Schematic lattice in 2D with one vacancy. We have assumed a cut–off Lennard–Jones interaction potential. Shown are examples for the single particle integral domains ω_i around lattice sites $\mathbf{s}_i$, given by the hexagonal Wigner–Seitz cell surrounding the site $\mathbf{s}_i$. The grey scale indicates the (exaggerated) 1–particle energies ϕ_i^{2p} from Eq. (6.4) due to the all other fixed particles. Different colors mark different shells around the vacant position up to fifth shell neighborhood. The integral over $\exp(-\beta\phi_i^{\text{2p}})$ within the Wigner–Seitz cell gives the single–particle integral; $Z_{\text{sv},1}$ for the cell next to the vacancy (red particle), $Z_{\text{sv},2}$ for the cell in second–shell distance to the vacancy (orange particle) and Z_{s} for the cell in the upper right corner (black particle).

factor of $\binom{M}{N}$. Finally, we can rewrite the leading term as follows.

$$Q_1 \;=\; \frac{1}{\lambda^{3N}}\binom{M}{N}(Z_{\text{s}})^{N-N_{\text{v}}\sum_{i=1}^{n_{\text{m}}}g_i}\prod_{i=1}^{n_{\text{m}}}(Z_{\text{sv},i})^{g_iN_{\text{v}}} \tag{6.18}$$

The first order approximation of the free energy density is,

$$\begin{aligned}
\frac{\beta F_1}{N} &\;=\; -\frac{1}{N}\ln Q_1 \\
&\;=\; -\ln\frac{Z_{\text{s}}}{\lambda^3} - \frac{1}{N}\ln\left\{\binom{M}{N}\right\} - \frac{M-N}{N}\sum_{i=1}^{n_{\text{m}}}g_i\ln\left(\frac{Z_{\text{sv},i}}{Z_{\text{s}}}\right)
\end{aligned} \tag{6.19}$$

In the thermodynamic limit in which we let $N, M \to \infty$ while keeping the particle number density $\rho = N/V$ constant, one can rewrite the second term in Eq. (6.19) using

the Stirling approximation for large numbers[1].

$$
\begin{aligned}
-\frac{1}{N} \ln\left\{ \binom{M}{N} \right\} &= -\frac{1}{N} \ln\left(\frac{M!}{N!(M-N)!} \right) \\
&= -\frac{M}{N} \ln\left(\frac{M}{M-N} \right) + \ln\left(\frac{N}{M-N} \right) \\
&= \frac{1}{1-n_{\mathrm{vac}}} \ln n_{\mathrm{vac}} + \ln\left(\frac{1-n_{\mathrm{vac}}}{n_{\mathrm{vac}}} \right) \quad \text{with } n_{\mathrm{vac}} = 1 - \frac{N}{M} \\
&= \frac{n_{\mathrm{vac}}}{1-n_{\mathrm{vac}}} \ln n_{\mathrm{vac}} + \ln\left(1-n_{\mathrm{vac}} \right) \ .
\end{aligned}
\tag{6.20}
$$

We can combine Eqs. (6.20) and (6.19) to rewrite the first order approximation for free energy density as follows.

$$
\begin{aligned}
\frac{\beta F_1}{N} = -&\ \ln\frac{Z_{\mathrm{s}}}{\lambda^3} + \frac{n_{\mathrm{vac}}}{1-n_{\mathrm{vac}}} \ln n_{\mathrm{vac}} + \ln(1-n_{\mathrm{vac}}) \\
-&\ \frac{n_{\mathrm{vac}}}{1-n_{\mathrm{vac}}} \sum_{i=1}^{n_{\mathrm{m}}} g_i \ln\left(\frac{Z_{\mathrm{sv},i}}{Z_{\mathrm{s}}} \right) \ .
\end{aligned}
\tag{6.21}
$$

In order to obtain the equilibrium vacancy concentration $n_{\mathrm{vac,eq}}$, one should minimize the free energy density with respect to n_{vac}.

$$
\begin{aligned}
\frac{\partial\left(\beta F_1/N \right)}{\partial n_{\mathrm{vac}}} =&\ -\frac{1}{Z_{\mathrm{s}}}\frac{\partial Z_{\mathrm{s}}}{\partial n_{\mathrm{vac}}} + \frac{1}{(1-n_{\mathrm{vac}})^2} \ln n_{\mathrm{vac}} - \frac{1}{(1-n_{\mathrm{vac}})^2} \sum_{i=1}^{n_{\mathrm{m}}} g_i \ln\left(\frac{Z_{\mathrm{sv},i}}{Z_{\mathrm{s}}} \right) \\
&\ -n_{\mathrm{vac}} \sum_{i=1}^{n_{\mathrm{m}}} g_i \left\{ \frac{1}{Z_{\mathrm{sv},i}}\frac{\partial Z_{\mathrm{sv},i}}{\partial n_{\mathrm{vac}}} - \frac{1}{Z_{\mathrm{s}}}\frac{\partial Z_{\mathrm{s}}}{\partial n_{\mathrm{vac}}} \right\} \\
\approx&\ -\frac{1}{Z_{\mathrm{s}}}\frac{\partial Z_{\mathrm{s}}}{\partial n_{\mathrm{vac}}} + \ln n_{\mathrm{vac}} - \sum_{i=1}^{n_{\mathrm{m}}} g_i \ln\left(\frac{Z_{\mathrm{sv},i}}{Z_{\mathrm{s}}} \right) \ ,
\end{aligned}
\tag{6.22}
$$

where in the last step we have assumed $n_{\mathrm{vac}} \ll 1$. The equilibrium vacancy concentration $n_{\mathrm{vac,eq}}$ minimizes the free energy density and sets Eq. (6.22) to zero. As a result, $n_{\mathrm{vac,eq}}$ reads

$$
n_{\mathrm{vac,eq}} \approx \exp\left(\frac{1}{Z_{\mathrm{s}}}\frac{\partial Z_{\mathrm{s}}}{\partial n_{\mathrm{vac}}} \right) \prod_{i=1}^{n_{\mathrm{m}}} \left(\frac{Z_{\mathrm{sv},i}}{Z_{\mathrm{s}}} \right)^{g_i} \ .
\tag{6.23}
$$

---

[1]$\lim_{N\to\infty} \ln N! = N \ln N - N$

On the other hand, by denoting the density of lattice sites with $\rho_M = \frac{M}{V}$, the assumption of $n_{\text{vac}} \ll 1$ means that $\rho_M \approx \rho$. As a result, the exponent in Eq. (6.23) turns into,

$$
\begin{aligned}
\frac{1}{Z_s} \frac{\partial Z_s}{\partial n_{\text{vac}}} &= \frac{\partial \ln Z_s}{\partial \rho_M} \frac{\partial \rho_M}{\partial n_{\text{vac}}} = \frac{\partial \ln Z_s}{\partial \rho_M} \frac{\rho}{(1 - n_{\text{vac}})^2} \\
&\approx \rho \frac{\partial \ln Z_s}{\partial \rho} \\
&\approx -\rho \frac{\partial \beta F/N}{\partial \rho} = -\frac{\beta p}{\rho} \ .
\end{aligned}
\tag{6.24}
$$

In the last step we have used $\beta F/N \approx -\ln Z_s$ and the thermodynamic relation for pressure $p = \rho^2 \partial(F/N)/\partial \rho$. Using $n_{\text{vac,eq}} = \exp(-\beta \Delta G_v)$, we arrive at our central result for the Gibbs free energy of vacancy formation.

$$
\Delta G_v = \frac{p}{\rho} - \beta^{-1} \sum_{i=1}^{n_{\text{m}}} g_i \ln \left(\frac{Z_{\text{sv},i}}{Z_s} \right) \ .
\tag{6.25}
$$

This relation is useful for a substance whose particles interaction is expressed as pair interaction and the configurational integral are obtainable via Eq. (6.10). For hard spheres where $n_{\text{m}} = 1$ and $g_1 = 12$, this formula is very accurate [16]. The pressure term actually determines the order of magnitude of n_{vac} ($\sim 10^{-5}$ at coexistence) and the second term provides a correction. Note that in this case the configurational integrals Z_s and $Z_{\text{sv},1}$ are calculating the free available volume for the free moving hard sphere particle.

For a ν–component system with $\nu \geq 2$ there is no clear interpretation for the configurational integrals in terms of moving particles. In order to apply the theory to a 2–component system for instance, one may consider the effect of single moving particles of each species separately in the first order approximation. In this way, the treatment in this approximation is similar to the one–component system. However, the higher order terms corresponding to the correlated motion of two or more particles become rapidly too complex due to the appearance of inter-species terms.

For the AO model (see Section 5.1) one can extend the theory in the following way. We work in the semi–grand ensemble with fixed number of colloidal particles and constant polymer chemical potential μ_{p} which is sustained with a coupled reservoir of polymers. Here, the integrand of the configuration partition function of the crystal is weighted by the corresponding term to the polymer Hamiltonian, i.e. the Hamiltonian of an ideal gas with constant chemical potential in the free volume fraction of the lattice. The configurational partition function of the crystal of hard–sphere colloids is therefore given by,

$$
Q(N, \mu_{\text{p}}, V, T) = \frac{1}{\lambda^{3N}} \sum_l \int \cdots \int_{\Omega_{pl}} d\mathbf{r}_1 \cdots d\mathbf{r}_N \ \Theta_{\text{OV}}(\{\mathbf{r}_i\}) \exp\left(\frac{e^{\beta \mu_{\text{p}}}}{\lambda_{\text{p}}^3} V_{\text{free}}(\{\mathbf{r}_i\}) \right) . \tag{6.26}
$$

Here, the $\mathbf{r}_i$ are colloid positions and Θ_{OV} is the colloid–colloid interaction term. Due to the hard–sphere nature of the interaction, this term is written in the form of a Heaviside step function which is 1 when there is no overlap of hard–spheres, i.e. $|\mathbf{r}_i - \mathbf{r}_j| > \sigma$ for every $\{i, j\} \in [1 \ldots N]$, and zero otherwise. Moreover, λ_{p} is the polymer de Broglie thermal wavelength and V_{free} is the free volume for one polymer expressed as a function of the positions of all colloids.

The cell cluster expansion for partition function (Eq. (6.12)) now starts with the zeroth order in which all colloid particles are fixed. The zeroth order configuration integral $Z_{0,\mathrm{AO}}$ is originating from polymers only since the hard–sphere colloids do not interact with each other at this limit and is given by

$$Z_{0,\mathrm{AO}} = \exp\left(\frac{e^{\beta\mu_{\mathrm{p}}}}{\lambda_{\mathrm{p}}^3}\left(N_{\mathrm{v}}V_{\mathrm{p}}^{(1)} + (N - N_{\mathrm{v}})V_{\mathrm{p}}^{(0)}\right)\right) , \qquad (6.27)$$

where $V_{\mathrm{p}}^{(1)}$ is the free volume for one polymer within the WS cell around a vacant site and $V_{\mathrm{p}}^{(0)}$ is the free volume for one polymer within the WS cell around an occupied site. The factor N_{v} resp. $N - N_{\mathrm{v}}$ arises from the configurational integral for one polymer over the whole lattice which picks up $V_{\mathrm{p}}^{(1)}$ at all vacant sites and $V_{\mathrm{p}}^{(0)}$ at all occupied sites. Note that the simple free volume model for the crystal discussed in Section 5.4.1 corresponds to the partition function $Z_{0,\mathrm{AO}}$ with $N_{\mathrm{v}} = 0$.

The configuration integral corresponding to a single moving colloid particle reads

$$\begin{aligned}
Z_{i,\mathrm{AO}}^l &:= \int_{\omega_{p_l}} \mathrm{d}\mathbf{r}_i\, \Theta_{\mathrm{OV}}\left(\mathbf{r}_i; \{\mathbf{r}_j\}\right) \exp\left(\frac{e^{\beta\mu_{\mathrm{p}}}}{\lambda_{\mathrm{p}}^3}V_{\mathrm{free}}(\mathbf{r}_i; \{\mathbf{r}_j\})\right) \quad \text{with } \mathbf{r}_j = \mathbf{s}_j (j \neq i) \\
&\approx \int_{\omega_{p_l}} \mathrm{d}\mathbf{r}_i\, \Theta_{\mathrm{OV}}\left(\mathbf{r}_i; \{\mathbf{r}_j\}\right) \exp\left(\frac{e^{\beta\mu_{\mathrm{p}}}}{\lambda_{\mathrm{p}}^3}V_{\mathrm{free}}(\mathbf{s}_i; \{\mathbf{r}_j\})\right) \\
&\approx Z_{0,\mathrm{AO}}\, Z_{i,\mathrm{HS}}^l .
\end{aligned} \qquad (6.28)$$

Here, we have approximated the available free volume for the polymers with a single moving particle $V_{\mathrm{free}}(\mathbf{r}_i; \{\mathbf{s}_j\})$ with the free volume with all particles frozen at their lattice sites $V_{\mathrm{free}}(\mathbf{s}_i; \{\mathbf{s}_j\})$. As a result, the configuration partition function of a single moving colloid is approximated by the product of $Z_{0,\mathrm{AO}}$ from Eq. (6.27) and $Z_i^l = Z_{i,\mathrm{HS}}^l$ from Eq. (6.10) with hard–sphere potential. By making this approximation, the polymer contribution is assumed to be unaffected by the free-to-move colloids. We expect this approximation to be accurate for $q \gtrsim 0.6$ where polymers preferably occupy vacant sites[2]. Using Eqs. (6.27) and (6.28), the first order approximation for the AO model

---

[2]see Chapter 5.4.3 and Fig. 5.13

partition function $Q_{1,\mathrm{AO}}$ is given by,

$$
\begin{aligned}
Q_{1,\mathrm{AO}} &= \frac{1}{\lambda^{3N}} \sum_l Z_{i,\mathrm{AO}}^l \approx \frac{1}{\lambda^{3N}} \sum_l Z_{0,\mathrm{AO}} \, Z_{i,\mathrm{HS}}^l \\
&\approx \frac{1}{\lambda^{3N}} \binom{N+N_{\mathrm{v}}}{N} \left(Z_{\mathrm{s}}^{\mathrm{HS}}\right)^{N-g_1 N_{\mathrm{v}}} \left(Z_{\mathrm{sv}}^{\mathrm{HS}}\right)^{g_1 N_{\mathrm{v}}} \\
&\quad \times \exp\left(\frac{e^{\beta\mu_{\mathrm{p}}}}{\lambda_{\mathrm{p}}^3} \left(N_{\mathrm{v}} V_{\mathrm{p}}^{(1)} + (N-N_{\mathrm{v}})V_{\mathrm{p}}^{(0)}\right)\right) ,
\end{aligned} \tag{6.29}
$$

where as in the single–component case (Eq. (6.18)) the distribution of N_{v} vacancies on the available $M = N + N_{\mathrm{v}}$ lattice sites converts the sum over l to a combinatorial factor. The configuration integral for a single moving hard–sphere particle with a vacant site in its neighborhood is denoted by $Z_{\mathrm{sv}}^{\mathrm{HS}}$, and $Z_{\mathrm{s}}^{\mathrm{HS}}$ represents one whose its neighboring lattice sites are completely filled. Using Eq. (6.29) the Helmholtz free energy per particle reads

$$
\begin{aligned}
\beta f_{1,\mathrm{AO}} &= \frac{\beta F_{1,\mathrm{AO}}}{N} = -\frac{1}{N} \ln Q_{1,\mathrm{AO}} \\
&= \frac{n_{\mathrm{vac}}}{1-n_{\mathrm{vac}}} \ln n_{\mathrm{vac}} + \ln\left(1-n_{\mathrm{vac}}\right) \\
&\quad - \ln\left(\frac{Z_{\mathrm{s}}^{\mathrm{HS}}}{\lambda^3}\right) - \frac{g_1 n_{\mathrm{vac}}}{1-n_{\mathrm{vac}}} \ln\left(\frac{Z_{\mathrm{sv}}^{\mathrm{HS}}}{Z_{\mathrm{s}}^{\mathrm{HS}}}\right) \\
&\quad - \frac{e^{\beta\mu_{\mathrm{p}}}}{\lambda_{\mathrm{p}}^3} \left(\frac{n_{\mathrm{vac}}}{1-n_{\mathrm{vac}}} V_{\mathrm{p}}^{(1)} + \frac{1-2n_{\mathrm{vac}}}{1-n_{\mathrm{vac}}} V_{\mathrm{p}}^{(0)}\right) .
\end{aligned} \tag{6.30}
$$

Here the logarithm of the combinatorial factor in Eq. (6.29) is calculated by using the Stirling approximation since in the thermodynamic limit $N, M \to 0$ while $\rho = N/V$ is kept constant (see Eq. (6.20)). Considering the definition of polymer reservoir packing fraction $\eta_{\mathrm{p,r}}$ from Eq. (5.5), by minimizing the free energy per particle with respect to the vacancy concentration n_{vac} we have,

$$
\begin{aligned}
\frac{\partial \beta f_{1,\mathrm{AO}}}{\partial n_{\mathrm{vac}}} &= \frac{1-2n_{\mathrm{vac}}}{(1-n_{\mathrm{vac}})^2} \ln n_{\mathrm{vac}} - \frac{1}{Z_{\mathrm{s}}^{\mathrm{HS}}} \frac{\partial Z_{\mathrm{s}}^{\mathrm{HS}}}{\partial n_{\mathrm{vac}}} - \frac{g_1(1-2n_{\mathrm{vac}})}{(1-n_{\mathrm{vac}})^2} \ln\left(\frac{Z_{\mathrm{sv}}^{\mathrm{HS}}}{Z_{\mathrm{s}}}\right) \\
&\quad - \frac{g_1 n_{\mathrm{vac}}}{1-n_{\mathrm{vac}}} \left(\frac{1}{Z_{\mathrm{sv}}^{\mathrm{HS}}} \frac{\partial Z_{\mathrm{sv}}^{\mathrm{HS}}}{\partial n_{\mathrm{vac}}} - \frac{1}{Z_{\mathrm{s}}^{\mathrm{HS}}} \frac{\partial Z_{\mathrm{s}}^{\mathrm{HS}}}{\partial n_{\mathrm{vac}}}\right) \\
&\quad - \frac{\eta_{\mathrm{p,r}}}{\frac{\pi}{6}(q\sigma_{\mathrm{c}})^3} \left(\frac{(1-2n_{\mathrm{vac}})V_{\mathrm{p}}^{(1)} - V_{\mathrm{p}}^{(0)}}{(1-n_{\mathrm{vac}})^2} + \frac{n_{\mathrm{vac}}}{1-n_{\mathrm{vac}}} \frac{\partial V_{\mathrm{p}}^{(1)}}{\partial n_{\mathrm{vac}}} + \frac{1-2n_{\mathrm{vac}}}{1-n_{\mathrm{vac}}} \frac{\partial V_{\mathrm{p}}^{(0)}}{\partial n_{\mathrm{vac}}}\right) \\
&\approx \ln n_{\mathrm{vac}} + \frac{\beta p_{\mathrm{HS}}}{\rho} - g_1 \ln\left(\frac{Z_{\mathrm{sv}}^{\mathrm{HS}}}{Z_{\mathrm{s}}^{\mathrm{HS}}}\right) - \frac{\eta_{\mathrm{p,r}}}{\frac{\pi}{6}(q\sigma_{\mathrm{c}})^3} \left(V_{\mathrm{p}}^{(1)} - V_{\mathrm{p}}^{(0)} + \frac{\partial V_{\mathrm{p}}^{(0)}}{\partial n_{\mathrm{vac}}}\right) , \tag{6.31}
\end{aligned}
$$

where in the last step we have used $n_\mathrm{vac} \ll 1$ and the approximation of the hard–sphere pressure βp_HS from Eq. (6.24). The partial derivative of $V_\mathrm{p}^{(0)}$ with respect to n_vac can be written as

$$
\begin{aligned}
\frac{\partial V_\mathrm{p}^{(0)}}{\partial n_\mathrm{vac}} &= \frac{\partial V_\mathrm{p}^{(0)}}{\partial \rho_M} \frac{\partial \rho_M}{\partial n_\mathrm{vac}} = \frac{\partial V_\mathrm{p}^{(0)}}{\partial \rho_M} \frac{\rho}{(1 - n_\mathrm{vac})^2} \\
&\approx \rho \frac{\partial V_\mathrm{p}^{(0)}}{\partial \rho} .
\end{aligned}
\tag{6.32}
$$

where $\rho_M = M/V$ is the lattice site density and in the last step it is approximated by the particle number density since $n_\mathrm{vac} \ll 1$. Note that $-\rho_\mathrm{p,r} V_\mathrm{p}^{(0)}$ corresponds to the polymer contribution to the free energy density in an ideal crystal (see Section 5.2). Therefore, the outcome of Eq. (6.32) can be interpreted as the polymers contribution to the pressure of the system. Finally, the equilibrium vacancy concentration for the AO model $n_\mathrm{vac,eq}^\mathrm{AO}$ reads[3]

$$
\begin{aligned}
\ln n_\mathrm{vac,eq}^\mathrm{AO} &\approx -\frac{\beta p_\mathrm{HS}}{\rho} + g_1 \ln\left(\frac{Z_\mathrm{sv}^\mathrm{HS}}{Z_\mathrm{s}^\mathrm{HS}}\right) + \frac{\eta_\mathrm{p,r}}{\frac{\pi}{6}(q\sigma_\mathrm{c})^3}\left(V_\mathrm{p}^{(1)} - V_\mathrm{p}^{(0)} + \rho \frac{\partial V_\mathrm{p}^{(0)}}{\partial \rho}\right) \\
&\approx -\frac{\beta p_\mathrm{AO}}{\rho} + g_1 \ln\left(\frac{Z_\mathrm{sv}^\mathrm{HS}}{Z_\mathrm{s}^\mathrm{HS}}\right) + \frac{\eta_\mathrm{p,r}}{\frac{\pi}{6}(q\sigma_\mathrm{c})^3}\left(V_\mathrm{p}^{(1)} - V_\mathrm{p}^{(0)}\right)
\end{aligned}
\tag{6.33}
$$

In the first form, the connection to the equilibrium vacancy concentration of a hard–sphere system is shown. Here, starting from its hard–sphere value at $\eta_\mathrm{p,r} = 0$ the vacancy concentration increases linearly with polymer reservoir packing fraction. On the other hand, the second representation relates the equilibrium vacancy concentration to an equation of state term and an entropic term. The volume V_p^i is determined numerically for different q by a simple Monte–Carlo routine [140]. The obtained results for $q = 0.3$ with $\rho = 1.2\sigma^3$, and for $q = 0.6, 0.8$ with $\rho = 1.1\sigma^3$ from Ref. [17] are presented in Section 6.4.2.

6.4   Numerical results

We have investigated four types of systems: Hard spheres as model system for colloids, the Lennard–Jones potential, Nickel as an exemplary case of a metal treated with EAM, and the AO model for colloid–polymer mixture. While for the latter only the

---

[3] In Ref. [17] we have used $Z_\mathrm{s}^\mathrm{HS} \approx Z_\mathrm{sv}^\mathrm{HS}$. Therefore, the integral term $-g_1 \ln\left(Z_\mathrm{sv}^\mathrm{HS}/Z_\mathrm{s}^\mathrm{HS}\right)$ and the polymers contribution to the pressure $\rho(\partial V_\mathrm{p}^{(0)}/\partial \rho)$ are missing in the expression for $n_\mathrm{vac,eq}^\mathrm{AO}$.

results for thermal vacancies are represented here, the free energy per particle using the first order approximation is also calculated for the other three. In case of LJ we also have calculated the equation of state and compared it with the parametrized equation of state of van der Hoef [120,141]. For EAM, we have employed three different versions for Nickel [137–139] and obtained the sublimation line. The results show good agreement with available simulation results. Finally, for the AO model we have compared the results from the analytical expression in Eq. (6.33) with the result of constrained minimization of effective free energy density (see Section 5.4.1) for three different size ratios. The agreement between the two becomes better by increasing q as is expected.

6.4.1 Hard spheres

The interaction between two hard spheres with diameter σ is given by u_{HS} as a function of their center distance r_{ij}.

$$u_{\mathrm{HS}}(r_{ij}) \;=\; \begin{cases} \infty & r_{ij} \leq \sigma \\ 0 & \text{otherwise} \end{cases}, \tag{6.34}$$

For a hard–sphere system, the internal energy Φ is zero and the configuration integrals correspond to the available volume for the freely moving particle. The maximum layer of neighbors which should be taken into account is $n_{\mathrm{m}} = 1$ whose number of particles is $g_1 = 12$. The relevant configurational integrals are Z_{s} and $Z_{\mathrm{sv},1}$ which subsequently correspond to a particle with all its neighboring lattice site fille with particles and one which is missing a neighboring particle.

The free energy per particle obtained by the first order approximation of configuration integrals (Eq. (6.15)) is within 1% of available simulation results. The remaining discrepancy is lifted by taking into account the second order term which corresponds to two moving particles [140]. This unveils the rapid convergence of the Stillinger series for a hard–sphere system. Therefore, one can assume the first term already contains the basic physics of the model. Due to the short range of the hard–sphere potential the equilibrium vacancy concentration from Eq. (6.25) reads

$$n_{\mathrm{vac,eq}} = \exp\left(-\frac{\beta p}{\rho}\right)\left(\frac{Z_{\mathrm{sv},1}}{Z_{\mathrm{s}}}\right)^{12}. \tag{6.35}$$

As it is shown in Fig. 6.3, the corresponding results for $n_{\mathrm{vac,eq}}$ shows very good agreement with the simulation data from Refs. [102,103] above the liquid–solid coexistence density $\rho = N/V = 1.040$. Here, the equation–of–state term $p/\rho \gtrsim 10 k_{\mathrm{B}}T$ is the main contributor to the Gibbs free energy of vacancy formation ΔG_{v}, while the vacancy integral term is responsible for about $-1\,k_{\mathrm{B}}T$.
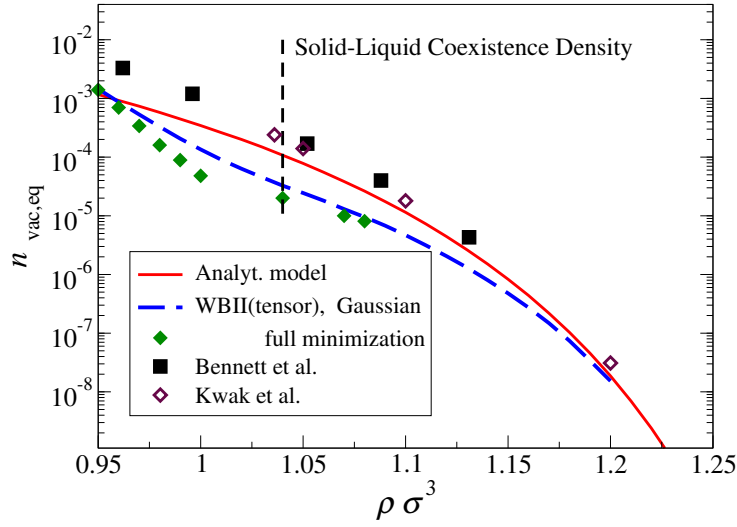
Figure 6.3: Vacancy concentration versus density for hard spheres compared with simulation results of Bennett et al. [103] and Kwak et al. [102]. The error bars for the simulation data are unknown. The FMT results obtained by constrained (blue curve) and full minimization (green diamonds) of the WBII(tensor) functional is also included.

Within DFT descriptions of the hard spheres, WBII(tensor) is one of the FMT functionals which account for crystallization and predicts a correct order of magnitude for the vacancy concentration around the liquid–solid coexistence density [80]. In Fig. 6.3, we also include the results for constrained and full minimization of this functional. For a more detailed information on the FMT results for vacancy concentration see Section 4.5.2.

6.4.2 The AO model

For the AO model, an expression for $n_{\text{vac,eq}}$ is given by Eq. (6.33) which shows that in the first order approximation the Gibbs free energy of vacancy formation $\beta \Delta G_{\text{v}} = -\ln n_{\text{vac,eq}}$ decreases linearly with $\eta_{\text{p,r}}$ from its hard sphere value at $\eta_{\text{p,r}} = 0$. The main contribution to the linear coefficient is obtained by calculating ΔV_{p} which is the difference in the available free volume for polymers within a Wigner–Seitz cell for a vacant cell $V_{\text{p}}^{(1)}$ and an occupied one $V_{\text{p}}^{(0)}$ while the colloids are assumed to be fixed at their lattice sites. There is a modification from the AO model pressure $\beta p_{\text{AO}}/\rho$ which is obtained analytically in the following way. Consider the free volume fraction of an ideal crystal α which is the ratio of the free available volume for polymers V_{free} in an ideal fcc crystal (no vacancy) to the total volume of the cell V_{cell}. The free volume

fraction is related to $V_{\mathrm{p}}^{(0)}$ as follows.

$$\alpha = \frac{V_{\mathrm{free}}}{V_{\mathrm{cell}}} = \frac{4V_{\mathrm{p}}^{(0)}}{a^3} = \frac{V_{\mathrm{p}}^{(0)}}{\rho}. \tag{6.36}$$

Here, a is the side length of the unit cell and $\rho = 4/a^3$ is the colloid density. For larger polymer–colloid size ratios, i.e. $q = 0.6, 0.8$, the free volume fraction of an ideal fcc crystal is zero[4]. Subsequently, $V_{\mathrm{p}}^{(0)}$ and its derivative with respect to ρ vanish for these size ratios. For smaller q's however, assuming that the 4–body overlaps of the excluded volumes are negligible, one can use the provided analytical form for the free volume fraction (Eq. (5.49)) and Eq. (6.36) to calculate $\partial V_{\mathrm{p}}^{(0)}/\partial\rho$.

$$\begin{aligned}\frac{\partial V_{\mathrm{p}}^{(0)}}{\partial\rho} &= \alpha + \rho\,\frac{\partial\alpha}{\partial\rho} \\ &= 2\alpha - 1 + \frac{\pi}{6}\,\rho\,(r - 9r^3) \quad \text{with} \quad r = \frac{a}{\sqrt{2}(1+q)\sigma_{\mathrm{c}}}\,.\end{aligned} \tag{6.37}$$

The obtained linear coefficients and the non–vanishing modification term for $q = 0.3$ is presented in table 6.1.

We also have computed $n_{\mathrm{vac,eq}}$ by the constrained minimization of an FMT functional for the AO model, the linearized WBII(tensor) functional. The obtained results approximately confirm the exponential increase of vacancy concentration as a function of polymer reservoir packing fraction $\eta_{\mathrm{p,r}}$. As it is shown in Fig. 6.4, there is a semiquantitative agreement between the FMT results and analytical relation for larger polymer colloid size ratios $q \gtrsim 0.6$. However, for lower size ratios the slope of $\ln n_{\mathrm{vac,eq}}(\eta_{\mathrm{p,r}})$ is considerably overestimated by the simple formula. This is due to the fact that at this size ratio, polymers tend to fill in the interstitials rather than the vacant site and this is not considered in the approximate zeroth order configuration integral $Z_{0,\mathrm{AO}}$ (see Eq. (6.27)).

---

[4]See page 87 and the discussion on the free volume fraction of an ideal crystal.

Table 6.1: The linear coefficient and its modification for the equilibrium vacancy concentration of the AO model.

$\{q, \rho\sigma_{\mathrm{c}}^3\}$	$\ln n_{\mathrm{vac,eq}}^{\mathrm{AO}}(\eta_{\mathrm{p,r}} = 0) = \ln n_{\mathrm{vac,eq}}^{\mathrm{HS}}$	$\Delta V_{\mathrm{p}} = V_{\mathrm{p}}^{(1)} - V_{\mathrm{p}}^{(0)}$	$\rho\,\frac{\partial V_{\mathrm{p}}^{(0)}}{\partial\rho}$
$\{0.3, 1.2\}$	-18.9	34.5	-7.6
$\{0.6, 1.1\}$	-12.6	1.4	0.0
$\{0.8, 1.2\}$	-12.6	0.15	0.0
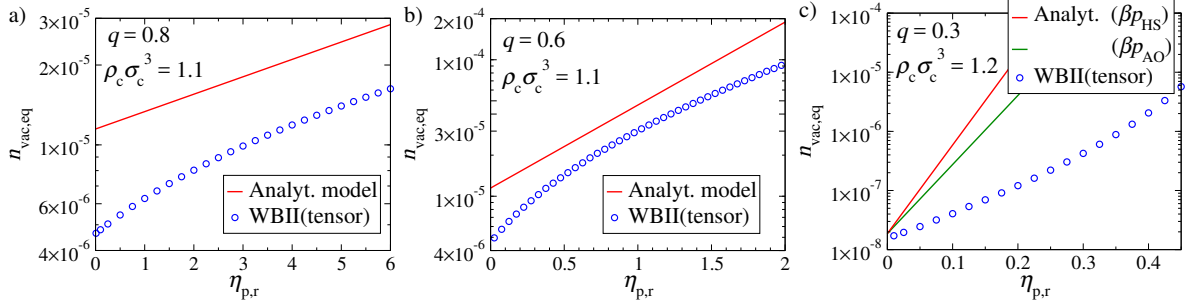
Figure 6.4: Equilibrium vacancy concentration for the AO model as a function of polymer reservoir packing fraction $\eta_{\mathrm{p,r}}$. The results are obtained by constrained minimization of WBII(tensor) functional for three parameter pairs of polymer–colloid size ratio and colloid density $\{q, \rho\sigma_{\mathrm{c}}^3\}$. Solid red lines correspond to the estimate of Eq. (6.33) while the AO model pressure is neglected. Solid green line for $q = 0.3$ is the same while the modification from Eq. (6.37) is considered.

6.4.3   The Lennard–Jones potential

In the case of LJ, we have used a truncated and shifted version of the potential $u_{\mathrm{LJ}}^{\mathrm{c}}(r)$.

$$u_{\mathrm{LJ}}(r) \;=\; 4\epsilon\left[-\left(\frac{r}{\sigma}\right)^{-6} + \left(\frac{r}{\sigma}\right)^{-12}\right],$$

$$u_{\mathrm{LJ}}^{\mathrm{c}}(r) \;=\; \begin{cases} u_{\mathrm{LJ}}(r) - u_{\mathrm{LJ}}(r_c) & \text{for } r \leq r_c \\ 0 & \text{otherwise} \end{cases}, \tag{6.38}$$

where r_{c} is the cut–off range which is either set to 6σ or 2.25σ in our studies.

For an fcc crystalline state, the pressure is obtained numerically for a range of particle densities and temperatures using the first order approximation for the free energy density of an ideal crystal $\beta F_1/N \approx -\ln Z_{\mathrm{s}}$. The configuration integral Z_{s} is calculated using Gauss–Legendre quadrature with 20 grid points in a cubic sub–volume of a Wigner–Seitz cell whose side length is chosen according to the ratio of the configuration integrand at the center and at the border of integration domain. At the sublimation line, the solid–gas coexistence density, we have $p \approx 0$. Therefore, we can determine the sublimation line by finding the densities at which the obtained pressure is zero. This is done for $r_{\mathrm{c}} = 2.25\sigma$ and 6σ and is shown in Fig. 6.5.a along with the result from the parametrized van der Hoef equation of state [120, 141]. For $r_{\mathrm{c}} = 6\sigma$ which is the same cutoff used as in Ref. [120], the low temperature results match perfectly the sublimation line of the van der Hoef equation of state. With increasing temperature, the higher order terms $Z_{ij} \ldots$ should be considered for calculation of the free energy density to compensate the deviation in the description of the sublimation lines.
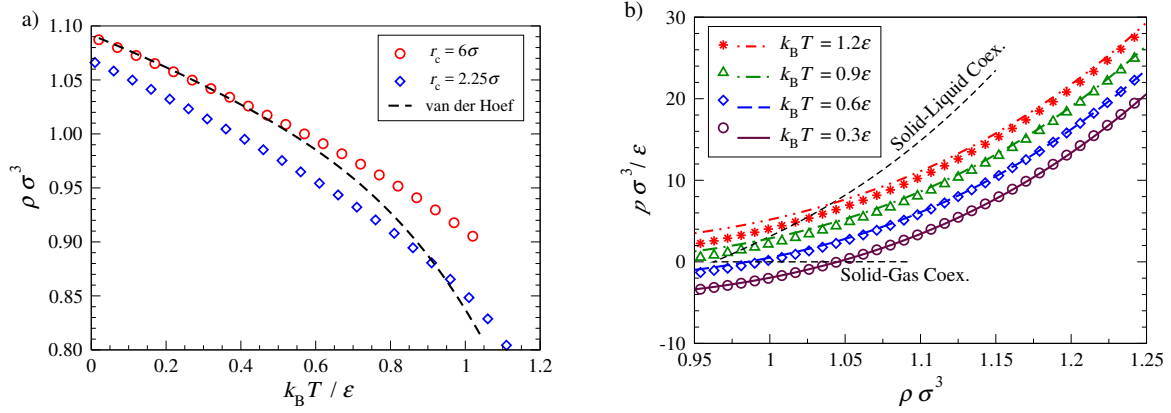
Figure 6.5: Phase diagram of Lennard–Jones system. a) Sublimation line obtained by finding the density at which the pressure is zero for two different cut–off ranges. The pressure is calculated from the first order approximation of the free energy density. The dashed line is the parametrized van der Hoef equation of state [120]. b) Comparison of the pressure of crystalline Lennard–Jones solid with $r_c = 6\sigma$ calculated for different temperatures (symbols) with van der Hoef equation of state (solid lines) from ref. [120].

Equation of state curves $p(\rho)$ for four different temperatures T for $r_c = 6\sigma$ are shown in Fig. 6.5.b. For temperatures below and around the triple temperature $k_B T_t \approx 0.7\epsilon$, the crystal equation of state obtained by the first order approximation of the free energy density is in good agreement with the parametrization of van der Hoef as expected. For higher temperatures deviations are visible especially at the lower densities. However, as a result of the upward shifting of the solid–liquid coexistence density, the results for stable crystals which occur at higher densities are still well described.

For $T = 0$, one may assume all N particles of an ideal crystal fixed at their lattice site. Denoting their pair interaction $u(r)$ the cohesive energy of such system reads

$$
U_{\mathrm{coh},0} = \frac{1}{2} \sum_{i=1}^{N} \sum_{\substack{j=1 \\ j \neq i}}^{N} u(r_{ij}) = \frac{N}{2} \sum_{\substack{j=1 \\ j \neq i}}^{N} u(r_{ij}) = N u_{\mathrm{coh}} \,,
\tag{6.39}
$$

where the distance between particles i and j is denoted by $r_{ij} = |\mathbf{r}_i - \mathbf{r}_j|$ and u_{coh} denotes the cohesive energy per particle. By choosing $u(r) = u_{\mathrm{LJ}}^c(r)$ from Eq. (6.38) with $r_c = 6\sigma$, we have the minimal cohesive energy $u_{\mathrm{coh}} \simeq -8.52\epsilon$ at $\rho\sigma^3 = 1.09$. At this temperature limit, the vacancy formation energy $E_v = \Delta G_v(T = 0)$ may be approximated by modulus of the difference between $U_{\mathrm{coh},0}$ with the cohesive energy of a crystal which contains a vacant site $U_{\mathrm{coh},1}$. Suppose the missing particle is removed from lattice site s_1 and the indices for other N particles run from $2 \ldots N+1$. Assuming all particles remained fixed at their lattice site after creating the vacancy, the cohesive

energy reads

$$
\begin{aligned}
U_{\mathrm{coh},1} &= \frac{1}{2} \sum_{i=2}^{N+1} \sum_{\substack{j=2 \\ j \neq i}}^{N+1} u(r_{ij}) \\
&= \sum_{i=1}^{N+1} \underbrace{\frac{1}{2} \sum_{\substack{j=1 \\ j \neq i}}^{N+1} u(r_{ij})}_{u_{\mathrm{coh}}} - \underbrace{\frac{1}{2} \sum_{i=2}^{N+1} u(r_{i1})}_{u_{\mathrm{coh}}} - \underbrace{\frac{1}{2} \sum_{j=2}^{N+1} u(r_{1j})}_{u_{\mathrm{coh}}} \\
&= (N-1) u_{\mathrm{coh}} \ .
\end{aligned} \tag{6.40}
$$

This implies that for $T \to 0$, the vacancy formation energy E_{v} for a system with pair interaction is approximately minus the cohesive energy per particle u_{coh}. The expected deviation is due to the displacement of the neighboring particles for relaxation of the lattice after creating the vacant site which minimizes E_{v}.

In order to calculate the Gibbs free energy of the vacancy concentration at finite temperatures, we have used Eq. (6.25) by considering the vacancies up to the 6th neighboring layer of the moving particle $n_{\mathrm{m}} = 6$.

$$
\Delta G_{\mathrm{v}} = \frac{p}{\rho} - \beta^{-1} \sum_{i=1}^{6} g_i \ln \left(\frac{Z_{\mathrm{sv},i}}{Z_{\mathrm{s}}} \right) \ . \tag{6.41}
$$

The vacancy configuration integral terms $Z_{\mathrm{sv},i}$ with $i = 1 \ldots 6$ are calculated in the same way as Z_{s}. The obtained ΔG_{v} along the sublimation line are presented in Fig. 6.6.a up to the triple temperature at which the sublimation line forks into the liquid–solid coexistence line and the zero pressure line.

In the low temperature limit $T \to 0$, the obtained values for the Gibbs free energy of vacancy formation converges to $E_{\mathrm{v}} \simeq 8.06\epsilon$. The difference of E_{v} with $|u_{\mathrm{coh}}| \simeq 8.52\,\epsilon$ is partly recovered by considering higher order terms in the vacancy integral terms $n_{\mathrm{m}} > 6$. For LJ with $r_{\mathrm{cut}} = 6\sigma$ the maximum required value for n_{m} at low temperatures is 28. By considering this value for the maximum neighboring layer the vacancy formation at zero temperature is $E_{\mathrm{v}} \simeq 8.46\epsilon$. The remaining difference $\delta u_{\mathrm{coh}} = |u_{\mathrm{coh}}| - E_{\mathrm{v}}$ is due to the effect of the collective particle displacements after creating a vacancy at $T = 0$ which is not considered in the calculation of u_{coh}. This modification to u_{coh} can be approximated by a sum of single–particle displacement in the potential field of otherwise fixed particles [142]. For this purpose, $N - 1$ particles are fixed at their ideal lattice sites and the single remaining particle is shifted until the total energy is minimized. The sum over all 1–particle–shifts corresponds to the energy deviations

from the ideal lattice $\delta u_{\mathrm{coh}}^{\mathrm{1p}}$.

$$\delta u_{\mathrm{coh}}^{\mathrm{1p}} \;=\; \frac{1}{N} \sum_{i=1}^{N} \left\{ \min_{\mathbf{r}_i} \phi_i \left(\mathbf{r}_i; \mathbf{r}_j = \mathbf{s}_j \right) \right\} \quad \text{with } j \neq i \; . \tag{6.42}$$

For LJ with $r_{\mathrm{cut}} = 6\sigma$, this difference is $\delta u_{\mathrm{coh}}^{\mathrm{1p}} \approx 0.05$ which recovers the difference between u_{coh} and E_{v} [142]. For finite temperatures, the increase in probability of vacancy formation dictates itself by the entropy of vacancy formation $T\Delta S_{\mathrm{v}}$.

$$\Delta G_{\mathrm{v}} = E_{\mathrm{v}} - T\Delta S_{\mathrm{v}} \; . \tag{6.43}$$

Our results show that the often–made assumption ΔS_{v} being independent of the temperature holds only approximately (see Fig. 6.6.a).

We have compared our results with the simulation data of Jacucci et al. [134]. In their study, they have placed the vacant site in the middle of a rather small simulation box whose side length is three times the side length of the fcc cubic unit cell and contains 107 particles. In order to make a reasonable judgement on the quality of our approximation, note that the cutoff on the maximal number of shells n_{m} in Eq. (6.25) has to be chosen such that the maximum shell radius $\approx 1.5\,a$. This is the case for $n_{\mathrm{m}} = 4$ with maximum shell radius $\sqrt{2}a$. Moreover, with this choice it is ensured that there is no interaction between the vacancies in the periodic image of the simulation box. With this considerations, our data are consistent with the simulation data of Jacucci et al.

In Fig. 6.6.b we have represented the equilibrium thermal vacancy concentration $n_{\mathrm{vac,eq}}$ for a stable crystal in the T–ρ–plane. The vacancy concentrations are quickly calculated using Eq. (6.25) and its maximum occurs at the triple point with $n_{\mathrm{vac,eq}} \approx 10^{-4}$. Although it is the same result as HS near coexistence density (see page 125), it has a completely different origin. Unlike the HS case, the pressure term in Eq. (6.41) does not contribute since we are moving along the sublimation line and p is almost zero. Here, the main contributor to the Gibbs free energy of vacancy formation are the vacancy configuration integrals $Z_{\mathrm{sv},i}$.

6.4.4   The Embedded-Atom-Model

As an exemplary case for a metallic system, we have studied Nickel by means of the Embedded–Atom Model (EAM) which is a semi–empirical method for classical treatment of a many–body metallic system for calculating its total potential energy [143]. As it is mentioned earlier in Section 6.1, the 1–particle energy is calculated using Eqs. (6.5) and (6.6). The obtained ϕ_i's are then used to calculate the configuration integrals Z_{s} and $Z_{\mathrm{sv},i}$ from Eq. (6.25). We have examined three versions of parametrization of the EAM
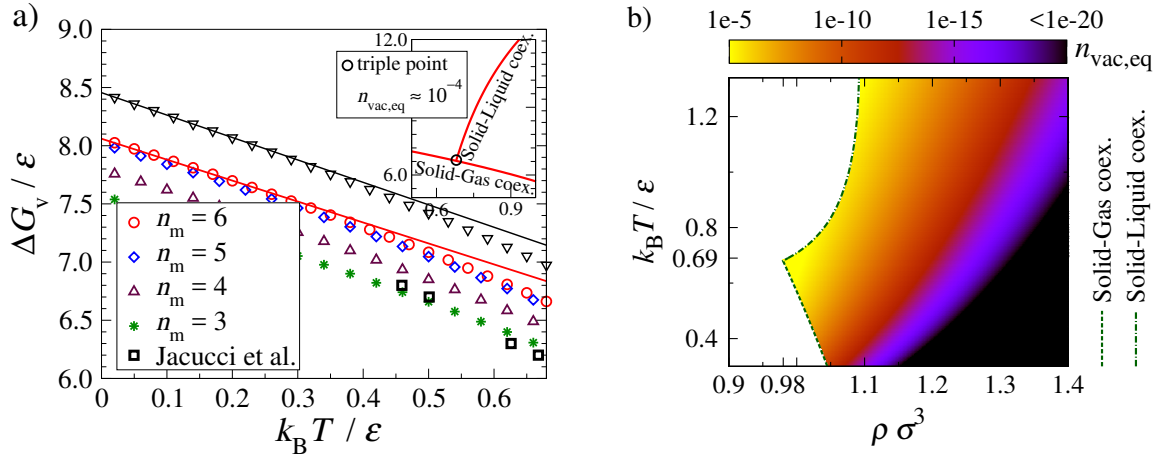
Figure 6.6: Vacancy concentration and the Gibbs free energy of its formation for the Lennard–Jones system (a) Gibbs energy of vacancy formation along the zero pressure line and the solid–liquid coexistence line, meeting in the triple point. Different symbols show the dependence of ΔG_v on the potential range through the maximum shell index n_m. The solid lines are $\Delta G_v = E_v - T\Delta S_v$ with $E_v = 8.06\epsilon$ and $\Delta S_v = 1.8\epsilon/k_B$ for the red curve and $E_v = 8.46\epsilon$ and $\Delta S_v = 1.9\epsilon/k_B$ for the black curve. The black squares are simulation data of Jacucci et al. [134], error bars are unknown. The inset is the same plot for the temperatures in vicinity of the triple point. Here, the sublimation line forks into the solid–liquid coexistence line and $p = 0$. (b) Equilibrium vacancy concentration in the ρ–T plane. The long–range cutoff $r_c = 6\sigma$ is used for obtaining these results. The maximum considered neighboring layer of a vacancy is $n_m = 6$.

potential given by Foiles (F85) in Ref. [137], Foiles, Baskes and Daw (FBD86) in Ref. [138], and Mishin et al. (M99) in Ref. [139]. All these potentials have been optimized with respect to a number of solid properties at $T = 0$. For F85 and FBD86, the total potential energy is decomposed into a repulsive and an attractive part. The repulsive part is the interaction of the nuclei of the atom i with the host nuclei $j = 1 \ldots N$, $j \neq i$ which is represented as the repulsive Coulomb interaction with the screened nuclei charges $Z(r)$.

$$\phi_i^{2p}(\mathbf{r}_1, \ldots, \mathbf{r}_N) = \frac{1}{2} \sum_{\substack{j=1 \\ j \neq i}}^{N} u(r_{ij}) \,,$$

$$u(r_{ij}) = \frac{1}{4\pi\epsilon_0} \frac{Z^2(r_{ij})e^2}{r_{ij}} \,, \tag{6.44}$$

where e is the elementary charge. While in F85 the screening function is fitted to a fourth order polynomial with cutoff range of 3.00Å, it is obtained in FBD86 by fitting a

Yukawa potential to experimental values.

The upper cut–off range of the screening function $Z(r)$ is 3.35Å for FBD86. The attractive part of the total potential energy is due to the energy gain of "embedding" atom i into the system. This embedding energy is expressed as a function of the local host electronic density ρ_i^a which is a superposition of the electronic density of atoms $j = 1 \ldots N$, $j \neq i$. The atomic electronic density of a single atom which is expressed as a function of the distance is the solution of Hartree-Fock equations for the electrons in the outer shells. Finally, the embedding function is a parametrization fit to a number of experimentally measured parameters: sublimation energy, equilibrium lattice constant, elastic constant, vacancy formation energy at $T = 0, \ldots$.

Unlike F85 and FBD86, M99 uses very general forms of the potential functions with no reference to their original physical meaning. For the two–body potential $u(r)$, the atomic electronic density of a single atom $\rho_{ij}^a(r)$, and the embedding function $F(\rho_i^a)$, we have used the tabulated values from Ref. [139]. Both $u(r)$ and $\rho_{ij}^a(r)$ have finite values in the range of 2.0Å $\leq r \leq 5.804$Å and are zero otherwise. The functions have been fitted to a number of observables: the equilibrium lattice constant, the cohesive energy, the vacancy formation energy, the vacancy migration energy, the intrinsic stacking fault energy, and the experimentally measured phonon–dispersion relations [139]. Despite the comprehensive list of fitting parameters, the obtained results for the melting temperature determined by molecular dynamic simulations for F85 and FBD86, 1720 K and 1750 K respectively, are much closer to the experimental value of 1728 K. The obtained results for M99 is 2240 K [144].

The sublimation line $p = 0$ is obtained using the first order approximation of the free energy density and numerical computation of the pressure. A comparison of the results with simulation data is represented in Fig. 6.7 which shows good agreement for F85 and M99 [144]. Furthermore, we have obtained the sublimation density for $T = 0$ by a linear fit to the sublimation curves. The obtained results are compared in table 6.2.

For $T = 0$, the cohesive energy of an ideal crystal with no vacancy and N atoms fixed at their lattice sites, is written as a function of the pair potential and the embedding function:

$$U_{\mathrm{coh},0} = \sum_{i=1}^{N} \left\{ \frac{1}{2} \sum_{\substack{j=1 \\ j \neq i}}^{N} u(r_{ij}) + F\left(\rho_i^a\right) \right\} = N u_{\mathrm{coh}} \qquad \text{with } \rho_i^a = \sum_{\substack{j=1 \\ j \neq i}}^{N} \rho_{ij}^a(r_{ij}) \quad (6.45)$$

Here, due to the non–linear nature of embedding functions F, there is no straightforward derivation of an analytical form for $U_{\mathrm{coh},1}$, the cohesive energy of a crystal with one vacant site. In Fig. 6.8, we compare the cohesive energy per particle
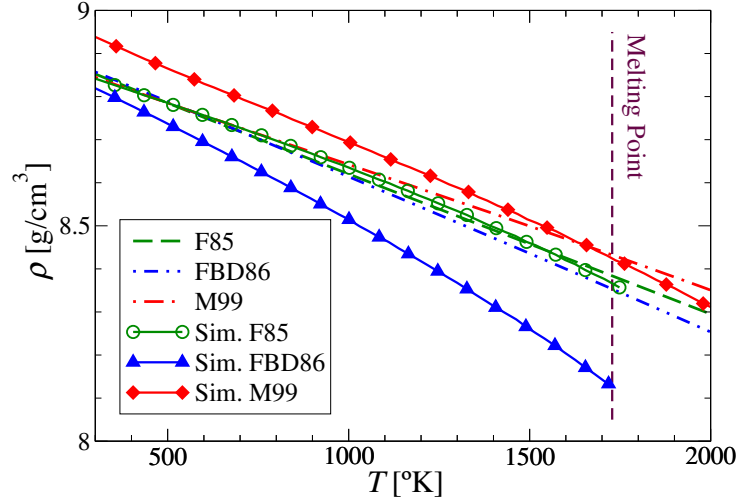
Figure 6.7: The variation of density with temperature along the zero pressure (sublimation) line for Nickel obtained by different versions of EAM: F85(green), FBD86(blue), and M99(red). The symbols connected with solid lines are MD simulation results [144].

u_{coh} with $\Delta U_{\mathrm{coh}} = U_{\mathrm{coh},1} - U_{\mathrm{coh},0}$ which corresponds to the vacancy formation energy $\Delta G_{\mathrm{v}}(T = 0) = E_{\mathrm{v}}$ without considering the relaxation of the lattice. Overall, $\Delta U_{\mathrm{coh}} \approx -E_{\mathrm{v}}$ is on the order of 30% of u_{coh} and it is not maximal at the equilibrium density at this temperature $\rho \approx 8.95 \ \mathrm{g/cm}^3$ unlike a system with pair potential, e.g. LJ. This implies that for a correct description of vacancies in metals, the consideration of many–body effects is essential.

By calculating the vacancy configuration integrals $Z_{\mathrm{sv},i}$ along the sublimation line $p = 0$, we have obtained the Gibbs free energy of vacancy formation ΔG_{v} at finite temperatures from Eq. (6.25). The obtained results in the limit of $T \to 0$ along with

Table 6.2: Sublimation density at $T = 0$ for Nickel obtained by EAM potentials. The first two columns are obtained by a linear fit to the sublimation curves from Fig. 6.7. We have reported in the last column the minimal density for the cohesive energy per particle u_{coh} computed for an ideal lattice whose particles are fixed at their lattice site.

| EAM potential | $\rho_{\mathrm{sub}}(T \to 0)$ [g/cm^3] | | |
| | linear fit to sublimation curve Fig. 6.7 | | |
	our method	MD simulation [144]	$\partial u_{\mathrm{coh}}/\partial \rho = 0$
F85 [137]	8.950	8.955	8.954
FBD86 [138]	8.971	8.984	8.963
M99 [139]	8.933	9.063	8.944
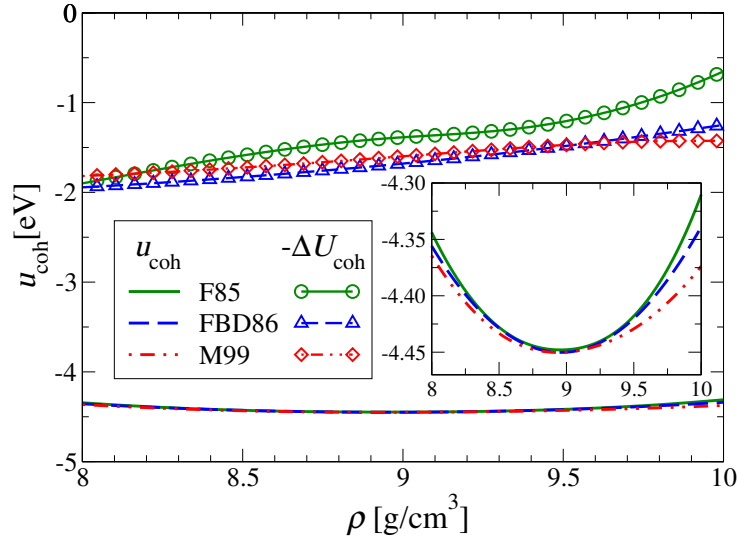
Figure 6.8: The cohesive energy of Nickel as a function of density obtained by different versions of EAM: F85(green), FBD86(blue), and M99(red). The lines with symbol represent ΔU_{coh}, the difference between the cohesive energy of an ideal lattice $U_{\mathrm{coh},0}$ with the one from a lattice with a vacant site $U_{\mathrm{coh},1}$. ΔU_{coh} corresponds to the vacancy formation energy at zero temperature without considering the relaxation of the lattice after it is created. The inset shows the cohesive energy per particle u_{coh} which for all different version of EAM has an approximate minimum of $u_{\mathrm{coh}} \approx -4.45$ eV at $\rho \approx 8.95$ g/cm^3.

ΔU_{coh} the cohesive energy difference of an ideal lattice with a lattice containing a vacant site at $T = 0$, are compared in table 6.3 with previously calculated results of Refs. [135, 138, 139]. Note that the only configuration integral appearing in the first order approximation of the free energy is Z_{s} which corresponds to one free particle in otherwise frozen particles at their lattice sites. This approximate free energy is later used for derivation of ΔG_{v} (Eq. (6.25)). Thus, at low temperatures the first order approximation of ΔG_{v} delivers precise results for E_{v} just by considering the modification to u_{coh}. This modification is approximated by computing the effect of single particle displacements and adding them up (see Eq. (6.42) and discussion above).

By increasing temperature, as it is shown in Fig. 6.9, ΔG_{v} behaves completely different depending on the type of EAM potential in action. Here, we have two types of potentials which are F85/FBD86 with conventional EAM picture of decomposing the total energy into repulsive pair part and attractive embedding part, versus M99 in which the physical interpretation is sacrificed for an optimization of potentials with respect to physical observables. For F85/FBD86, $\Delta G_{\mathrm{v}}(T)$ decreases monotonously with increasing T with an approximate slope, i.e. ΔS_{v}, reported in table 6.3 for low temperatures. The entropy of vacancy formation ΔS_{v} increases slightly for higher temperatures simi-

lar to the case of LJ (see Fig. 6.6.a). On the other hand, the linear behaviour of $\Delta G_v(T)$ is consistent with molecular simulation of copper which also has an fcc lattice structure, using FBD86 potential [146]. In case of M99 however, $\Delta G_v(T)$ remains almost constant at its zero temperature value $E_v \approx 1.61\text{eV}$ with a local maximum at $T \approx 500\text{K}$ with $\Delta G_v \approx 1.62\text{eV}$. This non-monotonous behavior of ΔG_v at finite temperatures is also reported in a qDFT study for Aluminium whose solid also has an fcc structure [147].

Another difference is in the variation of ΔG_v with the maximum considered neighboring layer n_m at a fixed temperature. While for F85/FBD86 we observe a monotonously increasing behaviour for ΔG_v as a function of n_m, just like the Lennard–Jones solid, for M99 there is an increase from $n_m = 1$ to $n_m = 3$ and from there a decrease is observed up to the final considered layer $n_m = 6$. The reason is the different approaches in parametrization of the EAM potentials, especially their pair part. As mentioned earlier, the F85 and FBD86 take the pair part as a purely repulsive short–range potential which effectively has a cut–off range at the first and third layer respectively. For M99 however, the pair potential is somewhat longer–ranged with a cut–off at the fifth neighboring layer and while it is repulsive for short ranges as expected, it also contains an attractive part at longer distances. Due to these oscillations present in the embedding function as well, we observe a non–monotonicity of ΔG_v both in temperature and n_m. We conclude that the parametrizations of EAM potentials affect the finite–temperature behavior of the observables. Thus the properties of the material at non–zero temperatures should be considered in the parametrization of the potentials from the beginning.

Table 6.3: Gibbs free energy of vacancy formation at $T = 0$ for Nickel obtained by EAM potentials. ΔU_{coh} is the difference between the cohesive energy of an ideal lattice whose particles are fixed at their lattice sites with the one which has a vacant site. This is obtained at the sublimation density of the corresponding EAM potential at $T = 0$ (first column of table 6.2). Since ΔG_v is not available directly for $T = 0$ via the computation of vacancy integrals, E_v is obtained by an approximate fit at low temperatures. The obtained values are in good agreement with the results from the corresponding references of the EAM potentials. For finite temperatures, it is often assumed that $\Delta G_v = E_v - T\Delta S_v$. The entropy of vacancy formation ΔS_v is obtained by a linear fit close to $T = 0$ for F85 and FBD86. The finite temperature behavior of M99 is completely different (see Fig. 6.9).

	ΔU_{coh} [eV]	E_v [eV]		ΔS_v [eV/ K]
F85	1.399	1.395	1.4 [137]	$7.63 \cdot 10^{-5}$
FBD86	1.689	1.691	1.63 [138]	$9.30 \cdot 10^{-5}$
M99	1.616	1.612	1.6 [139]	–
Exp.	–	$(1.58 - 1.63) \pm 0.05$ [145]		–
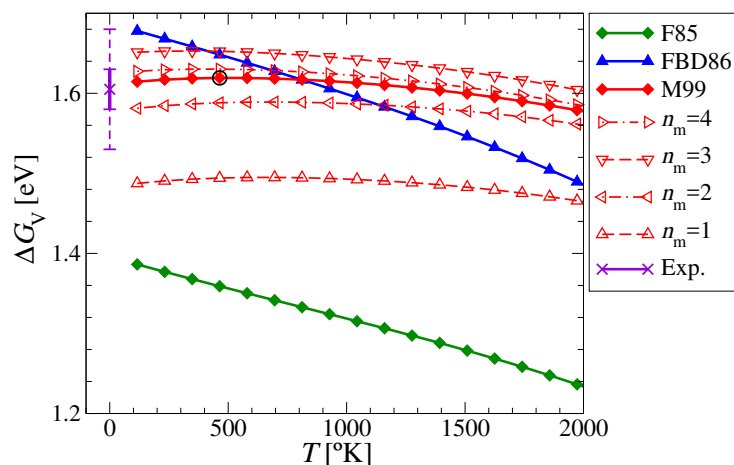
Figure 6.9: Gibbs free energy of vacancy formation in Nickel along the zero pressure line obtained by EAM potentials. For M99, the dependence on the maximum shell index n_{m} in the vacancy integral term of Eq. (6.25) is shown with broken lines. The maximum value of $\Delta G_{\mathrm{v}} = 1.62$ eV at $T \approx 500$ K is shown with a black circle. For F85 and FBD86 the temperature behavior and n_{m} dependency is similar to the LJ case (Fig. 6.6.b).

6.5 Summary and Conclusions

In the framework of the cell cluster theory, Stillinger has proposed an expansion for the partition function of a crystal in terms of the number of moving particles in an otherwise frozen lattice. The leading term truncation of the Stillinger series corresponds to one freely moving particle in its Wigner–Seitz cell while all the other particles are fixed to their lattice sites. We have shown that the first order approximation of the equation of state obtained by this leading term of the Stillinger series gives a good description for the hard sphere and Lennard–Jones model systems as well as for the exemplary case of Ni in the Embedded–Atom–Model.

Using the same truncation, we have derived a relation for equilibrium vacancy concentration of an fcc lattice. The corresponding Gibbs free energy of vacancy formation ΔG_{v} obtained by Eq. (6.25) shows good agreement with simulations in the hard sphere and Lennard–Jones case. The compact expression for ΔG_{v} allows for a transparent interpretation of the two contributing sources to the Gibbs free energy of vacancy formation which are the finite pressure and the missing cohesive energy of the particles in the neighboring layer(s) of a vacant site. While in a HS system the finite pressure is the main contributor to ΔG_{v}, in the LJ system this term vanishes since we are moving along the sublimation line $p = 0$ and the missing cohesive energy of the particles is the source of the Gibbs free energy of vacancy formation. For $T = 0$ in the LJ system, we

have shown that $E_{\mathrm{v}} = \Delta G_{\mathrm{v}}(T = 0) \approx u_{\mathrm{coh}}$ as is expected and the deviation which is due to the relaxation of the lattice after creating the vacancy is obtained by computing the effect of the single–particle displacements, i.e. vacancy integrals.

For Nickel as an exemplary case of metals we have taken advantage of the EAM potentials which are designed for classical treatment of a metallic system. Two types of EAM potentials are investigated in this case: F85 from Ref. [137] and FBD86 from Ref. [138], whose pair and embedding potentials has the physical spirit close to the original EAM [135], and M99 from Ref. [139] which does not have any constraints on the form of its potentials. For $T = 0$ we have recovered the obtained results for E_{v} from original works and shown that considering the many–body effects is essential since the cohesive energy of vacancy formation recovers only 30% of E_{v}. Furthermore, the different temperature behavior of ΔG_{v} depending on the type of the potential, F85/FBD86 versus M99, is discussed with the conclusion $\Delta G_{\mathrm{v}}(T)$ is significantly affected by the details of parametrization of the EAM potentials.

Having this compelling consequence, we propose that in further EAM parametrizations the Gibbs free energy of vacancy formation at finite temperatures should also be considered as one of the fitting observables. For this purpose, $\Delta G_{\mathrm{v}}(T)$ could be computed from Eq. (6.25) by means of quantum density functional theory (qDFT). Here, the required single particle integrals Z_{s} and $Z_{\mathrm{sv},i}$ are calculated with qDFT values for the 1–particle energies ϕ_i

Furthermore, in this truncation the partition function Q_1, free energy βF_1, and the equilibrium vacancy concentration $n_{\mathrm{vac,eq}}$ are experimentally measurable for colloidal crystals. Realization of this measurement is possible by letting a single particle move freely while fixing all the other ones at their lattice site by employing an array of laser tweezers [148,149]. The integrands of the required single–particle integrals Z_{s} and $Z_{\mathrm{sv},i}$ is directly obtained by recording the trajectory of the moving particle using video–microscopy [150].

We have observed an underestimation in the obtained free energy for LJ. This deficiency is partly recovered by considering the second order approximation and calculating the more complex configuration integral Z_{ij}^l [142]. A more exact description of the free energy density allows us to obtain further physical quantities, e.g. heat capacity at constant pressure C_{p}. On the other hand, by adding the second vacancy in the first order approximation, one could study the vacancy–vacancy interaction as a function of their dedicated lattice site distance $u_{\mathrm{vv}}(|\mathbf{s}_i - \mathbf{s}_j|)$. For a pair potential, e.g. LJ, u_{vv} is expected to have the same functionality of the distance as its pair potential, as for the EAM potentials it has a more complicated form due to the many–body embedding part of the potential [142].

Appendix A

Numerical Considerations in Implementing DFT

Having the formalism of the FMT introduced in Chapter 4 for the hard–spheres and Chapter 5 for the AO model, it is important to be able to implement it correctly in order to obtain numerical values of the desired physical quantities.

A.1 Discretization and symmetries

The first step in the setting up of the numerical environment is proper discretization of the system. As it is mentioned earlier, for investigating the crystalline state we consider an fcc unit cell whose side length is a.

$$a = \sqrt[3]{\frac{4\left(1 - n_{\mathrm{vac}}\right)}{\bar{\rho}}}. \tag{A.1}$$

Here, $\bar{\rho}$ is the bulk number density of the hard–spheres and $n_{\mathrm{vac}} \sim 10^{-4}$ is a finite value for the vacancy concentration. Note that the lengths are expressed in units of the hard–sphere diameter σ. The side length of the cubic unit cell is divided in N equal distances which lets every locally defined property of the unit cell to be saved in an array of $N \times N \times N$, , e.g. the local number density $\rho(x, y, z)$. For these discretized coordinates, the length element in the real and the reciprocal lattice space are given by,

$$\Delta x = \Delta y = \Delta z = \frac{a}{N} ,$$
$$\Delta k_x = \Delta k_y = \Delta k_z = \frac{2\pi}{L} . \tag{A.2}$$

The density of the hard–sphere particles are initiated as Gaussian peaks at the lattice sites of the fcc unit cell (see Fig. A.1). A Gaussian peak $G(\mathbf{r})$ whose width is denoted by α_G and is centered at $\mathbf{r}_0$, and the local number density of the hard–spheres $\rho(\mathbf{r})$ in an fcc unit cell are given as follows.

$$G(\mathbf{r}; \mathbf{r}_0) = \left(\frac{\alpha_\mathrm{G}}{\pi}\right)^{\frac{3}{2}} \exp\left(-\alpha_\mathrm{G}|\mathbf{r} - \mathbf{r}_0|^2\right) , \tag{A.3}$$

$$\rho(\mathbf{r}) = \sum_i (1 - n_\mathrm{vac}) G(\mathbf{r}; \mathbf{r}_i) , \tag{A.4}$$

where the sum is over the i lattice sites of the fcc unit cell. Note that $\rho(\mathbf{r})$ must respect the symmetries of the unit cell. Due to numerical precision, these symmetries do not usually hold which results in unwanted imaginary part in the Fourier transform of the density profile (see Eq. (A.10) and its following lines). In order to secure these symmetries, 1/8th of the unit cell is initiated by computing the relevant Gaussian peaks,

$$\rho_{1/8}(x, y, z) = \sum_i G(\mathbf{r} = (x, y, z); \mathbf{r}_0^i) \quad \text{with } 0 < x, y, z < \frac{a}{2} , \tag{A.5}$$

where $\mathbf{r}_0^i = (0, 0, 0)$, $(\frac{a}{2}, 0, 0)$, $(0, \frac{a}{2}, 0)$, and $(0, 0, \frac{a}{2})$. The initiated box is then symmetrized within itself by taking an average of its density profile and those of the rotated boxes which are obtained by setting the origin to the partially initiated particles at $\mathbf{r}_0^i$. The remaining array cells of the density in the cubic unit cell are copied from the appropriate cells in the initiated box in the following steps.

1. along the x–axis: $\rho(x, y, z) = \rho(a - x, y, z)$ with $0 < x, y, z < \frac{a}{2}$

2. along the y–axis: $\rho(x, y, z) = \rho(x, a - y, z)$ with $0 < x < a$ and $0 < y, z < \frac{a}{2}$

3. along the z–axis: $\rho(x, y, z) = \rho(x, y, a - z)$ with $0 < x, y < a$ and $0 < z < \frac{a}{2}$

Finally, the values of the array cells are scaled so that the total number density precisely results in $\bar{\rho} = 4(1 - n_\mathrm{vac})$.

A.2 Fourier transformation and convolution

In order to obtain the excess free energy density Φ of the initiated density profile $\rho(\mathbf{r})$ one should calculate the weighted densities n_α. The weighted (smeared–out) densities are the convolution of the hard–sphere weight functions (w^α from Eq. (4.4)) with the density profile:

$$n_\alpha(\mathbf{r}) = (\rho * w^\alpha)(\mathbf{r}) = \int d\mathbf{r}' \rho(\mathbf{r}') w^\alpha(\mathbf{r} - \mathbf{r}'). \tag{A.6}$$
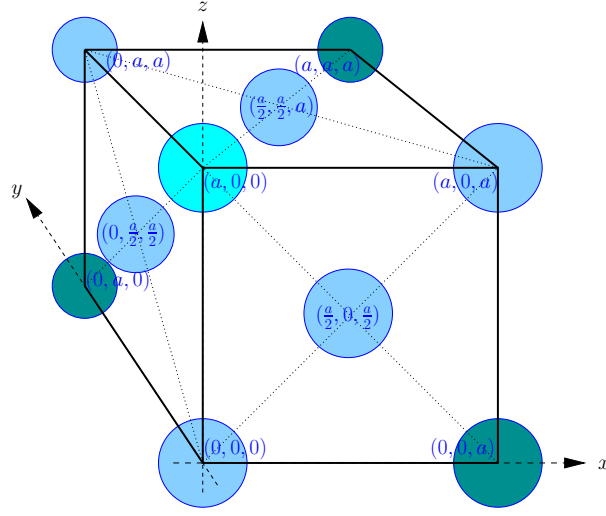
Figure A.1: Hard–sphere particles sitting at the lattice sites of a face-centered-cubic unit cell with side length a. The particles sitting at the rear faces/corner are not shown. The different colors represent different fcc close packing layers.

Considering computational costs of direct calculation of the convolution, it is more convenient to calculate it indirectly by taking advantage of convolution theorem. For two arbitrary well–defined functions f_1 and f_2, the convolution theorem states that the Fourier transform of their convolution $f_1 * f_2$ is equal to the product of their Fourier transforms $\tilde{f}_1 \times \tilde{f}_2$. Defining the forward and backward Fourier transform of the function f as,

$$\mathscr{F}\left[f(\mathbf{r})\right] = \tilde{f}(\mathbf{k}) = \int \mathrm{d}\mathbf{r}\, e^{-i\mathbf{k}\cdot\mathbf{r}}\, f(\mathbf{r}) \tag{A.7}$$

$$\mathscr{F}^{-1}\left[\tilde{f}(\mathbf{k})\right] = f(\mathbf{r}) = \frac{1}{(2\pi)^3}\int \mathrm{d}\mathbf{k}\, e^{i\mathbf{k}\cdot\mathbf{r}}\, \tilde{f}(\mathbf{k})\,, \tag{A.8}$$

a proof for the convolution theorem is given by the following.

$$\begin{aligned}
\mathscr{F}\left[f_1 * f_2\right](\mathbf{k}) &= \int \mathrm{d}\mathbf{r}\, e^{-i\mathbf{k}\cdot\mathbf{r}}\, (f_1 * f_2)(\mathbf{r}) \\
&= \int \mathrm{d}\mathbf{r}\, e^{-i\mathbf{k}\cdot\mathbf{r}} \int \mathrm{d}\mathbf{r}'\, f_1(\mathbf{r}') f_2(\mathbf{r} - \mathbf{r}') \\
&= \int \mathrm{d}\mathbf{r} \int \mathrm{d}\mathbf{r}'\, e^{-i\mathbf{k}\cdot\mathbf{r}'}\, f_1(\mathbf{r}')\, e^{-i\mathbf{k}\cdot(\mathbf{r}-\mathbf{r}')}\, f_2(\mathbf{r} - \mathbf{r}') \\
&= \tilde{f}_1(\mathbf{k})\tilde{f}_2(\mathbf{k})
\end{aligned} \tag{A.9}$$

Moreover, using Euler's relation $e^{-i\theta} = \cos\theta - i\sin\theta$ the Fourier transform of a real function $f(\mathbf{r})$ decomposes into a real part and an imaginary part.

$$\tilde{f}(\mathbf{k}) = \int d\mathbf{r}\ e^{-i\mathbf{k}\cdot\mathbf{r}}\ f(\mathbf{r}) = \int d\mathbf{r}\ \cos(\mathbf{k}\cdot\mathbf{r})\ f(\mathbf{r}) - i\int d\mathbf{r}\ \sin(\mathbf{k}\cdot\mathbf{r})\ f(\mathbf{r}) \quad (A.10)$$

For a completely symmetric function $f(\mathbf{r}) = f(-\mathbf{r})$ the integrand of the second term is symmetric. Therefore, the imaginary part is zero and the Fourier transform is completely real. On the other hand, if the function is completely asymmetric $f(\mathbf{r}) = -f(-\mathbf{r})$ the first term vanishes and the Fourier transform is imaginary.

In order to obtain the weighted densities, the Fourier transforms of the density profile is computed using the fftw library for C++ which performs discrete Fourier transform of a given complex array [151, 152]. Suppose the input array X is a 3D array whose dimensions are $[N_x, N_y, N_z]$. The forward and backward discrete Fourier transforms performed by fftw on X are given as follows,

$$\tilde{X}'[k_x, k_y, k_z] = \sum_{n_x=0}^{N_x-1}\sum_{n_y=0}^{N_y-1}\sum_{n_z=0}^{N_z-1} X[n_x, n_y, n_z]\exp\left[-2\pi i\left(k_x\frac{n_x}{N_x} + k_y\frac{n_y}{N_y} + k_z\frac{n_z}{N_z}\right)\right] , (A.11)$$

$$X'[n_x, n_y, n_z] = \sum_{n_x=0}^{N_x-1}\sum_{n_y=0}^{N_y-1}\sum_{n_z=0}^{N_z-1} \tilde{X}[k_x, k_y, k_z]\exp\left[2\pi i\left(n_x\frac{k_x}{N_x} + n_y\frac{k_y}{N_y} + n_z\frac{k_z}{N_z}\right)\right] . \quad (A.12)$$

A consecutive forward and backward fftw Fourier transform multiplies the input array by a factor of $N_x N_y N_z$. Furthermore, these expressions are not equivalent to those of continuous Fourier transform (Eqs. (A.7) and (A.8)) since they are not multiplied by the proper discretization units. Therefore, the output of the fftw routines, X' and $\tilde{X}'$, must be multiplied by proper factors as follows,

$$\tilde{X} = \Delta x\,\Delta y\,\Delta z\,\tilde{X}' = \left(\frac{a}{N}\right)^3\tilde{X}' ,$$
$$X = \frac{\Delta k_x\,\Delta k_y\,\Delta k_z}{(2\pi)^3}\,X' = \frac{1}{a^3}\,X' , \quad (A.13)$$

where a is the side length of the fcc unit cell (Eq. (A.1)) and we have used Eq. (A.2) for obtaining the normalization factor of forward and backward discrete Fourier transforms.

The resulting Fourier transform of density profile, i.e. $\tilde{\rho}$, is completely real since the density profile is initiated as a completely symmetric array. In order to ensure the symmetry considerations of the weighted densities w^α it is reasonable to calculate their Fourier transform analytically and store them to be used for the numerical implementations. This also reduces computational cost since we are not computing the Fourier

transform of these functions which are supposed to be used several times throughout the code (see below).

A.3   Implementation of the weighted densities

The Fourier transforms of the weight functions are given as follows[1].

$$
\begin{aligned}
\tilde{w}^3(k) &= \frac{4\pi}{k^3}\left(\sin(kR) - kR\cos(kR)\right) , \\
\tilde{w}^2(k) &= \frac{4\pi}{k}R\sin(kR) , \\
\tilde{w}^2_i(\mathbf{k}) &= i\,\frac{k_i}{k^3}\,4\pi R^2\left(kR\cos(kR) - \sin(kR)\right) = -i\,k_i\,R^2\,\tilde{w}^3(k) , \\
\tilde{w}^{\mathrm{T}}_{ij}(\mathbf{k}) &= \frac{1}{R}\,\tilde{w}^3(k)\,\delta_{ij} + \left(\tilde{w}^2(k) - \frac{3}{R}\tilde{w}^3(k)\right)\frac{k_i k_j}{k^2} .
\end{aligned}
\tag{A.14}
$$

The Fourier transforms of the scalar weight functions $\tilde{w}^3$ and $\tilde{w}^2$ only depend on the size of reciprocal space vector $k = |\mathbf{k}|$. As a result they are invariant under the reflections of their argument $\mathbf{k}$ under which one or more of elements of $\mathbf{k}$ are reversed $k_i \to -k_i$. This symmetry also holds for the diagonal elements of tensorial weight function since we have,

$$
\tilde{w}^{\mathrm{T}}_{ij}(\mathbf{k}') = \frac{1}{R}\,\tilde{w}^3(k')\,\delta_{ii} + \left(\tilde{w}^2(k') - \frac{3}{R}\tilde{w}^3(k')\right)\frac{k_i k_i}{k^2} = \tilde{w}^{\mathrm{T}}_{ij}(\mathbf{k}) .
\tag{A.15}
$$

As a result, the backward Fourier transform of the scalar weight function as well as the diagonal elements of $\tilde{\mathbf{w}}^{\mathrm{T}}$ are real. On the other hand, the vectorial weight functions and the off–diagonal elements of the tensorial weight function are anti symmetric. This makes their backward Fourier transform completely imaginary. In order to prevent any numerical inconsistency, these symmetries should be imposed by initiating $1/8$th of cubic unit cell and proper copying of them to the remaining array cells. For instance, the asymmetric property of $\tilde{\mathbf{w}}^2$ and the off–diagonal elements of $\tilde{\mathbf{w}}^{\mathrm{T}}_{ij}$ is imposed numerically by setting the middle cell of their corresponding arrays to zero.

On the other hand, since k and its powers appear in the denominator of the Fourier transforms of all weighted densities, for a proper implementation of these functions their value at $k = 0$ should be replaced by their analytical forms in $k \to 0$ limit. These

---

[1] See Appendix B for a detailed calculation.

limits are obtained by setting $k = 0$ in Eqs. (B.10), (B.12), (B.18), and (B.28).

$$
\begin{aligned}
\lim_{k \to 0} \tilde{w}^3(k) &= \frac{4\pi}{3} R^3 \ , \\
\lim_{k \to 0} \tilde{w}^2(k) &= 4\pi R^2 \ , \\
\lim_{k \to 0} \tilde{\mathbf{w}}^2(\mathbf{k}) &= 0 \ , \\
\lim_{k \to 0} \tilde{\mathbf{w}}^{\mathrm{T}}(\mathbf{k}) &= \frac{4\pi}{3} R^2 \ \mathbb{I} \ .
\end{aligned}
\tag{A.16}
$$

A.4 Equilibrium density profile and minimization of the free energy

After proper initialization of the density profile $\rho(\mathbf{r})$ and Fourier transform of the weighted densities $\tilde{w}^\alpha$, one can calculate the weight functions $n_\alpha(\mathbf{r})$ (Eq. (A.6)) by applying the convolution theorem (Eq. (A.9)). The free energy of the hard–sphere system is then calculated using these weighted densities in the desired form of the functional[2]. For obtaining the equilibrium properties of a bulk crystalline state the free energy density of the desired system should then be minimized. This is either achieved by constrained minimization or full minimization. In constrained minimization, the density profile is constrained to keep its initial Gaussian form while the Gaussian width α_{G} and the vacancy concentration n_{vac} are the minimization parameters.

$$
F_{\mathrm{eq}} = \min_{\{n_{\mathrm{vac}}, \alpha_{\mathrm{G}}\}} \mathcal{F}\left[\rho(\mathbf{r})\right] .
\tag{A.17}
$$

In full minimization, the goal is to find the solution of the equilibrium density profile $\rho_{\mathrm{eq}}(\mathbf{r})$, which minimizes the free energy density, in the following fundamental equation in DFT (see Eq. (3.34)).

$$
\ln\left(\lambda^3 \rho_{\mathrm{eq}}(\mathbf{r})\right) = c^{(1)}\left[\rho_{\mathrm{eq}}\right] + \beta V^{\mathrm{ext}}(\mathbf{r}) - \beta\mu \ ,
\tag{A.18}
$$

where $c^{(1)}$ denotes the single–particle direct correlation function which is the functional derivative of the excess free energy functional $\beta\mathcal{F}^{\mathrm{ex}}$ with respect to the density profile[3]. The thermal de Broglie wavelength denoted by λ is an irrelevant constant here. The

---

[2] An additional step should be taken to obtain the free energy in the AO model which is calculating the polymer density profile $\rho_{\mathrm{p}}(\mathbf{r})$ using Eq. (5.40) and consequently its corresponding weighted densities $n_{\alpha,\mathrm{p}}$.

[3] see Appendix C for explicit relations for $c^{(1)}$.

equilibrium density profile $\rho_{\text{eq}}(\mathbf{r})$ obtained by solving Eq. (A.18) has a bulk density ρ_0 which is a function of μ.

$$\rho_0(\mu) \;=\; \frac{1}{V} \int \mathrm{d}\mathbf{r}\,\rho_{\text{eq}}(\mathbf{r})\,, \qquad \text{with } V = a^3\,. \tag{A.19}$$

In principle, the lattice constant a (Eq. (A.1)) and the vacancy concentration n_{vac} (Eq. (4.64)) should adjust themselves to comply with Eq. (A.18). However, such a procedure is not feasible in practice [80]. Instead of this, for a given chemical potential μ (or bulk density ρ_0), the vacancy concentration, or equivalently the lattice constant, is kept constant as well. In the obtained constrained solution of Eq. (A.18), $\rho_0(\mu, n_{\text{vac}})$ (or $\mu = \mu(\rho_0, n_{\text{vac}})$) is in fact a Lagrangian multiplier which ensures Eq. (4.64) for the vacancy concentration holds[4].

A.4.1   Picard iterations

A self–consistent solution of Eq. (A.18) is obtained by starting from an initial density profile, e.g. a Gaussian profile (Eq. (A.4)). Then, at each step of the iterative solution, using the current density profile $\rho^{(i)}$ the weighted densities and consequently the single–particle direct correlation function $c^{(1)}$ are computed. Using these computed quantities in the right hand side of Eq. (A.18), a new density profile ρ^{new} is obtained. If this density profile is directly used as an input to the next step, the iterations do not converge to a solution. In order to avoid this kind of divergence, the changes in the solution should be constrained. This is achieved by introducing a mixing parameter $\alpha \in [0, 1]$ which controls the amount of changes in the new solution for the density profile as follows.

$$\rho^{(i+1)} \;=\; (1-\alpha)\rho^{(i)} + \alpha\rho^{\text{new}}\,. \tag{A.20}$$

While choosing small mixing parameter means slow convergence of the solution, a large value of α might result in local packing fractions n_3 larger than 1. Hence, the optimal choice of mixing parameter in Picard iterations depends on the problem and is usually determined empirically. For instance, it can be dynamically adopted during the iterations to improve the speed of convergence. For this purpose a maximal mixing parameter α_{max} is calculated as a function of n_3 so that $n_3 < 1$ holds [153].

For full minimization of the free energy of a crystal hard–sphere, I have chosen a constant experimental mixing parameter ranging from 10^{-2} to 10^{-5}. In order to compensate the slow divergence of the solution in case of small α's, the *Direct inversion in iterative subspace* is used after performing a few Picard iterations.

---

[4] For a detailed discussion see Section III.A in Ref. [80].

A.4.2 Direct inversion in iterative subspace

The *Direct inversion in iterative subspace* (DIIS) is a numerical method which speeds up the convergence and ensures more stability in the iterative solution of the self–consistent field method [154–156]. DIIS approximates the final solution by a linear combination of a finite number n of iterations output $\rho^{(i)}$.

$$\rho^{(n+1)}(\mathbf{r}) = \sum_{i=1}^{n} c_i \rho^{(i)}(\mathbf{r}) \ . \tag{A.21}$$

The coefficients of this linear combination, c_i's, are obtained by constructing a vector $\Delta\rho$ of residuals of the density profile $\Delta\rho^{(i)}$ and approximating it with a null vector in a mean–square sense.

$$\begin{aligned}
\Delta\rho^{(i)}(\mathbf{r}) &= \rho^{(i+1)}(\mathbf{r}) - \rho^{(i)}(\mathbf{r}) \ , \\
\Delta\rho(\mathbf{r}) &= \sum_{i=1}^{n} c_i \Delta\rho^{(i)}(\mathbf{r}) \ , \quad \text{while } \sum_{i=1}^{n} c_i = 1 \ .
\end{aligned} \tag{A.22}$$

As a result, in order to determine c_i's a set of $n+1$ linear equations should be solved which are given by,

$$\begin{pmatrix}
S_{1,1} & S_{1,2} & \cdots & S_{1,n} & -1 \\
S_{2,1} & S_{2,2} & \cdots & S_{2,n} & -1 \\
\vdots & \vdots & \ddots & \vdots & \vdots \\
S_{n,1} & S_{n,2} & \vdots & S_{n,n} & -1 \\
-1 & -1 & \vdots & -1 & 0
\end{pmatrix}
\begin{pmatrix}
c_1 \\ c_2 \\ \vdots \\ c_n \\ \lambda
\end{pmatrix}
=
\begin{pmatrix}
0 \\ 0 \\ \vdots \\ 0 \\ -1
\end{pmatrix} \ . \tag{A.23}$$

Here, λ is a Lagrangian multiplier and S_{ij} denotes the scalar product of $\Delta\rho^{(i)}$ and $\Delta\rho^{(j)}$. By solving Eq. (A.23), the required coefficients for obtaining a linear combination of $\rho^{(i)}$ (Eq. (A.21)) are obtained. An improved DIIS solution is only possible by updating the independent iteration outputs $\rho^{(i)}$. This is achieved by performing several Picard iterations after a DIIS step.

A.4.3 Convergence of the solution

For monitoring the convergence of solution, the following error function is defined.

$$\epsilon = \frac{1}{V} \int d\mathbf{r} \left(\rho^{(i+1)}(\mathbf{r}) - \rho^{(i)}(\mathbf{r}) \right)^2 \ . \tag{A.24}$$

In practice a threshold value should be set to mark the end of iterations, e.g. $\epsilon = 10^{-7}$. The required number of iterations cycles to converge to the solution depends on the mixing parameter α as well number of Picard iterations between two DIIS steps and DIIS vector size n in Eq. (A.21).

In some cases we are interested in properties of the exact solution although due to the numerical implementation converging to $\epsilon \simeq 0$ is very slow. Here, one can extrapolate the quantity of interest, e.g. the free energy, as a function of ϵ in order to obtain the exact result.

Considering Eq. (A.18) and its following discussion, another possible quantity for monitoring the convergence is the constrained chemical potential which reads

$$\mu(\rho_0, n_{\text{vac}}) = \frac{1}{V} \int d\mathbf{r} \left(\ln \left(\lambda^3 \rho_{\text{eq}}(\mathbf{r}) \right) - c^{(1)} \left[\rho_{\text{eq}}(\mathbf{r}) \right] \right) . \tag{A.25}$$

An analysis of the constrained chemical potential, give insight to the local convergence of the density profile.

APPENDIX B

FOURIER TRANSFORMATION OF THE WEIGHTED DENSITIES

The independent weight functions for a hard sphere of radius R are defined as follows:

$$
\begin{aligned}
w^3(\mathbf{r}) &= \theta\left(R - r\right), & \text{(B.1)} \\
w^2(\mathbf{r}) &= \delta\left(R - r\right), & \text{(B.2)} \\
\mathbf{w}^2(\mathbf{r}) &= \delta\left(R - r\right)\frac{\mathbf{r}}{r}, & \text{(B.3)} \\
\mathbf{w}^\mathrm{T}(\mathbf{r}) &= \delta(R - r)\frac{\mathbf{r} \otimes \mathbf{r}}{r^2}, & \text{(B.4)}
\end{aligned}
$$

where $r = |\mathbf{r}|$ and $\otimes$ denotes the dyadic product. We define the forward Fourier transformation of a function in real space as follows.

$$
\mathscr{F}\left[f(\mathbf{r})\right] = \tilde{f}(\mathbf{k}) = \int \mathrm{d}\mathbf{r}\, e^{-i\mathbf{k}\cdot\mathbf{r}}\, f(\mathbf{r}), \tag{B.5}
$$

Note that we have considered the normalization factor $1/(2\pi)^3$ in the backward Fourier transformation (see Eq. (A.8)). In order to obtain the Fourier transformation of the weight functions, we assume that the wave vector $\mathbf{k}$ is parallel to the z component of the real–space coordinate system. Therefore, in terms of the spherical coordinates (r, θ, φ), the exponent of the integrand in Eq. (B.5) reads

$$
\mathbf{k} \cdot \mathbf{r} = kr\cos\theta \qquad \text{with } k = |\mathbf{k}|\,. \tag{B.6}
$$

B.1   Fourier transformation of $w^3(\mathbf{r})$

The Fourier transformation of the first scalar weight function $w^3(\mathbf{r})$ is calculated as follows.

$$
\begin{aligned}
\tilde{w}^3(\mathbf{k}) &= \int e^{-i\mathbf{k}\cdot\mathbf{r}}\,\theta\,(R-r)\,\mathrm{d}\mathbf{r} = \int_0^R\int_0^\pi\int_0^{2\pi} r^2\sin\theta\, e^{-ikr\cos\theta}\,\mathrm{d}\varphi\,\mathrm{d}\theta\,\mathrm{d}r \\
&= 2\pi\int_0^R \left[\frac{r}{ik}e^{-ikr\cos\theta}\right]_{\theta=0}^{\pi}\mathrm{d}r \\
&= \frac{4\pi}{k}\int_0^R r\sin(kr)\,\mathrm{d}r \ .
\end{aligned}
\tag{B.7}
$$

The integral can be calculated by integrating by parts $\int u\mathrm{d}v = uv - \int v\mathrm{d}u$ with $u = r$ and $\mathrm{d}v = \sin(kr)\mathrm{d}r$.

$$
\begin{aligned}
\int r\sin(kr)\,\mathrm{d}r &= -\frac{r}{k}\cos(kr) + \frac{1}{k}\int\cos(kr)\,\mathrm{d}r \\
&= \frac{1}{k^2}\left(-kr\cos(kr) + \sin(kr)\right) \ .
\end{aligned}
\tag{B.8}
$$

Finally, $\tilde{w}^3$ is calculated by using Eq. (B.8) in Eq. (B.7).

$$
\tilde{w}^3(k) = \frac{4\pi}{k^3}\left(\sin(kR) - kR\cos(kR)\right) \ .
\tag{B.9}
$$

For small values of k one can use the Taylor expansion of $\sin x$ and $\cos x$ to write $\tilde{w}^3(k)$ as a polynomial in terms of k^n. Denoting the factorial of n as $n!$, the low k limit of $\tilde{w}^3$ reads

$$
\begin{aligned}
\tilde{w}^3(k) &= \frac{4\pi}{k^3}\left\{kR - \frac{1}{3!}k^3R^3 + \frac{1}{5!}k^5R^5 - \frac{1}{7!}k^7R^7 + \mathcal{O}(k^9)\right.\\
&\qquad\qquad \left. -kR + \frac{1}{2!}k^3R^3 - \frac{1}{4!}k^5R^5 + \frac{1}{6!}k^7R^7 - \mathcal{O}(k^9)\right\} \\
&= \frac{4\pi}{3}R^3 - \frac{2\pi}{15}k^2R^5 + \frac{\pi}{210}k^4R^7 + \mathcal{O}(k^6) \ .
\end{aligned}
\tag{B.10}
$$

B.2   Fourier transformation of $w^2(\mathbf{r})$

The Fourier transformation of the second scalar weight function w^2 which is a Dirac delta function is obtained as follows.

$$
\begin{aligned}
\tilde{w}^2(\mathbf{k}) &= \int e^{-i\mathbf{k}\cdot\mathbf{r}}\,\delta\left(R-r\right)\mathrm{d}\mathbf{r} = \int_0^\pi\int_0^{2\pi}\int_0^\infty r^2\sin\theta e^{-ikr\cos\theta}\,\delta\left(R-r\right)\mathrm{d}r\,\mathrm{d}\varphi\,\mathrm{d}\theta \\
&= 2\pi\int_0^\pi R^2\sin\theta e^{-ikR\cos\theta}\,\mathrm{d}\theta \\
&= 2\pi\left[\frac{R}{ik}e^{-ikR\cos\theta}\right]_{\theta=0}^\pi \\
&= \frac{4\pi}{k}R\sin(kR)\,.
\end{aligned}
\tag{B.11}
$$

For small values of k the Fourier transformation of w^2 can be expressed as,

$$
\begin{aligned}
\tilde{w}^2(k) &= \frac{4\pi}{k}R\left(kR-\frac{1}{6}k^3R^3+\frac{1}{120}k^5R^5-\mathcal{O}(k^7)\right) \\
&= 4\pi R^2-\frac{2\pi}{3}k^2R^4+\frac{\pi}{30}k^4R^6-\mathcal{O}(k^6)\,.
\end{aligned}
\tag{B.12}
$$

B.3   Fourier transformation of $\mathbf{w}^2(\mathbf{r})$

The Fourier transformation of the scalar weight functions are calculated under the assumption that the z component of the real space vector is parallel to the reciprocal vector $\mathbf{k}$. The obtained Fourier transformations should be invariant under any rotation of the coordination system. This is important in the calculation of the Fourier transformation of the vectorial $\mathbf{w}^2$ and the tensorial $\mathbf{w}^\mathrm{T}$ weight functions. For the vectorial weight function, it is necessary to express the real space unit vector in direction of vector $\mathbf{r}=(r,\theta,\varphi)$ in terms of the polar θ and the azimuthal φ angles in the spherical coordinates.

$$
\frac{\mathbf{r}}{r} = \begin{pmatrix} \sin\theta\cos\varphi \\ \sin\theta\sin\varphi \\ \cos\theta \end{pmatrix}\,.
\tag{B.13}
$$

The Fourier transformation of the vectorial weight function is calculated as follows.

$$
\begin{aligned}
\tilde{\mathbf{w}}^2(\mathbf{k}) &= \int e^{-i\mathbf{k}\cdot\mathbf{r}} \frac{\mathbf{r}}{r} \delta\left(R - r\right) \mathrm{d}\mathbf{r} \\
&= \int_0^\pi \int_0^{2\pi} \int_0^\infty r^2 \sin\theta\, e^{-ikr\cos\theta} \begin{pmatrix} \sin\theta\cos\varphi \\ \sin\theta\sin\varphi \\ \cos\theta \end{pmatrix} \delta\left(R - |\mathbf{r}|\right) \mathrm{d}r\,\mathrm{d}\varphi\,\mathrm{d}\theta \\
&= \int_0^\pi R^2 \sin\theta\, e^{-ikR\cos\theta} \begin{pmatrix} 0 \\ 0 \\ 2\pi\cos\theta \end{pmatrix} \mathrm{d}\theta\,,
\end{aligned}
\tag{B.14}
$$

where in the last step the integration of the periodic functions $\sin\varphi$ and $\cos\varphi$ for φ from 0 to 2π is zero. This implies that the resulting Fourier transformation is in the direction of the real space z axis which is equivalent to the unit vector in reciprocal space $\mathbf{k}/k$. As a result,

$$
\tilde{\mathbf{w}}^2(\mathbf{k}) = \frac{\mathbf{k}}{k}\, 2\pi R^2 \int_0^\pi \sin\theta\cos\theta\, e^{-ikR\cos\theta} \mathrm{d}\theta\,.
\tag{B.15}
$$

The integral can be computed by a change of variable as $x = \cos\theta$ whose differential element is $\mathrm{d}x = -\sin\theta\,\mathrm{d}\theta$.

$$
\begin{aligned}
\tilde{\mathbf{w}}^2(\mathbf{k}) &= \frac{\mathbf{k}}{k}\, 2\pi R^2 \int_{-1}^1 x e^{-ikRx}\mathrm{d}x \\
&= \frac{\mathbf{k}}{k}\, 2\pi R^2 \left(\int_{-1}^1 x\cos(kRx)\mathrm{d}x - i \int_{-1}^1 x\sin(kRx)\mathrm{d}x \right) \\
&= i\frac{\mathbf{k}}{k}\, 4\pi R^2 \left[\frac{x}{kR}\cos(kRx) - \frac{1}{k^2 R^2}\sin(kRx) \right]_{x=0}^1\,.
\end{aligned}
\tag{B.16}
$$

Note that the first integral in the second line is zero since its integrand is asymmetric with respect to $x \to -x$. For the second integral, since $x\sin(kRx)$ is symmetric with the same variable change, its result with the current boundaries, i.e. $x = -1$ to 1, is twice the one with $x = 0$ to 1. The result for the second integral is given by Eq. (B.8) with $r = x$. Finally, the Fourier transformation of the vectorial weight function reads

$$
\begin{aligned}
\tilde{\mathbf{w}}^2(\mathbf{k}) &= i\frac{\mathbf{k}}{k^3}\, 4\pi \left(kR\cos(kR) - \sin(kR) \right) \\
&= -i\,\mathbf{k}\,\tilde{w}^3(k)\,,
\end{aligned}
\tag{B.17}
$$

where $\tilde{w}^3(k)$ is the Fourier transformation of $w^3(\mathbf{r})$ from Eq. (B.9). One can use $w^3(k \to 0)$ from Eq. (B.10) and rewrite Eq. (B.17) for small k as follows.

$$\tilde{\mathbf{w}}^2(\mathbf{k}) = -i \frac{\mathbf{k}}{k} \left(\frac{4\pi}{3} k R^3 - \frac{2\pi}{15} k^3 R^5 + \frac{\pi}{210} k^5 R^7 + \mathcal{O}(k^7) \right) . \tag{B.18}$$

B.4 Fourier transformation of $\mathbf{w}^{\mathrm{T}}(\mathbf{r})$

For the tensorial weight function the Fourier transformation is calculated as follows.

$$\tilde{\mathbf{w}}^{\mathrm{T}}(\mathbf{k}) = \int e^{-i\mathbf{k}\cdot\mathbf{r}} \, \delta(R - r) \, \frac{\mathbf{r} \otimes \mathbf{r}}{r^2} \mathrm{d}\mathbf{r}$$

$$= \int_0^\pi \int_0^\infty \int_0^{2\pi} e^{-ikr\cos\theta} \, \delta(R - r) \, \frac{\mathbf{r} \otimes \mathbf{r}}{r^2} \, r^2 \sin\theta \mathrm{d}\varphi \, \mathrm{d}r \, \mathrm{d}\theta . \tag{B.19}$$

The dyadic product of the real space unit vector (Eq. (B.13)) with itself in the integrand can be expressed in terms of the polar and the azimuthal angles.

$$\frac{\mathbf{r} \otimes \mathbf{r}}{r^2} = \begin{pmatrix} \sin\theta\cos\varphi \\ \sin\theta\sin\varphi \\ \cos\theta \end{pmatrix} \otimes \begin{pmatrix} \sin\theta\cos\varphi \\ \sin\theta\sin\varphi \\ \cos\theta \end{pmatrix}$$

$$= \begin{pmatrix} \sin^2\theta\cos^2\varphi & \sin^2\theta\sin\varphi\cos\varphi & \sin\theta\cos\theta\cos\varphi \\ \sin^2\theta\sin\varphi\cos\varphi & \sin^2\theta\sin^2\varphi & \sin\theta\cos\theta\sin\varphi \\ \cos\theta\sin\theta\cos\varphi & \cos\theta\sin\theta\sin\varphi & \cos^2\theta \end{pmatrix} . \tag{B.20}$$

Note that in the calculation of the Fourier transformation the non–diagonal terms vanish due to the integration of the periodic functions in φ, i.e. $\sin\varphi$, $\cos\varphi$, and their product. For the functions of φ in the diagonal terms we can write,

$$\int_0^{2\pi} \cos^2\varphi \, \mathrm{d}\varphi = \int_0^{2\pi} \frac{1 + \cos(2\varphi)}{2} \, \mathrm{d}\varphi = \pi$$

$$\int_0^{2\pi} \sin^2\varphi \, \mathrm{d}\varphi = \int_0^{2\pi} \frac{1 - \cos(2\varphi)}{2} \, \mathrm{d}\varphi = \pi \tag{B.21}$$

Using Eqs. (B.21) and (B.20) in Eq. (B.19) we have,

$$
\begin{aligned}
\tilde{\mathbf{w}}^{\mathrm{T}}(\mathbf{k}) &= \int_0^\pi \int_0^\infty \int_0^{2\pi} e^{-ikr\cos\theta}\, \delta\left(R-r|\right) \frac{\mathbf{r}\otimes\mathbf{r}}{r^2}\, r^2 \sin\theta \mathrm{d}\varphi\, \mathrm{d}r\, \mathrm{d}\theta \\
&= R^2 \int_0^\pi e^{-ikR\cos\theta}
\begin{pmatrix}
\pi\sin^3\theta & 0 & 0 \\
0 & \pi\sin^3\theta & 0 \\
0 & 0 & 2\pi\sin\theta\cos^2\theta
\end{pmatrix} \mathrm{d}\theta \\
&= \pi R^2 \int_0^\pi e^{-ikR\cos\theta} \left(\sin^3\theta\, \mathbb{I} + \left(2\cos^2\theta\sin\theta - \sin^3\theta\right)\, \mathbf{e}_z \otimes \mathbf{e}_z \right) \mathrm{d}\theta \\
&= \pi R^2 \int_0^\pi e^{-ikR\cos\theta} \left(\sin^2\theta\, \mathbb{I} + \left(3\cos^2\theta - 1\right)\, \mathbf{e}_z \otimes \mathbf{e}_z \right) \sin\theta\, \mathrm{d}\theta \\
&= \pi R^2 \left(A\, \mathbb{I} + B\, \frac{\mathbf{k}\otimes\mathbf{k}}{k^2} \right) .
\end{aligned}
\tag{B.22}
$$

where $\mathbb{I}$ is the 3×3 unit matrix, $\mathbf{e}_z$ denotes the real space unit vector along the z axis, and in the last step we have used the equivalency of $\mathbf{e}_z$ and the unit vector in reciprocal space $\mathbf{k}/k$. The undetermined integrals A and B are calculated as follows.

$$
\begin{aligned}
A &= \int_0^\pi \sin^2\theta e^{-ikR\cos\theta}\, \sin\theta\, \mathrm{d}\theta \\
&= \int_{-1}^1 (1-x^2)e^{-ikRx}\, \mathrm{d}x \quad \text{with } x = \cos\theta \\
&= \int_{-1}^1 \overbrace{(1-x^2)\cos(kRx)}^{\text{symmetric } x\to -x}\, \mathrm{d}x - i \underbrace{\int_{-1}^1 \overbrace{(1-x^2)\sin(kRx)}^{\text{asymmetric } x\to -x}\, \mathrm{d}x}_{=\,0} \\
&= 2\int_0^1 (1-x^2)\cos(kRx)\, \mathrm{d}x \\
&= 2\underbrace{\left[(1-x^2)\frac{\sin(kRx)}{kR}\right]_{x=0}^1}_{=\,0} + \frac{4}{kR}\underbrace{\int_0^1 x\sin(kRx)\, \mathrm{d}x}_{\text{see Eq. (B.8)}} \\
&= \frac{4}{k^3 R^3}\left(\sin(kR) - kR\cos(kR)\right) = \frac{1}{\pi R^3}\, \tilde{w}^3(k) ,
\end{aligned}
\tag{B.23}
$$

where in the last step we have used Eq. (B.8) and $\tilde{w}^3(k)$ is the Fourier transformation of $w^3(\mathbf{r})$ which is given in Eq. (B.9). The second integral B from Eq. (B.22) is calculated

similarly.

$$
\begin{aligned}
B &= \int_0^\pi \left(3\cos^2\theta - 1\right) e^{-ikR\cos\theta} \sin\theta \, \mathrm{d}\theta \\
&= \int_{-1}^1 (3x^2 - 1) e^{-ikRx} \mathrm{d}x \qquad \text{with } x = \cos\theta \\
&= 2\int_0^1 (3x^2 - 1)\cos(kRx)\mathrm{d}x \\
&= 2\left[(3x^2 - 1)\frac{\sin(kRx)}{kR}\right]_{x=0}^1 - \frac{12}{kR}\int_0^1 x\sin(kRx)\mathrm{d}x \\
&= \frac{4}{kR}\sin(kR) - \frac{12}{k^3 R^3}\left(-kR\cos(kR) + \sin(kR)\right) \\
&= \frac{1}{\pi R^2}\tilde{w}^2(k) - \frac{3}{\pi R^3}\tilde{w}^3(k) \,,
\end{aligned}
\tag{B.24}
$$

where $\tilde{w}^3(k)$ and $\tilde{w}^2(k)$ are respectively the Fourier transformations of $w^3(\mathbf{r})$ from Eq. (B.9) and $w^2(\mathbf{r})$ from Eq. (B.11). Finally, using the provided expressions for A (Eq. (B.23)) and B (Eq. (B.24)) in Eq. (B.22), the Fourier transformation of the tensorial weight function reads

$$
\tilde{\mathbf{w}}^{\mathrm{T}}(\mathbf{k}) = \frac{1}{R}\,\tilde{w}^3(k)\,\mathbb{I} + \left(\tilde{w}^2(k) - \frac{3}{R}\tilde{w}^3(k)\right)\frac{\mathbf{k}\otimes\mathbf{k}}{k^2}\,.
\tag{B.25}
$$

Assuming $\mathbf{k} = (k_1, k_2, k_3)$, the individual terms in $\tilde{\mathbf{w}}^{\mathrm{T}}(\mathbf{k})$ are given as follows.

$$
\begin{aligned}
\tilde{w}_{ij}^{\mathrm{T}}(\mathbf{k}) = \quad & \delta_{ij}\,\frac{4\pi}{k^3 R}\left(\sin(kR) - kR\cos(kR)\right) \\
&+ \frac{k_i k_j}{k^2}\,\frac{12\pi}{k^3 R}\left(\left(\frac{k^2 R^2}{3} - 1\right)\sin(kR) + kR\cos(kR)\right)\,,
\end{aligned}
\tag{B.26}
$$

where δ_{ij} denotes the Kronecker delta function.

$$
\delta_{ij} = \begin{cases} 1 & i = j \\ 0 & i \neq j. \end{cases}
\tag{B.27}
$$

Furthermore, using Eqs. (B.10) and (B.12) the Fourier transformation of the tensorial weight function (Eq. (B.25)) for small k is rewritten as follows:

$$
\begin{aligned}
\tilde{\mathbf{w}}^{\mathrm{T}}(\mathbf{k}) = \quad & \left(\frac{4\pi}{3}R^2 - \frac{2\pi}{15}k^2 R^4 + \frac{\pi}{210}k^4 R^6 + \mathcal{O}(k^6)\right)\mathbb{I} \\
&- \left(\frac{4\pi}{15}k^2 R^4 - \frac{2\pi}{105}k^4 R^6 + \mathcal{O}(k^6)\right)\frac{\mathbf{k}\otimes\mathbf{k}}{k^2}\,.
\end{aligned}
\tag{B.28}
$$

ANALYTICAL EXPRESSIONS FOR EXPLICIT TERMS IN FMT

C.1 Hard–Spheres

As discussed in Section A.4, for obtaining the equilibrium properties of a system of interest, the equilibrium density profile ρ_{eq} is computed by an iterative solution. For this purpose, in each step of the iterations the weighted densities $n_\alpha^{(i)}$ are calculated as the convolution of the density profile $\rho^{(i)}$ and the weighted densities w^α. Consequently the single–particle correlation function $c^{(1)}$ should be computed in order to obtain ρ_{new} from Eq. (A.18). The new density profile is then mixed with $\rho^{(i)}$ to calculate $\rho^{(i+1)}$ (see Eq. (A.20)).

The single–particle direct correlation function $c^{(1)}$ for a hard–sphere system reads

$$-c^{(1)}(\mathbf{r}) \;=\; \frac{\delta \beta \mathcal{F}^{\text{ex}}\left[\rho(\mathbf{r})\right]}{\delta \rho(\mathbf{r})} = \frac{\delta}{\delta \rho} \int d\mathbf{r} \; \Phi\left(\{n^\alpha\}\right) \tag{C.1}$$

$$\;=\; \sum_\alpha \frac{\partial \Phi}{\partial n_\alpha} * w^\alpha \,, \tag{C.2}$$

where the sum is over all weighted densities and $*$ denotes the convolution. Here, I present the analytical expressions for the derivatives of the excess free energy $\Phi = \Phi_1 + \Phi_2 + \Phi_3$ with respect to the weighted densities. For an FMT functional,

the general forms for Φ_i's are given as follows.

$$\Phi_1 = -n_0 \ln(1 - n_3) , \tag{C.3}$$

$$\Phi_2 = \varphi_1(n_3) \frac{n_1 n_2 - \mathbf{n}_1 \cdot \mathbf{n}_2}{(1 - n_3)} , \tag{C.4}$$

$$\Phi_3 = \varphi_2(n_3) \frac{3 \left(-n_2 \, \mathbf{n}_2 \cdot \mathbf{n}_2 + \mathbf{n}_2 \cdot \mathbf{n}_\mathrm{T} \cdot \mathbf{n}_2 + n_2 \mathrm{Tr}[(\mathbf{n}_\mathrm{T})^2] - \mathrm{Tr}[(\mathbf{n}_\mathrm{T})^3]\right)}{16\pi(1 - n_3)^2} . \tag{C.5}$$

By choosing $\varphi_1^\mathrm{RF} = \varphi_2^\mathrm{RF} = 1$ the RF(tensor) functional is obtained while for WBII(tensor) we have,

$$\varphi_1^\mathrm{WBII}(n_3) = 1 + \frac{2n_3 - n_3^2 + 2(1 - n_3) \ln(1 - n_3)}{3n_3} \tag{C.6}$$

$$= 1 + \frac{1}{9} \, n_3^2 + \frac{1}{18} \, n_3^3 + \mathcal{O}(n_3^4) , \tag{C.7}$$

$$\varphi_2^\mathrm{WBII}(n_3) = 1 - \frac{2n_3 - 3n_3^2 + 2n_3^3 + 2(1 - n_3)^2 \ln(1 - n_3)}{3n_3^2} \tag{C.8}$$

$$= 1 - \frac{4}{9} \, n_3 + \frac{1}{18} \, n_3^2 + \frac{1}{45} \, n_3^3 + \mathcal{O}(n_3^4) . \tag{C.9}$$

where the Taylor expansions (Eqs. (C.7) and (C.9)) are used in $n_3 \to 0$ limit in order to avoid numerical errors.

Note that in Eq. (C.5) the scalar weighted densities n_0 and n_1, as well as the vectorial weighted density $\mathbf{n}_1$, can respectively be expressed as a function of n_2 and $\mathbf{n}_2$ (see Eq. (4.4)). Therefore, in the following the required partial derivatives for calculating the excess chemical potential $\mu^\mathrm{ex} = -c^{(1)}$ (Eq. (C.2)) are only calculated for the independent weighted densities, i.e. n_2, n_3, $\mathbf{n}_2$, and $\mathbf{n}_\mathrm{T}$.

The derivatives with respect to n_2 are given by,

$$\frac{\partial \Phi_1}{\partial n_2} = -\frac{\ln(1 - n_3)}{4\pi R^2} , \tag{C.10}$$

$$\frac{\partial \Phi_2}{\partial n_2} = \varphi_1(n_3) \frac{n_2}{2\pi R(1 - n_3)} , \tag{C.11}$$

$$\frac{\partial \Phi_3}{\partial n_2} = \varphi_2(n_3) \frac{3 \left(-\mathbf{n}_2 \cdot \mathbf{n}_2 + \mathrm{Tr}[(\mathbf{n}_\mathrm{T})^2]\right)}{16\pi(1 - n_3)^2} . \tag{C.12}$$

For calculating the partial derivative of Φ with respect to n_3 we have,

$$\frac{\partial \Phi_1}{\partial n_3} = \frac{n_2}{4\pi R^2(1-n_3)} \cdot \tag{C.13}$$

$$\frac{\partial \Phi_2}{\partial n_3} = \left(\frac{\varphi_1(n_3)}{1-n_3} + \frac{\partial \varphi_1(n_3)}{\partial n_3}\right)\frac{n_2^2 - \mathbf{n}_2 \cdot \mathbf{n}_2}{4\pi R(1-n_3)}, \tag{C.14}$$

$$\frac{\partial \Phi_3}{\partial n_3} = \left(\frac{2\varphi_2(n_3)}{1-n_3} + \frac{\partial \varphi_2(n_3)}{\partial n_3}\right) \tag{C.15}$$

$$\times \frac{3\left(-n_2\,\mathbf{n}_2\cdot\mathbf{n}_2 + \mathbf{n}_2\cdot\mathbf{n}_\mathrm{T}\cdot\mathbf{n}_2 + n_2\mathrm{Tr}[(\mathbf{n}_\mathrm{T})^2] - \mathrm{Tr}[(\mathbf{n}_\mathrm{T})^3]\right)}{16\pi(1-n_3)^2} \cdot \tag{C.16}$$

where the partial derivatives of φ_i are zero for the RF(tensor) functional and for the WBII(tensor) functional using Eq. (C.9) we have,

$$\frac{\partial \varphi_1^{\mathrm{WBII}}}{\partial n_3} = \frac{-2n_3 - n_3^2 - 2\ln(1-n_3)}{3n_3^2} \tag{C.17}$$

$$= \frac{2}{9}n_3 + \frac{1}{6}n_3^2 + \frac{2}{15}n_3^3 + \frac{1}{9}n_3^4 + \mathcal{O}(n_3^5), \tag{C.18}$$

$$\frac{\partial \varphi_2^{\mathrm{WBII}}}{\partial n_3} = \frac{4n_3 - 2n_3^2 - 2n_3^3 + 4(1-n_3)\ln(1-n_3)}{3n_3^3} \tag{C.19}$$

$$= -\frac{4}{9} + \frac{1}{9}n_3 + \frac{1}{15}n_3^2 + \frac{2}{45}n_3^3 + \mathcal{O}(n_3^4), \tag{C.20}$$

where as before the Taylor expansions (Eqs. (C.18) and (C.20)) are provided to be used in $n_3 \to 0$ limit. The derivatives of Φ with respect to the vectorial and the tensorial weight functions are given by,

$$\frac{\partial \Phi_2}{\partial \mathbf{n}_2} = \varphi_1(n_3)\frac{-\mathbf{n}_2}{2\pi R(1-n_3)}, \tag{C.21}$$

$$\frac{\partial \Phi_3}{\partial \mathbf{n}_2} = \varphi_2(n_3)\frac{3\left(-n_2\,\mathbf{n}_2 + \mathbf{n}_\mathrm{T}\cdot\mathbf{n}_2\right)}{8\pi(1-n_3)^2}, \tag{C.22}$$

$$\frac{\partial \Phi_3}{\partial \mathbf{n}_\mathrm{T}} = \varphi_2(n_3)\frac{3\left(\mathbf{n}_2 \otimes \mathbf{n}_2 + 2n_2\mathbf{n}_\mathrm{T} - 3\mathbf{n}_\mathrm{T}^2\right)}{16\pi(1-n_3)^2} \cdot \tag{C.23}$$

The excess chemical potential which is needed for obtaining the equilibrium density profile in full minimization (see Section A.4), is numerically obtained by using the partial derivatives of the excess free energy density (Eqs. (C.12)-(C.23)) in Eq. (C.2).

C.2   The AO model

In the AO model for a given colloid density profile ρ_c the equilibrium polymer density $\rho_{p,eq}$ is obtained as follows (see Section 5.3),

$$\rho_{p,eq}(\mathbf{r}) \;=\; \rho_{p,r} \exp\left[c_p^{(1)}(\mathbf{r}) \right] \;, \quad \text{with } c_p^{(1)}(\rho_c(\mathbf{r})) = -\sum_\alpha \frac{\partial \Phi_{HS}}{\partial n_{\alpha,c}} * w_p^\alpha \;, \tag{C.24}$$

where Φ_{HS} is the excess free energy of a pure hard–sphere system, i.e. $\Phi_1 + \Phi_2 + \Phi_3$ from Eq. (C.5), $n_{\alpha,c}$ are the weighted densities of the colloid, and w_p^α are the polymer weighted densities (Eq. (4.4) with $R_i = R_p$). Note that the independent polymer weight functions are given as follows,

$$w_p^1 \;=\; \frac{w_p^2}{4\pi R_p} = \frac{w_p^2}{4\pi q R_c} \;, \qquad\qquad w_p^0 = \frac{w_p^2}{4\pi R_p^2} = \frac{w_p^2}{4\pi q^2 R_c^2} \;, \tag{C.25}$$

$$\mathbf{w}_p^0 \;=\; \frac{\mathbf{w}_p^2}{4\pi R_p^2} = \frac{\mathbf{w}_p^2}{4\pi q^2 R_c^2} \;, \tag{C.26}$$

where $q = R_p/R_c$ is the polymer–colloid size ratio. In the previous section, the partial derivatives with respect to the non–independent weighted densities were easily replaced with their corresponding independent ones. Here this should be done with caution since for instance the term containing partial derivatives of Φ_1 reads

$$\sum_\alpha \frac{\partial \Phi_1}{\partial n_{\alpha,c}} * w_p^\alpha \;=\; \frac{\partial \Phi_1}{\partial n_{3,c}} * w_p^3 + \frac{\partial \Phi_1}{\partial n_{0,c}} * w_p^0 \tag{C.27}$$

$$=\; \frac{\partial \Phi_1}{\partial n_{3,c}} * w_p^3 + \left(4\pi R_c^2 \frac{\partial \Phi_1}{\partial n_{2,c}} \right) * \left(\frac{1}{4\pi R_p^2} w_p^2 \right) \;, \tag{C.28}$$

where the second term is equivalent to $\partial \Phi_1/\partial n_2$ from Eq. (C.10) with an additional $1/q^2$ coefficient. As a result, for the convolutions with the independent polymer weighted densities, i.e. w_p^2, w_p^3, $\mathbf{w}_p^2$, and $\mathbf{w}_p^T$, a compensating coefficient $C_{i,\alpha}$ should be considered. This compensating coefficients modify the partial derivatives of the hard–sphere excess free energy density Φ_i^{HS} with respect to colloid weighted density $n_{\alpha,c}$ and relate it to those calculated in the previous section as follows.

$$\frac{\partial \Phi_{HS}}{\partial n_{\alpha,c}} \;=\; \sum_{i=1}^{3} C_{i,n_\alpha} \frac{\partial \Phi_i}{\partial n_\alpha} \tag{C.29}$$

The partial derivatives with respect to $n_{3,c}$ as well as the corresponding terms to the tensorial weight function $\mathbf{n}_{T,c}$ are respectively the same as those provided in Eqs. (C.13)-(C.16) and C.23. Therefore,

$$C_{i,n_3} = C_{i,\mathbf{n}_T} = 1 , \qquad \text{for } i = 1, 2, 3 . \tag{C.30}$$

For the compensating coefficients of partial derivative with respect to $n_{2,c}$ and $\mathbf{n}_{2,c}$ we have,

$$C_{1,n_2} = \frac{1}{q^2} , \quad C_{2,n_2} = C_{2,\mathbf{n}_2} = \frac{1}{2}\left(1 + \frac{1}{q}\right) , \quad C_{3,n_2} = C_{3,\mathbf{n}_2} = 1 . \tag{C.31}$$

Using Eqs. (C.30) and (C.31) in Eq. (C.29), the required partial derivatives for calculating the single–particle correlation function for polymers $c_{\text{p}}^{(1)}$ (Eq. (C.24)) are obtained. Consequently the polymer density profile $\rho_{\text{p,eq}}$ and its corresponding weighted densities $n_{\alpha,\text{p}}$ are computed. Finally, the excess free energy density for the AO model Φ_{AO} is calculated as follows,

$$\Phi_{\text{AO}} = \Phi_{\text{HS}} + \sum_{\alpha} n_{\alpha,\text{p}} \frac{\partial \Phi_{\text{HS}}}{\partial n_{\alpha,\text{c}}} . \tag{C.32}$$

with the partial derivative of the hard–sphere excess free energy density with respect to $n_{\alpha,\text{c}}$ from Eq. (C.30).

Using Eq. (C.32) the colloid single–particle correlation function $c_{\text{c}}^{(1)}$ reads

$$\begin{aligned}
-c_{\text{c}}^{(1)} &= \sum_{\alpha} \frac{\partial \Phi_{\text{AO}}}{\partial n_{\alpha,\text{c}}} * w_{\text{c}}^{\alpha} \\
&= -c_{\text{HS}}^{(1)} + \sum_{\alpha} \left[\sum_{\alpha'} n_{\alpha',\text{p}} \frac{\partial^2 \Phi_{\text{HS}}}{\partial n_{\alpha,\text{c}} \partial n_{\alpha',\text{c}}} \right] * w_{\text{c}}^{\alpha} .
\end{aligned} \tag{C.33}$$

Here $c_{\text{HS}}^{(1)} = c^{(1)}$ from Eq. (C.2) and the second partial derivative in brackets is given by,

$$\frac{\partial^2 \Phi_{\text{HS}}}{\partial n_{\alpha,\text{c}} \partial n_{\alpha',\text{c}}} = \sum_{i=1}^{3} C_{i,n_{\alpha'}} \frac{\partial^2 \Phi_i}{\partial n_\alpha \partial n_{\alpha'}} \tag{C.34}$$

where the compensating coefficients $C_{i,n_{\alpha'}}$ are the ones from Eqs. (C.30) and (C.31). The second partial derivatives of the hard–sphere excess free energy density, i.e. $\Phi = \Phi_1 + \Phi_2 + \Phi_3$ with Φ_i from Eq. (C.5), are calculated in the following.

For Φ_1 we have,

$$\frac{\partial^2 \Phi_1}{\partial n_2 \partial n_3} = \frac{1}{4\pi R^2 (1 - n_3)} \, , \tag{C.35}$$

$$\frac{\partial^2 \Phi_1}{\partial n_3{}^2} = \frac{n_2}{4\pi R^2 (1 - n_3)^2} \, . \tag{C.36}$$

For Φ_2 we have,

$$\frac{\partial^2 \Phi_2}{\partial n_2{}^2} = \varphi_1(n_3) \frac{1}{2\pi R(1 - n_3)} \, , \tag{C.37}$$

$$\frac{\partial^2 \Phi_2}{\partial \mathbf{n_2}{}^2} = \varphi_1(n_3) \frac{-1}{2\pi R(1 - n_3)} \, , \tag{C.38}$$

$$\frac{\partial^2 \Phi_2}{\partial n_2 \partial n_3} = \left(\frac{\varphi_1(n_3)}{1 - n_3} + \frac{\partial \varphi_1(n_3)}{\partial n_3} \right) \frac{n_2}{2\pi R(1 - n_3)} \, , \tag{C.39}$$

$$\frac{\partial^2 \Phi_2}{\partial \mathbf{n_2} \partial n_3} = \left(\frac{\varphi_1(n_3)}{1 - n_3} + \frac{\partial \varphi_1(n_3)}{\partial n_3} \right) \frac{-\mathbf{n_2}}{2\pi R(1 - n_3)} \, , \tag{C.40}$$

$$\frac{\partial^2 \Phi_2}{\partial n_3{}^2} = \left(\frac{2\varphi_1(n_3)}{(1 - n_3)^2} + \frac{\partial \varphi_1(n_3)}{\partial n_3} \frac{2}{1 - n_3} + \frac{\partial^2 \varphi_1(n_3)}{\partial n_3{}^2} \right) \frac{n_2^2 - \mathbf{n_2} \cdot \mathbf{n_2}}{4\pi R(1 - n_3)} \, , \tag{C.41}$$

where φ_1 for the WBII(tensor) functional and its first derivative with respect to n_3 are respectively provided in Eqs. (C.9) and (C.20), and for its second derivative we have,

$$\frac{\partial^2 \varphi_1^{\mathrm{WBII}}(n_3)}{\partial n_3{}^2} = \frac{4n_3 - 2n_3^2 + 4(1 - n_3)\ln(1 - n_3)}{3n_3^3(1 - n_3)} \tag{C.42}$$

$$= \frac{2}{9} + \frac{1}{3}n_3 + \frac{2}{5}n_3^2 + \frac{4}{9}n_3^3 + \mathcal{O}(n_3^4) \, . \tag{C.43}$$

For non–zero second derivatives of Φ_3 we have,

$$\frac{\partial^2 \Phi_3}{\partial n_2 \partial \mathbf{n_2}} = \varphi_2(n_3) \frac{-3\,\mathbf{n_2}}{8\pi(1 - n_3)^2} \, . \tag{C.44}$$

$$\frac{\partial^2 \Phi_3}{\partial n_2 \partial \mathbf{n_T}} = \varphi_2(n_3) \frac{3\,\mathbf{n_T}}{8\pi(1 - n_3)^2} \, . \tag{C.45}$$

$$\frac{\partial^2 \Phi_3}{\partial \mathbf{n_2} \partial \mathbf{n_T}} = \varphi_2(n_3) \frac{3\,\mathbf{n_2}}{8\pi(1 - n_3)^2} \, . \tag{C.46}$$

$$\frac{\partial^2 \Phi_3}{\partial \mathbf{n_2}^2} = \varphi_2(n_3) \frac{3\left(-n_2 + \mathbf{n_T}\right)}{8\pi(1-n_3)^2} \ . \tag{C.47}$$

$$\frac{\partial^2 \Phi_3}{\partial \mathbf{n_T}^2} = \varphi_2(n_3) \frac{3\left(n_2 - 3\mathbf{n_T}\right)}{8\pi(1-n_3)^2} \ . \tag{C.48}$$

$$\frac{\partial^2 \Phi_3}{\partial n_2 \partial n_3} = \left(\frac{2\varphi_2(n_3)}{1-n_3} + \frac{\partial \varphi_2(n_3)}{\partial n_3}\right) \frac{3\left(-\mathbf{n_2} \cdot \mathbf{n_2} + \mathrm{Tr}[(\mathbf{n_T})^2]\right)}{16\pi(1-n_3)^2} \ . \tag{C.49}$$

$$\frac{\partial^2 \Phi_3}{\partial \mathbf{n_2} \partial n_3} = \left(\frac{2\varphi_2(n_3)}{1-n_3} + \frac{\partial \varphi_2(n_3)}{\partial n_3}\right) \frac{3\left(-n_2\,\mathbf{n_2} + \mathbf{n_2} \cdot \mathbf{n_T}\right)}{8\pi(1-n_3)^2} \ . \tag{C.50}$$

$$\frac{\partial^2 \Phi_3}{\partial \mathbf{n_T} \partial n_3} = \left(\frac{2\varphi_2(n_3)}{1-n_3} + \frac{\partial \varphi_2(n_3)}{\partial n_3}\right) \frac{3\left(\mathbf{n_2} \otimes \mathbf{n_2} + 2n_2\mathbf{n_T} - 3\mathbf{n_T^2}\right)}{16\pi(1-n_3)^2} \ . \tag{C.51}$$

$$\frac{\partial^2 \Phi_3}{\partial n_3^2} = \left(\frac{6\varphi_2(n_3)}{(1-n_3)^2} + \frac{\partial \varphi_2(n_3)}{\partial n_3} \frac{2}{1-n_3} + \frac{\partial^2 \varphi_2(n_3)}{\partial n_3^2}\right)$$
$$\times \frac{3\left(-n_2\,\mathbf{n_2} \cdot \mathbf{n_2} + \mathbf{n_2} \cdot \mathbf{n_T} \cdot \mathbf{n_2} + n_2\mathrm{Tr}[(\mathbf{n_T})^2] - \mathrm{Tr}[(\mathbf{n_T})^3]\right)}{16\pi(1-n_3)^2} \ , \tag{C.52}$$

where φ_2 for the WBII(tensor) functional (Eq. (C.9)) and its first derivative with respect to n_3 is calculated in Eq. (C.20) while its second derivative reads

$$\frac{\partial^2 \varphi_2^{\mathrm{WBII}}(n_3)}{\partial n_3^2} = \frac{-12n_3 + 2n_3^2 - 4(3 - 2n_3)\ln(1 - n_3)}{3n_3^4} \tag{C.53}$$

$$= \frac{1}{9} + \frac{2}{15}\,n_3 + \frac{2}{15}\,n_3^2 + \frac{8}{63}\,n_3^3 + \mathcal{O}(n_3^4) \ . \tag{C.54}$$

Using the second derivatives of the excess free energy density (Eqs. (C.36)-(C.54)) in Eq. (C.34), we can calculate $c_c^{(1)}$ from Eq. (C.33).

The full minimization for the AO model starts from an initial Gaussian density profile (see Eq. (A.4)) for the colloids. In each iteration, the colloid weighted densities $n_{\alpha,c}$ are calculated for obtaining $c_c^{(1)}$ and the polymer density profile $\rho_{p,eq}$ (Eq. (C.24)). After calculating the polymer weighted densities $n_{\alpha,p}$, the colloid excess chemical potential $\beta\mu_c^{ex} = -c_c^{(1)}$ (Eq. (C.33)) is obtained to be used in Eq. (A.18). The new colloid density profile is mixed with the current one to be used in the next iteration (see Eq. (A.20)).

Appendix D

Maxwell construction

The Maxwell or common tangent construction is a well known method for obtaining the phase coexistence densities ρ_1 and ρ_2 at a given temperature. At these densities, the pressure p and the chemical potential μ are equal.

$$
\begin{aligned}
p_1 &= p_2 \, , \\
\mu_1 &= \mu_2 \, ,
\end{aligned}
\tag{D.1}
$$

where $p_i = p(\rho_i)$ and $\mu_i = \mu(\rho_i)$. Assuming the free energy densities of the system in these two phases are analytically available, the chemical potential of the system is obtained as its derivative with respect to the density at constant temperature.

$$
\mu(\rho) = \frac{\partial f}{\partial \rho} \, .
\tag{D.2}
$$

Having the chemical potential, the pressure is obtained as,

$$
p(\rho) = -f(\rho) + \rho\mu(\rho) \, .
\tag{D.3}
$$

The process of equating the pressure and the chemical potential, and finding the densities at which the phase transition occurs is shown schematically in Fig. D.1. The method is known as the common tangent construction, as one should find a straight line which is tangent to the branches of the free energy density at the coexisting densities. The slope of the line is equal to the slope of the free energy curves, i.e. the chemical potential.

In practice, one may fit a polynomial to the available data points for the free energy density in order to find an analytical form and initiate the common tangent construction. For this purpose, having an initial guess for the coexistence densities $\rho_{0,i}$, we have
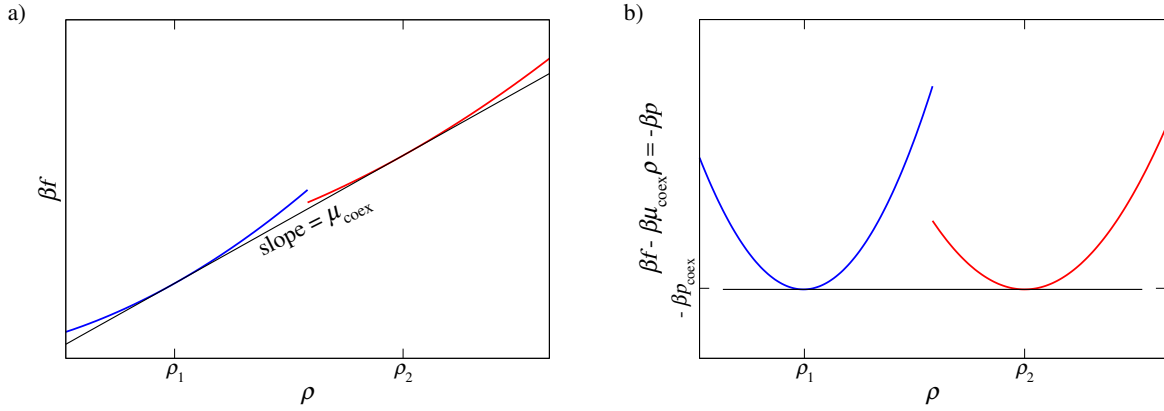
Figure D.1: Common tangent construction of the free energy curves for obtaining the coexisting densities as well as the pressure and the chemical potential. a) The red and blue curves represents the free energy density curves for two generic phases of the system. The black curve is the common tangent whose slope is equal to the chemical potential of the curves at its single–point–intersection with them: the coexistence densities. b) The grand free energy density, $w = f - \mu\rho$ which is equal to $-p$ as a function of densities. Red and blue curves represent the same phase as (a). The black curve from (a) turns into a horizontal line whose ordinate is equivalent to the coexistence pressure multiplied by -1.

fitted parabolas to the free energy density curves.

$$
\begin{aligned}
f_1(\rho) &= a_1 + b_1(\rho - \rho_{0,1}) + c_1(\rho - \rho_{0,1})^2 \\
f_2(\rho) &= a_2 + b_2(\rho - \rho_{0,2}) + c_2(\rho - \rho_{0,2})^2
\end{aligned}
\tag{D.4}
$$

This enables us to have analytical form for the chemical potential and pressure of two states. Using Eq. (D.2) the analytical form of the chemical potentials μ_i reads

$$
\begin{aligned}
\mu_1(\rho) &= b_1 + 2c_1(\rho - \rho_{0,1}) , \\
\mu_2(\rho) &= b_2 + 2c_2(\rho - \rho_{0,2}) .
\end{aligned}
\tag{D.5}
$$

By equating the chemical potentials $\mu_1(\rho_1) = \mu_2(\rho_2) = \mu_{\text{coex}}$, the coexistence density of the second phase ρ_2 may be expressed as a function of its corresponding value for first phase ρ_1.

$$
\rho_2 = \rho_{0,2} + \frac{b_1 - b_2}{2c_2} + \frac{c_1}{c_2}(\rho_1 - \rho_{0,1}) .
\tag{D.6}
$$

On the other hand, by combining the analytical forms of the free energy densities from Eq. (D.4) and the chemical potentials from Eq. (D.5), one can obtain an analytical form

for the pressure using Eq. (D.3).

$$
\begin{aligned}
p_1(\rho) &= -a_1 + b_1\rho_{0,1} + c_1(\rho - \rho_{0,1})(\rho + \rho_{0,1}) \, , \\
p_2(\rho) &= -a_2 + b_2\rho_{0,2} + c_2(\rho - \rho_{0,2})(\rho + \rho_{0,2}) \, .
\end{aligned} \tag{D.7}
$$

By equating the pressure of the two phases at the coexistence densities $p_1(\rho_1) = p_2(\rho_2) = p_{\mathrm{coex}}$ and using Eq. (D.6), the coexistence density of the first phase ρ_1 can be expressed in terms of the fitting parameters a_i, b_i, and c_i, and the initial guesses for the coexistence densities $\rho_{0,i}$.

$$
\begin{aligned}
\rho_1 &= \frac{-\frac{1}{2}(b_1 - b_2) + c_1\rho_{0,1} - c_2\rho_{0,2} + \sqrt{\frac{c_2}{c_1}k}}{c_1 - c_2} \\
&\text{with}\quad k = \frac{1}{4}(b_1 - b_2)^2 - (a_1 - a_2)(c_1 - c_2) \\
&\qquad\qquad + (c_1 b_2 - c_2 b_1)(\rho_{0,1} - \rho_{0,2}) + c_1 c_2(\rho_{0,1} - \rho_{0,2})^2 \, ,
\end{aligned} \tag{D.8}
$$

which can be later used in Eq. (D.6) to obtain the coexistence density of the second phase ρ_2. In case the difference of the obtained results with initial guesses is larger than a given tolerance, e.g. $|\rho_i - \rho_{0,i}| > 0.001$, the parabolas from Eq. (D.4) are re–initiated with the previous results for ρ_i as the new $\rho_{0,i}$ and the procedure is repeated.

APPENDIX E

EXCESS FREE ENERGY OF A 0D CAVITY FOR THE AO MODEL

The concept of a 0D cavity, a cavity which can not hold more than one particle, is already introduced in Section 4.2. There we have discussed that an FMT functional which accounts for freezing must necessarily results in 0D free energy under appropriate form of confining external potential. Moreover, it is possible to construct a functional from 0D as explained in Section 4.2 (see Eq. (4.27) and its following discussion).

For extending the idea to the AO model, consider a cavity which either contains one colloidal hard–sphere or the polymer ideal gas. The grand partition sum is written as

$$
\begin{aligned}
\Xi_{\text{AO}} &= \sum_{N_\text{p}=0}^{\infty} \sum_{N_\text{c}=0}^{\infty} \frac{Z_{N_\text{c},N_\text{p}}^{\text{AO}} e^{\beta\mu_\text{c}N_\text{c}} e^{\beta\mu_\text{p}N_\text{p}}}{N_\text{c}!N_\text{p}!} \\
&= \sum_{N_\text{p}=0}^{\infty} \frac{Z_{N_\text{c}=0,N_\text{p}}^{\text{AO}} e^{\beta\mu_\text{p}}}{N_\text{p}!} + Z_{N_\text{c}=1,N_\text{p}=0}^{\text{AO}} e^{\beta\mu_\text{c}} \\
&= \sum_{N_\text{p}=0}^{\infty} \frac{(Z_{1,\text{p}})^{N_\text{p}} e^{\beta\mu_\text{p}N_\text{p}}}{N_\text{p}!} + Z_{1,\text{c}} e^{\beta\mu_\text{c}} \\
&= \exp\left(Z_{1,\text{p}} e^{\beta\mu_\text{p}}\right) + Z_{1,\text{c}} e^{\beta\mu_\text{c}} ,
\end{aligned}
\tag{E.1}
$$

where $Z_{N_\text{c},N_\text{p}}^{\text{AO}}$ is the configuration partition function for the AO model with N_c colloids and N_p polymers, and $Z_{1,\text{i}}$ is the single particle partition function for species i. For the

number of colloidal particles N_c we can write,

$$
\begin{aligned}
N_c &= \frac{\partial \ln \Xi_{AO}}{\partial \beta \mu_c} = \frac{Z_{1,c} e^{\beta \mu_c}}{\exp\left(Z_{1,p} e^{\beta \mu_p}\right) + Z_{1,c} e^{\beta \mu_c}} \ , \\
&\Rightarrow \ Z_{1,c} e^{\beta \mu_c} = \frac{N_c \exp\left(Z_{1,p} e^{\beta \mu_p}\right)}{1 - N_c} \ . & \text{(E.2)} \\
&\Rightarrow \ \beta \mu_c = \ln\left[\frac{N_c \exp\left(Z_{1,p} e^{\beta \mu_p}\right)}{Z_{1,c}\left(1 - N_c\right)}\right] \ . & \text{(E.3)}
\end{aligned}
$$

Similarly, for the number of polymer chains N_p we have,

$$
\begin{aligned}
N_p &= \frac{\partial \ln \Xi_{AO}}{\partial \beta \mu_p} = \frac{Z_{1,p} e^{\beta \mu_p} \exp\left(Z_{1,p} e^{\beta \mu_p}\right)}{\exp\left(Z_{1,p} e^{\beta \mu_p}\right) + Z_{1,c} e^{\beta \mu_c}} = \frac{Z_{1,p} e^{\beta \mu_p}}{1 + \frac{N_c}{1 - N_c}} \ , \\
&\Rightarrow \ Z_{1,p} e^{\beta \mu_p} = \frac{N_p}{1 - N_c} \ . & \text{(E.4)} \\
&\Rightarrow \ \beta \mu_p = \ln\left[\frac{N_p}{Z_{1,p}\left(1 - N_c\right)}\right] \ . & \text{(E.5)}
\end{aligned}
$$

where we have used Eq. (E.2). Now we can rewrite Eq. (E.1) by the expressions obtained from Eqs. (E.2) and (E.4) in order to calculate the pressure of the system.

$$
\beta p = \ln \Xi_{AO} = \frac{N_p}{1 - N_c} - \ln\left(1 - N_c\right) \ . \tag{E.6}
$$

As a result, we are able to calculate the free energy of a 0D cavity for the AO model.

$$
\begin{aligned}
\beta F &= -\beta p + \beta \mu_c N_c + \beta \mu_p N_p \\
&= -\frac{N_p}{1 - N_c} + \ln\left(1 - N_c\right) \\
&\quad + N_c \ln\left[\frac{N_c \exp\left(Z_{1,p} e^{\beta \mu_p}\right)}{Z_{1,c}\left(1 - N_c\right)}\right] + N_p \ln\left[\frac{N_p}{Z_{1,p}\left(1 - N_c\right)}\right] \ . \tag{E.7}
\end{aligned}
$$

Here, we have used the expressions for $\beta \mu_c$ from Eq. (E.3), $\beta \mu_p$ from Eq. (E.5), and βp from Eq. (E.6).

In order to determine the unknown expressions for the single–particle partition functions $Z_{1,i}$, consider the colloidal particles as ideal gas particles. The grand partition sum for such a system is written as follows:

$$
\begin{aligned}
\Xi_{AO}^{id} &= \sum_{N_c=0}^{\infty} \sum_{N_c=0}^{\infty} \frac{(Z_{1,c})^{N_p}(Z_{1,p})^{N_p} e^{\beta \mu_c N_c} e^{\beta \mu_p N_p}}{N_c! N_p!} \\
&= \exp\left(Z_{1,c} e^{\beta \mu_c} + Z_{1,p} e^{\beta \mu_p}\right) \ , \tag{E.8}
\end{aligned}
$$

The number of different species N_i and consequently their corresponding chemical potentials μ_i and the pressure of the system p_i are calculated as follows.

$$
\begin{aligned}
N_c &= \frac{\partial \ln \Xi}{\partial \beta \mu_c} = Z_{1,c} e^{\beta \mu_c} , \qquad N_p = \frac{\partial \ln \Xi}{\partial \beta \mu_p} = Z_{1,p} e^{\beta \mu_p} \\
\Rightarrow \quad \beta \mu_c &= \ln \left(\frac{N_c}{Z_{1,c}} \right) , \qquad\qquad \beta \mu_p = \ln \left(\frac{N_p}{Z_{1,p}} \right) \\
\beta p &= \ln \Xi = Z_{1,c} e^{\beta \mu_c} + Z_{1,p} e^{\beta \mu_p} = N_c + N_p
\end{aligned}
\tag{E.9}
$$

Therefore, the ideal part of the free energy for the AO model reads

$$
\begin{aligned}
\beta F^{\text{id}} &= -\beta p + \beta \mu_c N_c + \beta \mu_p N_p \\
&= -N_c - N_p + N_c \ln \left(\frac{N_c}{Z_{1,c}} \right) + N_p \ln \left(\frac{N_p}{Z_{1,p}} \right)
\end{aligned}
\tag{E.10}
$$

By subtracting βF^{id} from the total free energy from Eq. (E.7), we obtain the excess free energy of a 0D cavity for the AO model.

$$
\begin{aligned}
\beta F^{\text{ex}} &= \beta F - \beta F^{\text{id}} \\
&= -\frac{N_p}{1 - N_c} + \ln \left(1 - N_c \right) + N_c + N_p \\
&\quad + N_c \ln \left(\frac{\exp \left(Z_{1,p} e^{\beta \mu_p} \right)}{1 - N_c} \right) + N_p \ln \left(\frac{1}{1 - N_c} \right) \\
&= (1 - N_c - N_p) \ln (1 - N_c) + N_c .
\end{aligned}
\tag{E.11}
$$

By replacing N_i with the corresponding packing fractions η_i, Eq. (E.12) is recovered.

$$
\Phi_{0D}^{\text{AO}} = \eta_c + \ln(1 - \eta_c)(1 - \eta_c - \eta_p) ,
\tag{E.12}
$$

As discussed in Section 5.3, since Φ_{0D}^{AO} has either constant or linear terms in the polymer density ρ_p the obtained functional for higher dimensions is also linear in ρ_p (see Eq. (E.12) and the following discussion).

APPENDIX F

EMBEDDED ATOM MODEL

The total energy of a system E_{coh} provides information about the structure and thermal properties of a solid. In a classical system whose particles interaction is described by a pairwise potential u, E_{coh} is simply calculated as,

$$E_{\mathrm{coh}} \;=\; \frac{1}{2} \sum_{\substack{i,j \\ i \neq j}} u\left(r_{ij}\right) , \qquad \text{with } r_{ij} = |\mathbf{r}_i - \mathbf{r}_j| , \tag{F.1}$$

where $\mathbf{r}_i$ denotes the position of atom i. Here, the ansatz is that the atomic bonds act independently and the presence of one does not affect the others. In a metallic system however, this is not true since the interactions are of many–body nature. This can be shown for instance by looking at the strong deviation of the solid cohesive energy E_{coh} with the Gibbs free energy of vacancy formation ΔG_{v} which for a pairwise interaction is $E_{\mathrm{coh}} \approx \Delta G_{\mathrm{v}}$.

Embedded Atom method (EAM) is an attempt to approximate the many–body interactions which are neglected in Eq. (F.1). In this approach, the total energy of the metal is calculated as the obtained energy of *embedding* a single atom into the electron density provided by "host" atoms [135, 157].

$$E_{\mathrm{coh}} \;=\; \frac{1}{2} \sum_{\substack{i,j \\ i \neq j}} u\left(r_{ij}\right) + \sum_i F\left(\rho_i^{\mathrm{a}}\right) , \qquad \text{with } \rho_i^{\mathrm{a}} = \sum_{j \neq i} \rho^{\mathrm{a}}\left(r_{ij}\right) \tag{F.2}$$

Here, u is an electrostatic two–body potential, F is the embedding energy, ρ_i^{a} is the local electron density at the position of atom i. The latter is calculated as a superposition of $\rho^{\mathrm{a}}(r_{ij})$ the spherically averaged electron density of atom j.

Fur numerical implementation, the required functions are atomic electron density ρ^{a}, embedding function F, and the pair interaction u. In the following, three different

parametrization of these undetermined functions for Nickel are presented. Throughout these chapter, the energies are expressed in eV, the length unit is Å, and the densities are expressed as number in $Å^3$.

F.1 F85

In the parametrization of the EAM potential presented by Foiles (F85) in Ref. [137], the total potential energy is decomposed into a repulsive part due to the interaction of the nuclei and an attractive part given by the embedding function (see Eq. (F.2)). The short–range purely repulsive part of the potential is given by the repulsive Coulomb interaction of atom i and the screened nuclei charges $Z(r)$ of the host $j \neq i$.

$$u(r_{ij}) = \frac{1}{4\pi\epsilon_0} \frac{Z^2(r_{ij})e^2}{r_{ij}} \; , \tag{F.3}$$

where e is the elementary charge. In F85, the screening function $Z^2(r)$ is fitted to a fourth order polynomial for distances smaller than the cut–off range r_{cut}.

$$Z^2(r) = \begin{cases} a_1(r_{\mathrm{cut}} - r)^3 + a_2(r_{\mathrm{cut}} - r)^4 \; , & \text{for } r < r_{\mathrm{cut}} \\ 0 & \text{otherwise} \; . \end{cases} \tag{F.4}$$

For Nickel the cut–off range of the screening potential is $r_{\mathrm{cut}} = 3.0045$ and the coefficients are $a_1 = 0.070937$ and $a_2 = 0.146031$.

The atomic electron density ρ^{a} is obtained based on the Hartree–Fock calculations of Clementi and Roetti and of McLean and McLean [158, 159], and is approximated by a mixture of ρ_s^{a} and ρ_d^{a} which are respectively the density of outer s and d orbitals.

$$\rho^{\mathrm{a}}(r) = n_s\rho_s^{\mathrm{a}}(r) + (n - n_s)\rho_d^{\mathrm{a}}(r) \; . \tag{F.5}$$

Here, n is the total number of outer electrons and n_s gives an effective measure of the contribution of the s–orbital–like electrons which is obtained by a fitting to the hydrogen heat of solution [135]. The spherically averaged s–like electron density ρ_s^{a} is computed by,

$$\rho_s^{\mathrm{a}}(r) = \frac{1}{4\pi} \left| \sum_i C_i R_i(r) \right|^2 \qquad \text{with } R_i(r) = \sqrt{\frac{(2\zeta_i)^{(2n_i+1)}}{(2n_i)!}} \; r^{n_i-1}e^{-\zeta_i r} \; . \tag{F.6}$$

The required parameters for obtaining ρ_s^{a}, as well as ρ_d^{a} which is computed by a similar expression, are presented in table F.1.

Finally, the embedding function is determined by choosing functional forms which meet some general requirements, namely,

Table F.1: Parameters used to calculate the atomic electron density ρ^{a}. The total electron density is given by Eq. (F.5) with $n = 10$ and $n_s = 0.85$ for Nickel. The spherically averaged s– and d–like electron densities, i.e. ρ_s^{a} and ρ_s^{a} respectively, are computed using Eq. (F.6).

| | 4s | | | 3d | | |
i	n_i	ζ_i	C_i	n_i	ζ_i	C_i
1	1	54.88885	-0.00389	3	12.67582	0.4212
2	1	38.48431	-0.02991	3	5.43253	0.70658
3	2	27.42703	-0.03189			
4	2	20.88204	0.15289			
5	3	10.95707	-0.20048			
6	3	7.31958	-0.05423			
7	4	3.9265	0.49292			
8	4	2.15289	0.61875			

- $F = 0$ for $\rho^{\mathrm{a}} = 0$,

- F decreases to a simple minimum with a value greater than the sublimation energy,

- The minimum of F occurs at ρ_0^{a} which is slightly greater than average electron density in equilibrium,

- it increases for $\rho^{\mathrm{a}} > \rho_0^{\mathrm{a}}$.

The functional forms which meet these requirements are adjusted to describe the bulk equilibrium solid. This is achieved by a fitting to the equilibrium lattice constant, the sublimation energy, the elastic constants, the vacancy formation energy, and the energy difference of bcc and fcc lattice structures [137]. The obtained embedding function F is presented as knots of a spline in table F.2. For spline interpolation the usual convention of setting curvature to zero at endpoints is used[1].

F.2   FBD86

Similar to F85, there are two distinct contribution to the total potential energy in the parametrization presented by Foiles, Baskes and Daw (FBD86) in Ref. [138]. For FBD86,

---

[1] See Section 3.3 of Ref. [160] for a numerical implementation of splines in C.

Table F.2: Parameters used to calculate the screening $Z^2(r)$ and the embedding F functions of F85 for Nickel [137]. The screening function $Z^2(r)$ is calculated by using a_1, a_2, and r_{cut} in Eq. (F.4). The embedding function $F(\rho_i^{\text{a}})$ is obtained by spline interpolation of the provided values with the usual convention of setting curvature to zero at endpoints.

a_1	a_2	r_{cut}		ρ_i^{a}	F
0.070937	0.146031	3.0045		0	0
				0.01446	-3.5847
				0.02891	-5.1449
				0.05783	-3.4041

the embedding function $F(\rho_i^{\text{a}})$ is specified so that for a given metal density, or equivalently the lattice constant a in an fcc solid, the sublimation energy E_{sub} is given by [161],

$$E_{\text{sub}}(a) \;=\; -E_{\text{sub}}^0 \left(1 + a^*\right) e^{-a^*} , \qquad \text{with } a^* = \left(\frac{a}{a_0} - 1\right) / \left(E_{\text{sub}}/9B\Omega\right) . \tag{F.7}$$

Here, E_{sub}^0 is the sublimation energy at zero temperature and pressure, a^* gives a measure of deviation of the lattice constant from its equilibrium value a_0, B is the bulk modulus, and Ω is the equilibrium volume per atom. As a result of the definition of the embedding function in FBD86, the obtained result for the equilibrium lattice constant, sublimation energy, and the bulk modulus are guaranteed to be correct for pure material.

The electron density is given by Eq. (F.5) with the undetermined contribution of s–like orbital n_s. The relative values of n_s is primarily determined by the heats of mixing alloys. There is an overall scale factor which is not determined by the fitting. Foils et al. have chosen arbitrarily $n_s = 1$ for Copper and hence for Nickel we have $n_s = 1.5166$.

Finally, the repulsive potential due to the interaction of the nuclei is given by the same expression as F85 Eq. (F.3). However, the screening function Z in FBD86 is different from that of F85 and it reads

$$Z(r) \;=\; Z_0 \left(1 + \beta r^\nu\right) e^{-\alpha r} , \tag{F.8}$$

where Z_0 is assumed to be the number of outer electrons of the atom and ν is empirically chosen so that a good representation of the elastic constant is achieved. For Nickel these parameters are $Z_0 = 10$ and $\nu = 1$. The values of the undetermined parameters α and β are primarily calculated by fitting to the shear moduli and the vacancy formation energy of the pure material. A summary of the required parameters for Nickel are presented in table F.3.

Table F.3: Parameters defining the EAM potentials of FBD86 for Nickel [138]. Z_0, α, β, and ν are used in Eq. (F.8) in order to obtain screening function Z and consequently the repulsive electrostatic interaction of the nuclei (Eq. (F.3)). For calculating the electron density for Nickel n_s and n are used in Eq. (F.5). The embedding function F is constructed in a way to respect the Rose et al. equation of state (Eq. (F.7)) with the following provided values for a_0, E_{sub}^0, and B). In practice, it is more convenient to calculate a few spline knots for obtaining the embedding function for a range of electron densities before the actual computations.

Z_0	α	β	ν	n_s	n	a_0	E_{sub}^0	B
10.0	1.8633	0.8957	1	1.5166	10.0	3.52	4.45	180

F.3 M99

The EAM potential given by Mishin et al. (M99) in Ref. [139] uses the same formalism in Eq. (F.2). However, the potential functions have very general form with no reference to their original physical meaning. Therefore there is no restriction on expressing the attractive and the repulsive contributions in terms of the pair potential and the embedding functions respectively.

The functions have been fitted to an optimum number of observables in order to avoid "overfitting". For this purpose Mishin et al. have split an extended database of experimental and *ab initio* calculations in two sets. The first set of observables are used for fitting the functions. The functions are later tested with the second set. The fitting observables are namely the equilibrium lattice constant, the cohesive energy of the fcc phase, the vacancy formation energy, the vacancy migration energy, the intrinsic stacking fault energy, and the experimentally measured phonon–dispersion relations. Moreover, the potentials are fitted to *ab initio* energies of the hcp, bcc, and diamond structure for comparison, while other structural energies are used in the testing stage [139]. The obtained functions are provided as tabulated values and are presented here in table F.4.

Table F.4: Tabulated values of the potential functions in M99 for Nickel [139].

r	$u(r)$	$\rho^{\mathrm{a}}(r)$	ρ_i^{a}	$F(\rho_i^{\mathrm{a}})$
2.0000	0.7597	0.0671	0.0000	0.0000
2.1585	0.1812	0.0727	0.050	-0.2164
2.3170	20.1391	0.0761	0.100	-0.5094
2.4755	20.2214	0.0755	0.150	-0.8488
2.6340	20.2153	0.0691	0.200	-1.2042
2.7924	20.1766	0.0579	0.250	-1.5453
2.9509	20.1291	0.0440	0.300	-1.8419
3.1094	20.0909	0.0301	0.350	-2.0714
3.2679	20.0643	0.0193	0.400	-2.2426
3.4264	20.0423	0.0123	0.450	-2.3721
3.5849	20.0252	0.0081	0.500	-2.4766
3.7434	20.0139	0.0057	0.550	-2.5698
3.9019	20.0089	0.0043	0.600	-2.6542
4.0604	20.0084	0.0031	0.650	-2.7296
4.2189	20.0078	0.0021	0.700	-2.7958
4.3773	20.0043	0.0014	0.750	-2.8525
4.5358	0.0006	0.0008	0.800	-2.8995
4.6943	0.0044	0.0004	0.850	-2.9364
4.8528	0.0052	0.0002	0.900	-2.9631
5.0113	0.0037	0.0001	0.950	-2.9793
5.1698	0.0022	0.0000	0.975	-2.9834
5.3283	0.0024	0.0000	1.000	-2.9848
5.4868	0.0020	0.0000	1.025	-2.9840
5.6453	0.0004	0.0000	1.050	-2.9838
5.8037	0.0000	0.0000	1.100	-2.9990

Bibliography

[1] J. D. Patterson and B. C. Bailey, *Solid-state physics: introduction to the theory* (2007).

[2] V. Prasad, D. Semwogerere, and E. R. Weeks, Journal of Physics: Condensed Matter **19**, 113102 (2007): *Confocal microscopy of colloids*.

[3] H. N. Lekkerkerker and R. Tuinier, *Colloids and the depletion interaction*, Vol. 833 of *Lecture Notes in Physics* (2011).

[4] S. Asakura and F. Oosawa, The Journal of Chemical Physics **22**, 1255 (1954): *On Interaction between Two Bodies Immersed in a Solution of Macromolecules*.

[5] A. Vrij, Pure and Applied Chemistry **48**, 471 (1976): *Polymers at interfaces and the interactions in colloidal dispersions*.

[6] J.-P. Hansen and I. R. McDonald, *Theory of Simple Liquids: With Applications to Soft Matter* (2013).

[7] R. Evans, Advances in Physics **28**, 143 (1979): *The nature of the liquid-vapour interface and other topics in the statistical mechanics of non-uniform, classical fluids*.

[8] C. Ebner, W. F. Saam, and D. Stroud, Phys. Rev. A **14**, 2264 (1976): *Density-functional theory of simple classical fluids. I. Surfaces*.

[9] Y. Rosenfeld, Phys. Rev. Lett. **63**, 980 (1989): *Free-energy model for the inhomogeneous hard-sphere fluid mixture and density-functional theory of freezing*.

[10] P. Tarazona, Phys. Rev. Lett. **84**, 694 (2000): *Density Functional for Hard Sphere Crystals: A Fundamental Measure Approach*.

[11] R. Roth, R. Evans, A. Lang, and G. Kahl, Journal of Physics: Condensed Matter **14**, 12063 (2002): *Fundamental measure theory for hard-sphere mixtures revisited: the White Bear version*.

[12] H. Hansen-Goos and R. Roth, Journal of Physics: Condensed Matter **18**, 8413
      (2006): *Density functional theory for hard-sphere mixtures: the White Bear version
      mark II.*

[13] E. J. Mittemeijer, in *Fundamentals of Materials Science: The Microstructure–Property
      Relationship Using Metals as Model Systems* (2010), Chap. 5 The Crystal imperfec-
      tion and Chap. 8 Diffusion.

[14] F. H. Stillinger, Z. W. Salsburg, and R. L. Kornegay, The Journal of Chemical
      Physics **43**, 932 (1965): *Rigid Disks at High Density.*

[15] W. G. Rudd, Z. W. Salsburg, A. P. Yu, and F. H. Stillinger, The Journal of Chemical
      Physics **49**, 4857 (1968): *Rigid Disks and Spheres at High Densities. III.*

[16] M. Mortazavifar and M. Oettel, EPL (Europhysics Letters) **105**, 56005 (2014):
      Thermal vacancies in close–packing solids.

[17] M. Mortazavifar and M. Oettel, Journal of Physics: Condensed Matter **28**, 244018
      (2016): *A fundamental measure density functional for fluid and crystal phases of the
      Asakura–Oosawa model.*

[18] M. Kardar, *Statistical physics of particles* (2007).

[19] P. Hohenberg and W. Kohn, Phys. Rev. **136**, B864 (1964): *Inhomogeneous Electron
      Gas.*

[20] N. D. Mermin, Phys. Rev. **137**, A1441 (1965): *Thermal Properties of the Inhomoge-
      neous Electron Gas.*

[21] H. Goldstein, C. P. Poole, and J. L. Safko, *Classical Mechanics* (2000).

[22] L. S. Ornstein and F. Zernike, in *Proc. Akad. Sci.(Amsterdam)* (1914), Vol. 17, p. 793.

[23] M. Levy, Proceedings of the National Academy of Sciences **76**, 6062 (1979): *Uni-
      versal variational functionals of electron densities, first-order density matrices, and nat-
      ural spin-orbitals and solution of the v-representability problem.*

[24] P. W. Ayers and M. Levy, Journal of Chemical Sciences **117**, 507 (2005): *Gener-
      alized density-functional theory: Conquering theN-representability problem with exact
      functionals for the electron pair density and the second-order reduced density matrix.*

[25] M. Levy, Phys. Rev. A **26**, 1200 (1982): *Electron densities in search of Hamiltonians.*

[26] W. S. B. Dwandaru and M. Schmidt, Phys. Rev. E **83**, 061133 (2011): *Variational
      principle of classical density functional theory via Levy's constrained search method.*

[27] J. A. White, A. González, F. L. Román, and S. Velasco, Phys. Rev. Lett. **84**, 1220 (2000): *Density-Functional Theory of Inhomogeneous Fluids in the Canonical Ensemble.*

[28] J. A. Hernando and L. Blum, Journal of Physics: Condensed Matter **13**, L577 (2001): *Density functional formalism in the canonical ensemble.*

[29] J. A. Hernando, Journal of Physics: Condensed Matter **14**, 303 (2002): *Density functional theory in the canonical ensemble: I. General formalism.*

[30] D. de las Heras and M. Schmidt, Phys. Rev. Lett. **113**, 238304 (2014): *Full Canonical Information from Grand-Potential Density-Functional Theory.*

[31] N. Ashcroft and N. Mermin, *Solid State Physics* (2011).

[32] W. W. Wood and J. D. Jacobson, The Journal of Chemical Physics **27**, 1207 (1957): *Preliminary Results from a Recalculation of the Monte Carlo Equation of State of Hard Spheres.*

[33] B. J. Alder and T. E. Wainwright, The Journal of Chemical Physics **27**, 1208 (1957): *Phase Transition for a Hard Sphere System.*

[34] Y. Rosenfeld, M. Schmidt, H. Löwen, and P. Tarazona, Phys. Rev. E **55**, 4245 (1997): *Fundamental-measure free-energy density functional for hard spheres: Dimensional crossover and freezing.*

[35] B. Derjaguin, L. Landau, *et al.*, Acta physicochim. URSS **14**, 633 (1941): *Theory of the stability of strongly charged lyophobic sols and of the adhesion of strongly charged particles in solutions of electrolytes.*

[36] E. J. W. Verwey and J. T. G. Overbeek, Trans. Faraday Soc. **42**, B117 (1946): *Long distance forces acting between colloidal particles.*

[37] M. G. Noro and D. Frenkel, The Journal of Chemical Physics **113**, 2941 (2000): *Extended corresponding-states behavior for particles with variable range attractions.*

[38] T. Alfrey, E. B. Bradford, J. W. Vanderhoff, and G. Oster, J. Opt. Soc. Am. **44**, 603 (1954): *Optical Properties of Uniform Particle-Size Latexes∗.*

[39] E. W. Fischer, Kolloid–Zeitschrift **160**, 120 (1958): *Elektronenmikroskopische Untersuchungen zur Stabilität von Suspensionen in makromolekularen Lösungen.*

[40] de Kruif, C. G., Rouw, P. W., Jansen, J. W., and Vrij, A., J. Phys. Colloques **46**, C3 (1985): *Hard sphere properties and crystalline packing of lyophilic silica colloids.*

[41] P. N. Pusey and W. van Megen, Nature **320**, 340 (1986): *Phase behaviour of concentrated suspensions of nearly hard colloidal spheres.*

[42] T. Sugimoto, *Monodispersed particles* (2001).

[43] H. J. Schöpe, G. Bryant, and W. van Megen, Phys. Rev. E **74**, 060401 (2006): *Small changes in particle-size distribution dramatically delay and enhance nucleation in hard sphere colloidal suspensions.*

[44] H. J. Schöpe, G. Bryant, and W. van Megen, The Journal of Chemical Physics **127**, 084505 (2007): *Effect of polydispersity on the crystallization kinetics of suspensions of colloidal hard spheres when approaching the glass transition.*

[45] E. J. J. van Rensburg, Journal of Physics A: Mathematical and General **26**, 4805 (1993): *Virial coefficients for hard discs and hard spheres.*

[46] F. H. Ree and W. G. Hoover, The Journal of Chemical Physics **40**, 939 (1964): *Fifth and Sixth Virial Coefficients for Hard Spheres and Hard Disks.*

[47] F. H. Ree and W. G. Hoover, The Journal of Chemical Physics **46**, 4181 (1967): *Seventh Virial Coefficients for Hard Spheres and Hard Disks.*

[48] N. Clisby and B. M. McCoy, Journal of Statistical Physics **122**, 15 (2006): *Ninth and Tenth Order Virial Coefficients for Hard Spheres in D Dimensions.*

[49] R. J. Wheatley, Phys. Rev. Lett. **110**, 200601 (2013): *Calculation of High-Order Virial Coefficients with Applications to Hard and Soft Spheres.*

[50] N. F. Carnahan and K. E. Starling, The Journal of Chemical Physics **51**, 635 (1969): *Equation of State for Nonattracting Rigid Spheres.*

[51] J. K. Percus and G. J. Yevick, Phys. Rev. **110**, 1 (1958): *Analysis of Classical Statistical Mechanics by Means of Collective Coordinates.*

[52] J. K. Percus, Phys. Rev. Lett. **8**, 462 (1962): *Approximation Methods in Classical Statistical Mechanics.*

[53] M. S. Wertheim, Phys. Rev. Lett. **10**, 321 (1963): *Exact Solution of the Percus-Yevick Integral Equation for Hard Spheres*, .

[54] H. Reiss, H. L. Frisch, and J. L. Lebowitz, The Journal of Chemical Physics **31**, 369 (1959): *Statistical Mechanics of Rigid Spheres.*

[55] J. L. Lebowitz, E. Helfand, and E. Praestgaard, The Journal of Chemical Physics **43**, 774 (1965): *Scaled Particle Theory of Fluid Mixtures.*

[56]   R. Evans, *Density functional theory for inhomogeneous fluids I: Simple fluids in equilibrium*, *Lectures at 3rd Warsaw School of Statistical Physics: Kazimierz Dolny* (2009).

[57]   J. K. Percus, Journal of Statistical Physics **15,** 505 (1976): *Equilibrium state of a classical fluid of hard rods in an external field*.

[58]   J. K. Percus, Journal of Statistical Physics **28,** 67 (1982): *One-dimensional classical fluid with nearest-neighbor interaction in arbitrary external field*.

[59]   Y. Singh, Physics Reports **207,** 351 (1991): *Density-functional theory of freezing and properties of the ordered phase*.

[60]   P. Tarazona and R. Evans, Molecular Physics **47,** 1033 (1982): *Long ranged correlations at a solid-fluid interface A signature of the approach to complete wetting*.

[61]   M. Oettel, S. Dorosz, M. Berghoff, B. Nestler, and T. Schilling, Phys. Rev. E **86,** 021404 (2012): *Description of hard-sphere crystals and crystal-fluid interfaces: A comparison between density functional approaches and a phase-field crystal model*.

[62]   T. V. Ramakrishnan and M. Yussouff, Phys. Rev. B **19,** 2775 (1979): *First-principles order-parameter theory of freezing*.

[63]   M. Plapp, *Phase–field Models*, *Lectures at Summer School for Phase–field models for the evolution of complex structures: Peyresq(France)* (2013).

[64]   K. R. Elder, M. Katakowski, M. Haataja, and M. Grant, Phys. Rev. Lett. **88,** 245701 (2002): *Modeling Elasticity in Crystal Growth*.

[65]   K. R. Elder and M. Grant, Phys. Rev. E **70,** 051605 (2004): *Modeling elastic and plastic deformations in nonequilibrium processing using phase field crystals*.

[66]   A. Jaatinen and T. Ala-Nissila, Journal of Physics: Condensed Matter **22,** 205402 (2010): *Extended phase diagram of the three–dimensional phase field crystal model*.

[67]   S. van Teeffelen, R. Backofen, A. Voigt, and H. Löwen, Phys. Rev. E **79,** 051404 (2009): *Derivation of the phase-field-crystal model for colloidal solidification*.

[68]   H. Emmerich, Journal of Physics: Condensed Matter **21,** 464103 (2009): *Phase–field modelling for metals and colloids and nucleation therein: an overview*.

[69]   H. Löwen, Journal of Physics: Condensed Matter **22,** 364105 (2010): *A phase-field-crystal model for liquid crystals*.

[70]   R. Spatschek, *Phase Field Crystal*, *Lectures at Summer School for Phase–field models for the evolution of complex structures: Peyresq(France)* (2013).

[71] J. L. Lebowitz, Phys. Rev. **133**, A895 (1964): *Exact Solution of Generalized Percus-Yevick Equation for a Mixture of Hard Spheres*.

[72] Y. Rosenfeld, M. Schmidt, H. Löwen, and P. Tarazona, Journal of Physics: Condensed Matter **8**, L577 (1996): *Dimensional crossover and the freezing transition in density functional theory*.

[73] P. Tarazona and Y. Rosenfeld, Phys. Rev. E **55**, R4873 (1997): *From zero-dimension cavities to free-energy functionals for hard disks and hard spheres*.

[74] P. Tarazona, Physica A: Statistical Mechanics and its Applications **306**, 243 (2002): *Fundamental measure theory and dimensional interpolation for the hard spheres fluid*, .

[75] W. G. Hoover and F. H. Ree, The Journal of Chemical Physics **49**, 3609 (1968): *Melting Transition and Communal Entropy for Hard Spheres*.

[76] E. G. Noya, C. Vega, and E. de Miguel, The Journal of Chemical Physics **128**, 154507 (2008): *Determination of the melting point of hard spheres from direct coexistence simulation methods*.

[77] T. Zykova-Timan, J. Horbach, and K. Binder, The Journal of Chemical Physics **133**, 014705 (2010): *Monte Carlo simulations of the solid-liquid transition in hard spheres and colloid-polymer mixtures*.

[78] G. A. Mansoori, N. F. Carnahan, K. E. Starling, and T. W. Leland, The Journal of Chemical Physics **54**, 1523 (1971): *Equilibrium Thermodynamic Properties of the Mixture of Hard Spheres*.

[79] Y.-X. Yu and J. Wu, The Journal of Chemical Physics **117**, 10156 (2002): *Structures of hard-sphere fluids from a modified fundamental-measure theory*.

[80] M. Oettel, S. Görig, A. Härtel, H. Löwen, M. Radu, and T. Schilling, Phys. Rev. E **82**, 051404 (2010): *Free energies, vacancy concentrations, and density distribution anisotropies in hard-sphere crystals: A combined density functional and simulation study*.

[81] A. Santos, Phys. Rev. E **86**, 040102 (2012): *Class of consistent fundamental-measure free energies for hard-sphere mixtures*.

[82] H. Hansen-Goos, M. Mortazavifar, M. Oettel, and R. Roth, Phys. Rev. E **91**, 052121 (2015): *Fundamental measure theory for the inhomogeneous hard-sphere system based on Santos' consistent free energy*.

[83] E. Kierlik and M. L. Rosinberg, Phys. Rev. A **42**, 3382 (1990): *Free-energy density functional for the inhomogeneous hard-sphere fluid: Application to interfacial adsorption.*

[84] S. Phan, E. Kierlik, M. L. Rosinberg, B. Bildstein, and G. Kahl, Phys. Rev. E **48**, 618 (1993): *Equivalence of two free-energy models for the inhomogeneous hard-sphere fluid.*

[85] E. Thiele, The Journal of Chemical Physics **38**, 1959 (1963): *Comparison of the Classical Theories of Unimolecular Reactions. II. A Model Calculation, .*

[86] Y. Rosenfeld, The Journal of Chemical Physics **98**, 8126 (1993): *Free energy model for inhomogeneous fluid mixtures: Yukawa–charged hard spheres, general interactions, and plasmas.*

[87] E. Kierlik and M. L. Rosinberg, Phys. Rev. A **44**, 5025 (1991): *Density-functional theory for inhomogeneous fluids: Adsorption of binary mixtures.*

[88] P. Tarazona, J. A. Cuesta, and Y. Martínez-Ratón, *Theory and Simulation of Hard-Sphere Fluids and Related Systems* (2008), pp. 247–341.

[89] H. Hansen-Goos and R. Roth, The Journal of Chemical Physics **124**, 154506 (2006): *A new generalization of the Carnahan-Starling equation of state to additive mixtures of hard spheres.*

[90] K. R. Mecke, International Journal of Modern Physics B **12**, 861 (1998): *Integral geometry in statistical physics.*

[91] P.-M. König, R. Roth, and K. R. Mecke, Phys. Rev. Lett. **93**, 160601 (2004): *Morphological Thermodynamics of Fluids: Shape Dependence of Free Energies.*

[92] P.-M. König, P. Bryk, K. Mecke, and R. Roth, EPL (Europhysics Letters) **69**, 832 (2005): *Curvature expansion of density profiles.*

[93] P. Bryk, R. Roth, K. R. Mecke, and S. Dietrich, Phys. Rev. E **68**, 031602 (2003): *Hard–sphere fluids in contact with curved substrates.*

[94] M. Oettel, H. Hansen-Goos, P. Bryk, and R. Roth, EPL (Europhysics Letters) **85**, 36003 (2009): *Depletion interaction of two spheres: Full density functional theory vs. morphometric results.*

[95] A. Härtel, M. Oettel, R. E. Rozas, S. U. Egelhaaf, J. Horbach, and H. Löwen, Phys. Rev. Lett. **108**, 226101 (2012): *Tension and Stiffness of the Hard Sphere Crystal-Fluid Interface.*

[96] A. Santos, The Journal of Chemical Physics **136**, 136102 (2012): *Note: An exact scaling relation for truncatable free energies of polydisperse hard-sphere mixtures.*

[97] J. A. Gualtieri, J. M. Kincaid, and G. Morrison, The Journal of Chemical Physics **77**, 521 (1982): *Phase equilibria in polydisperse fluids.*

[98] P. Sollich, Journal of Physics: Condensed Matter **14**, R79 (2002): *Predicting phase equilibria in polydisperse systems.*

[99] P. Sollich, P. B. Warren, and M. E. Cates, in *Advances in Chemical Physics* (2007), pp. 265–336.

[100] J. F. Lutsko, Phys. Rev. E **87**, 014103 (2013): *Direct correlation function from the consistent fundamental-measure free energies for hard-sphere mixtures.*

[101] R. Speedy, Journal of Physics: Condensed Matter **10**, 4387 (1998): *Pressure and entropy of hard-sphere crystals.*

[102] S. K. Kwak, Y. Cahyana, and J. K. Singh, The Journal of Chemical Physics **128**, 134514 (2008): *Characterization of mono- and divacancy in fcc and hcp hard-sphere crystals.*

[103] C. H. Bennett and B. J. Alder, The Journal of Chemical Physics **54**, 4796 (1971): *Studies in Molecular Dynamics. IX. Vacancies in Hard Sphere Crystals.*

[104] Y. Rosenfeld, D. Levesque, and J.-J. Weis, The Journal of Chemical Physics **92**, 6818 (1990): *Free-energy model for the inhomogeneous hard-sphere fluid mixture: Triplet and higher-order direct correlation functions in dense fluids.*

[105] H. N. W. Lekkerkerker, W. C.-K. Poon, P. N. Pusey, A. Stroobants, and P. B. Warren, EPL (Europhysics Letters) **20**, 559 (1992): *Phase Behaviour of Colloid + Polymer Mixtures.*

[106] F. L. Calderon, J. Bibette, and J. Biais, EPL (Europhysics Letters) **23**, 653 (1993): *Experimental Phase Diagrams of Polymer and Colloid Mixtures.*

[107] S. M. Ilett, A. Orrock, W. C. K. Poon, and P. N. Pusey, Phys. Rev. E **51**, 1344 (1995): *Phase behavior of a model colloid-polymer mixture.*

[108] R. L. C. Vink and J. Horbach, The Journal of Chemical Physics **121**, 3253 (2004): *Grand canonical Monte Carlo simulation of a model colloid–polymer mixture: Coexistence line, critical behavior, and interfacial tension.*

[109] M. Dijkstra, R. van Roij, R. Roth, and A. Fortini, Phys. Rev. E **73**, 041404 (2006): *Effect of many-body interactions on the bulk and interfacial phase behavior of a model colloid-polymer mixture.*

[110] M. Dijkstra, J. M. Brader, and R. Evans, Journal of Physics: Condensed Matter **11**, 10079 (1999): *Phase behaviour and structure of model colloid-polymer mixtures*.

[111] M. Schmidt, H. Löwen, J. M. Brader, and R. Evans, Phys. Rev. Lett. **85**, 1934 (2000): *Density Functional for a Model Colloid-Polymer Mixture*.

[112] J. M. Brader, R. Evans, and M. Schmidt, Molecular Physics **101**, 3349 (2003): *Statistical mechanics of inhomogeneous model colloid-polymer mixtures*.

[113] K. Binder, P. Virnau, and A. Statt, The Journal of Chemical Physics **141**, 140901 (2014): *Perspective: The Asakura Oosawa model: A colloid prototype for bulk and interfacial phase behavior*.

[114] M. Dijkstra, R. van Roij, and R. Evans, Phys. Rev. Lett. **81**, 2268 (1998): *Phase Behavior and Structure of Binary Hard-Sphere Mixtures*.

[115] M. Dijkstra, R. van Roij, and R. Evans, Phys. Rev. Lett. **82**, 117 (1999): *Direct Simulation of the Phase Behavior of Binary Hard-Sphere Mixtures: Test of the Depletion Potential Description*.

[116] M. Dijkstra, R. van Roij, and R. Evans, Phys. Rev. E **59**, 5744 (1999): *Phase diagram of highly asymmetric binary hard-sphere mixtures*.

[117] J. M. Brader, *Statistical Mechanics of a Model Colloid–Polymer Mixture*, Ph.D. thesis, H. H. Wills Physics Laboratory, University of Bristol, 2001.

[118] A. Santos, M. López de Haro, G. Fiumara, and F. Saija, The Journal of Chemical Physics **142**, 224903 (2015): *The effective colloid interaction in the Asakura–Oosawa model. Assessment of non-pairwise terms from the virial expansion*.

[119] X. Wang, J. Mi, and C. Zhong, The Journal of Chemical Physics **138**, 164704 (2013): *Density functional theory for crystal-liquid interfaces of Lennard-Jones fluid*.

[120] M. A. van der Hoef, The Journal of Chemical Physics **113**, 8142 (2000): *Free energy of the Lennard-Jones solid*.

[121] K. R. Hall, The Journal of Chemical Physics **57**, 2252 (1972): *Another Hard–Sphere Equation of State*.

[122] A. Gast, C. Hall, and W. Russel, Journal of Colloid and Interface Science **96**, 251 (1983): *Polymer–induced phase separations in nonaqueous colloidal suspensions*.

[123] E. J. Meijer and D. Frenkel, The Journal of Chemical Physics **100**, 6873 (1994): *Colloids dispersed in polymer solutions. A computer simulation study*.

[124] G. J. Fleer and R. Tuinier, Advances in Colloid and Interface Science **143**, 1 (2008): *Analytical phase diagrams for colloids and non-adsorbing polymer*.

[125] A. S. Bharadwaj and Y. Singh, The Journal of Chemical Physics **143**, 124503 (2015): *Fluid-solid transition in simple systems using density functional theory*.

[126] J. M. Häring, C. Walz, G. Szamel, and M. Fuchs, Phys. Rev. B **92**, 184103 (2015): *Coarse-grained density and compressibility of nonideal crystals: General theory and an application to cluster crystals*.

[127] A. Statt, P. Virnau, and K. Binder, Phys. Rev. Lett. **114**, 026101 (2015): *Finite-Size Effects on Liquid-Solid Phase Coexistence and the Estimation of Crystal Nucleation Barriers*.

[128] A. Statt, P. Virnau, and K. Binder, Molecular Physics **113**, 2556 (2015): *Crystal nuclei in melts: A Monte Carlo simulation of a model for attractive colloids*.

[129] Y. Kraftmakher, Physics Reports **299**, 79 (1998): *Equilibrium vacancies and thermophysical properties of metals*.

[130] Y. Kraftmakher, *Lecture Notes on Equilibrium Point Defects and Thermophysical Properties of Metals* (2000).

[131] B. Grabowski, T. Hickel, and J. Neugebauer, physica status solidi (b) **248**, 1295 (2011): *Formation energies of point defects at finite temperatures*.

[132] R. Nazarov, T. Hickel, and J. Neugebauer, Phys. Rev. B **85**, 144118 (2012): *Vacancy formation energies in fcc metals: Influence of exchange-correlation functionals and correction schemes*.

[133] S. Pronk, , and D. Frenkel, The Journal of Physical Chemistry B **105**, 6722 (2001): *Point Defects in Hard-Sphere Crystals*.

[134] G. Jacucci and M. Ronchetti, Solid State Communications **33**, 35 (1980): *Monte Carlo calculation of the concentration of lattice vacancies by the method of overlapping distributions*.

[135] M. S. Daw and M. I. Baskes, Phys. Rev. B **29**, 6443 (1984): *Embedded–atom method: Derivation and application to impurities, surfaces, and other defects in metals*.

[136] M. S. Daw, S. M. Foiles, and M. I. Baskes, Materials Science Reports **9**, 251 (1993): *The embedded–atom method: a review of theory and applications*.

[137] S. M. Foiles, Phys. Rev. B **32**, 3409 (1985): *Application of the embedded-atom method to liquid transition metals*.

[138] S. M. Foiles, M. I. Baskes, and M. S. Daw, Phys. Rev. B **33**, 7983 (1986): *Embedded-atom-method functions for the fcc metals Cu, Ag, Au, Ni, Pd, Pt, and their alloys*, .

[139] Y. Mishin, D. Farkas, M. J. Mehl, and D. A. Papaconstantopoulos, Phys. Rev. B **59**, 3393 (1999): *Interatomic potentials for monoatomic metals from experimental data and ab initio calculations*.

[140] M. H. Yamani and M. Oettel, Phys. Rev. E **88**, 022301 (2013): *Stable and metastable hard-sphere crystals in fundamental measure theory*.

[141] M. A. van der Hoef, The Journal of Chemical Physics **117**, 5092 (2002): *Gas–solid coexistence of the Lennard–Jones system*.

[142] M. Matty, M. Mortazavifar, and M. Oettel, Cluster expansion and vacancy interaction in fcc crystals, preprint (unpublished).

[143] M. S. Daw, S. M. Foiles, and M. I. Baskes, Materials Science Reports **9**, 251 (1993): *The embedded-atom method: a review of theory and applications*.

[144] R. E. Rozas and J. Horbach, A comparison of EAM models of Ni close to the melting temperature, preprint (unpublished).

[145] W. Wycisk and M. Feller-Kniepmeier, Journal of Nuclear Materials **69**, 616 (1978): *Quenching experiments in high purity Ni*.

[146] S. M. Foiles, Phys. Rev. B **49**, 14930 (1994): *Evaluation of harmonic methods for calculating the free energy of defects in solids*.

[147] A. Glensk, B. Grabowski, T. Hickel, and J. Neugebauer, Phys. Rev. X **4**, 011018 (2014): *Breakdown of the Arrhenius Law in Describing Vacancy Formation Energies: The Importance of Local Anharmonicity Revealed by Ab initio Thermodynamics*.

[148] D. G. Grier, Current Opinion in Colloid & Interface Science **2**, 264 (1997): *Optical tweezers in colloid and interface science*.

[149] I. Williams, E. C. Oguz, P. Bartlett, H. Löwen, and C. P. Royall, Nat. Commun. **4**, 2555 (2013): *Direct measurement of osmotic pressure via adaptive confinement of quasi hard disc colloids*.

[150] R. Zargar, B. Nienhuis, P. Schall, and D. Bonn, Phys. Rev. Lett. **110**, 258301 (2013): *Direct Measurement of the Free Energy of Aging Hard Sphere Colloidal Glasses*.

[151] M. Frigo and S. G. Johnson, in *Acoustics, Speech and Signal Processing, 1998. Proceedings of the 1998 IEEE International Conference on*, IEEE (1998), Vol. 3, pp. 1381–1384.

[152] M. Frigo and S. G. Johnson, Proceedings of the IEEE **93**, 216 (2005): *The design and implementation of FFTW3.*

[153] R. Roth, Journal of Physics: Condensed Matter **22**, 063102 (2010): *Fundamental measure theory for hard-sphere mixtures: a review.*

[154] P. Pulay, Chemical Physics Letters **73**, 393 (1980): *Convergence acceleration of iterative sequences. the case of scf iteration.*

[155] P. Pulay, Journal of Computational Chemistry **3**, 556 (1982): *Improved SCF convergence acceleration.*

[156] A. Kovalenko, S. Ten-no, and F. Hirata, Journal of Computational Chemistry **20**, 928 (1999): *Solution of three-dimensional reference interaction site model and hypernetted chain equations for simple point charge water by modified method of direct inversion in iterative subspace.*

[157] M. S. Daw and M. I. Baskes, Phys. Rev. Lett. **50**, 1285 (1983): *Semiempirical, Quantum Mechanical Calculation of Hydrogen Embrittlement in Metals.*

[158] E. Clementi and C. Roetti, Atomic Data and Nuclear Data Tables **14**, 177 (1974): *Roothaan-Hartree-Fock atomic wavefunctions: Basis functions and their coefficients for ground and certain excited states of neutral and ionized atoms, $Z \leq 54$.*

[159] A. McLean and R. McLean, Atomic Data and Nuclear Data Tables **26**, 197 (1981): *Roothaan-Hartree-Fock atomic wave functions Slater basis-set expansions for $Z = 55$–92.*

[160] W. H. Press, S. A. Teukolsky, W. T. Vetterling, and B. P. Flannery, *Numerical recipes in C* (1996), Vol. 2.

[161] J. H. Rose, J. R. Smith, F. Guinea, and J. Ferrante, Phys. Rev. B **29**, 2963 (1984): *Universal features of the equation of state of metals.*

LIST OF FIGURES

LIST OF TABLES

Curriculum vitae (Lebenslauf)

General Information

Name:	Mostafa Mortazavifar
Date and place of birth:	29.12.1984 / Tehran, Iran
Nationality:	Iranian
Personal email:	mostafa.mrtazavi@gmail.com

Education

9/1999 - 8/2002	Allameh-Helli High School, Tehran, Iran.
8/2002	Diploma in Mathematics and Physics, GPA 18.19/20.
9/2002 - 7/2003	Pre-University course in Mathematics and Physics, Allameh-Helli High School, Tehran, Iran. GPA: 19.63/20.
7/2003	National University Entrance Exam, ranked 348 out of 200,000 participants in Mathematics and Physics.
9/2003 - 8/2009	Undergraduate studies in Electrical Engineering, Amirkabir University of Technology (Tehran Polytechnic), Tehran, Iran.
8/2009	Bachelor of Science in Electrical Engineering (Telecommunication).
	Title of bachelor's thesis: *Design and analysis of an active frequency mixer with Substrate–Integrated–Waveguide transition lines.*
	Supervisor: Dr. Gholamreza Moradi (Associate Professor).
9/2009 - 12/2011	Graduate studies in Physics, Institute for Advanced Studies in Basic Sciences (IASBS), Gava-Zang, Zanjan, Iran.
12/2011	Master of Science in Condensed Matter Physics, GPA: 17.19/20.
	Title of master's thesis: *The abelian sandpile model with fractal dissipations.*
	Supervisor: Dr. Mohammad Dehghan Niry (Assistant Professor).
9/2012 - 10/2016	Postgraduate studies in Physics, Computational Soft Matter and Nanoscience (AG Prof. Oettel), Institut für Angewandte Physik, Eberhard Karls Universität Tübingen, Tübingen, Germany.
	Title of doctoral dissertation: *Equilibrium properties of crystals in the Hard–sphere and the Asakura–Oosawa model.*
	Supervisors: Prof. Dr. Martin Oettel, Prof. Dr. Roland Roth.